Volcanic Information Derived from Satellite Data

Dr Fred Prata

Climate and Atmosphere Department
Norwegian Institute for Air Research
Kjeller, Norway.
Email: fred.prata@nilu.no

April 18, 2011

Contents

Chapter 1

Context

Volcanic ash contains silicate minerals that can adversely affect the performance of jet engines, and in severe cases may result in flame out and loss of power. There are now many examples of incidents involving jet aircraft encounters with volcanic ash that have resulted in loss of power and severe damage to engines (Guffanti *et al.*, 2010). The recent eruptions at Eyjafjallajökull, Iceland in April and May 2010 prompted aviation regulators to ground airlines with subsequent loss of revenue and cost to the economy. The main information used to indicate whether "safe" levels of ash concentrations were within European airspace came from dispersion models. These models rely on wind information and more importantly require accurate input data on the source characteristics or source term, (e.g. eruption rate, timing, column height and particle size distribution, among other parameters) in order to provide an accurate forecast of ash concentrations in the atmosphere. During the Eyjafjallajökull eruptions the source term was poorly constrained and this led to criticisms of the veracity of the ash concentration forecasts. Satellite data provides a powerful means to constrain the source term and also provides information to validate model simulations. Unfortunately, although satellite data were available (and used), quantitative retrievals were not readily accessible as operational products (e.g. column abundances and particle size distributions). Several research institutes and agencies were able to provide retrievals on an *ad hoc* basis. There need to turn these *research* products into *operational* products.

Following the volcanic crisis, the two main European space agencies–ESA and Eumetsat, gathered European and international experts to a workshop held at ESA's Frascati site, to discuss and recommend ways to improve the provision of satellite data to the aviation industry. The recommendations from this workshop are provided in a comprehensive report (Zehner, 2010). One outcome of the workshop was a recognition that quantitative volcanic ash products using data from the Meteosat Second Generation (MSG), Spinning Enhanced Visible and InfraRed Imager (SEVIRI) could be used in near real-time to provide estimates of the particle sizes and mass loadings following ash eruptions. The major advantages of SEVIRI over other sensors in this context are:

1. Up to 5 minute temporal sampling.
2. Good spatial coverage and resolution (see Figure 1).
3. Five infrared channels covering ash and SO_2 detection.

Another, more subtle advantage when using geosynchronous measurements for high-latitude ash-rich

eruptions arises from the oblique view which provides a longer pathlength through the ash cloud and greater detectability for thin ash clouds (see later).

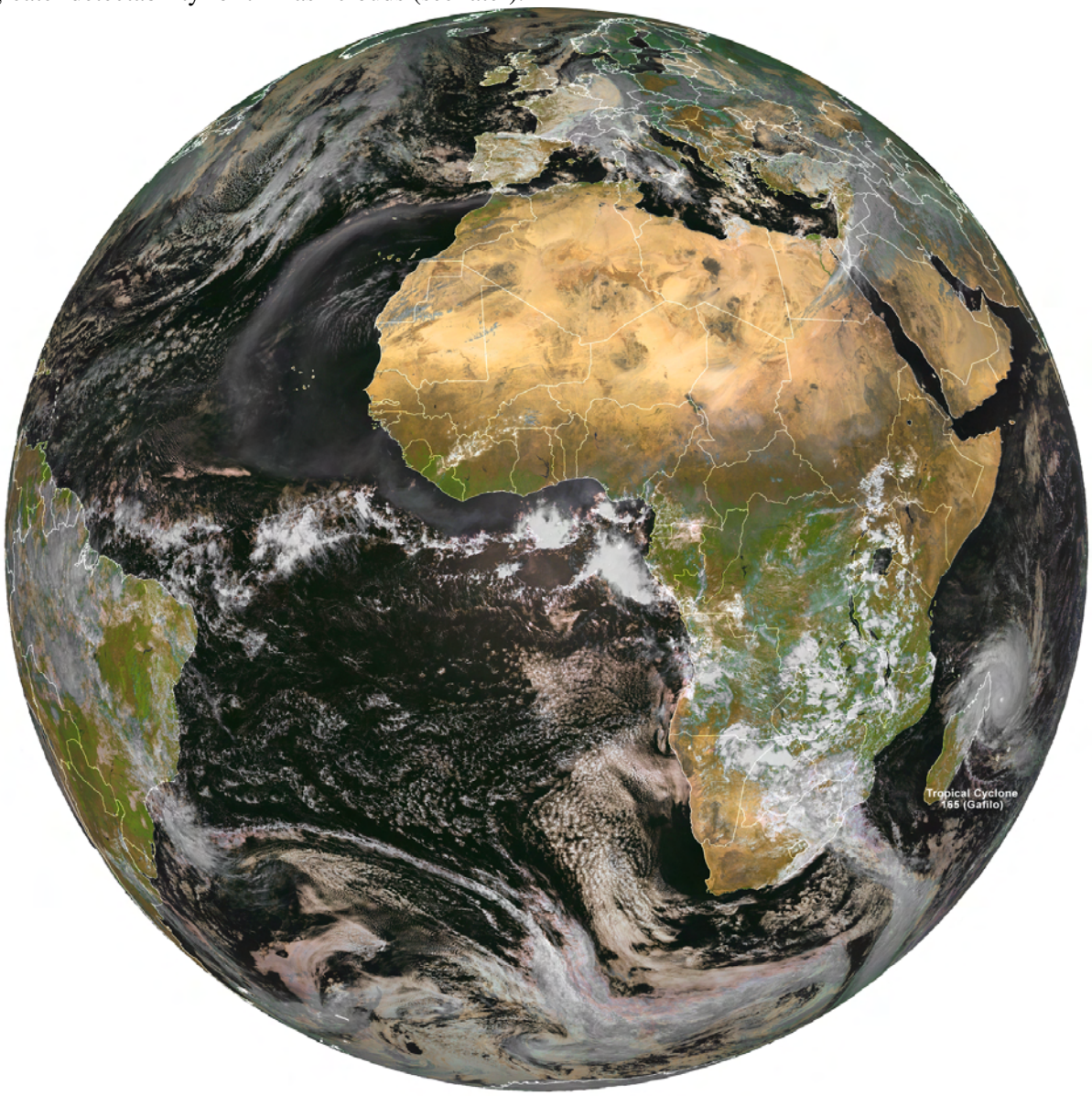

Figure 1. The SEVIRI view of Africa, Europe and the high-latitudes.

Eumetsat decided to investigate the possibility of implementing operational quantitative volcanic ash products to complement its existing services of near real time enhanced visible and infrared ash products. The new products were to be based on existing retrieval schemes and should include a validation protocol and an ability to determine SO_2. The main candidate for the ash retrieval is the well-known "reverse absorption" algorithm (Prata, 1989a,b) and the various improvements to it (e.g. Wen and Rose, 1994; Prata and Grant, 2001). For SO_2 it was decided to investigate the use of a regression-based approach, recognising that the

UV sensors GOME-2 and OMI would provide a more accurate estimate of the partial column abundance, but with limited temporal coverage (once per day and no nighttime measurements) it seems sensible to try to utilise SEVIRI. Given the unpredictable and sporadic nature of volcanic activity, it was decided to rely only on the infrared channels, so that both day and night coverage was possible using the same techniques and algorithms.

It is recognised that there are many improvements possible to ash detection and quantification from satellite measurements and that there is ongoing research into this problem. Thus, this report provides a first step towards operational ash products with the expectation that continuous validation and improvements will occur.

The remainder of this report is as follows: Chapter 2 provides a description of the SEVIRI instrument. Chapter 3 provides the framework for the retrieval scheme and discusses error sources and limitations of the algorithms. A simple "heuristic" model is introduced which encapsulates the main physics of the problem. Chapter 4 takes this further and discusses the more complex radiative transfer and microphysical models. Chapter 5 discusses SO_2 retrievals and describes the theoretical basis for using infrared channels to determine SO_2 partial column abundances. Chapter 6 discusses the results of the ash retrievals and Chapter 7 discusses the results of the SO_2 retrievals. Validation is also provided in these chapters. Chapter 8 provides a summary, conclusions and suggestions for further work. A thorough list of references is provided, but many of these are not referred to directly in the text, rather they are provided as background material for volcanic ash research literature. There are two Appendices that include a list of acronyms, and a description of the data-set. The code and source listings are provided in a separate document–"Retrieval Code and Listings". The data-sets, code (software) and retrieval products are also provided on separate media and will be housed by Eumetsat on their ftp server. The main data-set used in the Report is described in Appendix II. This data-set is a perhaps the most comprehensive set of satellite measurements for the April/May 2010 Eyjafjallajökull eruptions and covers the domain from 30 °W to 30 °E, 40 °N to 70 °N at 15 minute intervals for the period 14 April to 23 May, 2010.

Chapter 2

SEVIRI

2.1 The SEVIRI instrument

Only a very brief outline of the SEVIRI instrument is provided here. For more detailed information see: `http://www.eumetsat.int/Home/Main/Satellites/MeteosatSecondGeneration/Instruments/index.htm` and Schmetz *et al.*(2002). SEVIRI has 12 narrow-band ($\tilde{1}$ μm) channels covering the visible to the infrared regions of the electromagnetic spectrum. We are only concerned with the infrared channels, of which there are 5 of interest here (6.2–12.0 μm). The instrument is in geosynchronous orbit situated approximately over 0° longitude and 0° latitude. The total field of view is approximately 70° providing coverage of the Earth from about 70°S to 70°N and 70°W to 70°E. There are 3712 x 3712 pixels covering the full-disk. A subset of 1537x494 pixels were used in this study, which covers the geographic domain 30°W to 30°E, 40°N to 70°N. Pixel size in the infrared channels is approximately 10 km^2 at the sub-satellite point getting progressively larger at the edges to an extreme size of more than 100 km^2. For the case of the Eyjafjallajökull eruptions at 19.62°W, 63.63°N, the pixel size is $\sim$80 km^2. Table 1 shows the salient details of the five infrared channels employed in this study.

2.2 Infrared channels

Channel	Centre wavelength (μm)	Nominal Spectral Bandwidth (μm)	Dynamic Range (K)	Radiometric Noise (K)
WV62	6.25	5.35–7.15	0–300	0.21 250
WV73	7.35	6.85 –7.85	0–300	0.20 250
IR87	8.70	8.30–9.10	0–300	0.12 300
IR10	10.8	9.80–11.80	0–335	0.10 300
IR12	12.0	11.00–13.00	0–335	0.15 300

Table 2.1: Details of the SEVIRI infrared channels used in this study.

2.3 Earth location

Nominal geolocations of the SEVIRI pixels were obtained from a pre-computed data-set consisting of longitudes and latitudes on a 3712 x 3712 grid. It was assumed that these geolocations were of sufficient accuracy for the purpose of this study. The source of the data-set is:

Figure 2.1 shows a map of the SEVIRI pixel areas for the geographic region of interest. Close to Iceland pixel areas vary from 50–100 km^2; for most of the domain pixel areas are between 10–20 km^2.

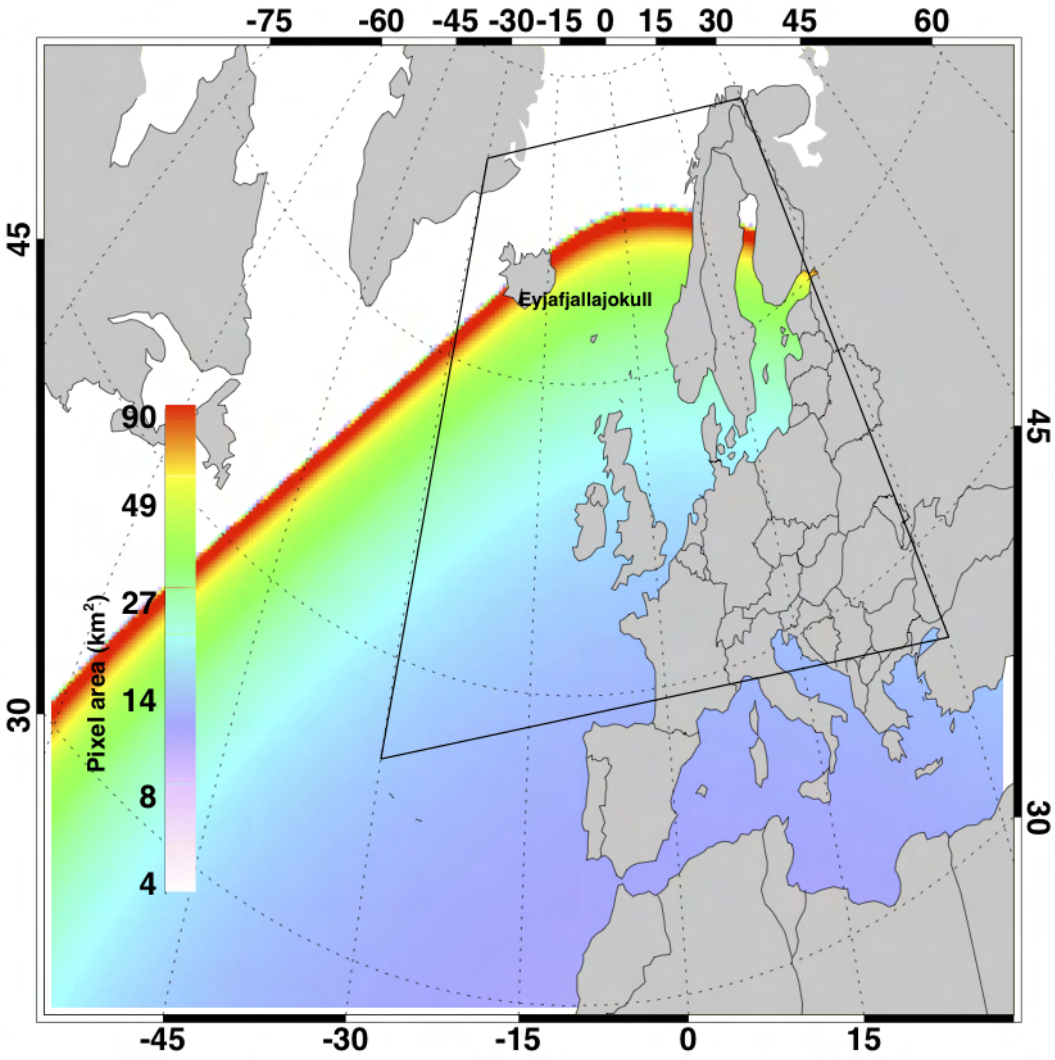

Figure 2.1: Pixel area (in km^2) and domain of interest, shown as the quadrilateral region.

2.4 Calibration

The data-set used was obtained from the NILU Eumetcast receiver and radiances were converted to brightness temperatures using the recommended procedures described in EUM/OPS-MSG/TEN/08/0024, v1, 28 January, 2008, available from `http://www.eumetsat.int`. Throughout this study only top-of-the-atmosphere brightness temperatures were used.

2.5 Parallax correction

A parallax correction was applied to all pixels using a nominal cloud height of 6 km. Although it is necessary to know the height of the cloud before applying the correction, no ash cloud height was available and so a nominal height was used. This assumption has no impact on the volcanic ash detection or the retrieval but in practice it would be worthwhile inserting an iterative step whereby the cloud height is obtained after an initial assumption and then a recomputation of the geolocations is applied. The computation of the cloud height may be done through an analysis of the data or obtained from an independent estimate (perhaps a model calculation). The code used to determine the parallax is listed in Appendix IV, of the Supplement to this Report.

2.6 Eyjafjallajökull data-set

The full data-set consists of:

1 1537 pixels by 494 lines.

2 Geographic region, approximately: 30°W to 30°E, 40°N to 70°N.

3 5 infrared channels: WV62, WV73, IR86, IR10 and IR12.

4 15 minute samples starting on 14.04.2010 00:00 UTC and ending on 22.05.2010 23:45 UTC.

The data are also described in Appendix II.

Chapter 3

Volcanic Ash Detection

3.1 Physical principles of ash detection in the infrared

Volcanic ash is a hazard to aircraft (Casadevall, 1994; Casadevall *et al.*, 1996; Miller and Casadevall, 1999). The problem of detecting volcanic clouds from satellites is really a problem of discrimination. Clouds absorb, emit and scatter radiation in the visible, infrared and microwave regions of the electromagnetic spectrum. At visible wavelengths, depending on the geometry of illumination (by the Sun or using a laser light source) and the geometry of observation, clouds may appear bright or dark. This is true of clouds of water, ice, silicates (volcanic ash), wind blown dust (desert dust), smoke (e.g. from a large forest fire) or any other naturally or anthropogenically generated cloud of particles. It is sometimes very clear that a particular cloud is meteorological in origin (for example, a cloud of water droplets or ice particles, or a mixed phase cloud), but often not so clear that it is not a meteorological cloud. Figure 3.1(a)–(h) show some satellite images of "anomalous" clouds in the atmosphere. These are daytime MODIS images that have been enhanced to provide a "true-colour" rendition of the scene. In all these scenes there are meteorological clouds and clouds due to other sources: (a) a thick ash column rising above Ruang volcano (Sangihie islands, Indonesia, 125.37 °E, 2.30 °N), (b) a drifting ash and gas plume recently emitted from Karthala volcano, Comoros (11.75 °S, 43.38 °E), (c) a low-level gas (predominantly SO_2 and H_2O) from Ambrym volcano, Vanuatu (16.25 °S, 168.12 °E), (d) an ash and gas plume over snow-covered terrain from Kluchevskoi volcano, Kamchatka (56.057 °N, 160.638 °E) , (e) an ash and gas plume from Kluchevskoi, but in the summer, (f) a noxious cloud generated from an industrial accident in southern England, (g) a dust outbreak travelling westwards over the Canary Islands (28.00 °N, 15.58 °W), and (h), wind-blown ash off the coast of Iceland. These examples illustrate some of the variability found in anomalous clouds when viewed by satellites during the day. Some clouds appear almost black (Fig. 3.1f) or dark grey (Fig. 3.1h), some are as white as water/ice clouds (Fig. 3.1c and Fig. 3.1d), while others take various sandy shades with brown and yellow hues (Fig. 3.1a, b, e and g). By using objective analysis of daytime visible imagery alone, it has been very difficult to unambiguously discriminate ash clouds from other clouds. During the nighttime, the task is made even more difficult. This is the main reason why researchers have turned their attention to using infrared data (e.g. Hanstrum and Watson, 1983; Prata, 1989a,b; Barton *et al.*, 1992; Ellrod *et al.*, 2003).

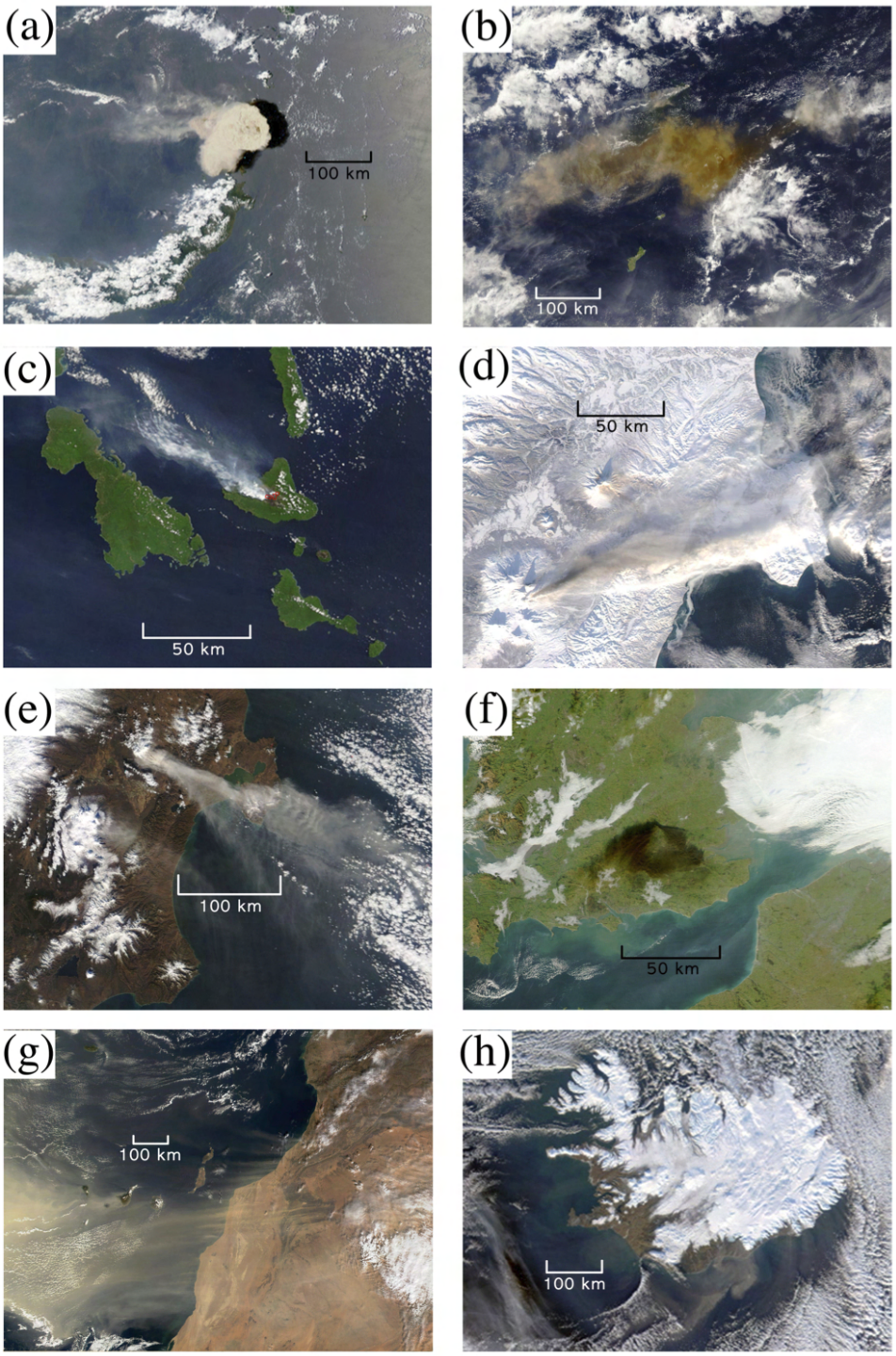

Figure 3.1: Daytime MODIS scenes showing ”anomalous” clouds. (a) Thick ash column from Ruang volcano, (b) drifting ash and gas plumes from Karthala volcano, (c) low-level gas cloud plume , (d) ash and gas plume over snow covered terrain (Kluichevskoi volcano), (e) ash and gas plume from Kluichevskoi during the summer, (f) a noxious gas cloud from an industrial fire in southern England, (g) a dust outbreak over the Canary islands, and (h) wind blown ash streaming off the southern coast of Iceland.

3.2 Modelling radiative transfer in ash clouds

3.2.1 Heuristic model

In order to isolate the important factors affecting the raditaive transfer (RT) inside an ash cloud, we propose a heuristic model with some simplifying assumptions. First, the atmosphere below the cloud layer is assumed to be totally transparent: I_a=0. Second, the earth's surface below the cloud is assumed to be a black-body: I_s=$B[T_s]$. Third, we consider nadir viewing only: ϕ=0, θ=0. Fourth, we consider the cloud to consist of homogeneous particles at a single temperature, T_c. Finally, rather than consider a broad spectrum of narrow bands we take just two:

$$I_{\lambda_1} = B_{\lambda_1}[T_s]\exp(-\tau_1) + (1-\exp(-\tau_1))B_{\lambda_1}[T_c], \tag{3.1}$$

$$I_{\lambda_2} = B_{\lambda_2}[T_s]\exp(-\tau_2) + (1-\exp(-\tau_2))B_{\lambda_2}[T_c]. \tag{3.2}$$

These two equations can be linearized (see Prata and Grant, 2001 for details) and noting that the cloud emissivity is $1-\exp(-\tau)$ we may write:

$$T_1 = T_s(1-\epsilon_1) + \epsilon_1 T_c, \tag{3.3}$$

$$T_2 = T_s(1-\epsilon_2) + \epsilon_2 T_c, \tag{3.4}$$

$$\epsilon_i = 1-\exp(-\tau_i), \tag{3.5}$$

$$\tau_i = k_i L, \tag{3.6}$$

where k_i is the absorption coefficient of the particles at wavelength i and L is the geometric thickness of the cloud. These equations can be solved to obtain,

$$\Delta T = \Delta T_c(X - X^\beta), \tag{3.7}$$

$$X = 1 - \frac{\Delta T_1}{\Delta T_c}, \tag{3.8}$$

$$\beta = \frac{k_2}{k_1}, \tag{3.9}$$

where, ΔT=$T_1 - T_2$, ΔT_c=T_s–T_c, and ΔT_1=T_s–T_1. The important physics is captured in the parameter β, the ratio of extinction coefficients at two wavelengths, λ_1 and λ_2. It is possible to explore the parameter range of β, guided by typical values for the extinction coefficients. Since the two wavelengths are usually close together the extinction coefficients are not very different and $\beta \approx 1$. A schematic of this model is shown in Figure 3.2. Figure 3.3 shows the variation of ΔT with T_1 for $\beta < 1$, $\beta > 1$ and $\beta = 1$. When $\beta < 1$, the extinction coefficient at $k_{\lambda_1} > k_{\lambda_2}$, which leads to a "**U**"–shaped curve, while for the opposite case $\beta > 1$ an "arch-shaped" curve results. If $\beta = 1$ then ΔT has no variation with T_1 and no information can be retrieved from this analysis. It turns out that for $\lambda_1 \approx 11$ μm and $\lambda_2 \approx 12$ μm, typical of channels on many satellite sensors, $\beta < 1$ for silicates (ash particles) and $\beta > 1$ for water molecules and ice particles. If one were free to design a sensor solely for ash detection, it would be sensible to select channels that optimize the "**U**"–shaped curve.

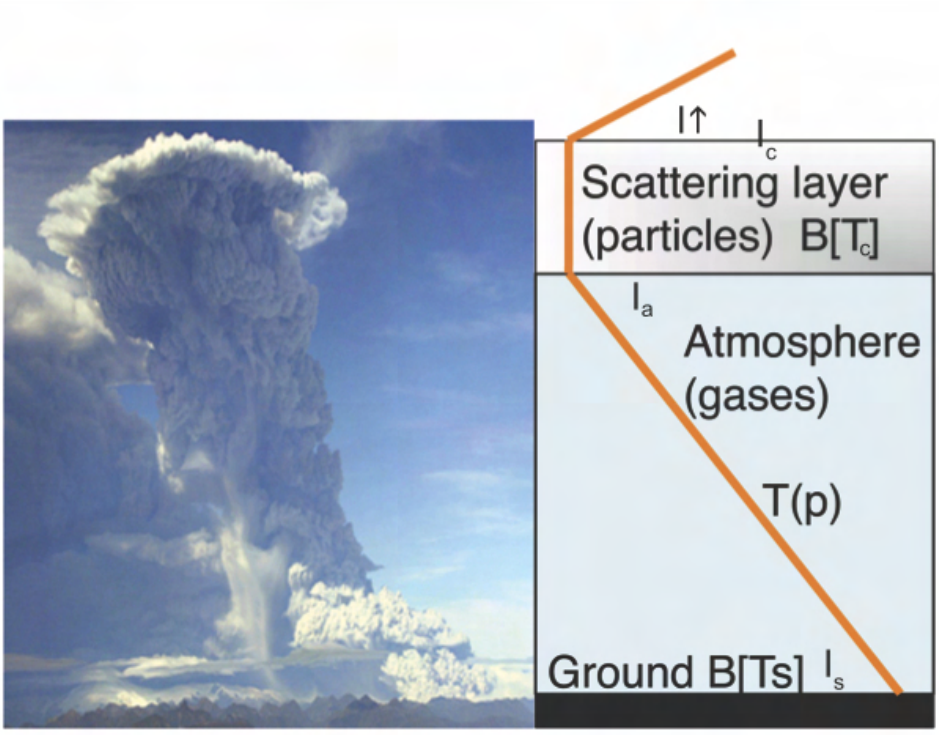

Figure 3.2: Idealised radiative transfer model for calculating the radiation propagation through an absorbing atmosphere and scattering layer of cloud particles. See text for the meaning of the various terms.

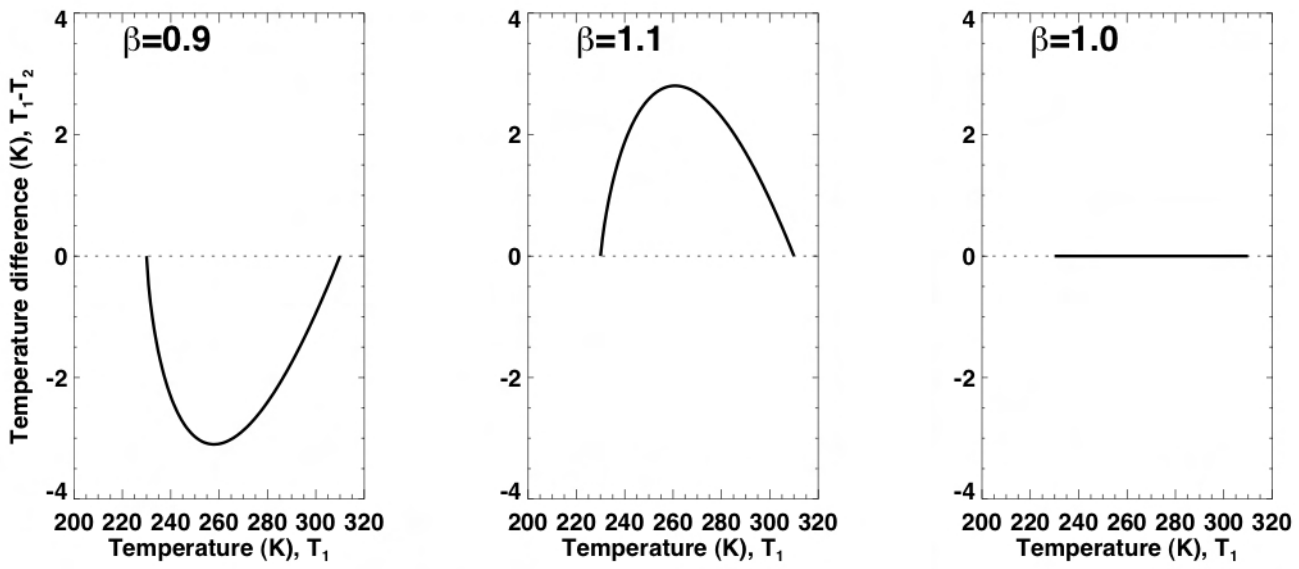

Figure 3.3: Variation of ΔT=$T_1 - T_2$ with T_1 for three values of the parameter β. When β=0.9 (left-panel) a characteristic "**U**"-shaped curve is found, indicative of silicate particles. Conversely, when β=1.1 (middle-panel) the curve is "arch-shaped" and indicates water molecules or ice particles. When β=1, there is no variation with T_1.

3.2.2 Solving the heuristic model

The simple model proposed here can be solved to determine the optical depth and radius corresponding to two measurements (T_{11}, T_{12}). Figure 3.4 shows curves generated from the heuristic model that illustrate the effects of particle radius and optical depth (infrared opacity) on the brightness temperatures and their difference. Each curve corresponds to a different mean effective radius (indicated in red), and optical depth (indicated in green).

The scatter of black points are actual SEVIRI observations, truncated with a value of BTD=0 K. By interpolating the curves in the data space (T_4, ΔT=T_4-T_5), values of the mean effective radius and infrared optical depth can be determined. In this example solutions are shown for points 1 and 2. It can be seen that as ΔT approaches 0, multiple solutions for the optical depth are realised for a single value of the effective radius. ΔT can approach 0 when either the ash clouds are very thick (then T_4 approaches T_c, the cloud-top temperature) or when the ash clouds are thin (then T_4 approaches T_s, the surface temperature).

3.2.3 Correcting for water vapour effects

One of the main problems with identifying ash in a cloud arises because often the ash is in a mixture with water molecules or ice particles. Water and ice clouds have $\beta > 1$ and therefore cause an opposite effect to that caused by ash clouds on the ΔT *vs* T_1 diagram[1] The simple model can be examined further to correct

[1]We use the subscripts 4 and 5 to indicate channels with wavelengths centred at 11 μm and 12 μm, a legacy from the use of AVHRR data, and more generally subscripts 1 and 2 to indicate two different channels, where channel 1 has a central wavelength

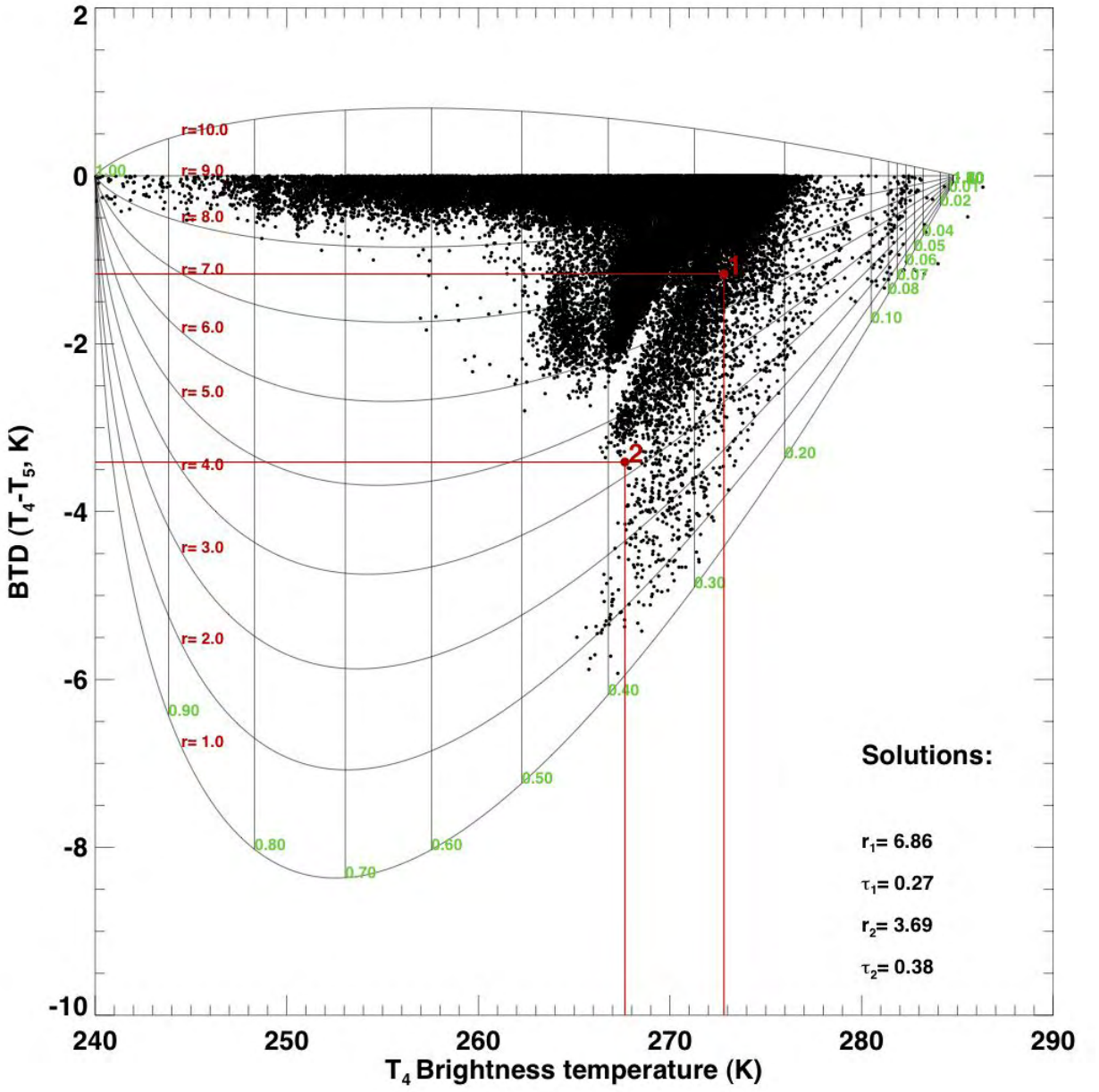

Figure 3.4: An example set of curves based on the heuristic model. In this case a simple parametric form for the variation of radius r with the parameter β has been developed. Solutions for two points are illustrated. The same principle for retrieval of r and optical depth, τ is used in the complex RT (see Chapter 4).

for water vapour effects, or at least understand how these effects manifest themselves. Assuming that the temperature difference observed arises from a linear combination of the signal from ash (ΔT_{ash}) and the signal due to water vapour (ΔT_{wv}). If the fraction of ash in the mixture is F, then we may write the observed

smaller than channel 2.

temperature difference as,

$$\Delta T = F\Delta T_s[Z - Z^{\beta}], \tag{3.10}$$

where,

$$Z = 1 - \frac{1}{F}\frac{\Delta T_1}{\Delta T_s},$$

The other parameters are defined as before. Ideally this procedure needs to be automated. There are several parameters that can be determined from the image data. These are:
(1) the clear-sky surface temperature T_s,
(2) the cloud-top temperature T_c,
(3) the clear-sky value of the water vapour correction, and
(4) the ratio of extinction coefficients β that governs the magnitude of the "U"-shaped distribution of negative differences.
A procedure for estimating these parameters from image data has been developed. A brief outline is given below.

1. T_s. This is easily estimated by finding the maximum value of T_1 occurring in the data.

2. T_c. This is more difficult to estimate from the data, because the lowest value may not necessarily correspond to the volcanic cloud. However, provided an area in close proximity to the suspect cloud can be delineated it may be reasonable to assume that the lowest value is the cloud-top temperature.

3. Water vapour correction. An empirical relation (Yu *et al.*, 2002) between the precipitable water in an atmospheric column and the brightness temperature difference $(T_1 - T_2)$ is used to estimate the water vapour effect"

   $$\Delta T_{wv} = \exp\left[6T_* - b\right], \tag{3.11}$$

   where $T_* = T_1/T_{max}$, and T_{max} is an arbitrary normalisation constant assigned a value of 320 K. The free parameter b essentially determines the value of the water vapour effect on $T_1 - T_2$ at the maximum value of T_1. Hence b can be determined directly from the image data, allowing realistic flexibility on the size of the water vapour correction determined by this semi-empirical approach.

4. β. Theoretical estimates of β suggest a value of around 0.7. A method for estimating β, T_s and T_c simultaneously has been developed by using the distribution of T_1 *vs* $T_1 - T_2$. The distribution is first histogrammed (or binned) into intervals of 0.5 K in T_1. Then, the lowest values in each bin are found and a curve is generated giving the outline of the distribution. The curve is smoothed and fitted using a nonlinear least squares model. The model has three parameters, *viz.*: T_s, $T_s - T_c$ and β that can be estimated from the fit.

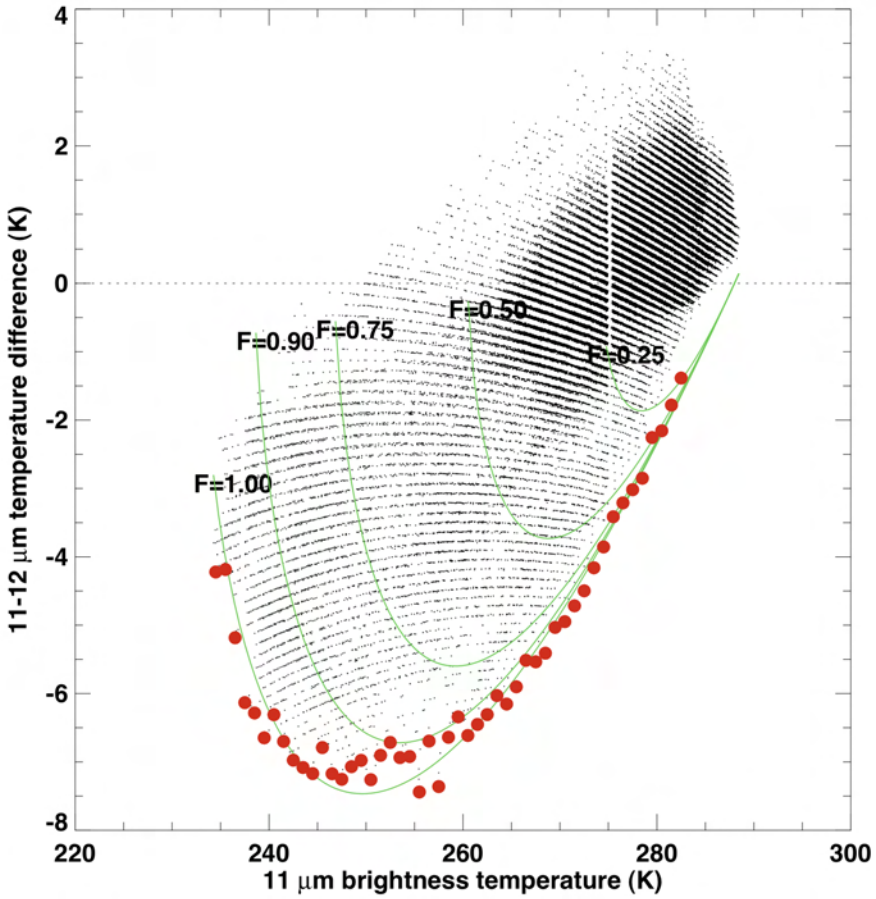

Figure 3.5: Distribution of $T_4 - T_5$ for an eruption of Ruapehu volcano. The green-coloured lines are isolines of the fraction of ash determined from Eq. (3.10). The red dots are estimates of the extrema of the distribution derived from the data.

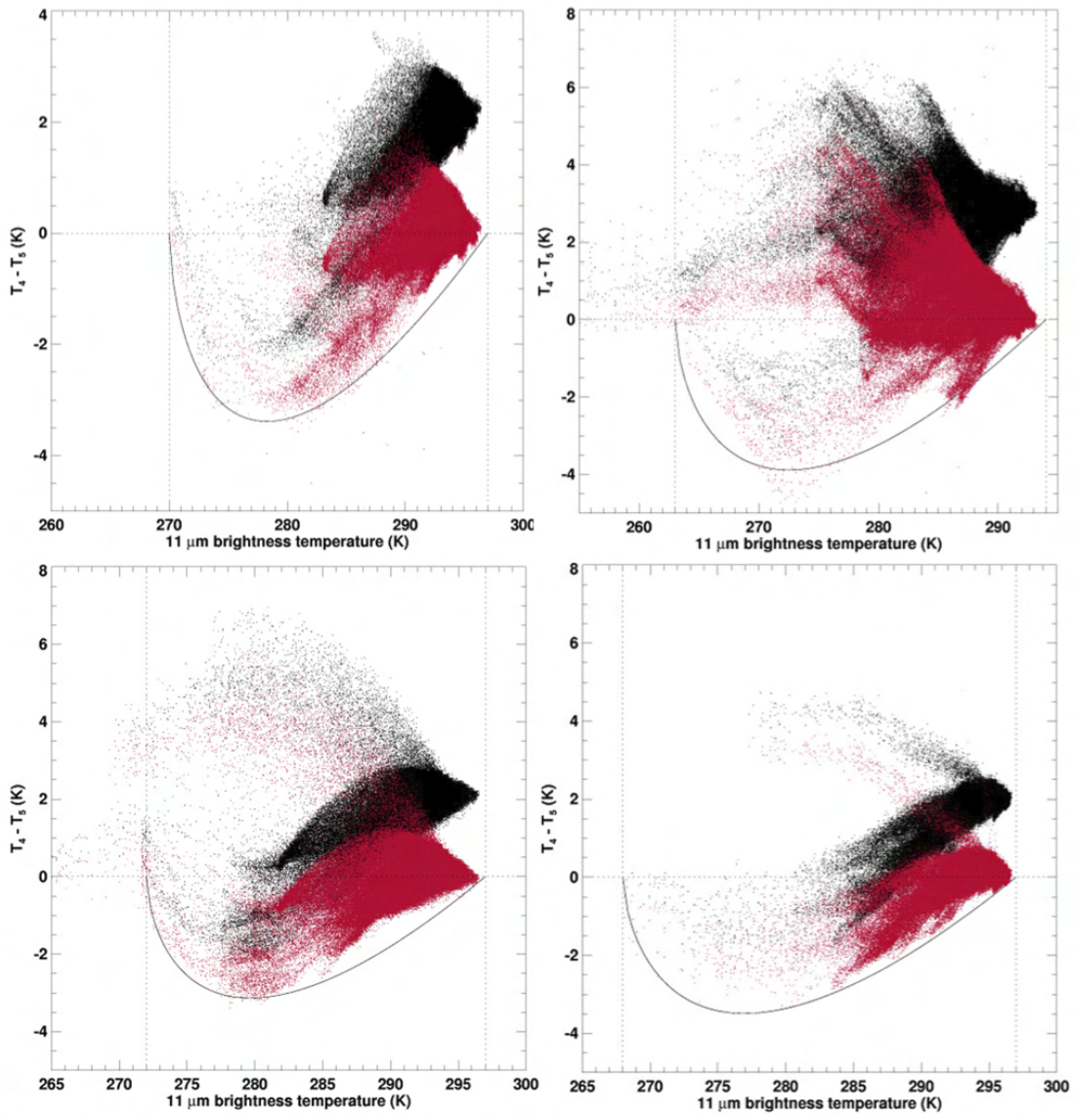

Figure 3.6: Temperature difference distributions without (black dots) and with (red dots) a water vapour correction for four different volcanic clouds using AVHRR data. T_4 and T_5 are AVHRR channel 4 (11 μm) and 5 (12 μm) brightness temperatures and correspond to T_1 and T_2 used in the theory here.

The curve-fitting procedure uses the model developed earlier with $F = 1$ and the partial derivatives of the model, which are analytic. Writing,

$$Y = \alpha(X - X^{\beta}),$$

where, Y=T_1-T_1, α=T_s-T_c, X=1-$\frac{\gamma}{\alpha}$, γ=T_s-T_1. The partial derivatives are,

$$\frac{\partial Y}{\partial \alpha} = (X - X^{\beta}) + \frac{\gamma}{\alpha} + \beta\frac{\gamma}{\alpha}(1 - \frac{\gamma}{\alpha})^{\beta-1},$$

$$\frac{\partial Y}{\partial \beta} = \alpha X^{\beta} Log\beta,$$

$$\frac{\partial Y}{\partial \gamma} = 1 - \beta X^{\beta-1}.$$

An example of the correction procedure is shown in Figure 3.6. The characteristic "**U**"-shaped curve indicating ash is apparent in the uncorrected (black dots) and water vapour-corrected (red dots) data. The solid line is determined from the simple model using a suitable value of β and values for T_s and T_c. The important point to note is that the water vapour correction does not simply decrease all the values uniformly, rather the correction rotates the points in a clockwise direction about a point close to ΔT=0 and T_{11}=T_s. This gives larger correction to points closer to T_s; points that are nearer the surface and hence expected to be affected greater by water vapour.

The simple model considers only absorption as the process for extinction of IR radiation. In reality scattering is also important and unfortunately this requires more complex modelling and the use of numerical methods.

3.3 Complex radiative transfer model

Prata (1989a,b), Wen and Rose (1994), Prata and Grant (2001) and Watson *et al.* (2004) have proposed RT models to solve the IR absorption/scattering processes for a volcanic ash cloud. The models essentially follow the theory outlined above, but the methods of solution differ in detail.

Wen and Rose (1994) and Prata and Grant (2001) have shown that by including a microphysical model of the ash particles with a detailed radiative transfer model, the infrared data can be inverted to reveal mean particle size and cloud opacity. When these parameters are integrated over the area covered by the cloud, the total mass and mass loading can be inferred from the data. These are quantifiable products that may be incorporated with dispersion models to generate risk maps for use by the aviation industry. An example of this kind of retrieval is given in Figure 3.7, for the Karthala eruption.

There are many satellites (polar and geosynchronous) that carry these infrared channels, so this product can be delivered globally. Table 3.1 gives details of some of the satellite instruments capable of providing ash mass loadings.

In the next Chapter we explore the complex radiative transfer model in more detail.

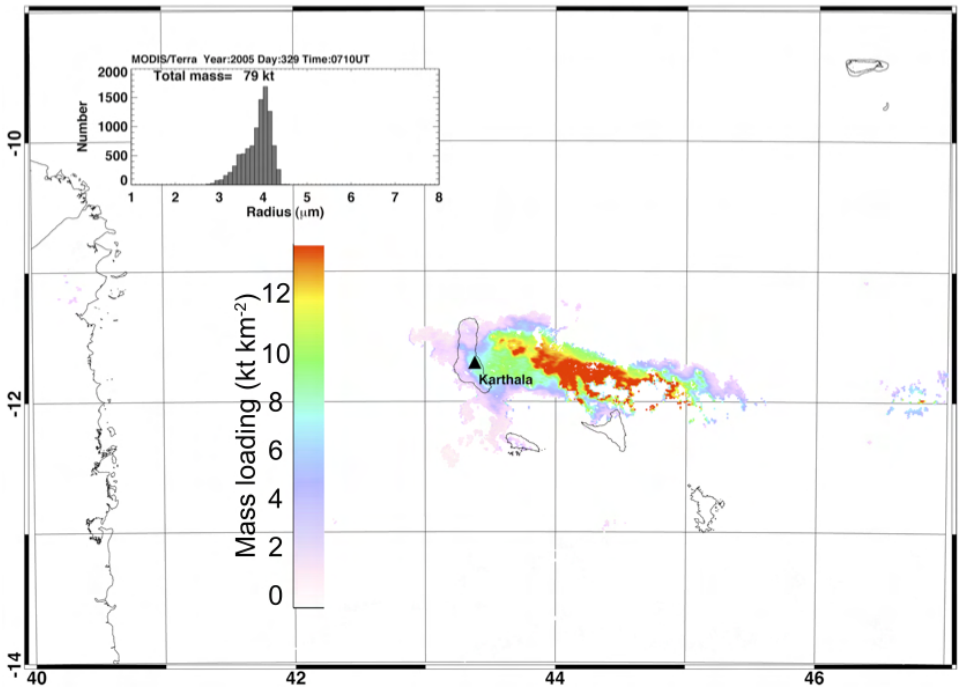

Figure 3.7: MODIS ash mass concentrations (kt km^{-2}) for an eruption of Karthala volcano in November, 2005.

Table 3.1: Details of past and current satellite instruments that can be used to detect ash and generate ash mass loading maps from infrared measurements.

Satellite	Instrument	Spatial resolution (km x km)	Temporal resolution (per day)	Time period covered
NOAA	AVHRR-2, -3	1 x 1	2	1981-present
NOAA	HIRS,-2, -3,-4	10 x 10[1]	2	1979-present
GOES	VISSR/VAS	5 x 5	24	1980-present
ENVISAT	ATSR-family	1 x 1	2[2]	1991-present
GMS-5	VISSR	5 x 5	24	1995-present
Terra/Aqua	MODIS	1 x 1	4[3]	1999-present
Aqua	AIRS	14 x 14	2	2002-present
MetOp	IASI	12 x 12	2	2007-present
MSG	SEVIRI	3 x 3	96	2006-present

[1]Earlier HIRS (1–3) instruments had a larger field of view of 18 x 18 km^2

[2]These satellite are in a 3-day repeat cycle, such that the same point imaged twice in one day will not be imaged again until 3 days later.

[3]Assuming two satellites in orbit at any given time

Chapter 4

Volcanic ash retrieval

4.1 Transmission of EM energy through a cloud

Satellite-borne infrared radiometers are used to measure atmospheric radiation in narrow (0.5–1.0 μm) wavelength bands, collecting energy from all components of the scene within the field-of-view of the instrument. In general terms it is possible to write down the radiative transfer equation (RTE) governing this kind of measurement, with some suitable approximations to make the problem tractable. A useful starting point is to consider a directional (downwards) measurement of a cloud-less atmosphere over a narrow band of infrared wavelengths, where contributions from solar radiation are negligible, ignore infra-red scattering and adopt plane-parallel geometry. With these conditions, we may write,

$$I_\lambda(\phi,\theta) = I_{s,\lambda}(\phi,\theta)\tau_{s,\lambda}(\phi,\theta) + \int_0^\infty B_\lambda[T(z)]\frac{\partial\tau_\lambda(z;\phi,\theta)}{\partial z}dz, \tag{4.1}$$

where,

I is the directional radiance measured at the sensor,

I_s is the radiation from the surface,

B is the Planck function,

T is temperature, $T(z)$ is the vertical temperature profile,

λ is wavelength,

z is height,

τ is the atmospheric transmittance,

ϕ is the azimuth angle, θ is the zenith angle,

All quantities are to be considered as averages over a narrow band–for notational convenience the band is designated by a single wavelength that represents the band-averaged central wavelength. The measured radiance consists of two terms: the first term represents radiation from the surface, and the second term

represents radiation (emission and absorption) from the atmosphere. The surface term can be divided further into surface emission and radiation from the atmosphere reflected back off the surface,

$$I_{s,\lambda} = \epsilon_{s,\lambda}(\phi,\theta)B_\lambda[T_s] + \frac{1}{2\pi}\int_\Omega I_{a,\lambda}(\phi,\theta)\rho_{s,\lambda}(\phi,\theta)\cos\theta\sin\theta d\Omega, \tag{4.2}$$

Here, Ω is the solid angle, $\epsilon_{s,\lambda}$ is the surface emissivity, ρ is the bi-direcional reflectance distribution function and T_s is the surface temperature. An assumption often made, and one that will be made here is to take,

$$\epsilon_{s,\lambda} = 1 - \rho_{s,\lambda}, \tag{4.3}$$

which assumes that the surface is Lambertian (i.e. there is no preferred direction for reflected radiation). Let us now introduce a plane-parallel cloud into this plane-parallel model[1] and adjust the RTE to include this layer.

$$I = I_s + I_a + I_c + I\uparrow, \tag{4.4}$$

where I_a is the atmospheric radiance (term 2 in [1.1]) but with the upper limit of the integral terminated at the base of the cloud (z_b), and I_c is the cloud radiance. We have omitted the notation for wavenumber and angular dependence for convenience. The term $I\uparrow$ represents atmospheric radiation above the cloud top (z_t) and can often be ignored. There is also radiation from above the cloud that is reflected off the cloud back towards the sensor, but this is a very small contribution and can be safely neglected. An idealised depiction of the model is shown in Figure 3.2. While scattering has been ignored in the atmosphere, it cannot be ignored in the cloud. In fact, without including the effects of scattering, the foundations for detecting ash clouds using infrared instruments would be flawed. The RTE for scattering by a layer of particles can be written,

$$\begin{aligned}\mu\frac{\partial I}{\partial t}(t,\mu) &= I(t,\mu) - (1-\varpi_o)B(T) \\ &- \frac{\varpi_o}{2}\int_{-1}^{1} P(\mu;\mu')I(\tau,\mu')d\mu'\end{aligned} \tag{4.5}$$

where $t = -\ln(-\tau)$ is the optical depth, μ is the cosine of the zenith angle, ϖ_o is the single scattering albedo and P is the axially-symmetric phase function. The cloud layer has an optical depth t_1 and we are only concerned with the upwelling radiance in the direction μ at the cloud top ($\tau = 0$). This equation can be solved using boundary conditions of no downward radiance incident on the cloud top,

$$I(0,-\mu) = 0, \tag{4.6}$$

and the upward radiance incident on the cloud base is due only to that emitted from the ground,

$$I(t_1,+\mu) = I_\nu. \tag{4.7}$$

The plus and minus signs signify upward and downward directions respectively. Thus to model the radiative transfer it is necessary to calculate (or measure) the radiance emitted by the surface and atmosphere beneath the cloud and be able to characterize the optical properties of the scatterers inside the cloud as a function of wavelength.

Given that the RTE described above is quite complex it is informative to use a highly simplified model that still captures the important features of infrared sensing of volcanic ash clouds. Such a model was described previously, so now we turn to the more complex treatment.

[1]The assumption of plane-parallel conditions is not particularly limiting, but simplifies the mathematical treatment. These equations can be re-cast for a spherical shell atmosphere and an arbitrary shaped cloud.

4.1.1 Retrieval method

The radiative transfer required to extract quantitative information from infrared window radiances (8–12 μm) employs Mie theory and plane parallel radiative transfer in an absorbing and scattering cloud. Given the real and imaginary parts of the index of refraction of the ash-cloud particle as a function of wavelength, and the particle shape and size distribution, the efficiencies for scattering, absorption and extinction are calculated using a Mie scattering program. There is scant information on particle shapes in real ash clouds and only approximate methods exist for calculating efficiencies for particles of arbitrary shapes. We assume that the particles are spherical and the exact Mie-theory computer program of Evans (1988) is employed to calculate the efficiencies. Some measurements exist for the particle size distribution at the edges of the Mt. St. Helens ash cloud (see the papers in Newell and Deepak, 1982). These data indicate that a log-normal (or Zold) size distribution gives a reasonable fit to the distribution. The measurements reported by King *et al.,* (1984) and Hoffman and Rosen (1984) of the El Chichón stratospheric aerosol layer (King *et al.*, 1984; Matson, 1984) fit a modified-γ size distribution quite well. These data generally pertain to volcanic aerosol layers that are relatively old and high in the atmosphere. Only the fine particles can be detected in the nascent and low (tropospheric) volcanic plumes, and it is assumed that the size distributions would be similar to those reported for El Chichón (Hofmann and Rosen, 1984) and Mt. St. Helens. Both size distributions have been used to perform the radiative transfer calculations, and although there were differences in detail between the results for the two distributions (see also Wen and Rose, 1994), the basic results and mass loadings were essentially the same.

The parameters used in the Mie program are described in Prata (1989b). Once the Mie program has been run for each value of the size parameter (mean particle size and monochromatic wavelength), scattering parameters are then fed into a plane-parallel discrete ordinates radiative transfer program (Stamnes and Swanson, 1981). Given the single scattering albedo, asymmetry parameter, extinction and scattering efficiencies as a function of monochromatic wavelength, and the cloud-top and surface temperatures, radiances emerging from the top of the cloud along n distinct streams (zenith angles) are computed. These radiances are calculated for cloud optical depths ranging from 0 to 8 at wavelengths corresponding to the thermal IR channels of the sensor (e.g. AVHRR, MODIS, SEVIRI etc.). At the completion of these calculations, a large two-dimensional (corresponding to the 11 μm and 12 μm channels) look-up table exists with entries at prescribed values of the mean particle size r_m and optical depth τ. Each entry in the table consists of pairs of brightness temperatures T_{11} and T_{12}. The retrieval then consists of locating the (r_m, τ) pairs within the look-up table that best match (T_{11}, T_{12}) measurements at each image pixel.

The calculations were performed assuming that there is no absorption of infrared radiation by water vapour. The effects of atmospheric water vapour absorption on the satellite brightness temperatures can be assessed by performing radiative transfer calculations. The radiative transfer model Modtran 3 (Berk *et al.*, 1989), was used to calculate the temperature difference between the the satellite measured brightness temperatures at 11 μm and 12 μm wavelengths, at each vertical level using the temperature and moisture structure from a nearby radiosonde profile. The results of this analysis show that the effect of water vapour is greatest at the lowest levels, where it typically exceeds 1 K. At higher levels, near to the location of the plume, the effect is less than 0.2 K. In the tropics and in high humidity conditions, the effect of water vapour absorption can mask out the ‘reverse’ absorption effect of volcanic ash clouds. This can lead to misidentification of volcanic clouds and is a limitation of the current thermal detection method.

4.1.2 Size distributions and scattering parameters

The modified-γ distribution has the functional form,

$$n(r) = N_o \frac{r^\alpha}{\Gamma[\frac{\alpha+1}{\gamma}]} b^{\frac{\alpha+1}{\gamma}} \exp(-br^\gamma), \tag{4.8}$$

where $n(r)$ is the number of particles per unit volume, r is the particle radius, Γ is the Gamma function (see Press *et al.*, 1986, page 156), N_o, b, α, and γ are parameters of the distribution. The size parameter, x, is related to the particle radius and the wavelength λ through,

$$x = \frac{2\pi r}{\lambda}. \tag{4.9}$$

Used here, γ=1, α=6, $b = 6/r_o$, and (1.19) reduces to,

$$n(x) = Cx^6 \exp\left(-\frac{6x}{x_o}\right),$$

where C is a constant replacing the other parameters. Within a distribution of sizes, the mode radius r_o corresponds to a mode size parameter x_o.

The log-normal distribution is described by,

$$n(x) = N_o \frac{1}{\sigma_x} \exp\left[-\frac{(Ln(x) - Ln(x_o))^2}{2\sigma_x^2}\right], \tag{4.10}$$

where, as before x is the size parameter. The parameter $\sigma_x = 2\pi\sigma_r/\lambda$ is related to the standard deviation (σ_r) of the distribution and is a measure of its spread. In the calculations performed with this distribution, σ_r was set to 0.5, 0.75, 1.0 and 1.25 μm, and results are reported for σ_r=1.0 μm.

The inputs to the Mie program are the real and imaginary parts of the refractive index (m), the size parameter and the size distribution. The outputs are the extinction efficiency ($\hat{Q}_{ext}$) and scattering efficiency ($\hat{Q}_{sca}$) and phase function ($P(\theta)$). For polydispersions these efficiency factors are related to the single particle efficiencies (Q_f)by,

$$\hat{Q}_f = \frac{\int_o^\infty \pi r^2 Q_f(\frac{2\pi r}{\lambda}, m) \frac{dn(r)}{dr} dr}{\int_o^\infty \pi r^2 \frac{dn(r)}{dr} dr}. \tag{4.11}$$

The absorption efficiency is,

$$\hat{Q}_{abs} = \hat{Q}_{ext} - \hat{Q}_{sca}. \tag{4.12}$$

The remaining parameters that are needed to perform the radiative transfer calculations and which relate to the cloud microphysical structure are, the single scattering albedo,

$$\varpi = \frac{\hat{Q}_{ext}}{\hat{Q}_{sca}}, \tag{4.13}$$

the asymmetry parameter,

$$g = \frac{1}{2} \int_{-1}^{1} P(\theta) \cos\theta d\cos\theta, \tag{4.14}$$

where θ is the scattering angle. The number of particles per unit volume in the cloud is,

$$N = \int_o^\infty \frac{dn}{dr} dr, \tag{4.15}$$

and the optical depth of the cloud is,

$$\tau_\lambda = \pi L \int_o^\infty r^2 Q_{ext}(r, \lambda) n(r) dr, \tag{4.16}$$

where L is the geometrical thickness of the cloud. The mass loading (kg m^{-2}, g m^{-2} or kt km^{-2})[2] is

$$M = \frac{4\pi}{3} \rho L \int_o^\infty r^3 n(r) dr, \tag{4.17}$$

where ρ is the density of the ash.

4.1.3 Mass loadings

The U. S. Military consider mass loadings > 50 mg m^{-3} a potential hazard to their aircraft operations. Przedpelski and Casadevall (1994) estimated a mass loading of ≈ 2000 mg m^{-3} at 25,000 ft (≈ 7.5 km) for the 15 December 1989 Redoubt eruption cloud that caused significant damage to a KLM Boeing 747-400 jet aircraft. Mass loadings include all particles with radii < 50 μm, which have atmospheric residence times of the order of at least a few hours. Having determined the particle size distribution, the geometrical thickness of the cloud and its areal extent, it is possible to estimate the mass concentartion of fine particles in an ash plume. The density of the ash is taken to be 2600 kg m^{-3} and the area of a pixel is taken is typically about 1-10 km^2 – this is a mean area for pixels for the AVHRR-2, MODIS and SEVIRI; pixels near the scan edges will be somewhat larger (up to several 10's km^2). Pixels are counted if they satisfy criterion (1), and the retrieved particle size is in the range $1 < r_m < 16$ μm. An estimate of the cloud thickness is crucial to the evaluation of mass concentrations. Data on cloud thicknesses are not available so they must be estimated by other means. Studies of plume rise in stable stratified atmospheres (e.g. Briggs, 1975) suggest that to a reasonable approximation the vertical extent of a plume can be estimated from the cloud-top height. For example, Manins (1985) has calculated the heights and vertical extents of stabilized smoke plumes as a function of power release and following Briggs (1975) suggests that the vertical extent (cloud thickness), Δz, of these plumes is given by,

$$\Delta z = 0.4 z_{top},$$

where z_{top} is the height of the plume top. New measurements from the Caliop lidar (Winker *et al.*, 2007) on board CALIPSO suggest that drifting volcanic plumes are no more than 1–3 km thick, but variable. The variability of cloud thickness along the plumes and the problem of not having simultaneous plume-top height and plume-base height data for each of the plumes, means that we cannot estimate plume thickness to any greater accuracy. The total mass can be calculated by multiplying (4.17) by the area of a pixel.

4.1.4 Practical procedure

In the (T_{11}, $T_{11} - T_{12}$) plane there exist isolines of constant mean particle radius, r_m^j. Each point on the isoline, r_m^j corresponds to particular values of the optical depth, $\tau^{j,i}$. Lines connecting equal values of $\tau^{j,i}$

[2] 1 g m^{-2} = 1 kt km^{-2}.

also exist. Given the measured values (T^*_{11}, T^*_{12}), the retrieval procedure requires us to find the 'best' values of (τ, r_m). A linear interpolation procedure is adopted:

- Find values of $T_{11}(\tau^{j,i}, r^j_m)$ that bracket T^*_{11}. Label these $T^1_{11}(r^j_m)$, $T^2_{11}(r^j_m)$,$T^1_{11}(r^{j+1}_m)$,$T^2_{11}(r^{j+1}_m)$
- Interpolate on the r^j_m isolines to find the appropriate $\Delta T^(r^j_m) = T_{11}(r^j_m) - T_5(r^j_m)$.

$$\Delta T(r^j_m) = w_1 \Delta T_2(r^j_m) + (1 - w_1)\Delta T_1(r^j_m),$$

$$w_1 = \frac{T^1_{11}(r^j_m) - T^*_{11}}{T^1_4(r^j_m) - T^2_{11}(r^j_m)}.$$

  Similarly for $\Delta T(r^{j+1}_m)$:

$$\Delta T(r^{j+1}_m) = w_2 \Delta T_2(r^{j+1}_m) + (1 - w_2)\Delta T_1(r^{j+1}_m),$$

  and the weight w_2 is defined in an analogous way to w_1.

- The required mean particle radius is obtained using linear interpolation,

$$r^*_m = w_r r^j_m + (1 - w_r) r^{j+1}_m,$$

$$w_r = \frac{\Delta T(r^{j+1}_m) - \Delta T^*}{\Delta T(r^{j+1}_m) - \Delta T(r^j_m)}.$$

- In practice there are n isolines of $r^j_m, j = 1, n$ and n is small ($n = 18$), and many more values of $\tau^{j,i}, i = 1, k$ ($k = 100$ is used in the current software). Thus $2nxk$ values of ΔT are precomputed.

In summary the solution process for determining mass loadings from two-channel IR sensors entails:

- Specify cloud geometry,
- Specify viewing geometry,
- Determine boundary conditions at the cloud,
- Specify the refractive indices of ash as a function of wavelength,
- Specify the size distribution and particle shape,
- Solve for cloud optical depth, particle size (radius) and mass.

Studies (e.g. Wen and Rose, 1994) have shown that the calculation is sensitive to the size distribution, particle shape and refractive indices used and that errors as large as 40% can arise from inaccurate knowledge of these parameters.

4.1.5 Specifying the boundary conditions

The measured top-of-the-atmosphere brightness temperatures are corrected for water vapour before use in the retrieval scheme using the procedure described in Yu *et al.* (2002). A better correction could be done if independent measurements of the water vapour field were available (e.g. from ECMWF analysis of forecast fields). It is also necessary to be able to specify the temperature of the surface (T_s) below the ash cloud and the ash cloud top temperature (T_c), neither of which are known. These could also be estimated from independent data. However, in order to maintain the speed and ease of use of this retrieval scheme, T_s and T_c are estimated from the SEVIRI data. These temperatures are estimated as:

$$T_s \approx max[T_{ij}],$$

$$T_c \approx min[T_{ij}],$$

where T_{ij} are the scene temperatures in the 12 μm SEVIRI channel. Estimates are obtained for each 15 minute scene. There are obvious inadequacies in this approach and several improvements could be envisaged. For example, the maximum scene temperature may occur over clear land during the daytime, while the ash cloud may be over open ocean. A simple way to improve the estimate is to use a *local* search algorithm, by seeking maxima and minima in the vicinity of the ash cloud. Estimating T_c is equivalent to obtaining a cloud top height. Thus T_c could also be obtained by using an independent cloud top height and assuming a lapse rate (or using a measured lapse rate) to convert to a cloud top height. These improvements are left to a later study.

Once T_s and T_c are obtained, they are used to find the closest look-up-table (LUT), specified in intervals of 5 K for:

$$200K < T_c < 300K,$$

$$225K < T_s < 305K.$$

To account for some water vapour absorption in the estimate of T_s, 2 K is subtracted from the estimate and to account for cloud absorption (emissivity < 1), 2 K is added to T_c. The retrieval files report the values of T_s and T_c used.

4.2 Microphysical volcanic cloud model

The new (e.g. MODIS) and advanced multispectral sensors (e.g. GLI, SEVIRI, AIRS, IASI) include many channels capable of providing detection and discrimination of volcanic ash clouds. A model of an ash cloud has been developed in order to exploit these new sensors. For completeness, we include information from the visible to infrared–although most of the discussion has centred on the infrared window radiances, it seems likely that the visible and near infrared data may also provide a means for ash cloud detection.

At near infrared wavelengths (e.g. λ=1.61 μm) ice clouds appear much darker than clouds of water droplets, because the imaginary part of the refractive index of ice is larger than that of water at this wavelength and consequently ice absorbs more strongly at this wavelength. A comparison of the refractive indices of water, ice and andesite (a common constituent of ash clouds) is given in Table 4.2.

Pollack *et al.* (1973) list refractive indices of andesite (and some other minerals) over a large range of wavelengths from the UV to the infrared. These data are not the only source of refractive index values

Table 4.1: Refractive indices for water, ice and andesite (a silica-rich mineral). The last column gives the reference to the origin of the data shown.

Wavelength (μm)	n_r	n_i	Reference
Ice			
0.63	1.309	1.04E-8	Masuda and Takashima (1990)
1.61	1.289	3.41E-4	Masuda and Takashima (1990)
Water			
0.63	1.332	1.44E-8	Masuda and Takashima (1990)
1.61	1.317	0.87E-4	Masuda and Takashima (1990)
Andesite			
0.68	1.470	1.70E-3	Pollack *et al.* (1973)
1.61	1.470	3.30E-3	Pollack *et al.* (1973)

for minerals; see for example, Volz (1973), Ivlev and Popova (1973) and Sokolik and Toon (1999). We have used the Pollack *et al.* values as a starting point to provide the input optical parameters required for more detailed radiative transfer calculations, and we propose a model of a volcanic ash cloud based on the Pollack *et al.* refractive indices of andesite. The ash cloud model consists of spherical andesite particles in a log-normal size distribution with a mean particle radius of 3 μm. The single-scatter albedo, asymmetry parameter and coefficients of absorption, scattering and extinction are calculated for the polydisperse particle size distribution using the Mie program discussed earlier. Prata and Grant (2001) provides a listing of the the variation of single-scatter albedo (ϖ), extinction coefficient (Q_{ext}), and asymmetry parameter (g) for wavelengths ranging from 0.3 μm to 14.5 μm−the range most commonly used in remote sensing of the earth's atmosphere. Also, shown are the results for a model ash cloud with mean particle radii of 1 and 5 μm. Table 4.2 lists the scattering parameters for 3 size ranges as a function of wavelength.

Table 4.2: Optical parameters for a model andesite ash cloud. The parameters are: ϖ–the single-scatter albedo, g– the asymmetry parameter, and Q_{ext}–the extinction efficiency factor. These parameters are given for three mean particle sizes, r_o=1, 3 and 5 μm.

	r_o=1.0 μm			r_o=3.0 μm			r_o=5.0 μm		
Wavelength (μm)	ϖ	g	Q_{ext}	ϖ	g	Q_{ext}	ϖ	g	Q_{ext}
0.30	0.8346	0.4579	2.0875	0.8344	0.4573	2.0873	0.8343	0.4570	2.0872
0.32	0.8241	0.4551	2.0875	0.8238	0.4543	2.0873	0.8237	0.4540	2.0872
0.34	0.8229	0.4548	2.0876	0.8225	0.4540	2.0873	0.8224	0.4536	2.0872
0.36	0.8104	0.4513	2.0876	0.8100	0.4503	2.0873	0.8098	0.4499	2.0872
0.38	0.8105	0.4515	2.0877	0.8100	0.4504	2.0873	0.8098	0.4499	2.0872
0.40	0.7987	0.4480	2.0877	0.7982	0.4467	2.0873	0.7980	0.4462	2.0872
0.42	0.7988	0.4482	2.0878	0.7982	0.4469	2.0874	0.7980	0.4462	2.0872
0.44	0.7877	0.4448	2.0879	0.7871	0.4433	2.0874	0.7868	0.4426	2.0872
0.46	0.7878	0.4451	2.0880	0.7871	0.4434	2.0874	0.7868	0.4427	2.0872
0.48	0.7879	0.4454	2.0880	0.7872	0.4436	2.0875	0.7868	0.4428	2.0872
0.50	0.7775	0.4421	2.0881	0.7766	0.4401	2.0875	0.7762	0.4392	2.0872
0.52	0.7776	0.4424	2.0882	0.7767	0.4403	2.0876	0.7763	0.4393	2.0872
0.54	0.7778	0.4428	2.0883	0.7768	0.4405	2.0876	0.7763	0.4394	2.0873
0.56	0.7679	0.4396	2.0884	0.7668	0.4371	2.0876	0.7663	0.4359	2.0873
0.58	0.7681	0.4400	2.0886	0.7669	0.4373	2.0877	0.7663	0.4361	2.0873
0.60	0.7683	0.4405	2.0887	0.7670	0.4376	2.0878	0.7664	0.4362	2.0874
0.70	0.7509	0.4363	2.0894	0.7490	0.4321	2.0881	0.7482	0.4302	2.0875
0.80	0.7357	0.4331	2.0903	0.7331	0.4274	2.0886	0.7320	0.4248	2.0878
0.90	0.7225	0.4313	2.0914	0.7191	0.4236	2.0892	0.7176	0.4202	2.0882
1.00	0.7112	0.4308	2.0928	0.7067	0.4209	2.0899	0.7048	0.4165	2.0887
1.10	0.7016	0.4319	2.0945	0.6960	0.4192	2.0908	0.6935	0.4136	2.0892
1.20	0.6937	0.4346	2.0966	0.6866	0.4186	2.0918	0.6836	0.4118	2.0899
1.30	0.6873	0.4392	2.0991	0.6786	0.4193	2.0931	0.6749	0.4109	2.0908
1.40	0.6871	0.4476	2.1021	0.6763	0.4234	2.0945	0.6720	0.4132	2.0917
1.50	0.6834	0.4562	2.1057	0.6702	0.4266	2.0963	0.6651	0.4144	2.0929
1.60	0.6853	0.4685	2.1101	0.6694	0.4331	2.0983	0.6632	0.4185	2.0942
1.70	0.6883	0.4830	2.1155	0.6691	0.4408	2.1007	0.6619	0.4236	2.0957
1.80	0.6926	0.4998	2.1219	0.6695	0.4499	2.1034	0.6610	0.4298	2.0975
1.90	0.6983	0.5189	2.1298	0.6706	0.4605	2.1066	0.6607	0.4371	2.0995
2.00	0.7019	0.5411	2.1395	0.6688	0.4728	2.1104	0.6572	0.4454	2.1019
2.10	0.7143	0.5655	2.1511	0.6749	0.4880	2.1148	0.6614	0.4565	2.1046
2.20	0.7248	0.5909	2.1651	0.6785	0.5038	2.1199	0.6627	0.4677	2.1076
2.30	0.7369	0.6174	2.1817	0.6829	0.5213	2.1258	0.6647	0.4803	2.1110
2.40	0.7507	0.6441	2.2014	0.6882	0.5406	2.1326	0.6672	0.4944	2.1150
2.50	0.7686	0.6699	2.2242	0.6977	0.5621	2.1404	0.6736	0.5109	2.1195
2.55	0.7750	0.6821	2.2369	0.6996	0.5727	2.1448	0.6739	0.5188	2.1219
2.60	0.7845	0.6935	2.2503	0.7049	0.5843	2.1494	0.6775	0.5279	2.1245
2.65	0.7885	0.7045	2.2645	0.7043	0.5953	2.1544	0.6752	0.5361	2.1273
2.70	0.7955	0.7145	2.2795	0.7072	0.6070	2.1597	0.6762	0.5453	2.1302
2.75	0.7931	0.7249	2.2949	0.6996	0.6183	2.1653	0.6670	0.5533	2.1333
2.80	0.7961	0.7338	2.3110	0.6983	0.6306	2.1712	0.6639	0.5630	2.1366

Table 4.3: *

Table 1.3 continued

	r_o=1.0 μm			r_o=3.0 μm			r_o=5.0 μm		
Wavelength (μm)	ϖ	g	Q_{ext}	ϖ	g	Q_{ext}	ϖ	g	Q_{ext}
2.85	0.8037	0.7407	2.3277	0.7022	0.6432	2.1776	0.6659	0.5738	2.1401
2.90	0.8091	0.7468	2.3448	0.7040	0.6559	2.1843	0.6658	0.5847	2.1437
2.95	0.8185	0.7507	2.3623	0.7106	0.6682	2.1914	0.6703	0.5963	2.1476
3.00	0.8275	0.7534	2.3800	0.7173	0.6802	2.1988	0.6750	0.6080	2.1517
3.05	0.8381	0.7545	2.3980	0.7265	0.6917	2.2067	0.6821	0.6198	2.1560
3.10	0.8464	0.7549	2.4158	0.7334	0.7028	2.2149	0.6871	0.6316	2.1605
3.15	0.8543	0.7544	2.4335	0.7404	0.7133	2.2235	0.6923	0.6433	2.1653
3.20	0.8635	0.7526	2.4511	0.7498	0.7229	2.2324	0.7000	0.6550	2.1702
3.25	0.8688	0.7511	2.4682	0.7546	0.7325	2.2416	0.7030	0.6666	2.1754
3.30	0.8739	0.7489	2.4848	0.7593	0.7414	2.2512	0.7062	0.6781	2.1807
3.35	0.8803	0.7458	2.5009	0.7664	0.7491	2.2611	0.7118	0.6892	2.1863
3.40	0.8862	0.7423	2.5163	0.7733	0.7560	2.2713	0.7174	0.7000	2.1920
3.45	0.8904	0.7390	2.5308	0.7779	0.7625	2.2817	0.7208	0.7107	2.1980
3.50	0.8943	0.7355	2.5444	0.7825	0.7682	2.2924	0.7242	0.7210	2.2041
3.60	0.9014	0.7281	2.5686	0.7915	0.7773	2.3146	0.7312	0.7403	2.2168
3.70	0.9101	0.7198	2.5882	0.8041	0.7821	2.3376	0.7427	0.7565	2.2302
3.80	0.9166	0.7120	2.6023	0.8140	0.7846	2.3614	0.7518	0.7706	2.2442
3.90	0.9233	0.7042	2.6105	0.8252	0.7842	2.3859	0.7628	0.7815	2.2586
4.00	0.9277	0.7108	2.5773	0.8341	0.7921	2.4195	0.7706	0.7975	2.2773
4.25	0.9352	0.6941	2.5293	0.8494	0.7846	2.4868	0.7858	0.8109	2.3174
4.50	0.9402	0.6765	2.4326	0.8623	0.7737	2.5565	0.7991	0.8122	2.3595
4.75	0.9432	0.6564	2.2915	0.8733	0.7630	2.6272	0.8107	0.8060	2.4037
5.00	0.9413	0.6419	1.9900	0.8819	0.7704	2.6963	0.8184	0.8058	2.4602
5.25	0.9389	0.6130	1.7826	0.8875	0.7668	2.7580	0.8242	0.7977	2.5105
5.50	0.9363	0.5811	1.5711	0.8942	0.7646	2.8121	0.8322	0.7894	2.5637
5.75	0.9300	0.5473	1.3668	0.8966	0.7648	2.8536	0.8351	0.7841	2.6194
6.00	0.9101	0.5133	0.9693	0.9004	0.7970	2.7883	0.8464	0.8093	2.7209
6.50	0.8380	0.4382	0.5776	0.8790	0.8161	2.5113	0.8356	0.8449	2.8205
7.00	0.6549	0.3645	0.3470	0.8058	0.8202	1.9370	0.7889	0.8848	2.6700
7.50	0.3096	0.2950	0.2404	0.5937	0.8105	1.1636	0.6491	0.9068	1.9243
8.00	0.0625	0.2346	0.2882	0.2155	0.7863	0.8026	0.3052	0.9043	1.1673
8.25	0.0655	0.2090	0.4060	0.2279	0.7644	0.9701	0.3203	0.8907	1.3045
8.50	0.1075	0.1876	0.6204	0.3284	0.7318	1.3266	0.4219	0.8611	1.6615
8.75	0.1541	0.1706	1.0082	0.4087	0.6886	1.7910	0.4909	0.8110	2.0317
9.00	0.2049	0.1552	1.7692	0.4686	0.6440	2.3946	0.5405	0.7500	2.4372
9.50	0.1948	0.1366	1.7248	0.4238	0.6592	2.5902	0.4845	0.7775	2.5805
10.00	0.2305	0.1146	1.7813	0.4522	0.6202	2.8094	0.5021	0.7457	2.7180
10.50	0.2495	0.1181	1.3480	0.4546	0.6133	2.8707	0.4883	0.7495	2.7459
11.00	0.3553	0.1286	0.8027	0.5088	0.5991	3.1600	0.4782	0.7452	2.8292
11.50	0.4019	0.0997	0.4043	0.6265	0.5784	3.2195	0.5362	0.7079	3.0643
12.00	0.3958	0.0778	0.2422	0.6997	0.5613	2.8904	0.6367	0.6834	3.3369
12.50	0.3572	0.0625	0.1627	0.7302	0.5433	2.4190	0.7080	0.6870	3.4567
13.00	0.2762	0.0515	0.1285	0.7139	0.5216	1.9619	0.7268	0.7007	3.3357
13.50	0.1904	0.0433	0.1110	0.6736	0.4931	1.5435	0.7210	0.7084	3.0193
14.00	0.1153	0.0377	0.1134	0.5966	0.4607	1.2558	0.6783	0.7107	2.6238

4.3 Other methods

There are now several ash detection algorithms in use or proposed, based on IR and visible satellite data. Table 4.4 shows a summary of ash detection schemes (with original references), based mostly on using infrared channels. Several of these techniques show great promise for detecting volcanic ash, but there are

Table 4.4: Summary of ash detection algorithms and techniques used with satellite infrared (IR) and visible channel data. (RA=Reverse Absorption; TVAP=; PCI=Principle Components; RAT=Ratio method; WVC=Water vapor correction method).

Name	Principle	Reference
RA	2-band IR (11 and 12 μm)	Prata (1989a,b)
Ratio	2-band IR (11 and 12 μm)	Holasek and Rose (1991)
4-Band	IR+Visible	Mosher (2000)
TVAP	3-band IR (3.9, 11 and 12 μm)	Ellrod *et al.* (2003)
PCI	Multi-band principal components	Hillger and Clark (2002a; 2002b)
WVC	2-band IR+water vapour correction	Yu *et al.* (2002)
RAT†	3-band IR (3.5, 11, 12 μm)	Pergola *et al.* (2004)
3-Band	3-band (IR and Visible)	Pavolonis *et al.* (2006)
β-ratios	Multi-band, optimal estimation	Pavalonis (2010a, b)

important nuances and caveats associated with all of these techniques (including the two-channel, 'reverse absorption' method) and we strongly recommend that the interested reader examine the original papers (listed in Table 4.4) carefully.

The two channel, reverse absorption technique is very useful in cases where the ash is not too thick and not too dispersed and is used at the VAACs (Watkin, 2003). The problems and pitfalls of using the reverse absorption technique have been discussed in the research literature (e.g. Simpson *et al.*, 2000; Prata *et al.*, 2001) and are well known to experienced meteorological analysts. Context is a key element in determining whether a particular cloud is an ash hazard or not, and trained meteorologists tasked with identifying ash clouds will use multiple sources of information including satellite imagery, pilot reports, ground observer reports, wind trajectories, and background information regarding regional volcanic activity and prior behaviour.

Two of the instruments listed in Table 3.1 are capable of measuring much more than ash mass loadings. These instruments, AIRS and IASI have high spectral resolution and by utilising more measurement channels it may be possible to infer something about the mineralogy of the ash. Indeed it may also be possible to discriminate dust (Fig. 3.1g) and wind blown ash (Fig. 3.1h) outbreaks from volcanic ash eruption clouds and plumes (Clarisse *et al.*, 2010a). Clerbaux *et al.* (2007) have shown the potential of IASI for measuring volcanic SO_2.

The analysis described above was predicated on the assumption that just a few (typically two) channels are available in the IR to discriminate ash from other airborne substances and perform retrievals. With AIRS and IASI more than 2000 channels are available and this opens up possibilities for doing more elaborate retrievals and also providing more constraints of the retrieval which usually leads to more accurate solutions (Gangale *et al.*, 2009; Clarisse *et al.*, 2010b. The same theory may be used in the case of high-spectral resolution IR data. Figure 4.1 shows a spectral transect (all AIRS lines along a single AIRS column) as a

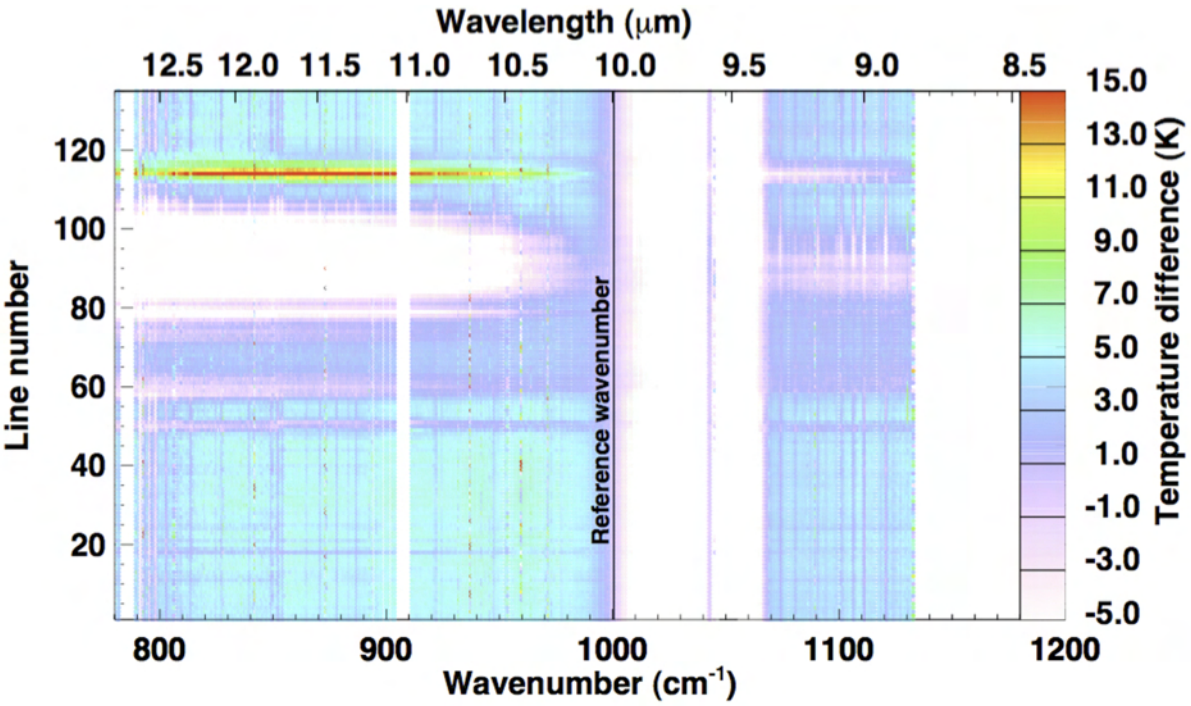

Figure 4.1: AIRS spectrum shown as a transect along a constant pixel number. The brightness temperature at 1000 cm^{-1} has been subtracted from the spectra and plotted as brightness temperature differences (BTDs).

function of wavenumber and contains a daunting amount of information. We may extend the ideas developed earlier to this high-spectral domain in a simple manner. The 'reverse absorption' or '2-channel' technique can be seen as a special case of sampling from a continuous spectral signature due to ash or water/ice clouds, now amenable to analysis from AIRS and IASI measurements. To illustrate how these signatures can be used in AIRS data, Figure 4.2 shows the ratio between the spectral brightness temperature (BT) and a reference brightness temperature at 1000 cm^{-1} (BT_{ref})[3] for six scene elements. The idea behind dividing by a reference brightness temperature is to approximate the emissivity variation of the spectra; the choice of 1000 cm^{-1} is arbitrary, but it is necessary to avoid absorption regions and the region around 1000 cm^{-1} is quite transparent. Within the region between 850–1000 cm^{-1}, the ratio for ice (blue line) increases with wavenumber, whereas for ash and desert dust it decreases. For a clear atmosphere there is a slight increase with wavenumber due to water vapour absorption. Water clouds generally have a slope between that of the ice cloud and the clear scene. Ice and water clouds behave this way because the radiance spectra for ice and water over this region decrease with increasing wavenumber, which is a consequence of the decrease in cloud emissivity with increasing wavenumber, which in turn is related to the spectral variation of the refractive indices of ice and water. This change of slope of the spectral ratio with wavenumber can be used to discriminate ash from ice, water clouds and clear scenes. The slopes are also sensitive to the optical depth of the cloud as well as the microphysics of the particles (refractive index, size, size distribution, and shape).

[3]The use of wavenumber, ν (in cm^{-1}) instead of wavelength, λ (in μm) is deliberate here because AIRS and IASI use this unit. ν (cm^{-1})=10000/λ (μm),

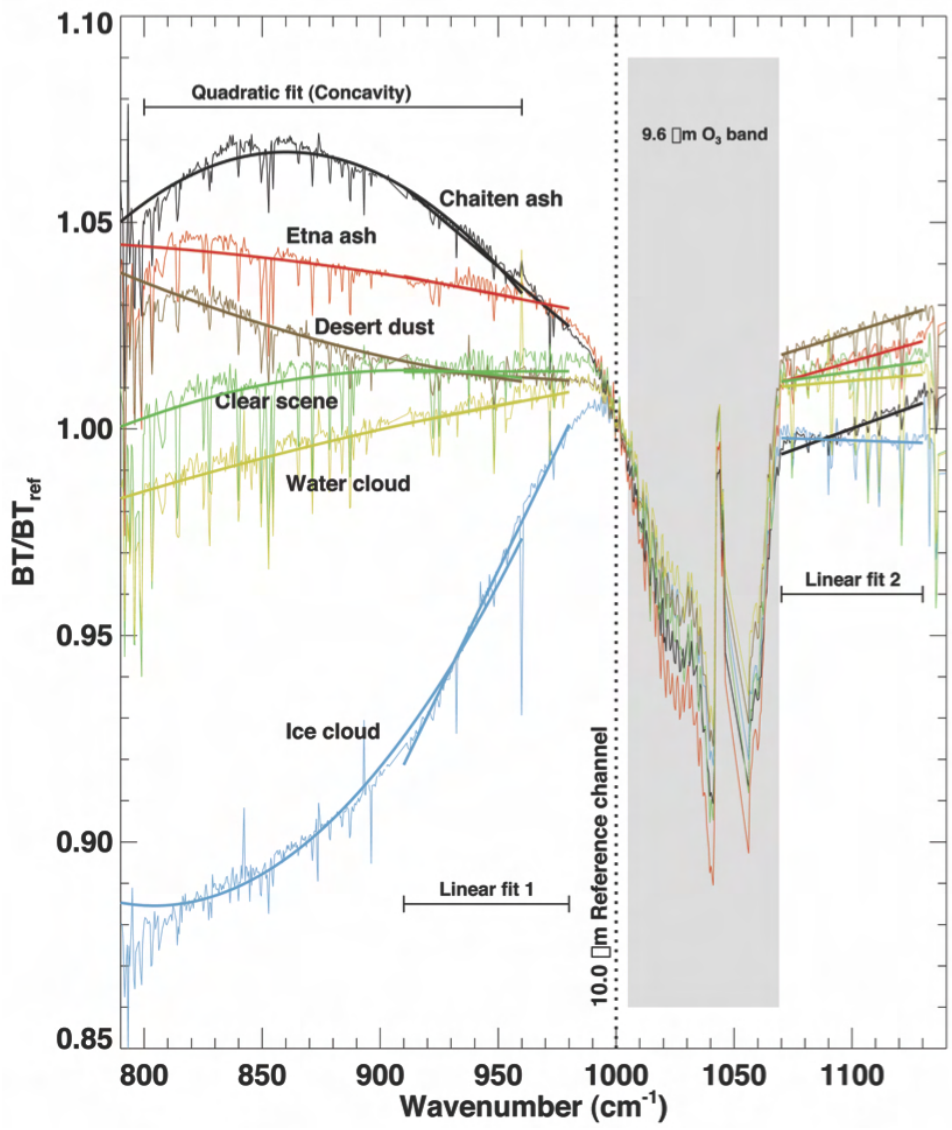

Figure 4.2: Spectral ratio of the TOA brightness temperature for a single AIRS pixel and for six different scenes: (1) a pixel containing semi-transparent ice cloud (blue line), (2) a water cloud (yellow line), (3) a clear pixel (green line), (4) desert dust (brown line), (5) a pixel affected by ash from an eruption of Etna (red line), and (6) a Chaitén ash-affected pixel (black line). The greyed-out region includes the strong O_3 absorption and is not used in the analyses. The spectral regions where linear and quadratic fits are performed are also indicated on the plot.

Spectral fits (rather than channel differences) can be performed to obtain objective parameters for discriminating ash, water, ice and other airborne substances. These fits are shown in Figure 4.2, labelled as 'the concavity' (a quadratic fit) and two linear fits. Furthermore, the shape or signature of the spectral variation is sensitive to many parameters, including particle size and composition. By using a detailed RT model it may be possible to infer, for the first time, composition of ash in the atmosphere providing useful insights into volcanic processes occurring in the interior of the volcano.

Chapter 5

SO_2 Retrieval

5.1 GOME-2 Retrievals

GOME-2 data were obtained from the University of Bremen and no further analysis was conducted on these data other than to re-plot them. (See Table 7.1 for a list of the GOME-2 data obtained for this study).

5.2 OMI Retrievals

OMI data were downloaded from the NASA DAAC as hdf5 formatted files for the period 30 April to 21 May 2010. The SO_2 data files corresponding to TRL and PBL were extracted. Because of the "row anomaly", level 2 data were quality controlled used the ChiSq field by rejecting all fields with a ChiSq$<$0.8. This value was determined by trial-and-error, by noting when the row anomaly mostly disappeared. Some valid data were removed by this process. (See Table 7.2 for a list of OMI data used in this study).

5.3 Infrared Schemes

5.3.1 8.6 μm retrieval

SO_2 has an absorption feature centred near to 8.6 μm that can be exploited to determine column abundance. The band is relatively weak so that saturation is unlikely, but there are constraints on using thermal data to determine SO_2 abundance. The main ones are: a need for thermal contrast, that is, the temperature of the absorbing layer needs to be different to the emitting (source) layer below, and the layer is largely free of other interfering gases and particles. Usually, the absorbing layer is colder. In addition the absorbing layer needs to be semi-transparent. If the layer becomes opaque then radiation from below will be completely absorbed and only emission from the layer will be observed. It is still possible to retrieve SO_2 in this case, but necessary to know the temperature of the layer. In the analysis provided here we assume that the layer is absorbing and that it is semi-transparent between 8–12 μm.

We assume a plane-parallel absorbing layer (SO_2) within an atmosphere consisting of mixed gases (no clouds) over a surface of uniform temperature. The radiance from the top of the layer, measured in a

SEVIRI channel can be written:

$$I_i = \eta_s I_i^s + (1 - \eta_s) I_i^{og} \tag{5.1}$$

Where the superscripts refer to SO_2(s) and other gases (og), principally water vapour and η represents the absorption by the gas layer. We can write a similar equation for a second channel j for which there is no absorption by the target gas (SO_2) and consequently, we have

$$I_j = I_j^{og} \tag{5.2}$$

For convenience the surface emission is included in the terms and . Combining these and linearising the radiances to brightness temperatures,

$$\Delta T_{ij} = \eta_s (T_i^s - T_i^{og}) + (T_i^{og} - T_j^{og}). \tag{5.3}$$

The second term on the right-hand side of (5.3) accounts for absorption by all other gases and in this case this is almost entirely due to water vapour. Denoting this as δT_{ij}, we see that it is simply the temperature difference that results by differential absorption by water vapour and is commonly used as a correction in the determination of SSTs from infrared measurements. The information that we are seeking is contained in the factor η_s. This can be written in terms of transmittance (t_s),

$$\eta_s = 1 - t_s, \tag{5.4}$$

$$t_s = \exp\left(-\int_{z_1}^{z_2} k\rho dz\right), \tag{5.5}$$

where k is the absorption coefficient for SO_2, ρ is the density of SO_2, z_1 and z_2 are the heights of the lower and upper boundaries of the absorbing layer. For a thin layer of gas of thickness L ($L = z_2 - z_1$), in which the absorption coefficient and density do not vary with z, (5.3) may be further reduced to:

$$\rho = \alpha + \beta \Delta T_{ij}, \tag{5.6}$$

where:

$$\beta = \frac{1}{kL(T_i^s - T_i^{og})}. \tag{5.7}$$

Equation (5.6) suggests a linear relation between the SO_2 absorber density the brightness temperature difference of two channels where one includes absorption by SO_2 and the other does not, provided the layer is thin (e.g. $\eta_s \approx k\rho L$). Given that the linearisation is an approximation and that the constants α and β are strictly not constant, (5.6) may well contain a degree of nonlinearity. The coefficient of linearity, β, becomes inaccurate as the thermal contrast between the absorbing layer and emission by other gases plus surface emission, diminishes. This can occur when water vapour and SO_2 are collocated in the layer or when the layer is close in temperature to the surface emission. We have also neglected emissivity variations in the underlying surface and ignored any spectral variation in the emissivity. For a gas layer over the ocean this is not a serious problem, but for a layer over land, particularly bare ground, emissivity variations need to be considered. The off-set constant, α, as explained previously is due to water vapour differential absorption between the two selected channels. In the absence of an absorbing gas layer,

$$\delta T_{ij} = -\frac{\alpha}{\beta}. \tag{5.8}$$

If water vapour absorption is greater in channel i than in channel j, $\alpha < 0$. Detailed radiative transfer calculations have been performed using the MODTRAN model for the ASTER channels but it is beyond the scope of this study to do similar calculations for the SEVIRI channels.

5.3.2 SEVIRI 7.3 μm retrieval

A simplified radiative transfer model is proposed for deriving SO_2 amount from the SEVIRI temperature measurements. The following is based on the paper by Prata *et al.* (2003), which explored the use of the TOVS/HIRS/2 channels for upper-troposphere SO_2 retrievals. For an SO_2 cloud the radiance observed from above, assuming no angular dependence is,

$$R_\lambda = \tau_t B[T_o, \lambda] + (1 - \tau_t) B[T_c, \lambda] \tag{5.9}$$

where, B is the Planck function, T_c is the mean temperature of the SO_2 cloud, τ_t is the total transmittance of the atmosphere including all gases and R_λ is the radiance measured at the sensor. If there were no SO_2 in the cloud then,

$$R_\lambda = \hat{R}_\lambda = \tau_a B[T_o, \lambda] \tag{5.10}$$

where τ_a is the transmittance of the atmosphere without SO_2. The radiance difference between the atmosphere with and without the SO_2 cloud is,

$$\Delta R = (1 - \tau_t) B[T_c, \lambda] + (\tau_t - \tau_a) B[T_o, \lambda] \tag{5.11}$$

Linearising about the mean temperature of the cloud and assuming that:

$$\tau_t = \tau_s \tau_a.$$

$$\Delta T = (1 - \tau_s \tau_a) B[T_c, \lambda] \left(\frac{\partial T}{\partial B}\right) - \tau_a (1 - \tau_s) B[T_o, \lambda] \left(\frac{\partial T}{\partial B}\right) \tag{5.12}$$

If the atmosphere were clear, then $\tau_a \approx 1$ and,

$$\Delta T \approx (1 - \tau_s) \Delta \hat{B} \left(\frac{\partial T}{\partial B}\right) \tag{5.13}$$

where $\Delta \hat{R} = B[T_c, \lambda] - B[T_o, \lambda]$. Since in general $T_o > T_c$ and $\tau_s < 1$, $\Delta T < 0$. It follows that we may write,

$$\Delta T = \alpha + \beta (1 - \tau_s). \tag{5.14}$$

where α and β are parameters to be estimated. The parameter β is,

$$\beta = \Delta \hat{R} \left(\frac{\partial T}{\partial B}\right), \tag{5.15}$$

and $\frac{\partial T}{\partial B}$ is evaluated at the temperature of the cloud. From analysis of data and from Modtran (Berk *et al.*, 1989) modelling for MODIS and HIRS instruments it has been found that,

$$\alpha \approx -8K.$$

For SEVIRI, the value of α was found to be between

$$-4 \leq \alpha \leq -2$$

.

5.3.2.1 Practical considerations

The simple model presented above permits the evaluation of τ_s from a measurement of ΔT. For SEVIRI data, the evaluation of ΔT is made by estimating $\hat{R}$ through a linear interpolation of a radiance measurement at 6.2 μm (SEVIRI channel 6) and a radiance measurement at 11.0 μm (SEVIRI channel 10). The use of the 11.0 μm channel is made in preference to a channel at 8.6 μm because this channel is also affected by SO_2 absorption and so cannot give a reliable estimate of the unperturbed atmospheric state. It is also possible to use the 12 μm SEVIRI channel, and later we do use this channel in preference to the 11 μm channel because it is less affected by volcanic ash, which we know is present. Thus,

$$\hat{R} = R^{lin} = a + b\lambda_{7.3} \tag{5.16}$$

$$b = \frac{B[T, \lambda_{6.2}] - B[T, \lambda_{11}]}{\lambda_{6.2} - \lambda_{11}}$$

$$a = B[T, \lambda_{6.2}] - b\lambda_{6.2}.$$

Finally,

$$\Delta R^{lin} = B[T, \lambda_{7.3}] - R^{lin}. \tag{5.17}$$

It can be seen that $\Delta R^{lin} < 0$. The data processing proceeds on a pixel-by-pixel basis.

5.3.2.2 Estimating the background radiance

The scheme outlined above relies on an estimate of the background (unperturbed) radiance at 7.3 μm, which has been obtained using a linear interpolation. The accuracy of the linear interpolation of radiance as a function of wavelength has been gauged by studying large amounts of SEVIRI data for cases where there are no SO_2 clouds present. In most situations this appears to be accurate (within ± 2 K in 95% of cases studied). There is however a notable bias with the interpolated value usually higher than the actual value. In some cases, with no SO_2 present, it was found that the linear interpolation was a poor estimate of the observed radiance. With just a small addition in complexity, an improvement to the scheme was made in the following mannner:

(1) Blackbody radiance curves are generated using the observed radiances at 6.2 and 11.0 μm, and 'pseudo' radiances ($R^*(T_{\lambda_1}, \lambda_2)$) are calculated at all three wavelengths:

$$R^*(T_{11.0}, 6.2) = B(T_{11.0}, 6.2),$$

$$R^*(T_{6.2}, 7.3) = B(T_{6.2}, 7.3),$$

$$R^*(T_{11.0}, 7.3) = B(T_{11.0}, 7.3),$$

$$R^*(T_{6.2}, 11.0) = B(T_{6.2}, 11.0).$$

The blackbody radiance curves bracket the range of possible observed radiances at 7.3 μm. (see Figure 5.1)
(2) An estimate of the observed radiance is obtained from:

$$\hat{R}_{7.3} = 0.5[R^*(T_{6.2}, 7.3) + R^*(T_{11.0}, 7.3)].$$

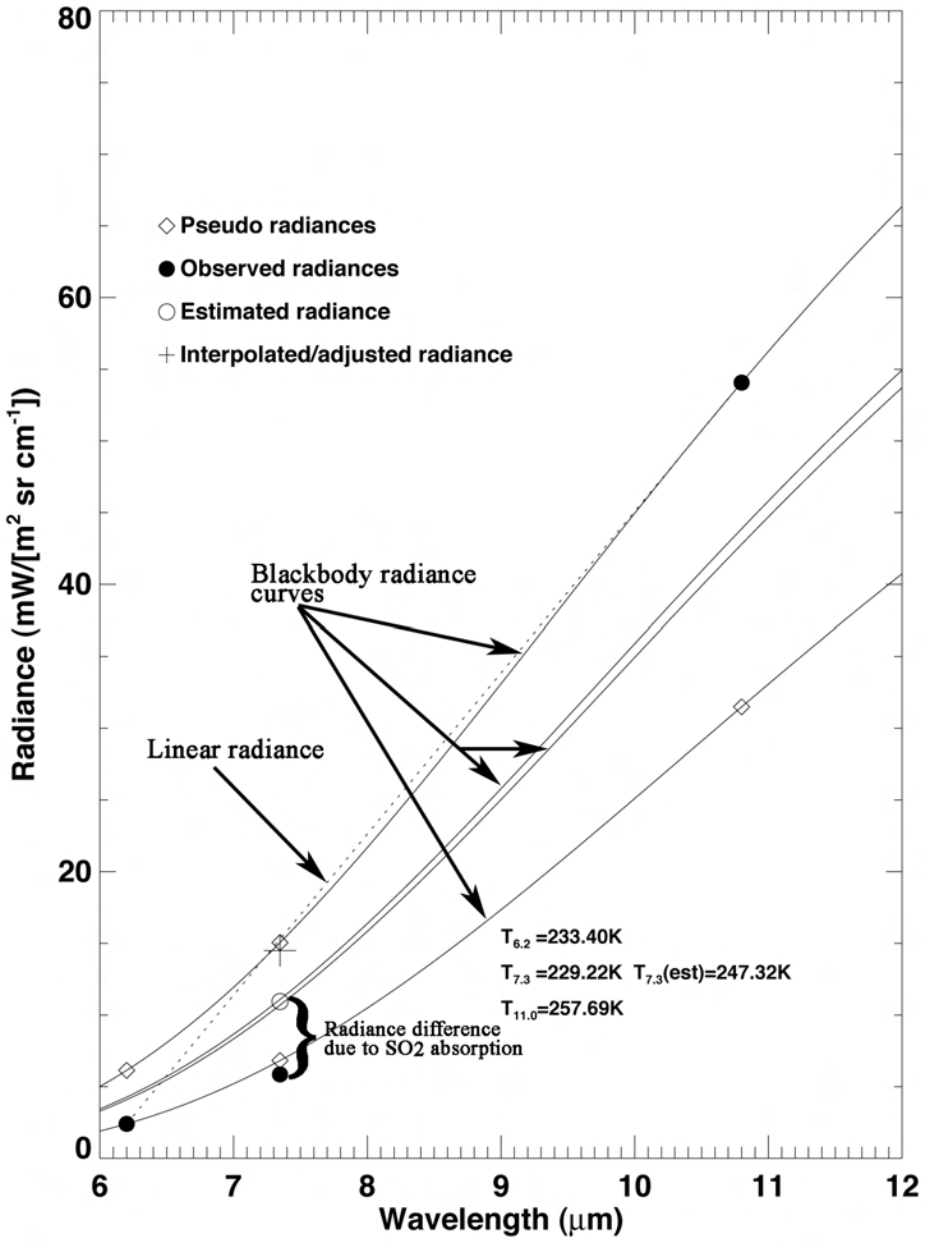

Figure 5.1: Radiance *vs.* Wavelength for a pixel which is free of SO_2 . The curves are blackbody radiances at the temperatures found by inverting the Planck function at 6.2 μm and 11.0 μm. The $+$ shows the adjusted linearly interpolated radiance at 7.3 μm, the open circle shows radiance at 7.3 μm, and the solid circles show the measured radiances.

(3) An adjustment to the linear interpolated 7.3 μm radiance is obtained from:

$$R_{7.3}^{adj} = 2.0[R^*(T_{11.0}, 7.3) - R^*(T_{6.2}, 7.3)].$$

(4) If the brightness temperature at 11.0 μm is above a certain threshold, then the 7.3 μm radiance estimate is obtained from the adjusted linear interpolated value; otherwise the average of the 'pseudo' radiances is used:

$$\hat{R}_{7.3} = R^{lin} - R^{adj} \;\; T_{11.0} > T_{thresh},$$
$$\hat{R}_{7.3} = 0.5[R^*(T_{6.2}, 7.3) + R^*(T_{11.0}, 7.3)] \;\; T_{11.0} \leq T_{thresh}.$$

The scheme attempts to account for the effects of multiple layer clouds within the pixel, whilst also remaining relatively simple to implement. The difficulty in estimating the background radiance lies

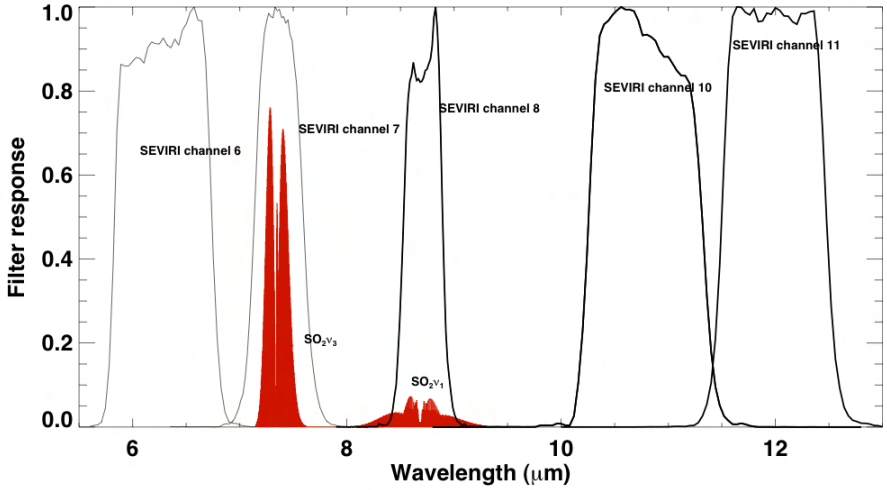

Figure 5.2: Positions of SEVIRI filter functions and vertical atmospheric transmittance (100 m atm cm and 1000 m atm cm) for the ν_1 and ν_3 SO_2 bands.

in the nonlinear temperature response from a pixel of mixed composition (i.e. clear-sky and clouds at multiple levels). Ideally the scheme should be designed to first estimate the fractional coverage of cloud within the pixel, together with an estimate of the clouds' height or radiating temperature. Then, under less restrictive assumptions the radiance at 7.3 μm is estimated from clear and cloud-sky radiances separately and combined by weighting the radiances with the fractional cover estimate. Further accuracy could be gained by employing a radiative transfer model with forward calculations and utilising the full suite of SEVIRI/2 channels. Such improvements are beyond the scope of this paper, and we readily concede that this retrieval scheme suffers limitations.

5.3.2.3 The effects of the surface

The analysis indicates that the surface radiance has only a small effect on the retrieval. This lack of dependence arises through the use of radiances from different channels for the same pixel when estimating the unperturbed radiance at 7.3 μm. For very thin veils of SO_2, the sensitivity of the scheme will prohibit accurate retrievals. A test is used to limit the retrieval to cases where,

$$T_{11.0} < 295K,$$

where $T_{11.0}$ is the (Planck) brightness temperature sensed in the 11.0 μm channel at the top of the atmosphere.

5.3.2.4 The effects of water vapour

Residual water vapour absorption may cause anomalies in the retrieval. If there is significant water vapour absorption within the SO_2 cloud then this will also show up as extra absorption in the 6.2 μm channel. This channel is used in the linear interpolation scheme so the algorithm will compensate for the effect of in-cloud water vapour. For cases where there are very high water vapour amounts lying below the SO_2 cloud it is possible that the retrieval will produce anomalous results. The effect will be worse if the SO_2 cloud is thin – this sets a limit on the lowest SO_2 amount that can be retrieved. There may also be situations where the vertical water vapour distribution causes the linear interpolation scheme to break-down, however these are unlikely to be common situations as they require unusual atmospheric conditions. Finally, SO_2 lying below significant water vapour will not produce a signal using this retrieval scheme because the 7.3 μm channel is sensitive to water vapour. This puts a constraint on the lowest level in the atmosphere for which SO_2 can be measured. A rule-of-thumb estimate for this is 3 km, which is the mean water vapour scale height (Randel *et al.*, 1996).

A test is employed to eliminate water vapour anomalies. The test is:

$$T_{11.1} > T_{6.7}. \tag{5.18}$$

Essentially this test regards the brightness temperature in the window channel (11.1 μm) as *always* being *larger* than the brightness temperature in the water vapour channel (6.7 μm). There are occasions when this may not be true (e.g. strong inversions). The test is conservative and eliminates such pixels from the retrieval process.

A further test checks that the brightness temperature at 8.2 μm (or 12.5 μm for NOAA-11 and beyond) is larger than the brightness temperature at 11.1 μm, when the 11.1 μm brightness temperature is low (250 K is used). This eliminates some volcanic ash signals and abnormal water vapour and cloud signals. The test is conservative.

5.3.2.5 The effects of clouds

Water/ice clouds lying above the SO_2 cloud will mask SO_2 absorption and consequently the scheme will not 'see' the SO_2. This can occur for very high, thick (cold) cloud, particularly in the tropics. A test has been devised to limit the retrieval to cases where,

$$T_{11.0} > 200K.$$

This test also doubles to eliminate problems arising from thin SO_2 veils overlying very cold surfaces (e.g. ice covered surfaces in winter).

A second test is employed to remove the effects of poor calibration, pixel misalignment and some abnormal conditions, notably very high water vapour loadings and strong cirrus cloud signals. The test is:

$$T_{8.6} - T_{11.0} < -10K. \tag{5.19}$$

For satellites after NOAA-10 the test is:

$$T_{12.0} - T_{11.0} < -10K. \tag{5.20}$$

The test is preliminary and needs refinement.

5.3.2.6 Sensitivity to cloud height

The conversion of ΔT measurements into transmittance is relatively straightforward via (10). The transmittance allows an estimate of the scaled absorber amounts q and w. Equations (3) and (4) can then be used to estimate the absorber amount u. However, this conversion has a dependence on pressure and temperature of the absorber; in other words it depends on the location of the SO_2 in the vertical. The dependence on pressure is stronger than that on temperature. Thus, the retrieval requires the user to supply a height estimate for the SO_2. Figure 3 illustrates the model dependence on height of the cloud.

5.3.2.7 Error analysis

Several sources of error have been identified in the retrieval of SO_2 from SEVIRI/2 infrared measurement. We class these errors into two types: those that contribute to the accuracy of the retrieval and those that limit the operation of the retrieval. The first type of errors (Type I) include as major sources:

- Inherent accuracy of the measurements–the NEΔT,
- Errors in estimating the background radiance,
- Transmittance modelling erors,
- Error in SO_2 cloud height estimation.

The NEΔT of SEVIRI channels 6, 10 and 11 are $\sim$0.5 K. The background radiance errors are difficult to estimate theoretically, but can be estimated by analysis of large amounts of SEVIRI/2 data when no SO_2 clouds are present. These analyses suggest an upper limit of this error to be $\pm$1 K. Transmittance modelling errors include SO_2 band parameter errors, errors due to using the double-exponential model, and errors in the relation between SO_2 transmittance and 7.3 μm temperature differences. The largest of these three sources of error is the latter and we have estimated this to be $\pm$1 K, based on radiative transfer simulations. Combining these errors and assuming that they are independent, the Type I error is:

$$\delta T_1 \approx \pm 1.5K.$$

This can be converted into an error in SO_2 amount by using the sensitivity of the model. Figure 4 illustrates Type I error in retrieved SO_2 for measurement and modelling errors and two cloud heights. For relatively low clouds, SO_2 amounts of < 5 D.U. (1 D.U. $= 1$ m atm-cm) are subject to large error and are probably indistinguishable from the noise (unless spatial coherence is evident). For higher clouds this lower threshold on the error increases to $\sim$20 D.U. In both cases errors of 5–10% are evident throughout the range of expected absorber amounts. The modelling errors dominate measurement errors–which is encouraging as improvements in the model are possible whilst improving measurement errors are only possible by some form of averaging (e.g. spatial and temporal).

The second type of errors (Type II) include:

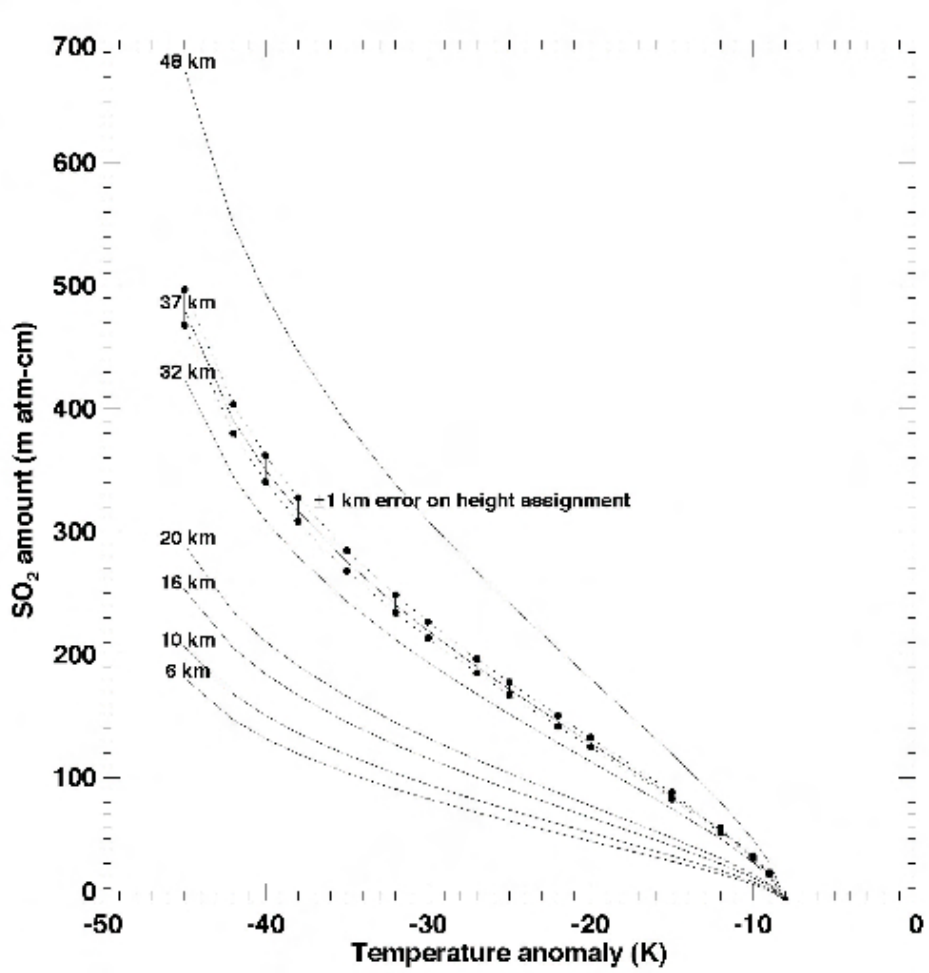

Figure 5.3: Temperature anomaly as a function of absorber amount for several cloud heights. Also shown are the range of variation of absorber amount for cloud height errors of ± 1 km and the total mass loadings for a uniform SO_2 cloud with an area of 10^6 km^2.

- Infrared contrast,
- Model sensitivity,
- Anomalous atmospheric conditions,
- Spectroscopic considerations.

Type II errors are systematic and result from basic violations of the measurement and/or atmospheric assumptions or from lack of knowledge of the physical processes. Because the technique described here involves an infrared atmsopheric emission measurement, the ability to retrieve SO_2 relies on the difference in temperature between the emitting source (the SO_2) and the background temperature (the surface, atmosphere or clouds). The lack of 'infrared contrast' fundamentally restricts the technique. Thus if the SO_2 cloud is at the same temperature as the surface/cloud/atmosphere below, it is not possible to reliably

retrieve the SO_2 amount regardless of its magnitude. Although on average the infrared contrast is adequate, there are persistent conditions where retrieval accuracy is limited. These include geographic locations where the surface below is as cold as the SO_2 cloud itself, for example, over ice-covered Antarctica and Greenland and climatic regions where the SO_2 cloud lies above the tops of high, thick clouds, such as tropical cumulonimbus clouds. Inspection of (9) shows that $\Delta T \rightarrow 0$, as the infrared contrast decreases (ΔB), regardless of the amount of SO_2 (τ_s).

Another drawback of the infrared measurement arises through lack of sensitivity of the model. There are two limiting cases for which SO_2 retrieval is problematic. For very high SO_2 amounts, inspection of (5) shows that as $\tau_t \rightarrow 0$, the measured radiance arises solely from the SO_2 cloud and consequently the infrared contrast is small. The transmittance model suggests that absorber amounts $>\sim$900 D.U. cause saturation. Using the optimal parameters for α and β in (10) with $\tau_s = 0$, suggests ΔT=-40 K. For very low SO_2 amounts, $\tau_s \rightarrow 1$ and (10) gives ΔT=α. This case can be investigated further by assuming that values with ΔT below $\alpha - |\delta T_1|$ are at the detection limit. In this case the model gives 3.7 D.U. for a cloud at a height of $\sim$8 km. In practice smaller amounts may be detected by assessing the spatial coherence of the data or by averaging pixels.

Atmospheric conditions for which the basic assumptions of the model are violated include cases where water vapour and/or cloud lies above the SO_2 cloud or when significant water vapour is collocated with the SO_2. Unusual inversions in the temperature and/or water vapour profile may also cause problems with the retrieval. All of these anomalous conditions do occur, but experience with processing the data suggests that they are not common. Perhaps the main area of concern is the occurrence of water vapour coexisting with SO_2 and/or occurring in large enough quantities to cause significant absorption across the 7.3 μm band. This problem is somewhat alleviated because the retrieval scheme makes use of radiance measurements at 6.2 μm, which changes as the mid-tropospheric water vapour changes in a similar fashion to the radiance change at 7.3 μm. Thus the scheme compensates for extra water vapour associated with the SO_2 cloud. Demonstrating unequivocally that water vapour is not a serious problem will need to wait until routine high spectral resolution data are available across the 7.3 μm band.

5.3.3 AIRS 7.3 μm retrieval

The following discussion is taken from the *Journal of Geophysical Research* paper by Prata and Bernardo (2006) which first introduced the technique for retrieving SO_2 from the high-spectral resolution AIRS measurements. It is included here for completeness.

The retrieval scheme is a two-step process. In the first step pixels that contain SO_2 are identified. In the second step a least squares procedure is used to find the amount of SO_2 in the pixel, based on off-line radiative transfer calculations. The upwelling radiance received by AIRS is assumed to consist of emission from the surface and from the atmosphere,

$$I_\nu = I_{\nu,s} + \int_0^\infty B_\nu[T(z)] \left(\frac{\partial \tau_\nu[z, q_1(z), q_2(z) ... q_n(z)]}{\partial z} \right) dz, \tag{5.21}$$

$I_{\nu,s}$ is the radiance emitted from the surface, B_ν is the Planck function, ν is wavenumber (cm^{-1}), $T(z)$ is the temperature as a function of height z, τ is the transmittance and $q_i(z), i = 1...n$ are constituent profiles of SO_2,H_2O, CO_2, O_3 etc. The aim of the analysis is to retrieve the column abundance, u_1 of SO_2, which is related to the constituent profile by,

$$u_1 = \int_0^\infty q_1(z) dz. \tag{5.22}$$

A portion of the AIRS spectrum between 1295 and 1405 cm^{-1} is used for the retrieval. Although SO_2 has absorption features at 2500 cm^{-1} and 1160 cm^{-1} these are not used in the retrieval. The 2500 cm^{-1} feature is often discernible in the data, while only the long wavelength side of the 1160 cm^{-1} feature can be identified in AIRS because there are no channels between 1170 and 1180 cm^{-1}. By using the 1295−1405 cm^{-1} interval, the surface emission term in (5.21) can be neglected, because the atmosphere is effectively black in this interval. Except for two small regions between 1320–1335 cm^{-1} and 1342–1358 cm^{-1}, the atmosphere appears to be opaque, and this is due principally to water vapour absorption. As the water vapour resides mostly in the lowest layers, closest to the surface, higher in the atmosphere the transmittance is higher. At some point in the atmosphere, which depends on the water vapour and SO_2 amounts, the atmosphere is sufficiently transparent and the SO_2 amount sufficiently large that the signal from the SO_2 dominates over that from the water vapour, and if the signal is greater than the instrumental noise, AIRS is able to detect and quantify the SO_2 absorption.

The total column background atmospheric SO_2 in the absence of volcanic activity is typically less than 1 Dobson unit[1] (DU) (<0.2 DU in the boundary layer). We assume that the SO_2 lies in a layer at $z = z_1$ to $z = z_2$ (above the boundary layer) so that equation (5.21) can be written,

$$\begin{aligned} I_\nu \approx & \int_0^{z_1} B_\nu[T(z)] \left(\frac{\partial \tau_\nu[z, q_2(z)...q_n(z)]}{\partial z} \right) dz \\ + & \int_{z_1}^{z_2} B_\nu[T(z)] \left(\frac{\partial \tau_\nu[z, q_1(z), q_2(z)...q_n(z)]}{\partial z} \right) dz \\ + & \int_{z_2}^{\infty} B_\nu[T(z)] \left(\frac{\partial \tau_\nu[z, q_2(z)...q_n(z)]}{\partial z} \right) dz. \end{aligned} \tag{5.23}$$

The AIRS retrieval relies on being able to correctly identify pixels within the image granule that are affected by SO_2. To do this we assume that the transmission of radiation within this restricted band, for each pixel, follows the Beer-Bougier-Lambert law:

$$I'_\nu = I_{\nu,0} \exp\left\{ - \int_o^{\infty} k_\nu(z) q(z) dz \right\}, \tag{5.24}$$

where I'_ν is the radiance at wavenumber ν leaving the SO_2 layer measured at the satellite (term 2 in Eq. 5.23), $I_{\nu,0}$ is the radiance entering the SO_2 layer from below and is equivalent to term 1 in (5.23), and k is the absorption coefficient. We assume that the radiance contributions from the atmosphere above the SO_2 layer (term 3 in (5.23)) are the same with or without the SO_2 layer. The radiance contributions reflected off the SO_2 layer are assumed to be negligible. We treat the radiation field as isotropic and assume that the atmosphere is locally horizontally homogeneous below and above the SO_2 layer. From (5.24) we can determine the absorbance spectrum,

$$A_\nu = -\ln\left\{ \frac{I'_\nu}{I_{o,\nu}} \right\} = \int_o^{\infty} k_\nu(z) q(z) dz. \tag{5.25}$$

For a single spectral Lorentz line or band and a single absorbing gas, the absorption can be written,

$$A\Delta\nu = \int_{\Delta\nu} \left\{ 1 - \exp[-\frac{1}{\pi} \int_{z_1}^{z_2} \frac{\alpha q(z)}{(\nu - \nu_0)^2 + \alpha^2} dz] \right\} d\nu, \tag{5.26}$$

[1] 1 DU = 2.6849 x 10^{16} molecules cm^{-2}.

where α is the line half-width and ν_0 is the location of the line centre. For a homogeneous path, the integral can be solved to yield (Goody, 1964),

$$A\Delta\nu = 2\pi\alpha\psi[L_0(\psi) + L_1(\psi)]\exp\{-\psi\}, \tag{5.27}$$

$$\psi = \frac{Su}{2\pi\alpha},$$

where S is the line strength, and L_0 and L_1 are modified Bessel functions. The weak, and strong absorption limits give a linear and square-root dependence respectively, of the absorption (A) on the absorber amount (u). The absorption due to a single spectral line or spectral band is often referred to as the equivalent width measured in units of cm^{-1}. In practice the absorbance is due to many lines, the path is inhomogeneous and there may be lines due to multiple absorbing gases, some with overlapping lines. Because the path is inhomogeneous there is a temperature and pressure dependence of the line parameters with height. A series of MODTRAN-3 simulations was carried out to examine how well this absorption model holds for the 7.3 μm SO_2 ν_3 -band.

Figure 5.2 shows a plot of the absorption (cm^{-1}) versus absorber amount (milli atm-cm or DU) for an SO_2 layer inserted at two heights in the atmosphere, for amounts up to 120 DU. Up to about 40 DU the relationship is linear, and follows the weak-line absorption limit. Beyond about 50 DU, the absorption is nonlinear and follows the square-root dependence of the strong-line limit. At high absorber amounts, the absorption tends to a constant and presumably the band is saturated resulting in a low sensitivity. Despite the presence of other interfering gases, the simulations suggest that the Lorentz band model is quite accurate. Calculation of the absorbance spectrum requires identification of a background or reference pixel (p_r,l_r), from which the reference radiance $I_{\nu,0}$ is determined. This pixel is found by comparing the absorbance spectrum of each pixel with a synthetic spectrum calculated using library line strengths (the HITRAN 96 database is used; Rothman *et al.*, 2003), MODTRAN-3 and a standard atmosphere perturbed by 100 DU of SO_2. Spectra were calculated using varying amounts of SO_2 (from 10 DU up to about 120 DU) and all have similar shapes and are highly correlated. For different atmospheres with different amounts of interfering gases, there are only small changes in the spectral features as determined by these simulations. The method of determining the optimal reference pixel relies solely on the degree of correlation between the absorbance spectrum computed from,

$$A_\nu = -Ln\left\{\frac{I_{p_t,l_t}}{I_{p_r,l_r}}\right\},$$

and that computed from,

$$S_\nu = -Ln\left\{\frac{I_s}{I_0}\right\},$$

where I_s is the synthetic radiance spectrum (1295−1405 cm^{-1}) with 100 DU of SO_2 and I_0 is the synthetic spectrum with background SO_2. I_{p_t,l_t} and I_{p_r,l_r} are measured AIRS radiance spectra (functions of ν–the reference to ν has been dropped for notational convenience) for the target pixel [p_t,l_t] and the reference pixel, [p_r,l_r], respectively, and p and l represent pixel and line number. The R^2 correlation is calculated from,

$$R = \frac{\frac{1}{n-1}\sum_{i=0}^{n-1}\tilde{A}_i\tilde{S}_i}{\sqrt{\frac{1}{n-1}\sum_{i=0}^{n-1}\tilde{A}_i{}^2}\sqrt{\frac{1}{n-1}\sum_{i=0}^{n-1}\tilde{S}_i{}^2}}. \tag{5.28}$$

The ordinates of the spectrum occur at discrete values of wavenumber, ν_i that are determined by the AIRS instrument characteristic, and n is the number of channels used (n≈140). $\tilde{A}$ and $\tilde{S}$ are the normalized

measured and synthetic absorbance spectrums, defined as,

$$\tilde{A}_i = \frac{A_i - \min(A_i)}{\max(A_i) - \min(A_i)},$$

$$\tilde{S}_i = \frac{S_i - \min(S_i)}{\max(S_i) - \min(S_i)}.$$

The reference pixel is deemed to be that pixel which produces the highest R^2 correlation over all other reference pixels in the image. Generally, this pixel is geographically close to the target pixel and thus the assumption that the atmospheres of the target and reference pixel be similar is likely to be met for each SO_2 pixel. The correlation is lowest when other gases interfere with the spectral matching, or when the SO_2 column amount is low or when clouds and collocated water vapour exist within the SO_2 layer or above it. The relation between the R^2 correlation and the column SO_2 need not necessarily be linear or even positive. High SO_2 amounts may occur in the presence of enhanced water vapour loadings and the spectral matching may, in this case, produce a low correlation. Note that it is the spectral shape that determines the correlation, not the absolute absorber amount. For thin SO_2 layers in very dry atmospheres over cold surfaces many of the underlying assumptions of the retrieval scheme break down and the R^2 correlations can be quite low regardless of the amount of SO_2 present.

The procedure is time-consuming, but is objective and optimal in some sense. Once the reference pixels have been found (there will be potentially up to one less reference pixels as there are target pixels), the absorbance spectra for all pixels with R^2 correlations above a specified value are calculated and a correlation image (containing the R^2 correlations between the synthetic and observed spectra for all pixels) determined. The correlation image and the reference pixel arrays are retained during the analysis procedure. Figure 5.3 shows a comparison between the observed absorbance spectrum (dotted black line) and the synthetic spectrum (continuous red line) for six pixels with different degrees of calculated correlation for the 10 May 2003 eruption of Anatahan. Also shown in the Figure are the retrieved SO_2 column amounts derived during the second stage of the retrieval process. The correlations vary from R^2=0.46 (panel a) to R^2=0.96 (panel f); in this case the pixel with the highest R^2-correlation also contains the highest SO_2 column amount. The location (pixel number and geographic coordinates) are also given on the Figure and it can be seen that in all cases but one, the reference pixel is on the same line number as the target pixel and in all cases the reference pixel is clear of any retrieved SO_2. There are some possible scenarios where the spectral matching might produce erroneous results. These might be when the reference pixel contains some SO_2, leading to an underestimate of the target SO_2 or when the reference pixel is geographically distant from the target pixel, and hence the atmospheric environment might be different. From experience with processing large amounts of AIRS data it seems these cases are rare. When SO_2 is present in a reference pixel it is expected that the R^2-correlation will be lower than for another SO_2-free pixel. However, it is possible to have an SO_2 cloud so large that it covers the entire AIRS granule (in that case one might choose to use a second contiguous granule) and we caution that there are other scenarios one could imagine that might affect the correlations.

The column SO_2 is now determined for pixels exceeding a specified R^2 from the absorbance spectrum using a linear least squares method. In this method a set of pre-computed spectra are determined at discrete levels in the atmosphere at 2 km intervals starting at 6 km and ending at 20 km. These are linearly combined to produce a least-squares "best fit" between the measured and computed spectra. The computed spectra include the effects of a constant pre-defined water vapour distribution and the least-squares is improved by providing an estimate of the height of the cloud layer, which is assumed to contain only SO_2 and enhanced water vapour (a constant amount for all retrievals). There is a strong dependence between absorbance and

the height of the SO_2 layer in the atmosphere, which is unknown. The height can be specified from a trajectory model run, or from some other independent source.

The amount of SO_2 retrieved using the 7.3 μm band is dependent on the location of the SO_2 layer in the atmosphere. There is a temperature dependence of the line strengths for this band. There is also a strong vertical dependence because of the interfering effects of water vapour. We define the cut-off height for SO_2 retrievals as the height in the atmosphere where the signal-to-noise ratio reaches unity. The NEΔT for AIRS channels between 3.7 and 13.5 μm is $\sim$0.2 K at 250 K, which gives NEΔI$\approx$0.1 mW/(m^2 sr cm^{-1}) for channels in the region 1295–1405 cm^{-1}. The signal strength can be calculated from simulations,

$$\Delta S_\nu = |I_{\nu,z'} - I_{\nu,0}|, \tag{5.29}$$

where $I_{\nu,z'}$ is the spectral radiance from an atmosphere with a prescribed amount of SO_2 placed at height z' in the atmosphere, and $I_{\nu,0}$ is the spectral radiance from an unperturbed, background atmosphere. The signal to noise ratio (SNR) is,

$$SNR = \frac{\sqrt{\frac{1}{\Delta\nu}\int_{\Delta\nu}\Delta S_\nu^2 d\nu}}{NE\Delta I}.$$

We define the cut-off height z_c=z' when SNR=1.0. Figure 4 shows the variation of SNR with height (z') for a tropical atmosphere with 50 DU placed at different levels in the atmosphere from the surface up to about 5 km. In this case the SNR=1 at $z' \approx 3$ km. It is apparent that for this case, below $\sim$2.5 km, the noise is twice the signal strength. For drier and wetter atmospheres, z_c decreases or increases, respectively; likewise for emplacements of larger masses of SO_2 the signal strength would be larger and the cut-off height would decrease. Under most atmospheric conditions absorption by water vapour across this band is significant below $\sim$ 3 km and we maintain that the AIRS instrument is effectively "blind" to SO_2 emissions in the boundary layer, and often below $\sim$3 km (but note that this cut-off height depends on the SNR). This constraint suggests that the 7.3 μm AIRS channels behave like a filter to reveal mostly upper troposphere/lower stratosphere (UTLS) SO_2, which is more likely to be climatically significant.

Another approach to assess the information content of the AIRS channels in the 1295–1405 cm^{-1} interval is to use weighting functions. The weighting function (e.g. Rodgers, 2000) is,

$$\mathcal{W}_\nu(z) = \frac{d\tau_\nu(z)}{dz},$$

which appears in the integrals of (5.3). Weighting functions for channels near 7.3 μm typically peak between 400–600 hPa depending on the water vapour, temperature and SO_2 vertical profiles. This suggests that this waveband has greatest sensitivity to SO_2 in the mid- to upper-troposphere (4–8 km). Given knowledge of these three profiles it is straightforward to calculate the $\mathcal{W}$'s for AIRS channels and determine which atmospheric layers are contributing to the measured radiances. The value in this approach is that it permits an objective means for selecting specific (high information content) AIRS channels for retrieving SO_2. Here we employ an *ad hoc* "two-step" method of first identifying SO_2 pixels through spectral matching and then retrieving the column abundance through a least-squares procedure and off-line radiative transfer calculations, utilizing all AIRS channels between $\sim$1320 cm^{-1} to $\sim$1395 cm^{-1}. We sacrifice any potential vertical SO_2 profile information in pursuing this approach.

Equation (5) in matrix notation may be written.

$$\vec{y} = \mathbf{K}\vec{x} \tag{5.30}$$

where $x = x_o \ldots x_N$ is a vector of layer absorber amounts to be determined, K is an MxN matrix consisting of absorption cross-sections at M wavenumbers and N atmospheric layers, and y is a vector of measured absorbances at M wavenumbers. The absorption cross-sections at 8 levels, starting at 6 km and ending at 20 km in 2 km steps, are pre-determined from a detailed radiative transfer program (Griffith, 1996). The least-squares solution to (5.30) is (Rodgers, 2000),

$$\vec{x} = (\mathbf{K}^T\mathbf{K})^{-1}\mathbf{K}^T\vec{y}. \tag{5.31}$$

Equation (5.31) is underdetermined because the basis functions K are approximately linear functions of each other. The dominant processes affecting the shapes of the spectral lines within the band are pressure and Doppler (thermal) broadening. Temperature decreases through the UTLS (Upper Troposphere-Lower Stratosphere) in an almost linear manner, giving absorption cross-sections in different layers which are very nearly linear functions of each other. To stabilise $\mathbf{K}$, we found it necessary to include the effects of a second gas– water vapour. Thus the basis functions consist of absorption cross-sections for a standard profile of water vapour with a single layer of enhanced SO_2 and H_2O at a prescribed level. The retrieval produces a layer abundance of SO_2, which we treat as a column amount. The retrieval scheme produces layer amounts in 8-layers, which are integrated to obtain a column amount. The information content in the layers is insufficient to expect an accurate vertical profile. Improvements to this scheme would include a better specification of the water vapour profile (potentially this could be determined from AIRS standard retrieval products) and simultaneous retrieval of SO_2 and H_2O. This would also help to identify enhancements in "in plume" water vapour associated with the volcanic cloud. In principle it is also possible to determine some vertical profile information on SO_2 by judicious choice of "micro-windows" within the ν_3-band.

The SO_2 is retrieved on a pixel by pixel basis using (5.31) for only those pixels that exceed a specified value of R^2. The units of SO_2 amount are molecules cm^{-2}, which we convert to milli atm cm or DU. The use of DU for SO_2 column abundance is done for consistency with the OMI, TOMS and GOME retrievals. The total mass loading (in Tg) is evaluated from:

$$M_{SO_2} = 2.8510^{-8} \sum_i u_i \beta_i(\theta), \tag{5.32}$$

where i is pixel number, u absorber amount (in DU), β is the area of a pixel (in km^2) evaluated assuming elliptical pixels on a spherical earth, and θ is the AIRS scan angle subtended at the earth's surface.

Each SO_2 retrieval is accompanied by an R^2-correlation map. R^2 $\approx$0.3 were found to delineate the boundary for SO_2 retrievals of 6 DU, which is considered to be the lower limit of SO_2 detection from AIRS. Usually we compute total SO_2 mass loadings for pixels with R^2=0.1 and R^2=0.7, which provides a range of certainty and an error bound for the retrieved products. Finally, the height of the SO_2 cloud is required as input to the retrieval. This information is derived using wind trajectories determined using the HYSPLIT model (Draxler and Rolph, 2003).

5.3.4 Regression-based Algorithm–RBA

An attempt was made to correlate the SO_2 retrievals from OMI, GOME-2 and AIRS with SEVIRI infrared radiances in channels 6.2, 7.3, 8.6, 11 and 12 μm. The basic idea is to use the information in the SEVIRI 7.3 μm and 8.6 μm to detect SO_2 and rely on the quantitative information in the OMI/GOME-2/AIRS retrievals to provide regression coefficients to convert the radiances to SO_2 partial columns.

$$SO_2^i = \sum_{j=1,5} a_j R_j, \tag{5.33}$$

where, R_j are radiances in SEVIRI channels WV62 (j=1), WV73 (j=2), IR86 (j=3), IR11 (j=4), and IR12 (j=5), a_j are regression coefficients and $SO_2{}^i$ are SO_2 partial columns from instrument i, corresponding to OMI, GOME-2 and AIRS. The regression was performed by collocating the SEVIRI pixels with the OMI, GOME-2 or AIRS fields-of-view, resulting in several individual SEVIRI pixels for each coincidence. The mean of these values were used in the regression. The cases studied showed little SO_2 information content and further study is required to assess whether this procedure can be successful. Some possible causes for the poor results include: (1) cloudiness in some pixels forming the mean, thus degrading the correlation; (2) nonlinearity in the relation between SEVIRI radiances and SO_2 partial column abundance; (3) water vapour absorption, and (4) vertical height dependence of SO_2 with SEVIRI radiances. These effects need to be explored in more detail in further studies.

The relation between upper troposphere SO_2 and the SEVIRI 7.3 μm radiances is explored further in Chapter 7.

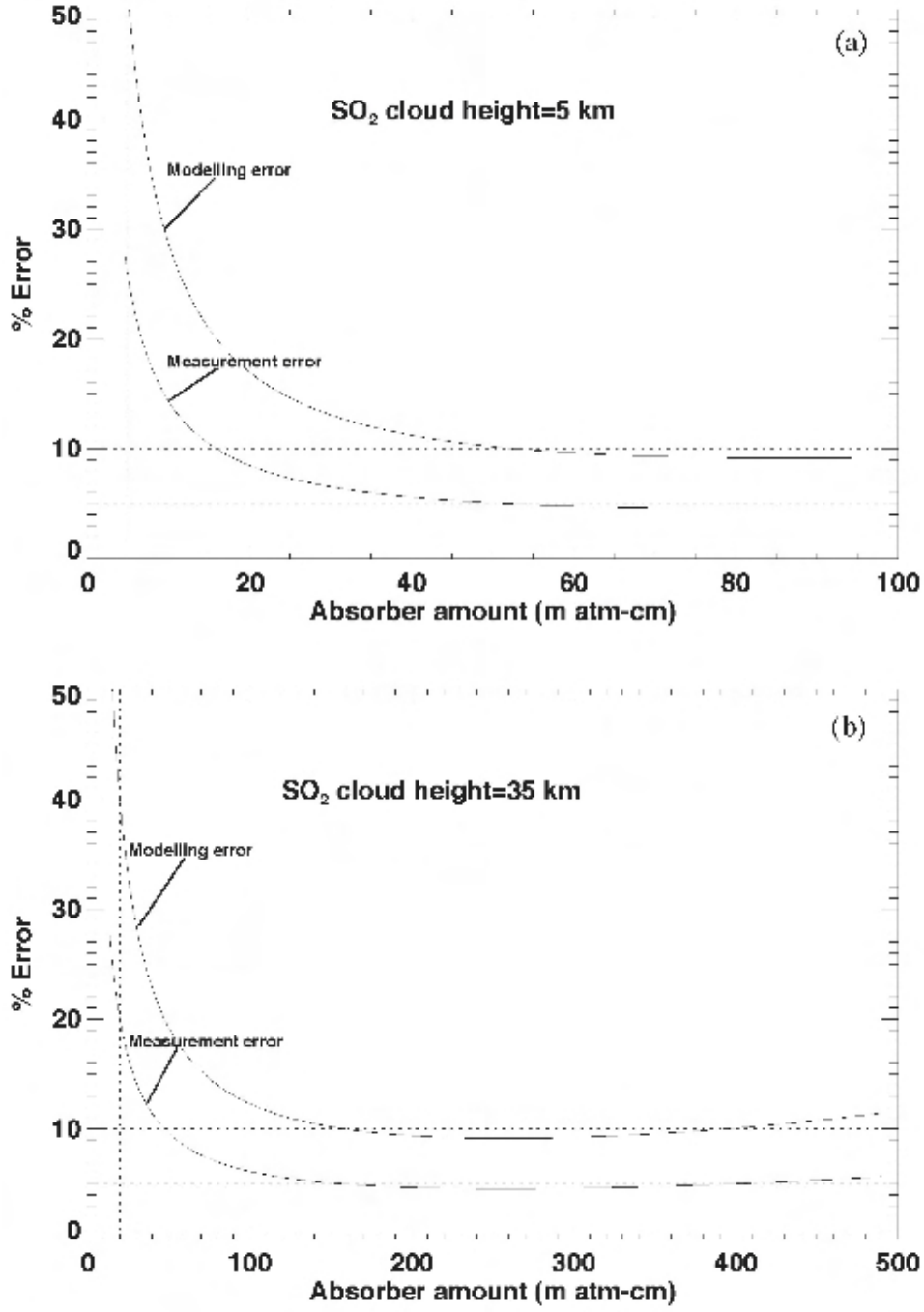

Figure 5.4: (a) Measurement and modelling errors as a function of absorber amount for a plume at 5 km height and low abundance. (b) Measurement and modelling errors as a function of absorber amount for a plume at 35 km height and high abundance.

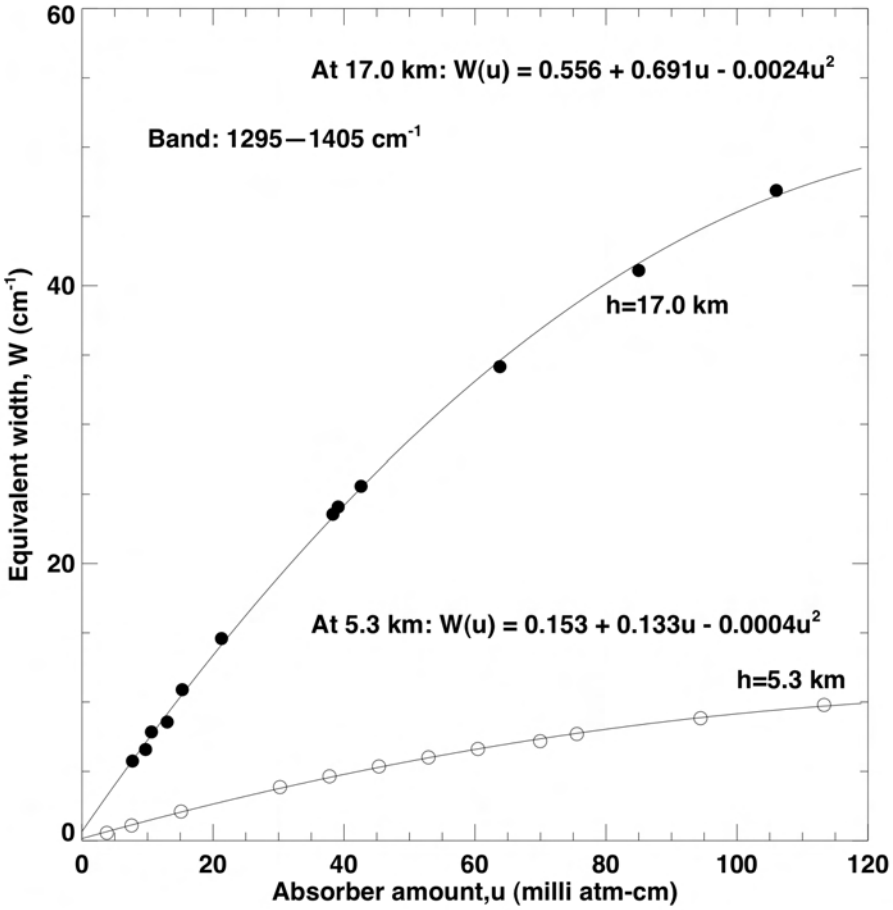

Figure 5.5: The equivalent width or absorption as a function of absorber amount determined from radiative transfer calculations for single SO_2 layers at 5.3 km and 17.3 km. For SO_2 columns $<$40 DU, the variation of absorption with absorber amount is approximately linear, while above 50 DU there is a square-root dependence.

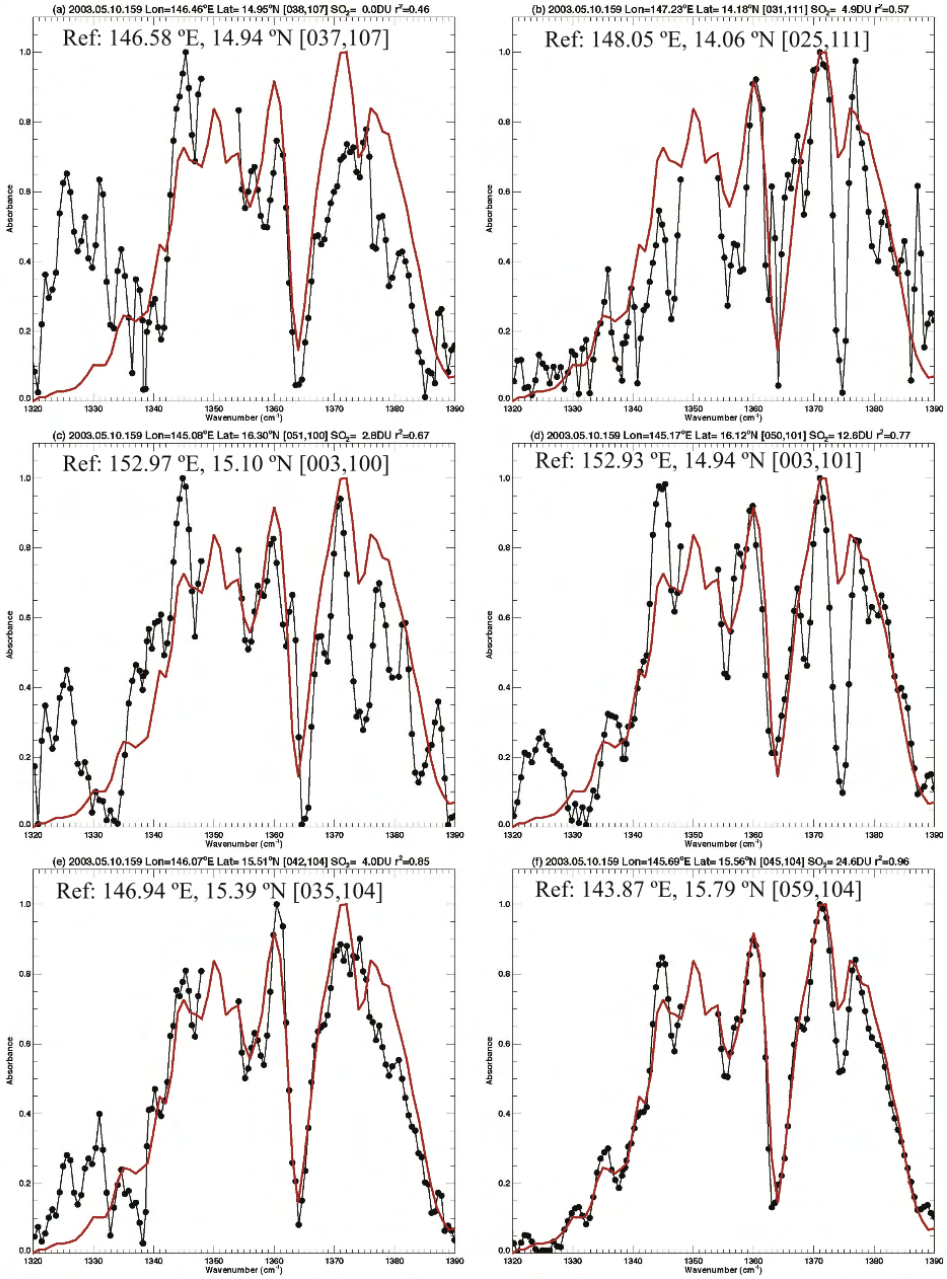

Figure 5.6: Spectral matching plots for measured absorbance spectra (dotted black lines) and synthetic absorbance spectra (red lines) for R^2 correlations ranging from 0.46 (panel a.) to 0.96 (panel f.). The gaps in the measured spectra between 1348–1354 cm^{-1} are measurement gaps and are excluded in the correlation analyses. The locations of the target pixel and the reference pixel are given in each panel. Note that the retrieved SO_2 column shown has been derived from least squares estimation and not by integrating the absorbance spectrum.

Chapter 6

Results–Ash

6.1 Radius, optical depth and mass

The retrieval results are reported in an ASCII file with the naming convention:

RTGyyyymmddhhtt.out

where:

yyyy=Year (e.g. 2010)
mm=Month of year (1–12)
dd=Day of month (1–31)
hh=Hour of day (1-24, UTC)
tt=Minute of hour (00,15,30,45, UTC)

The entries in each file consist of a short text header followed by the number of good retrievals with 14 entries for each successful retrieval with the following format:

Look-up file:/users/fredprata/Projects/seviri-eyja/dom-runs/domTs280Tc210.txt
T_c=212.618 (K) T_s=275.198 (K)
Number of retrievals= 6567
Number of good retrievals= 6545 Total mass= 0.215592 Tg

Lon	Lat	Mass	Radius	τ	θ	T_{11}	T_{12}	WVcor	Area	T_{73}	Line	Pix	Flag
(°)	(°)	(gm^{-2})	(μm)	–	(°)	(K)	(K)	(K)	(km^2)	(K)	–	–	

where:

Lon=Longitude (decimal degrees, east positive)
Lat=Latitude (decimal degrees, north positive)
Mass=Mass loading in gm^{-2}
Radius=Mean effective particle radius (μm)

τ=11 μm infrared optical depth (dimensionless)
θ=satellite zenith angle (decimal degrees)
T_{11}= 11 μm brightness temperature (K)
T_{12}= 12 μm brightness temperature (K)
WVcor=Water vapour correction (K)
Area=Area of pixel (km^2)
T_{73}= 7.3 μm brightness temperature (K)
Line=SEVIRI line number (dimensionless)
Pixel=SEVIRI pixel number (dimensionles)
Flag=Retrieval flag (1=good).

For a monomodial, uniform size distribution, the mass loading is calculated from:

$$m_l = \frac{4}{3}\rho\frac{r_e\tau}{Q_{ext}} \tag{6.1}$$

where, ρ is the bulk density of ash (taken as 2600 kgm^{-3}), r_e is the effective radius, τ_λ the infrared optical depth at wavelength, λ=11 μm, and $Q_{ext}(\lambda)$ the extinction efficiency parameter. Graphical results are presented for each 15 minute SEVIRI granule in the following manner (see Fig. 6.1):

The statistics panel displays information about the retrieval. The meaning of the parameters is:

1 Mean radius (Guassian)–the mean effective radius determined from a Gaussian fit to the retrieved distribution.

2 Mean radius (6-parameter fit)– the mean effective radius determined from a 6-parameter fit.

3 Total mass]–the sum of the mass loadings for all good pixel retrievals multiplied by the area of each pixel

4 Maximum mass loading–the highest mass loading found in the granule. This can be misleading as sometimes this is an isolated point and may be anomalous.

5 Pixels with mass loading $>$ 6 gm^{-2}–number of pixels exceeding this threshold and the percentage compared to the number of pixels found with mass loading $>$ 0 gm^{-2}.

6 Pixels with mass loading $>$ 4 gm^{-2}–number of pixels exceeding this threshold and the percentage compared to the number of pixels found with mass loading $>$ 0 gm^{-2}.

7 Pixels with mass loading $>$ 2 gm^{-2} and $<$ 4 gm^{-2}–number of pixels within these limits and the percentage compared to the number of pixels found with mass loading $>$ 0 gm^{-2}.

8 Pixels with mass loading $>$ 0.2 gm^{-2} and $<$ 2 gm^{-2}–number of pixels within these limits and the percentage compared to the number of pixels found with mass loading $>$ 0 gm^{-2}.

9 Pixels with mass loading $>$ 0 gm^{-2}–number of pixels exceeding this threshold and the percentage compared to all pixels in the granule.

10 Total number of pixels in the granule.

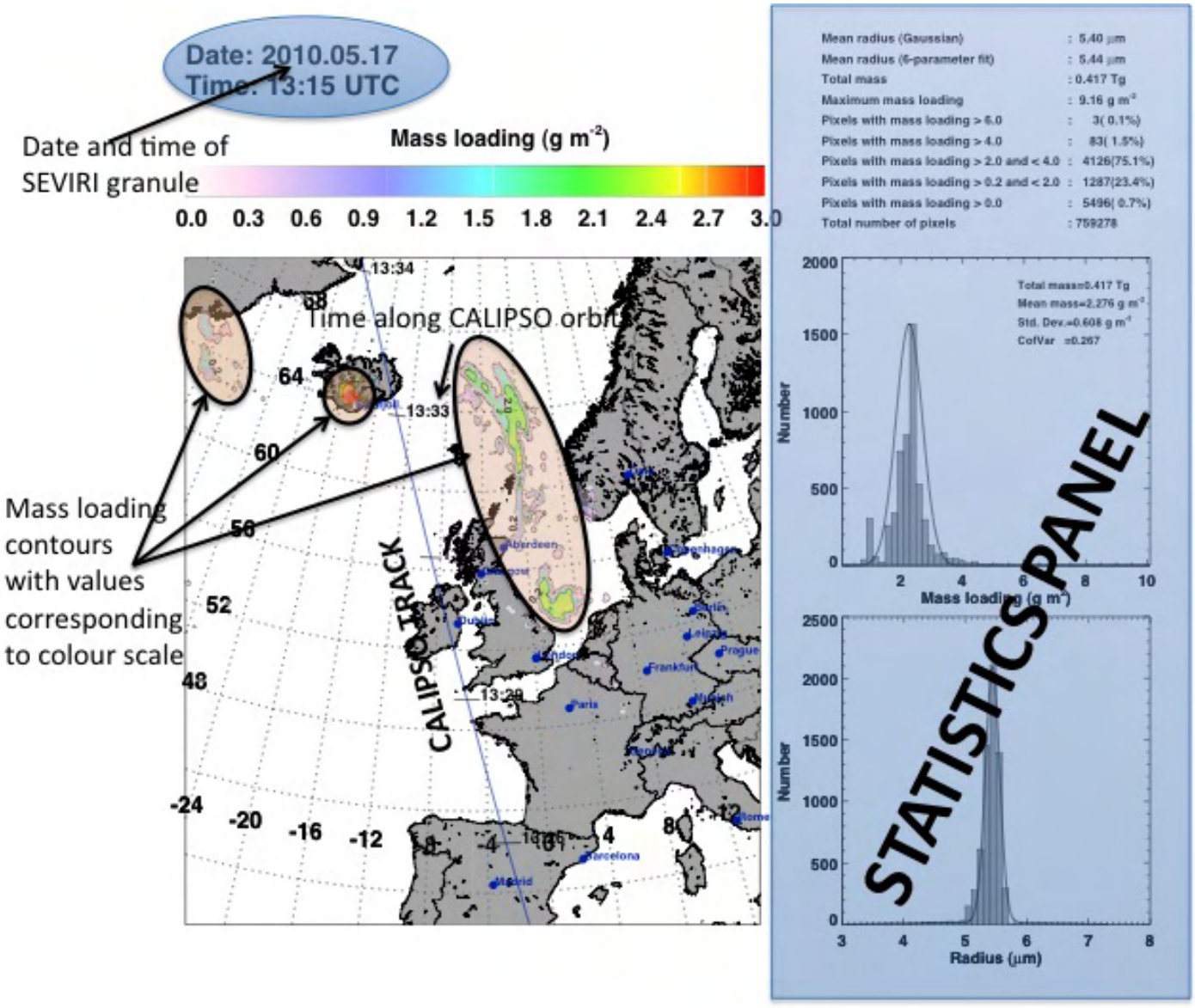

Figure 6.1: Example of the graphical output displaying results from the retrieval files.

Within the statistics panel, some moments for the mass distribution are also provided, e.g. the total mass, the mean mass loading, the standard deviation of the mass loading and the coefficient of variation. The following figures (Figs. 6.2–6.39) show results selected because there is a corresponding CALIPSO overpass (see Table 7.1)–all SEVIRI granules from 14.04.2010 00:00UT until 22.05.2010 23:45UT have been processed and plotted and these are provided as separate files.

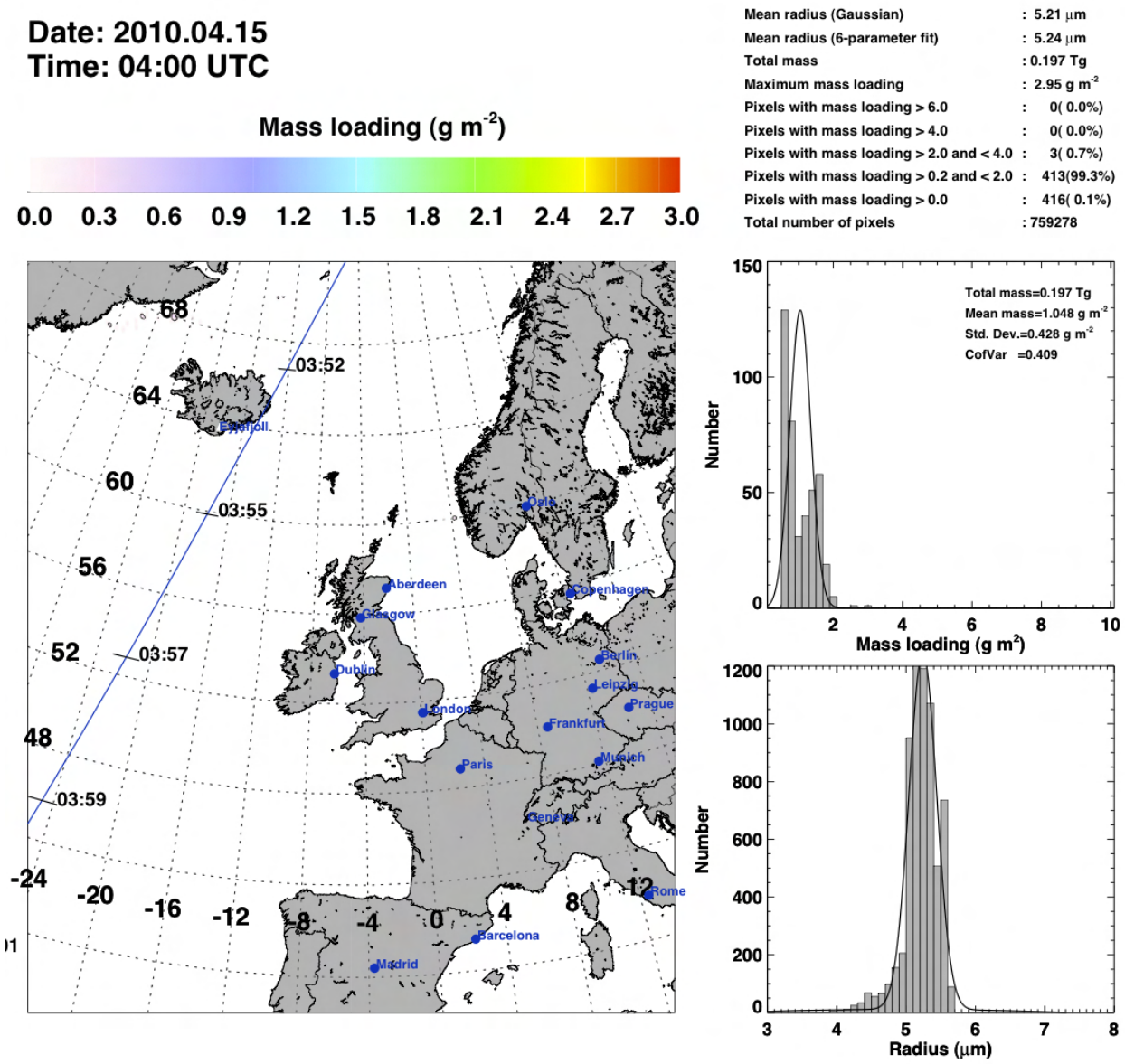

Figure 6.2: Date: 15 April 2010, Time: 04:00 UT.

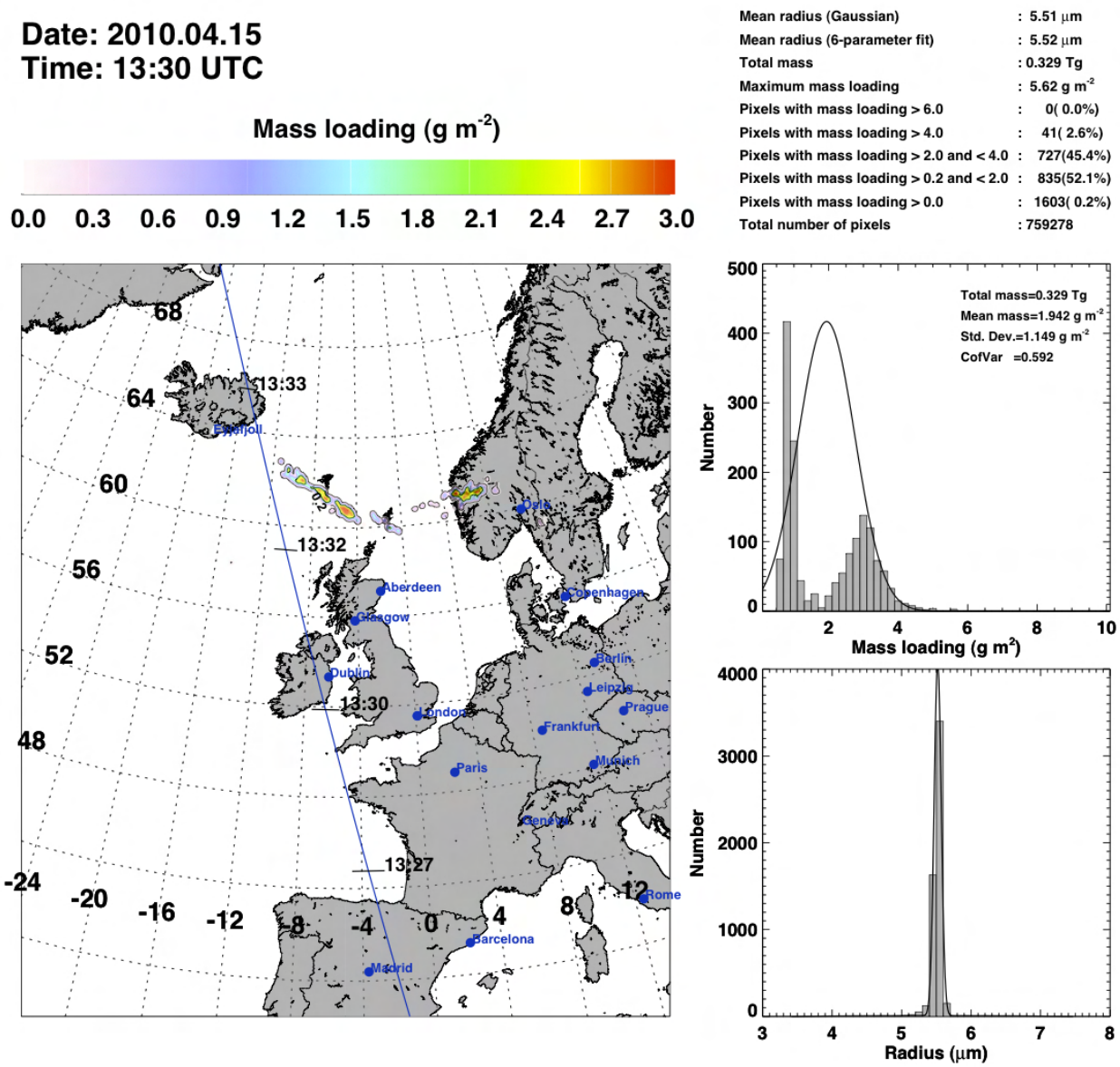

Figure 6.3: Date: 15 April 2010, Time: 13:30 UT.

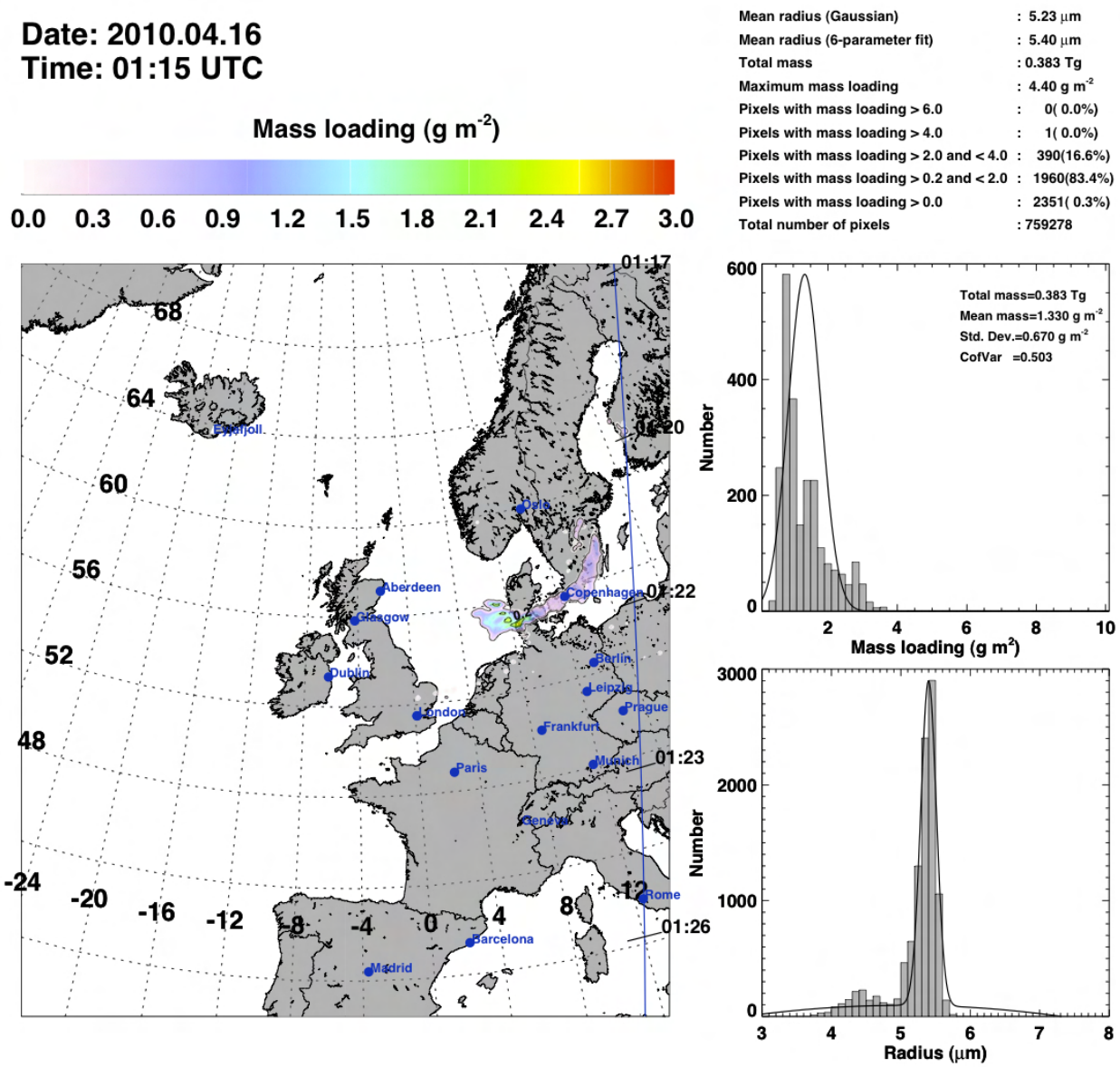

Figure 6.4: Date: 16 April 2010, Time: 01:15 UT.

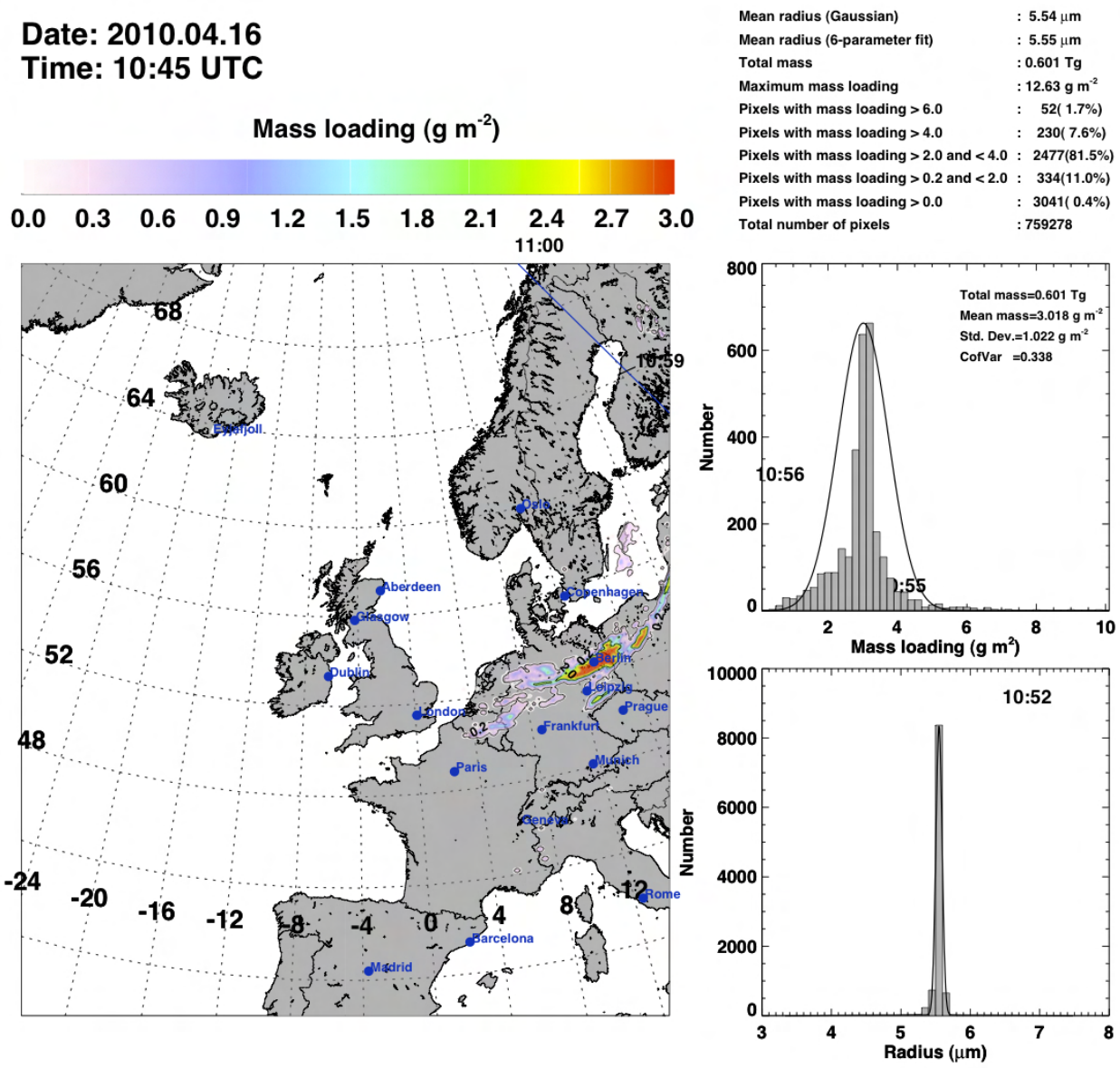

Figure 6.5: Date: 16 April 2010, Time: 10:45 UT.

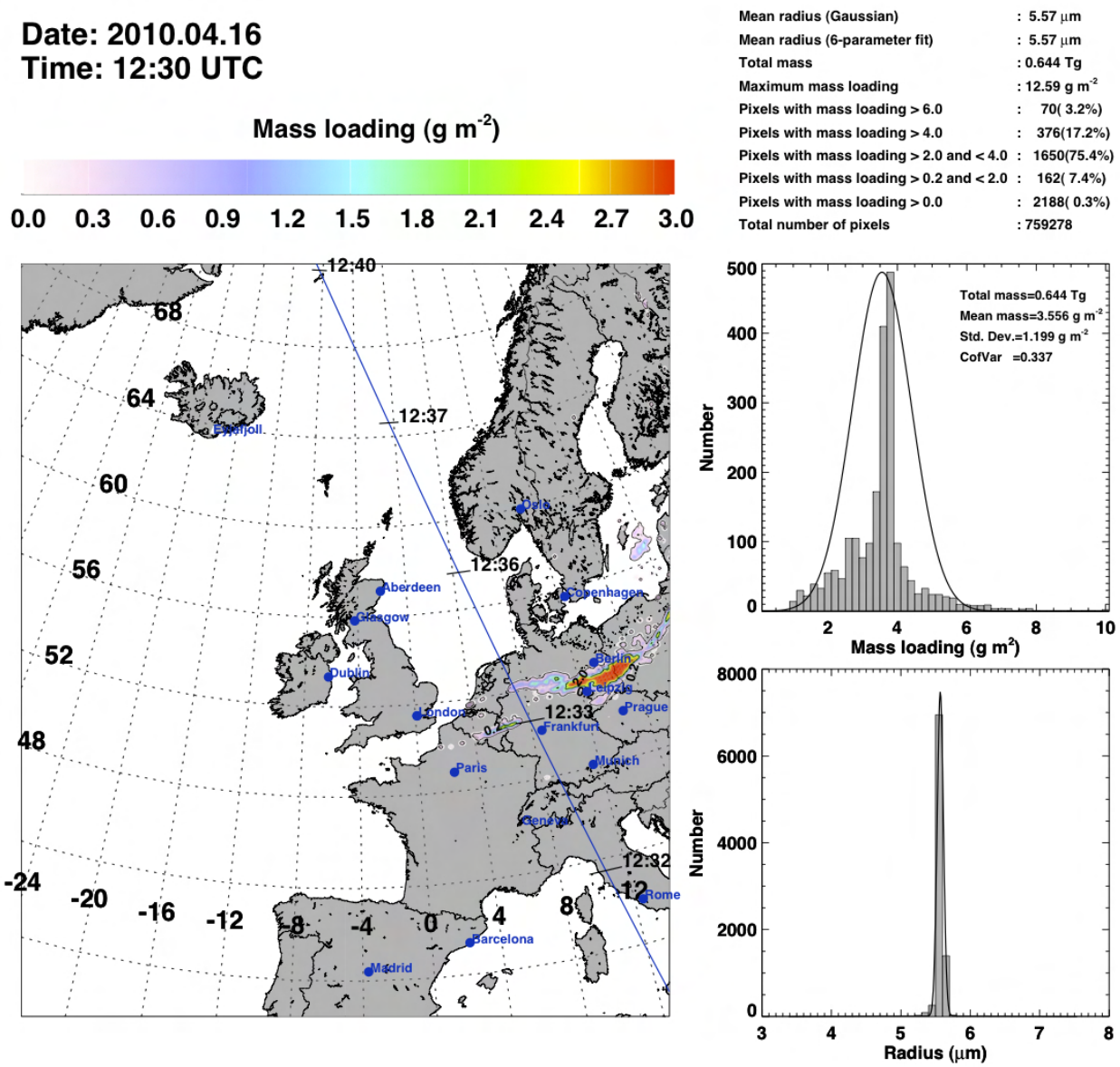

Figure 6.6: Date: 16 April 2010, Time: 12:30 UT.

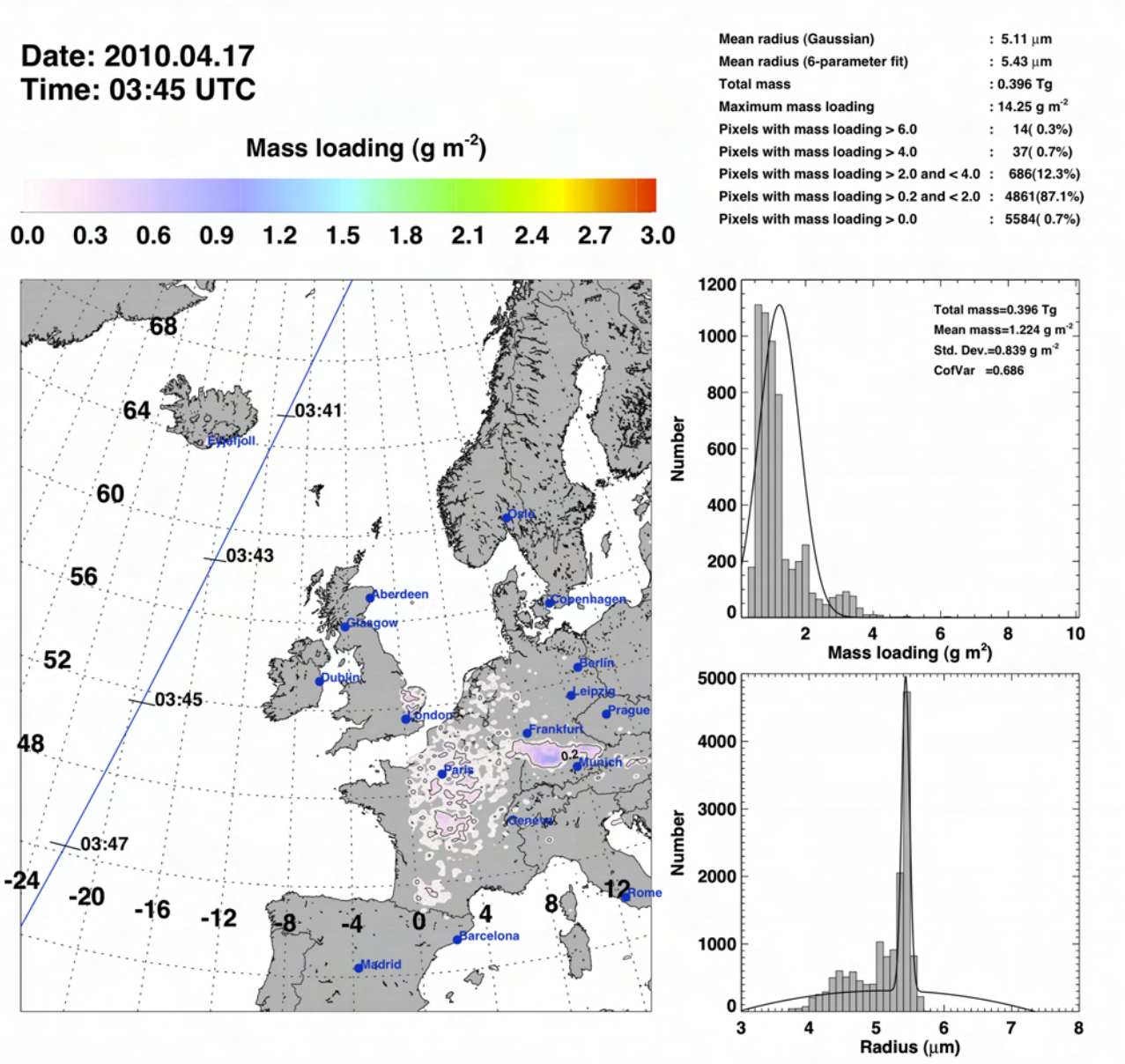

Figure 6.7: Date: 17 April 2010, Time: 03:45 UT.

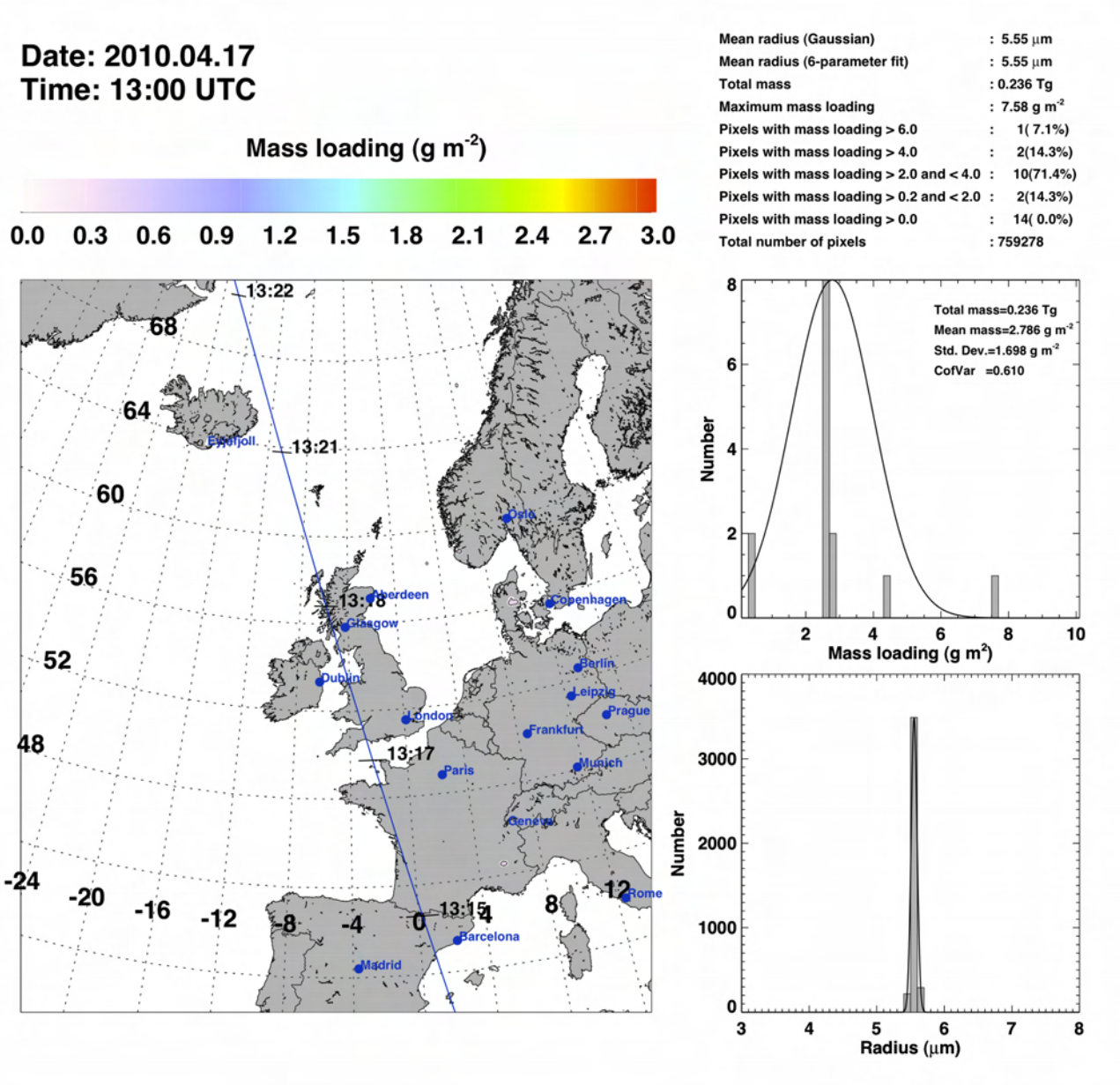

Figure 6.8: Date: 17 April 2010, Time: 13:00 UT.

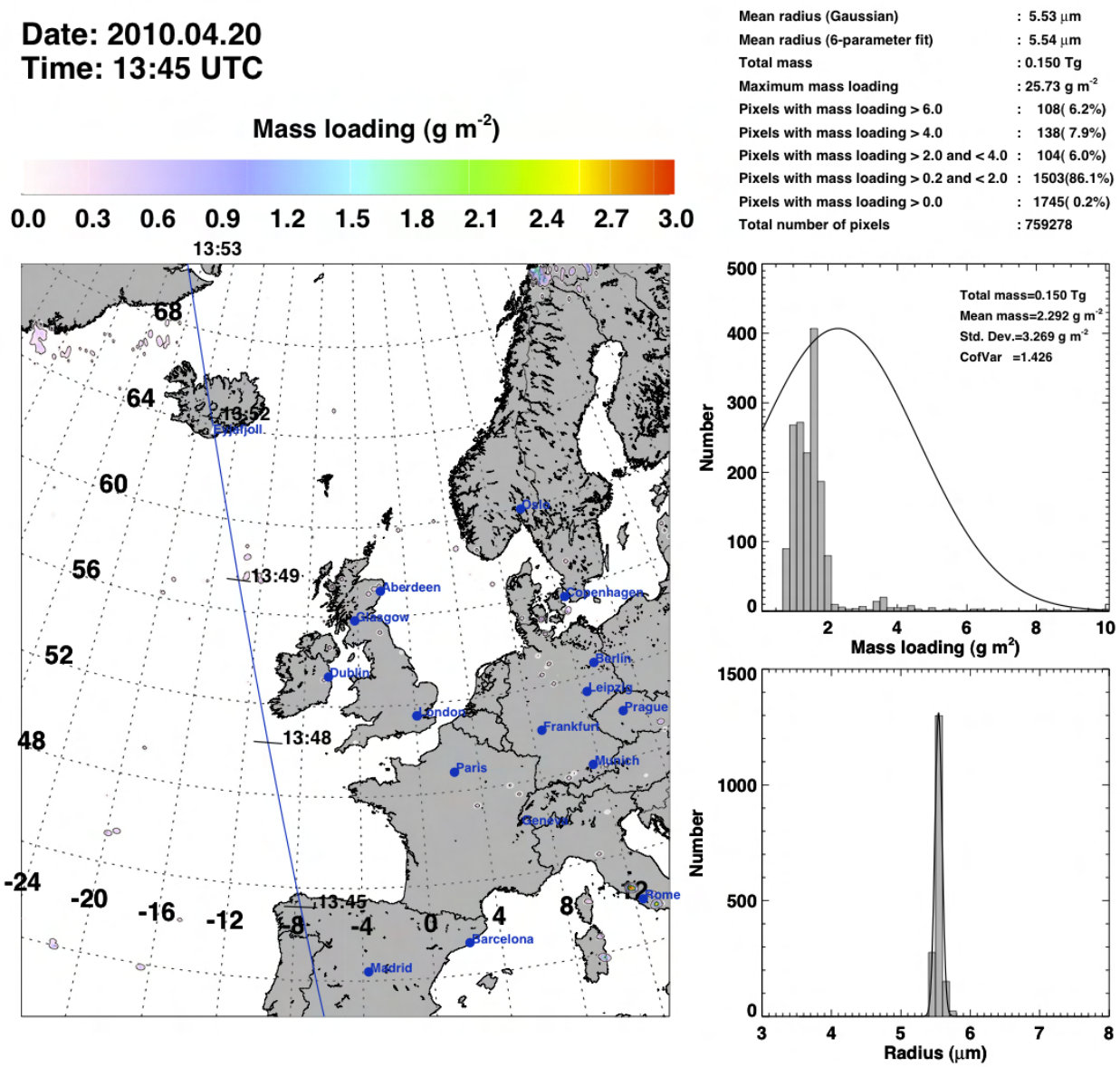

Figure 6.9: Date: 20 April 2010, Time: 13:45 UT.

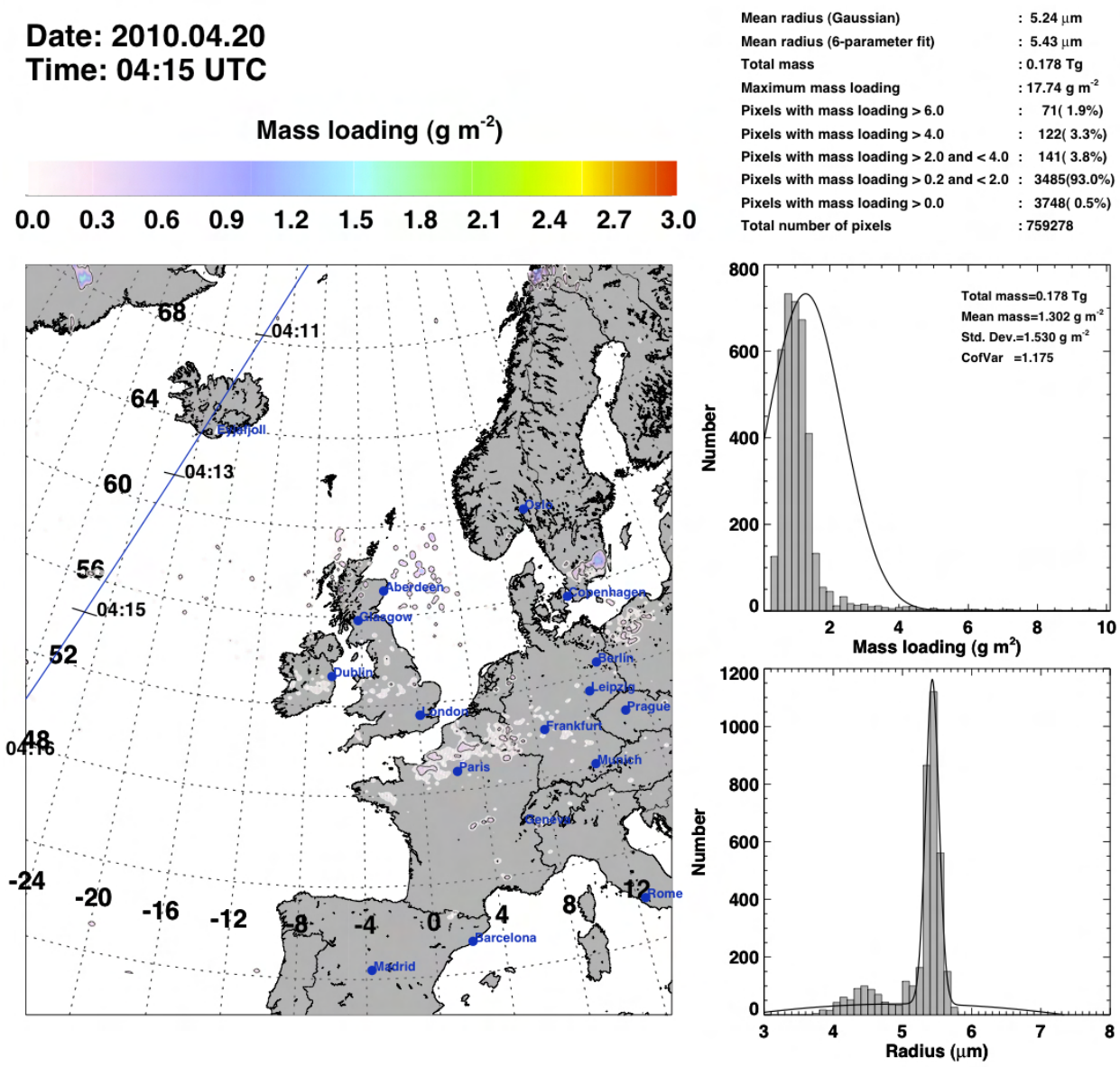

Figure 6.10: Date: 20 April 2010, Time: 04:15 UT.

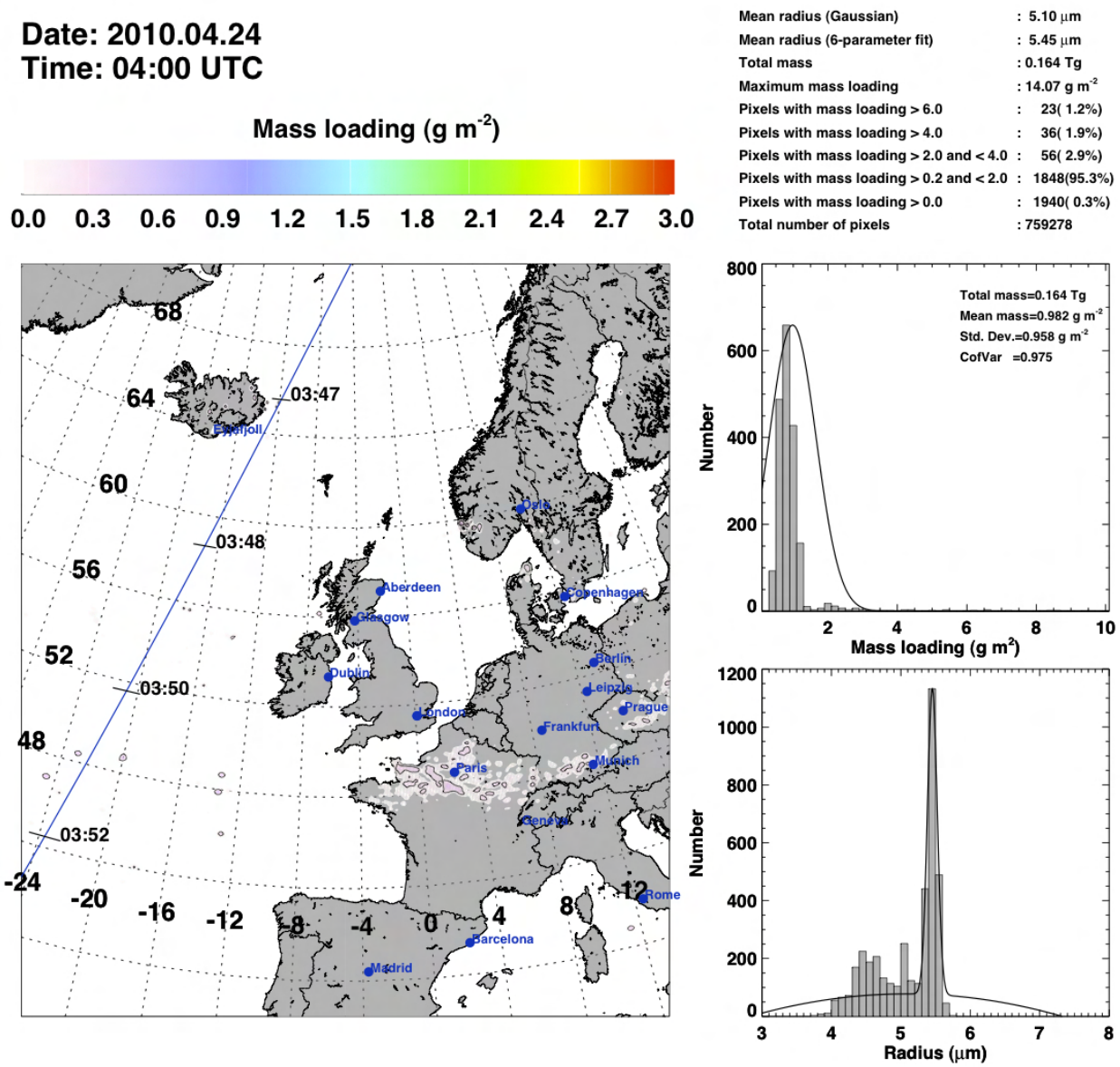

Figure 6.11: Date: 24 April 2010, Time: 04:00 UT.

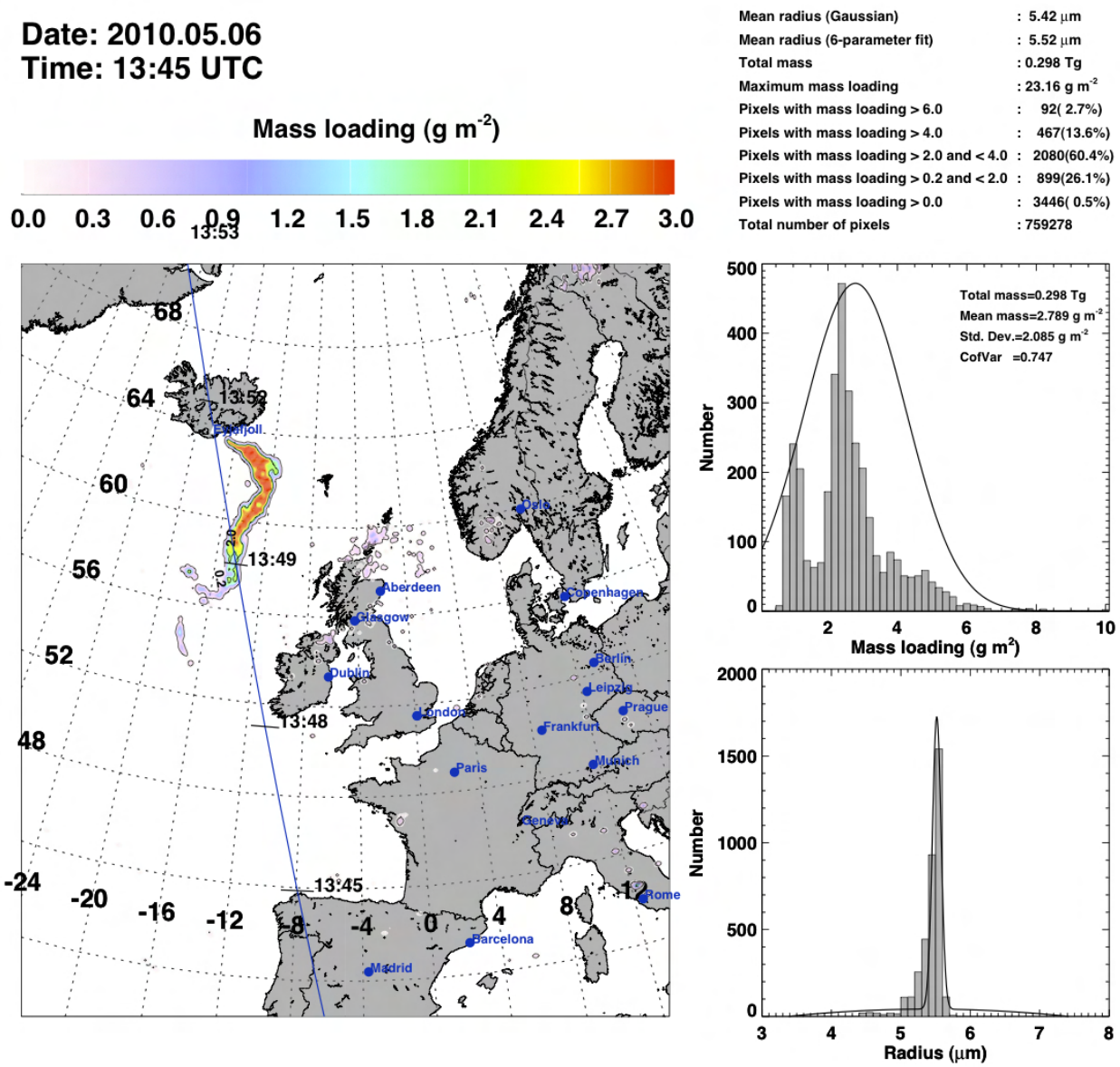

Figure 6.12: Date: 6 May 2010, Time: 13:45 UT.

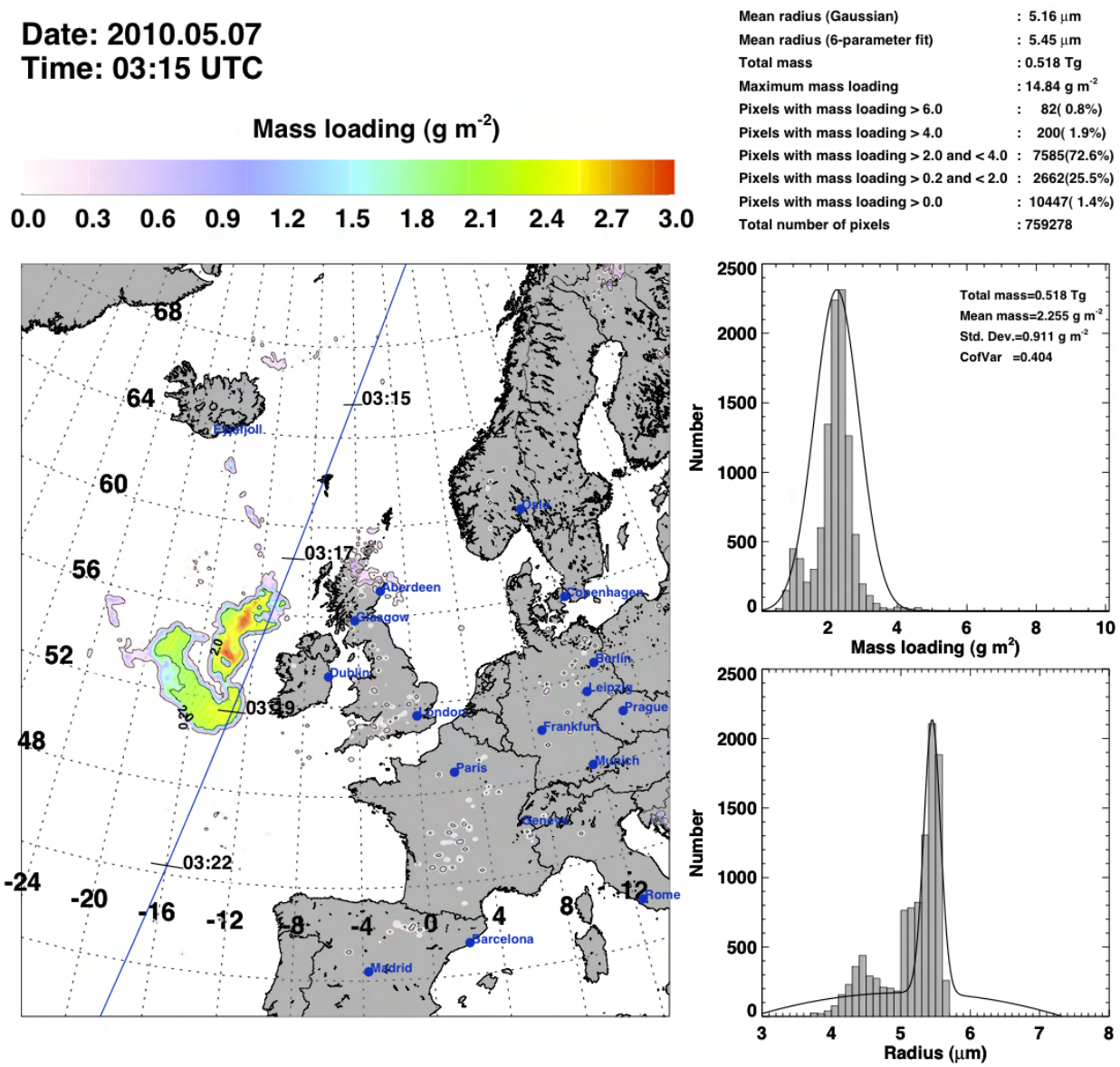

Figure 6.13: Date: 7 May 2010, Time: 03:15 UT.

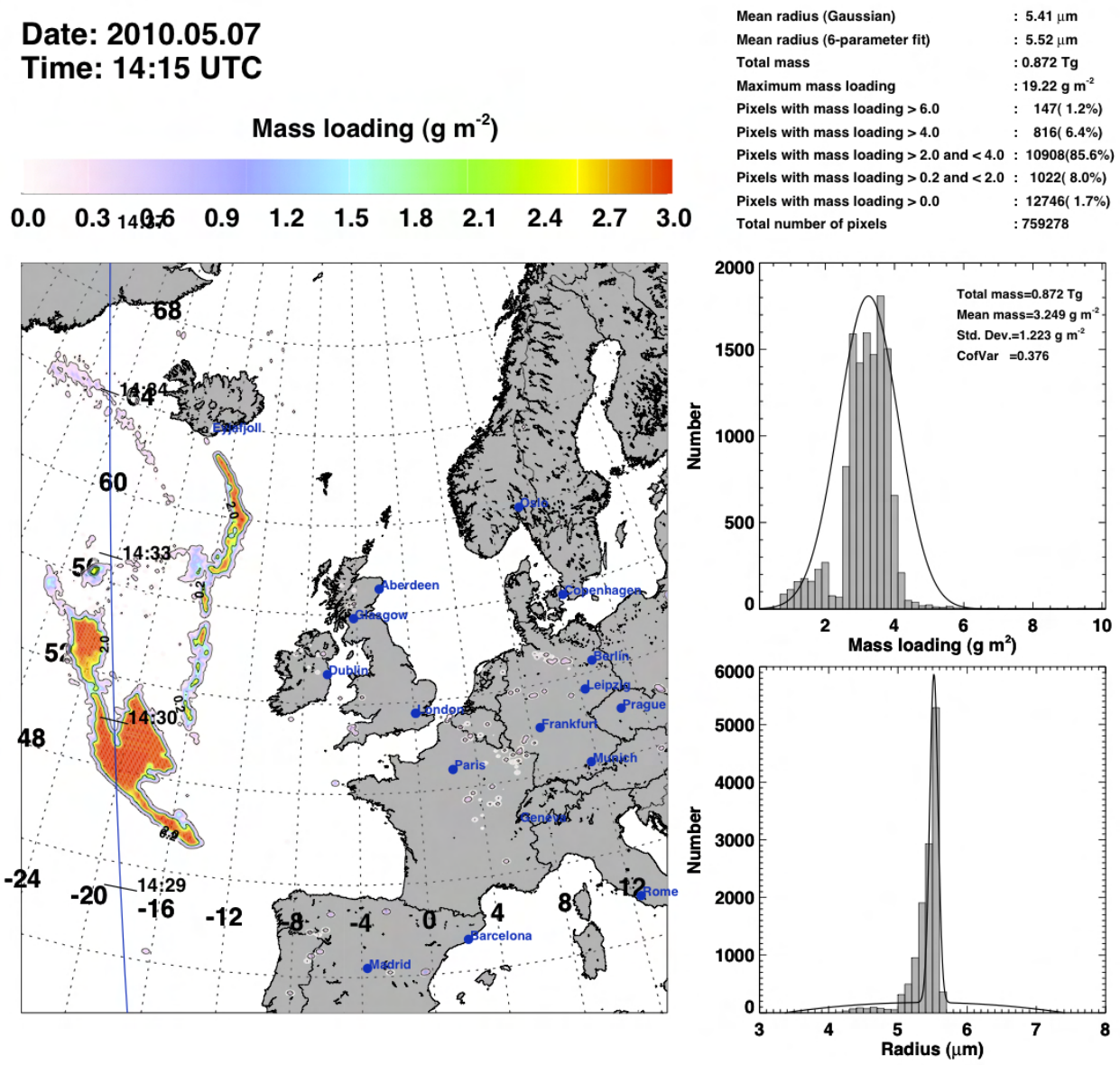

Figure 6.14: Date: 7 May 2010, Time: 14:15 UT.

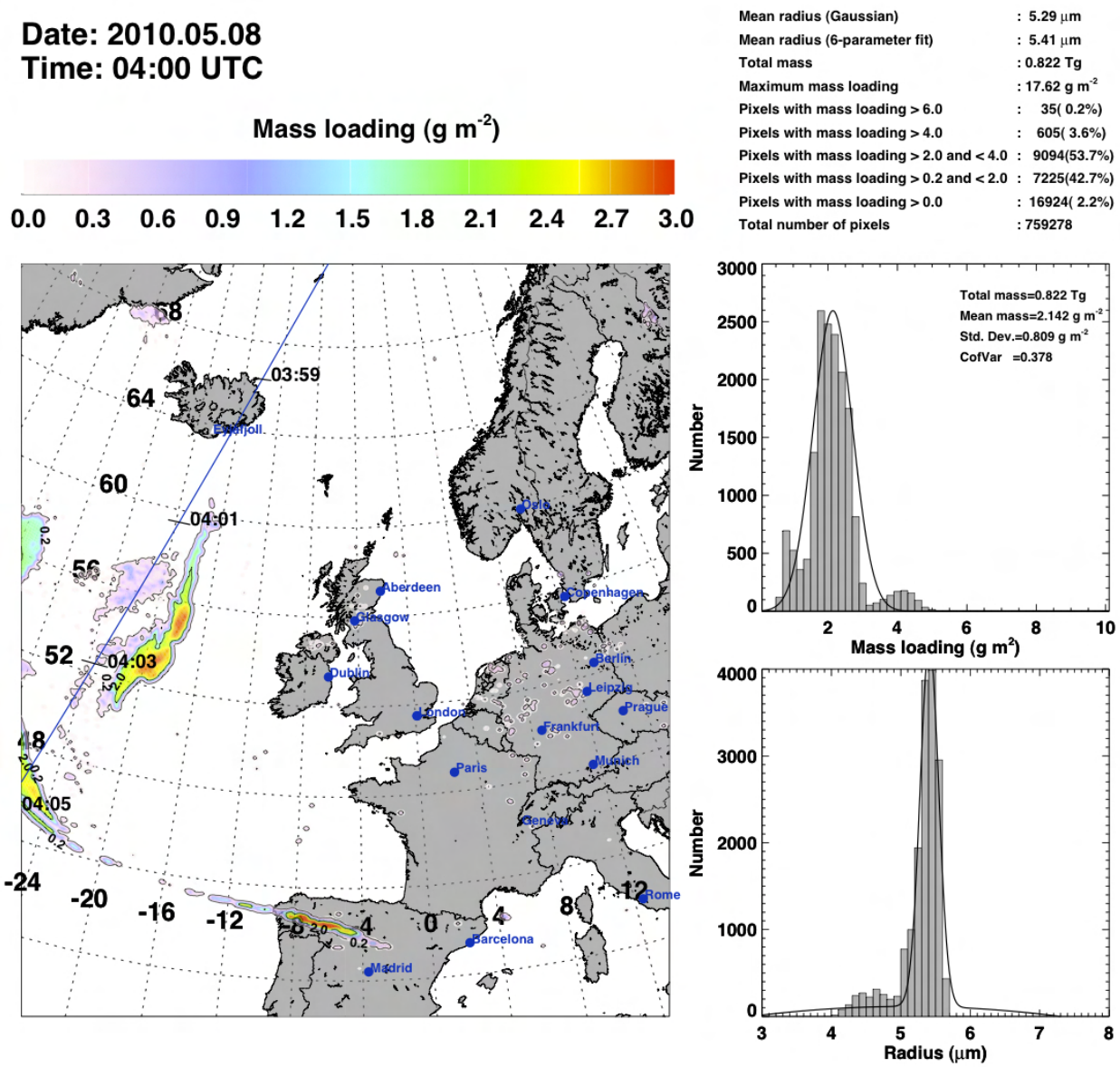

Figure 6.15: Date: 8 May 2010, Time: 04:00 UT.

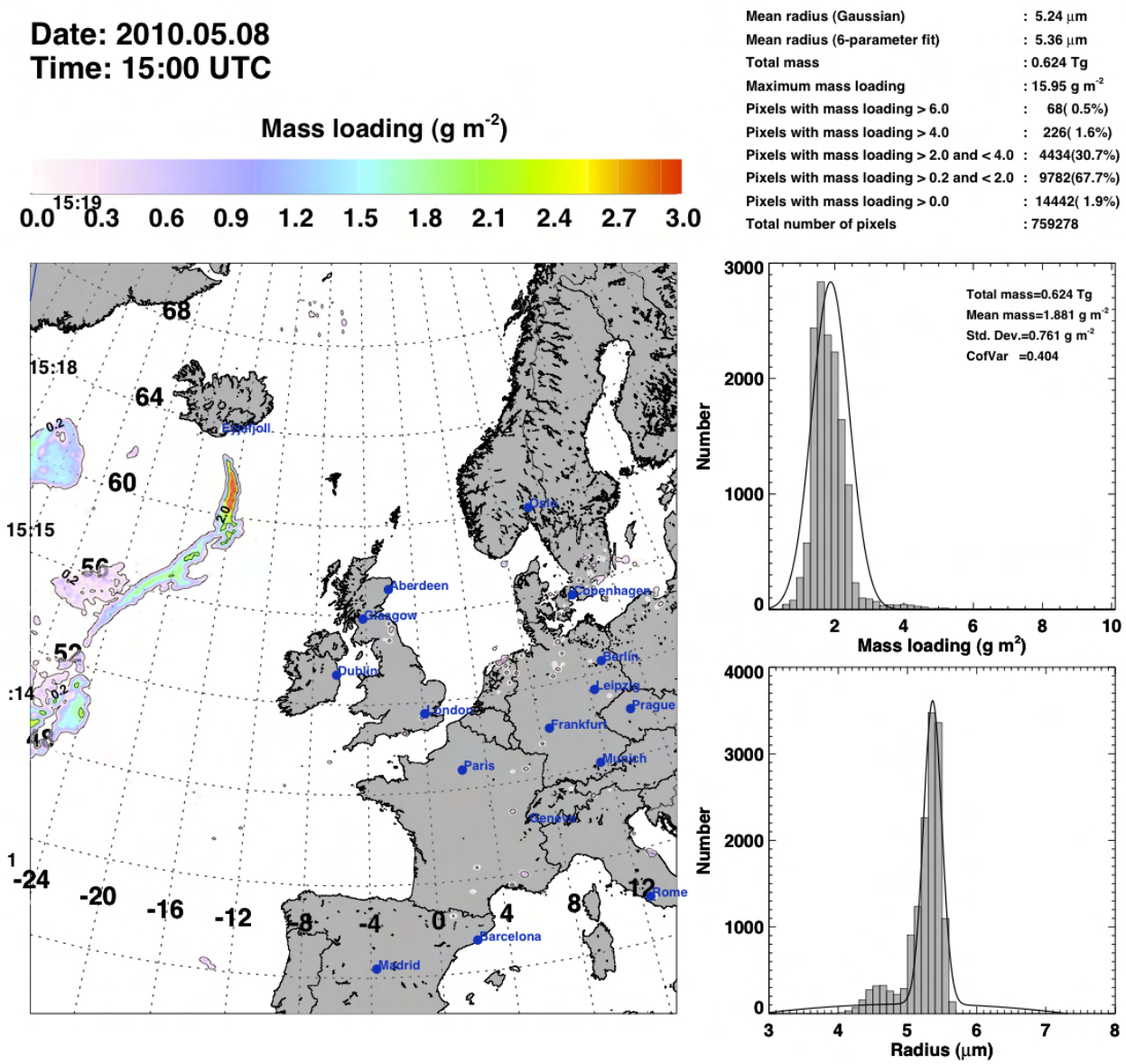

Figure 6.16: Date: 8 May 2010, Time: 15:00 UT.

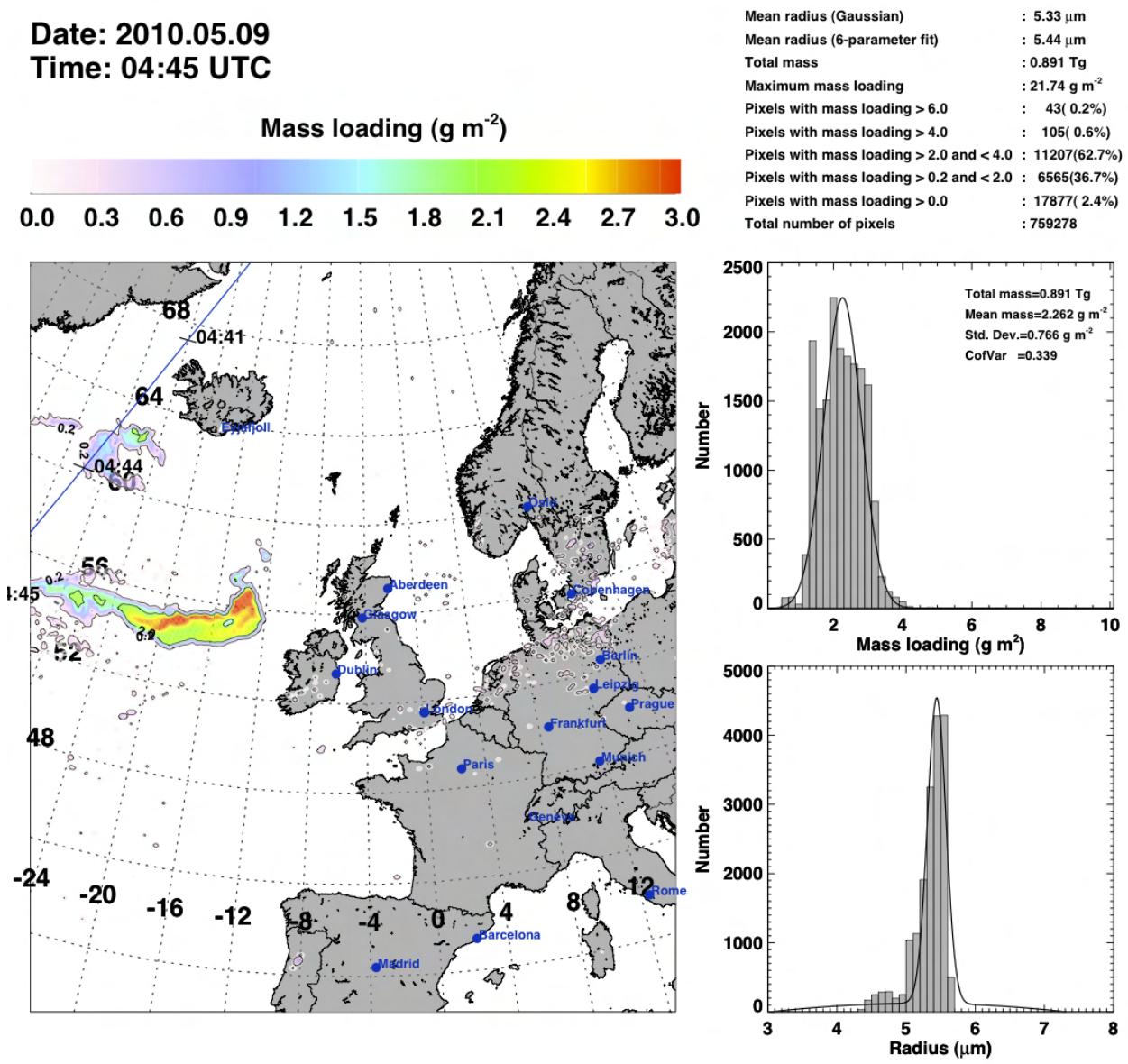

Figure 6.17: Date: 9 May 2010, Time: 04:45 UT.

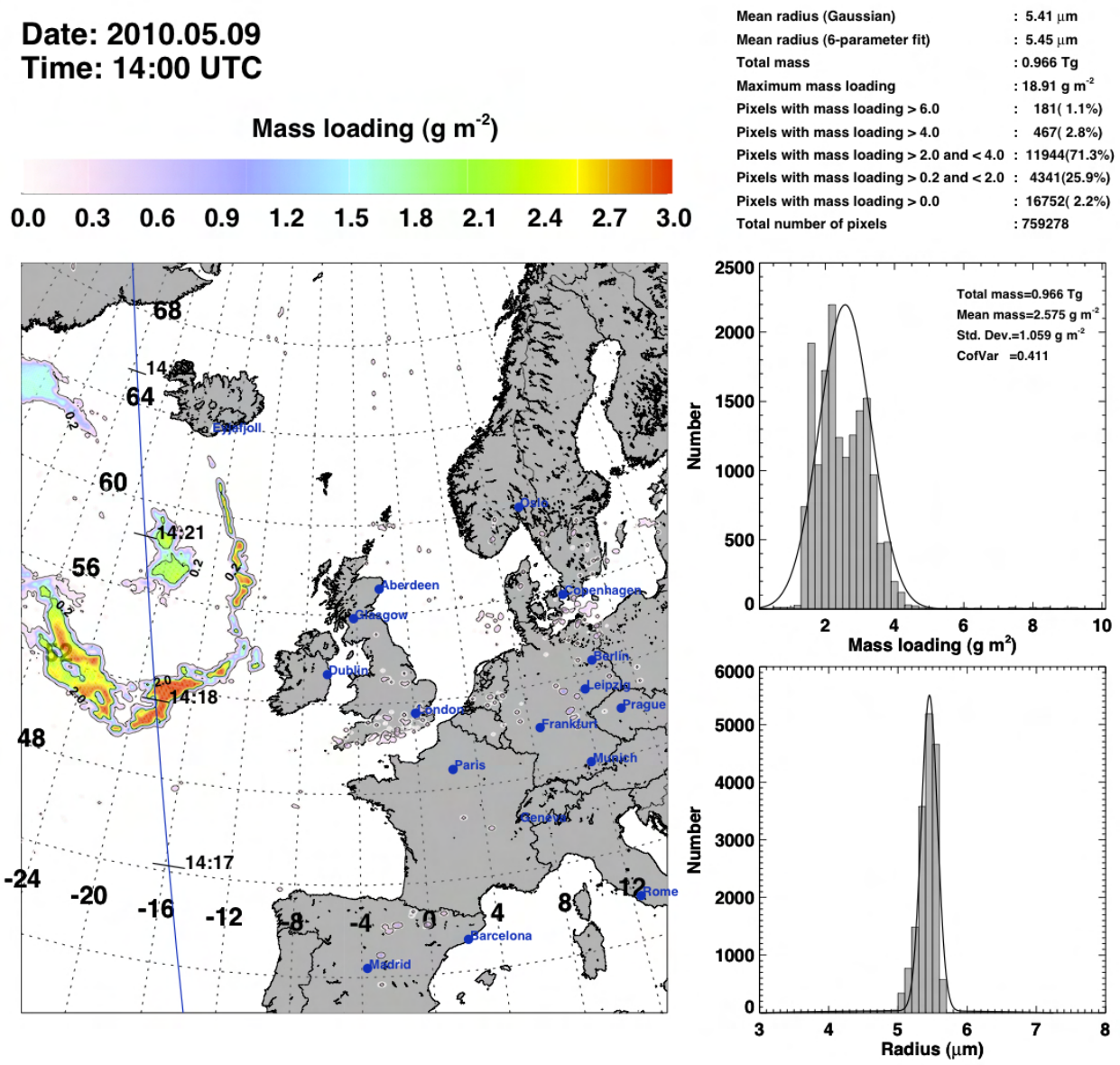

Figure 6.18: Date: 9 May 2010, Time: 14:00 UT.

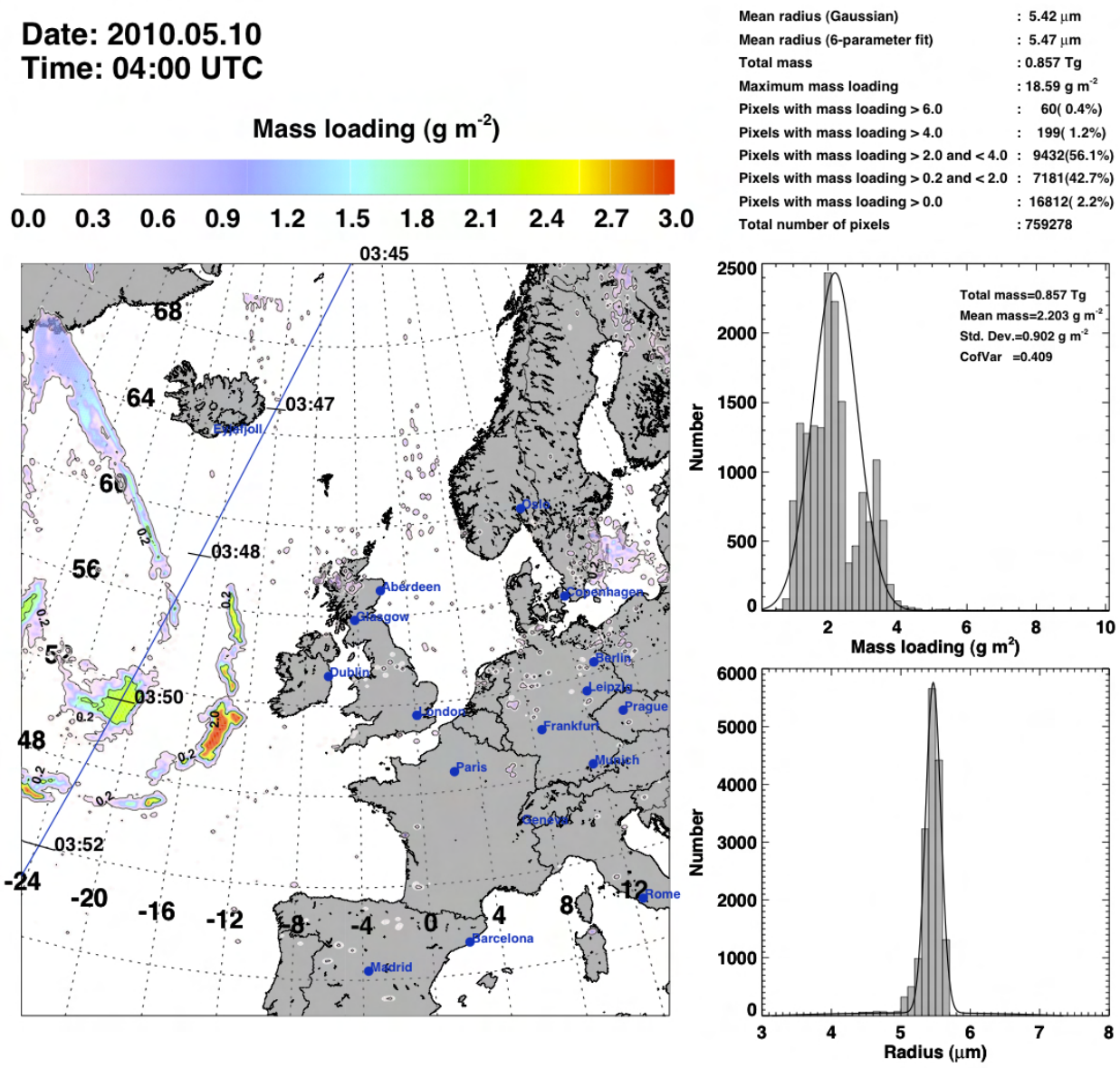

Figure 6.19: Date: 10 May 2010, Time: 04:00 UT.

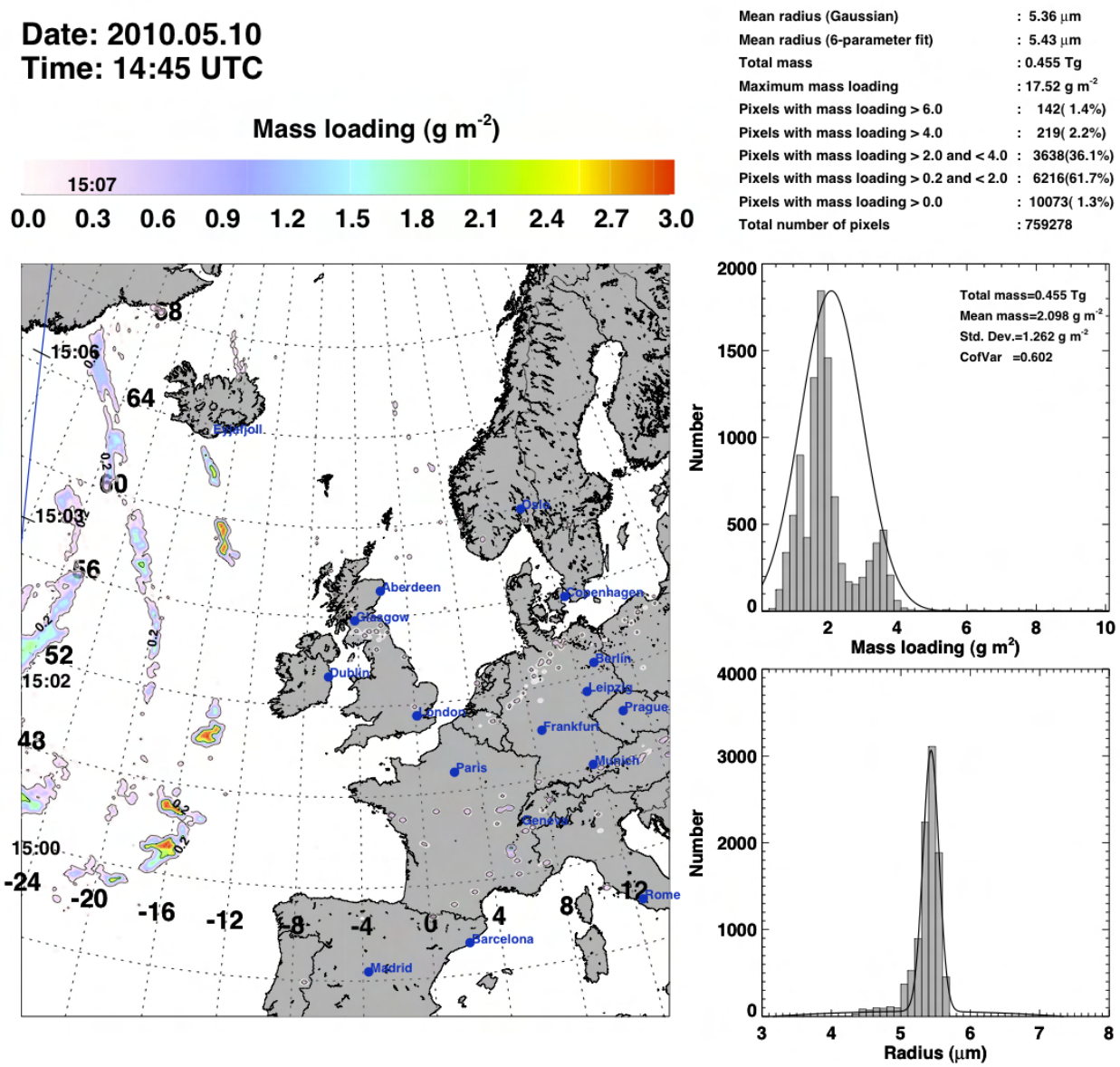

Figure 6.20: Date: 10 May 2010, Time: 14:45 UT.

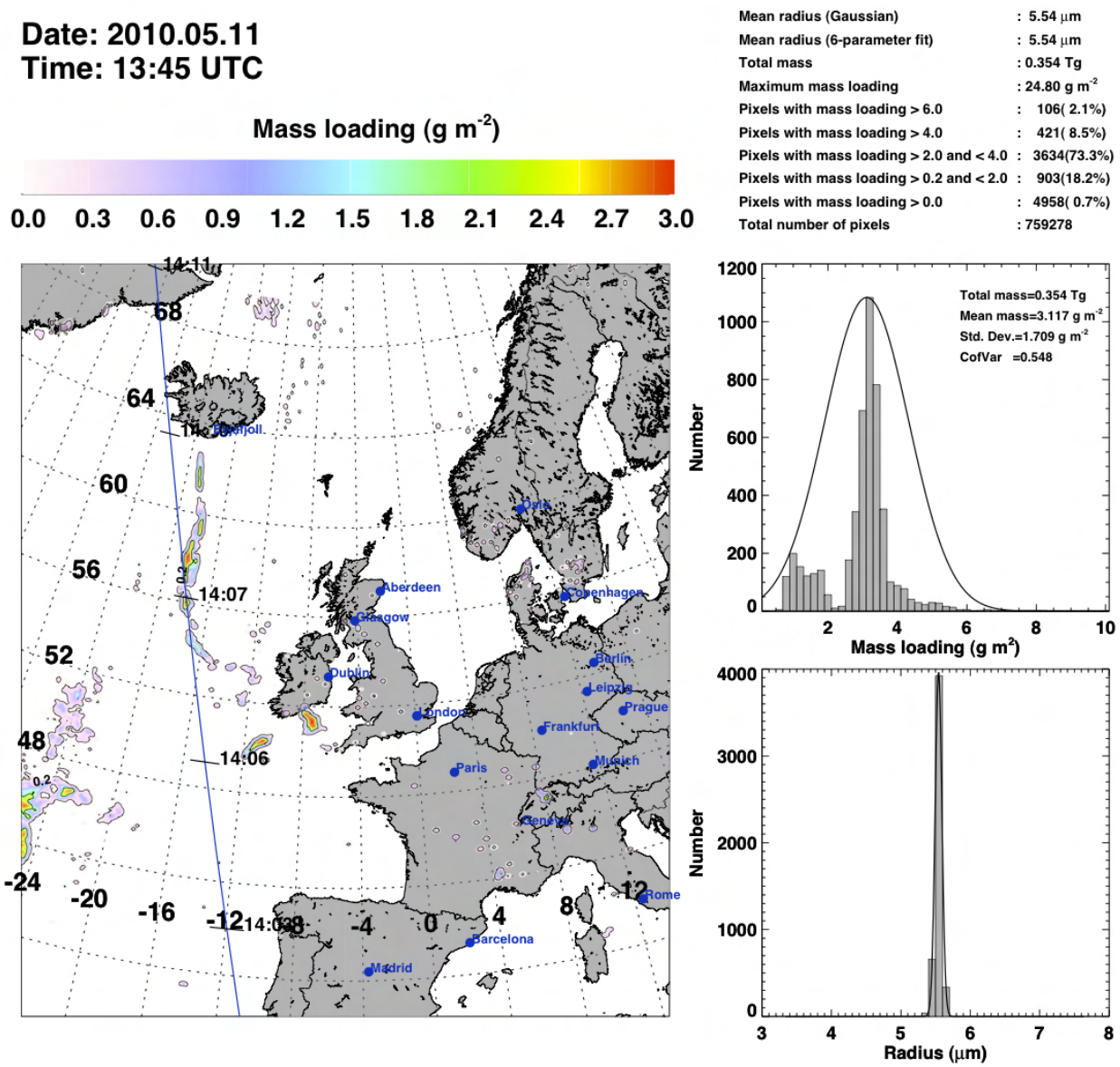

Figure 6.21: Date: 11 May 2010, Time: 13:45 UT.

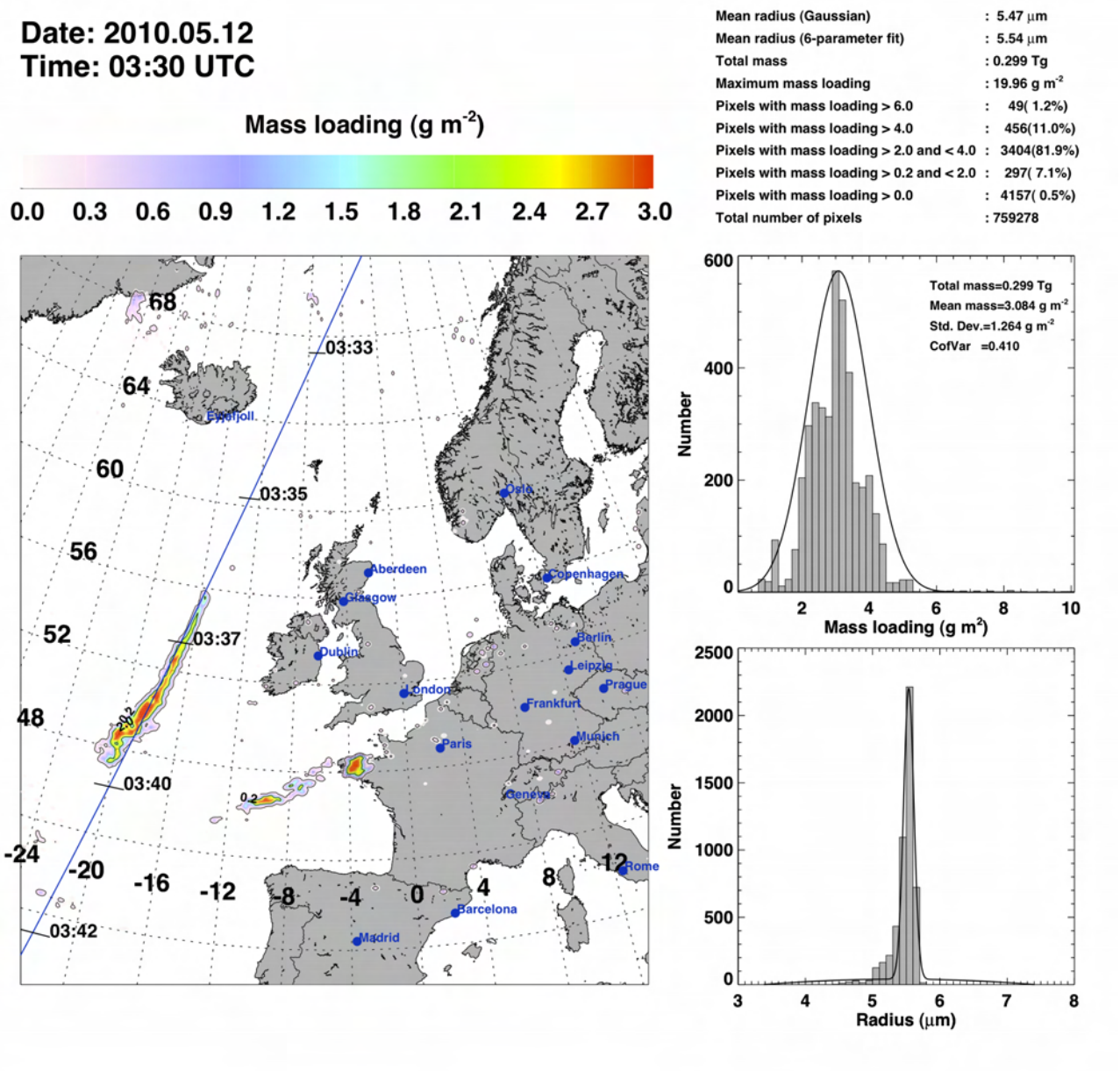

Figure 6.22: Date: 12 May 2010, Time: 03:30 UT.

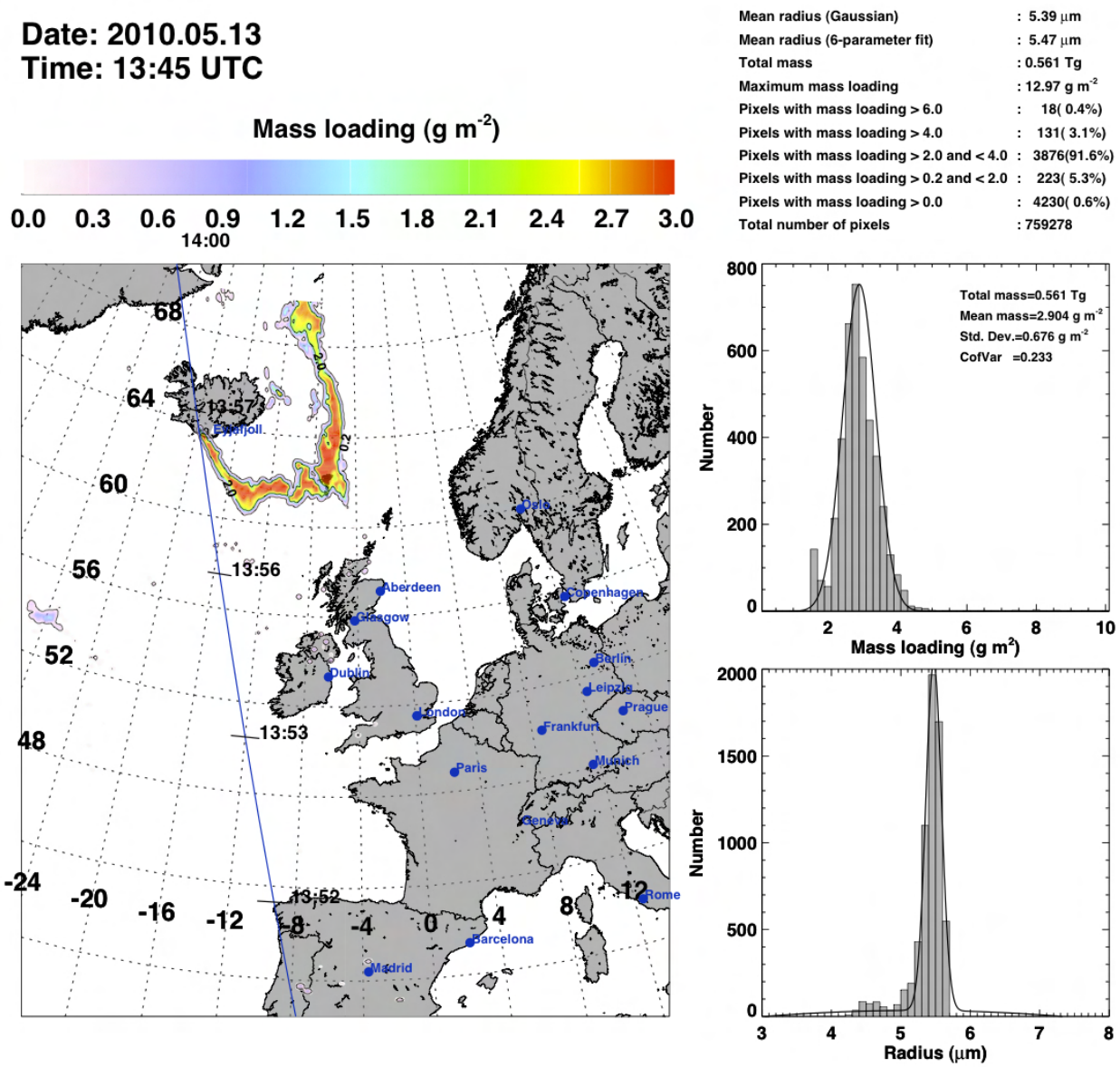

Figure 6.23: Date: 13 May 2010, Time: 13:45 UT.

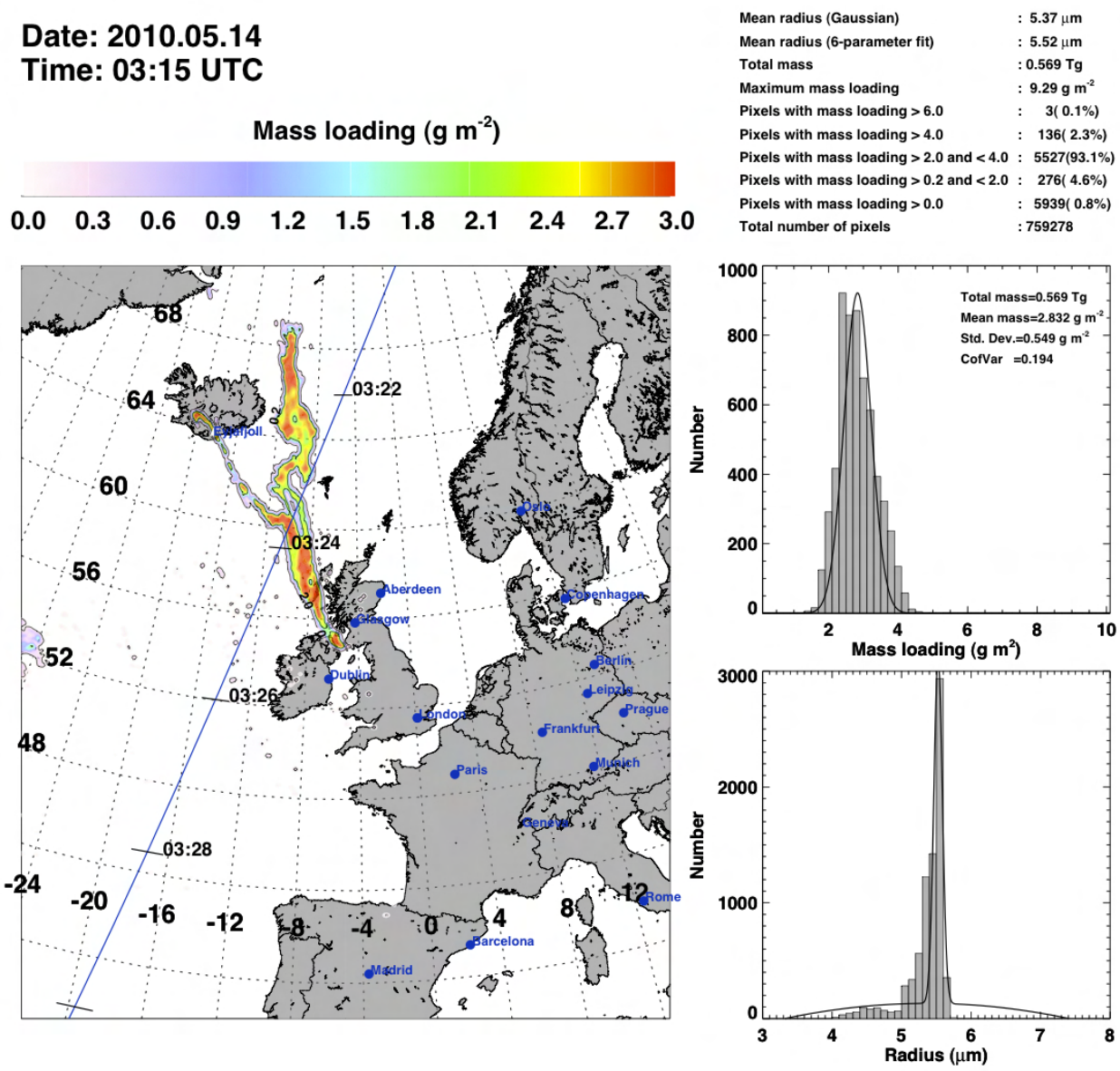

Figure 6.24: Date: 14 May 2010, Time: 03:15 UT.

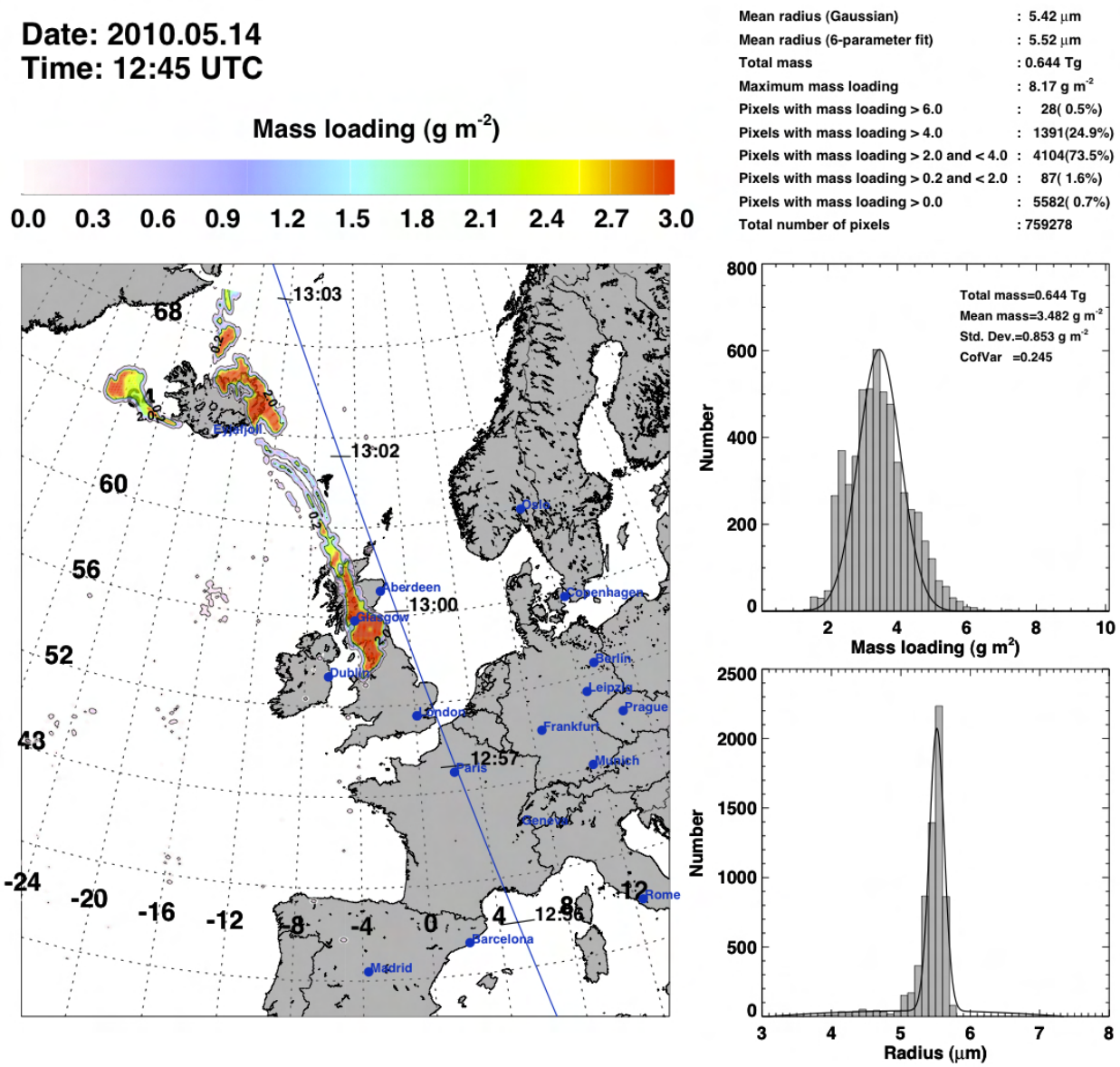

Figure 6.25: Date: 14 May 2010, Time: 12:45 UT.

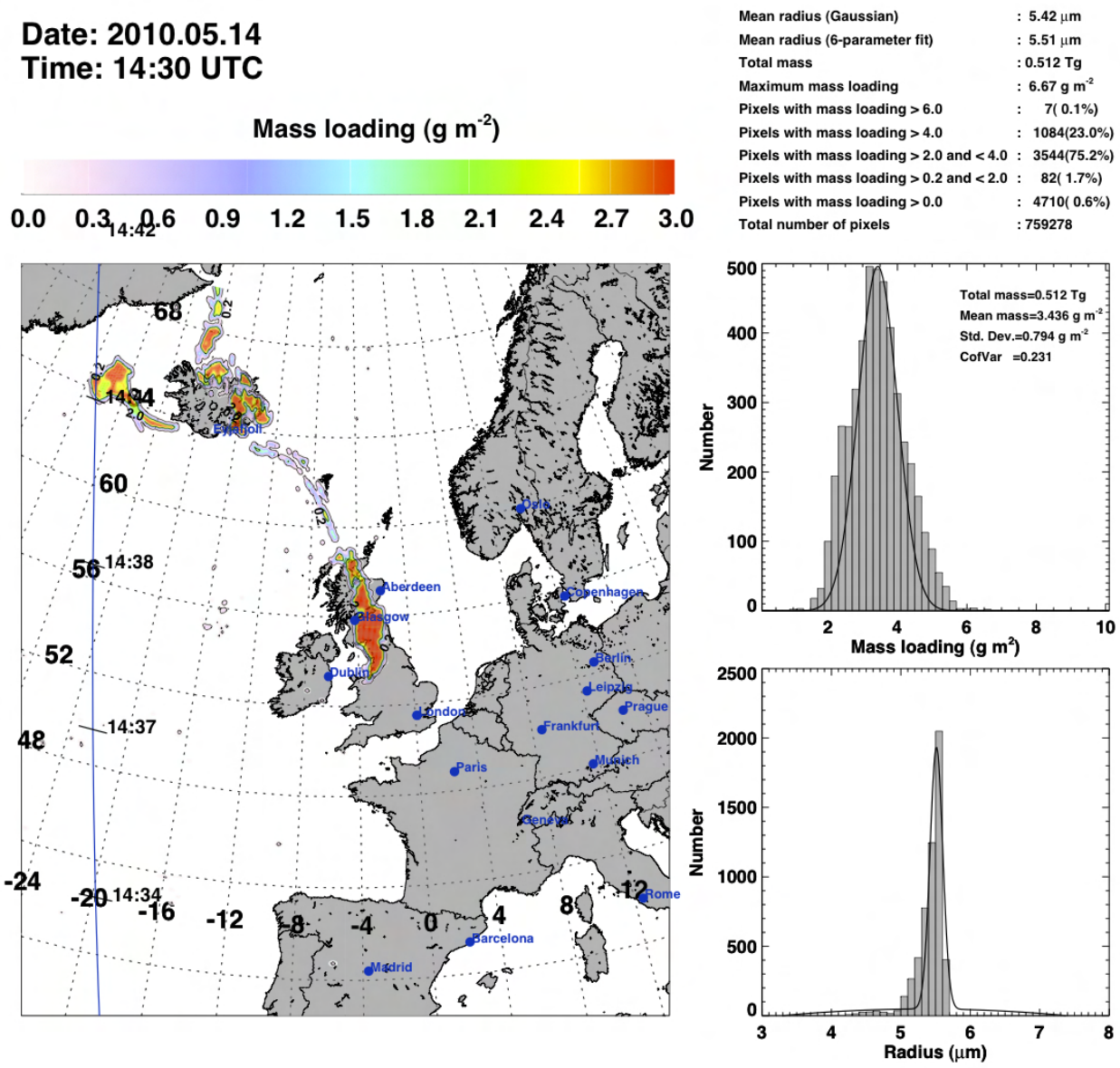

Figure 6.26: Date: 14 May 2010, Time: 14:30 UT.

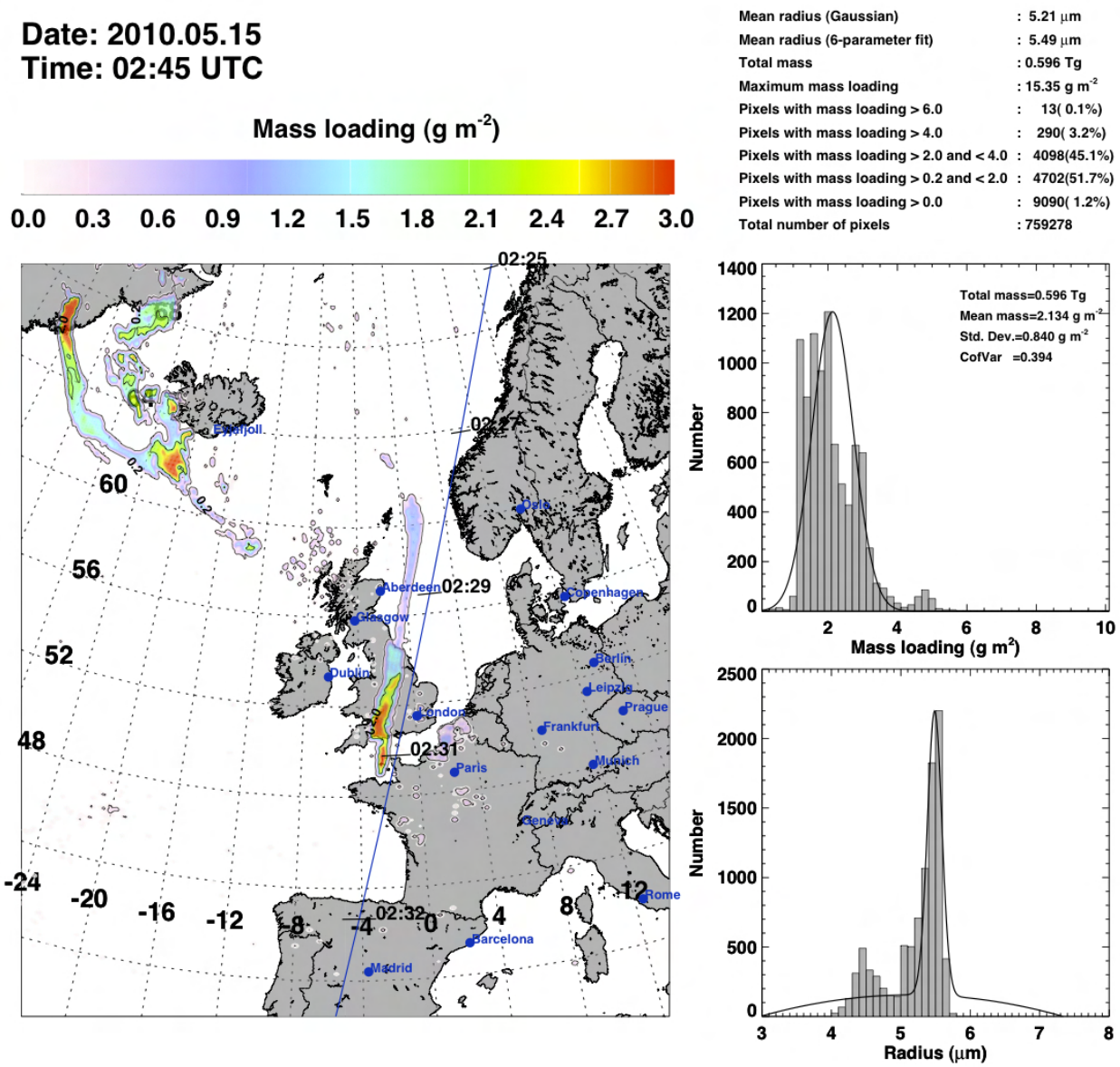

Figure 6.27: Date: 15 May 2010, Time: 02:45 UT.

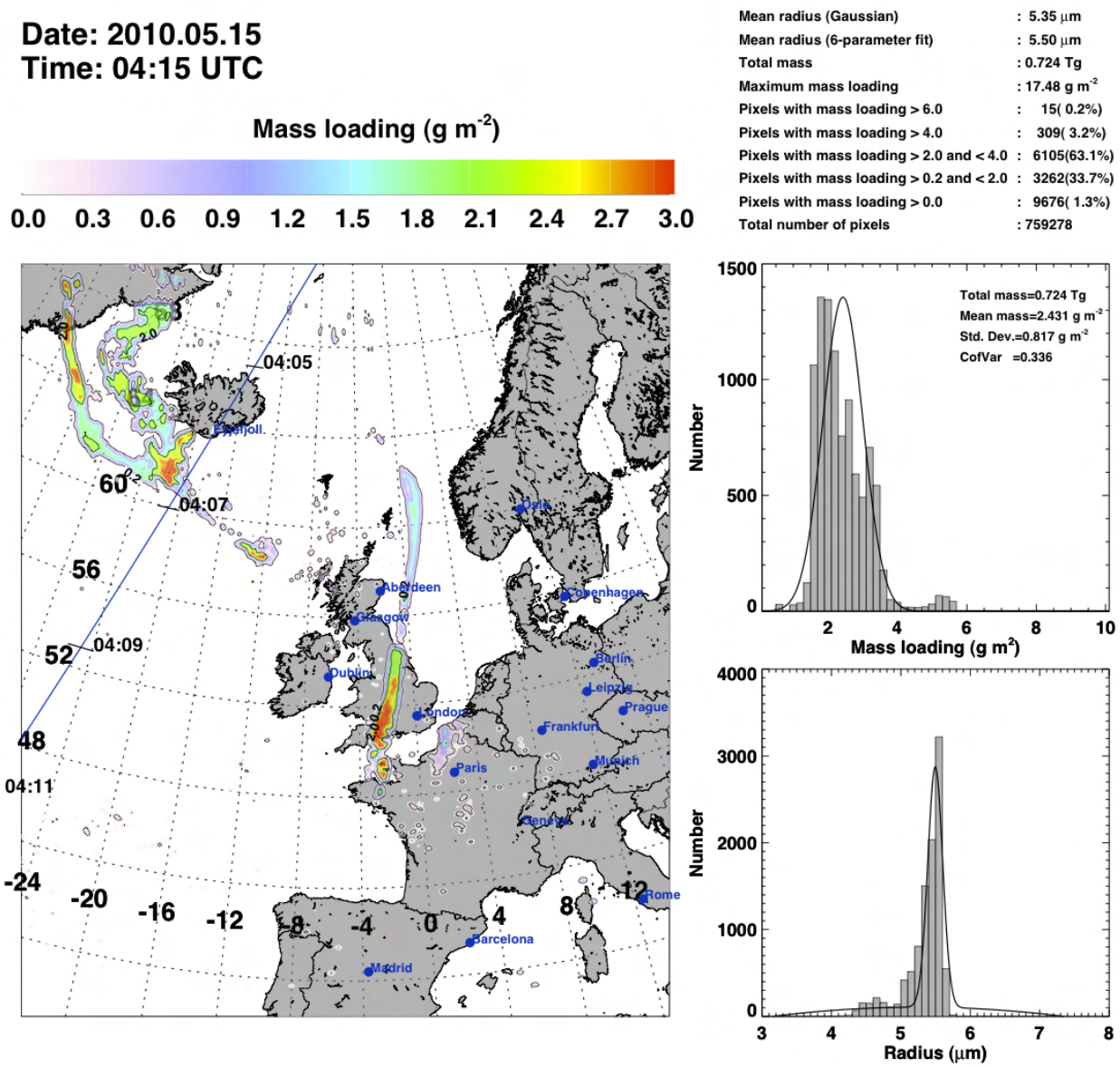

Figure 6.28: Date: 15 May 2010, Time: 04:15 UT.

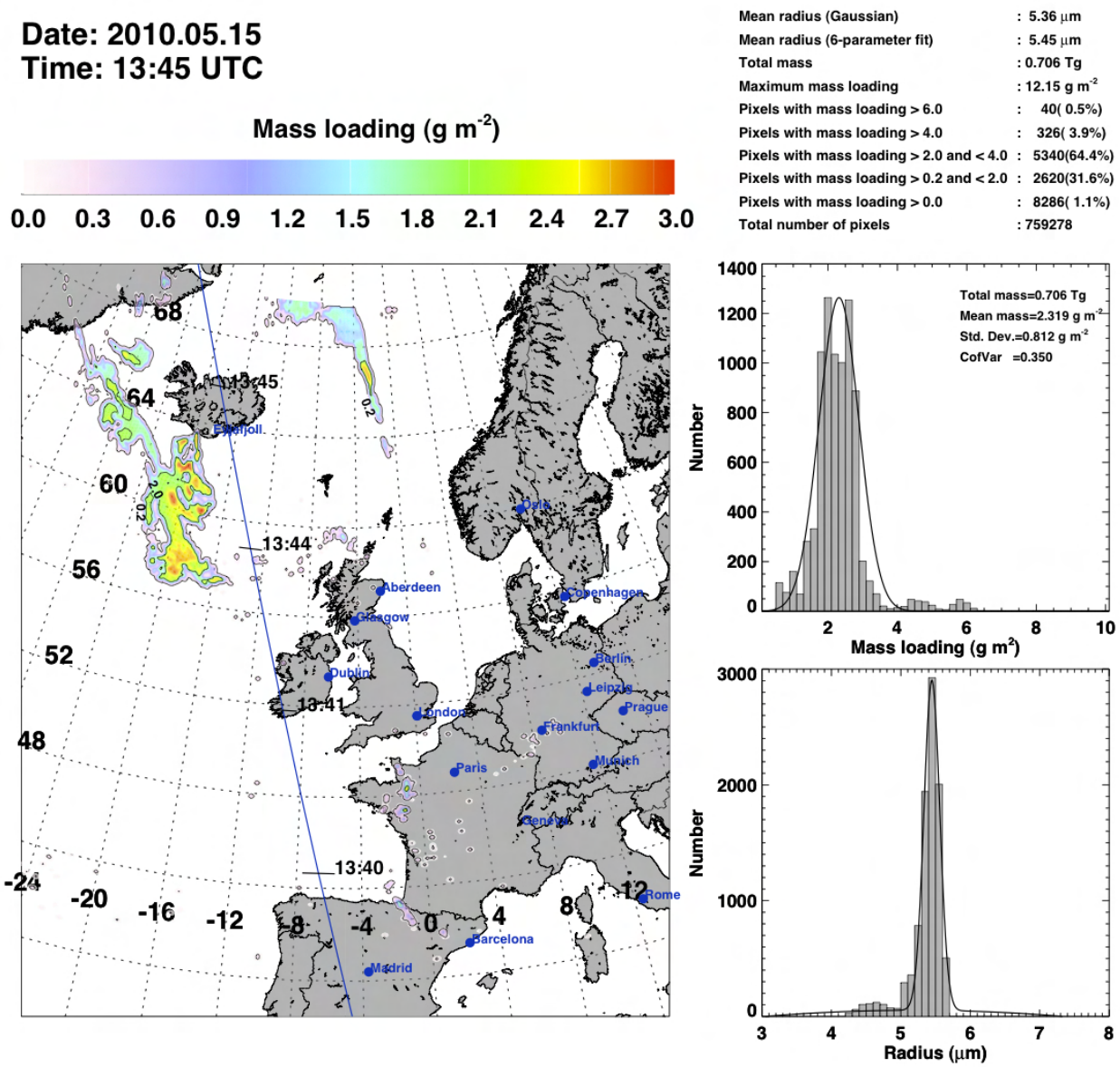

Figure 6.29: Date: 15 May 2010, Time: 13:45 UT.

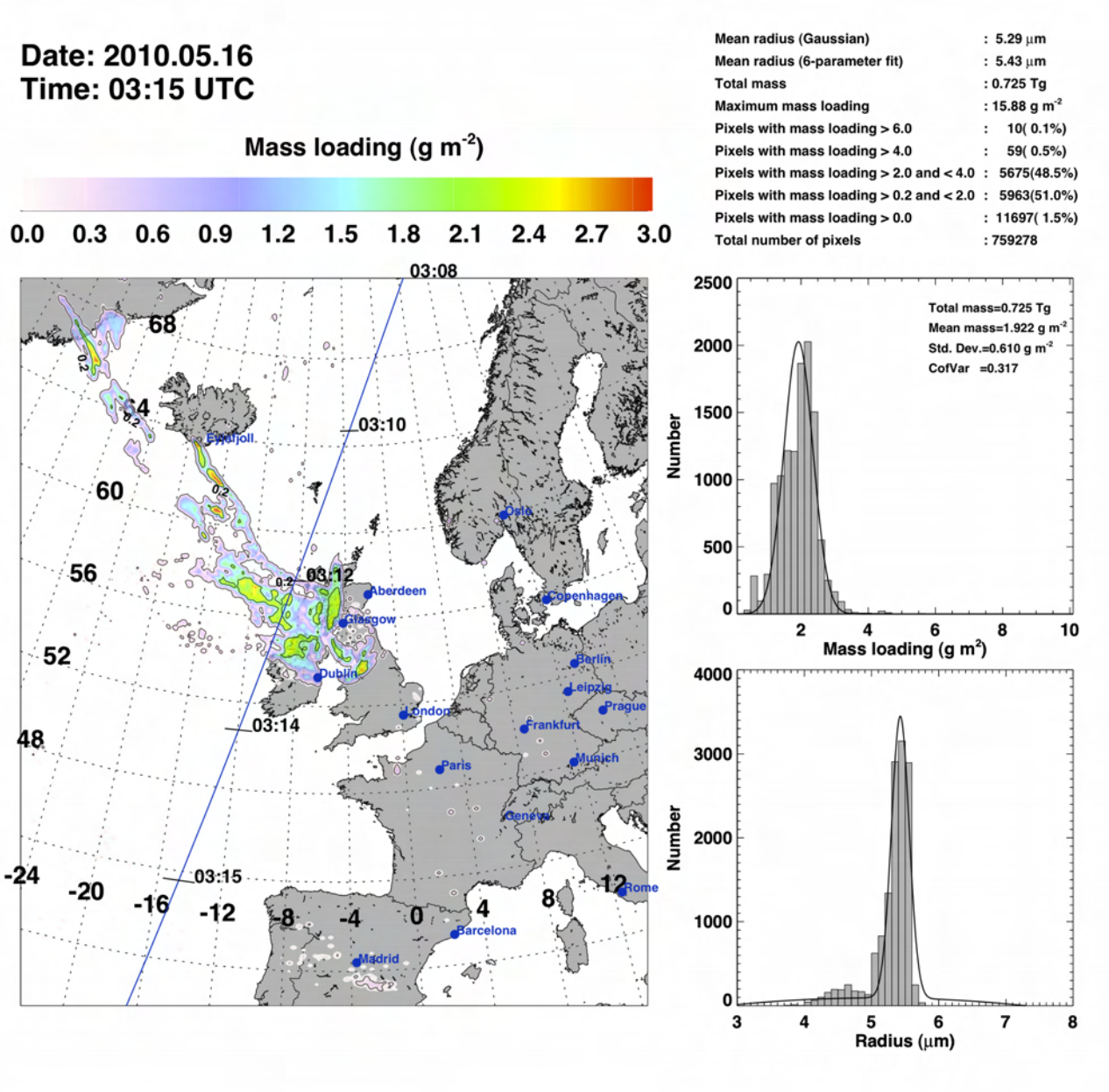

Figure 6.30: Date: 16 May 2010, Time: 03:15 UT.

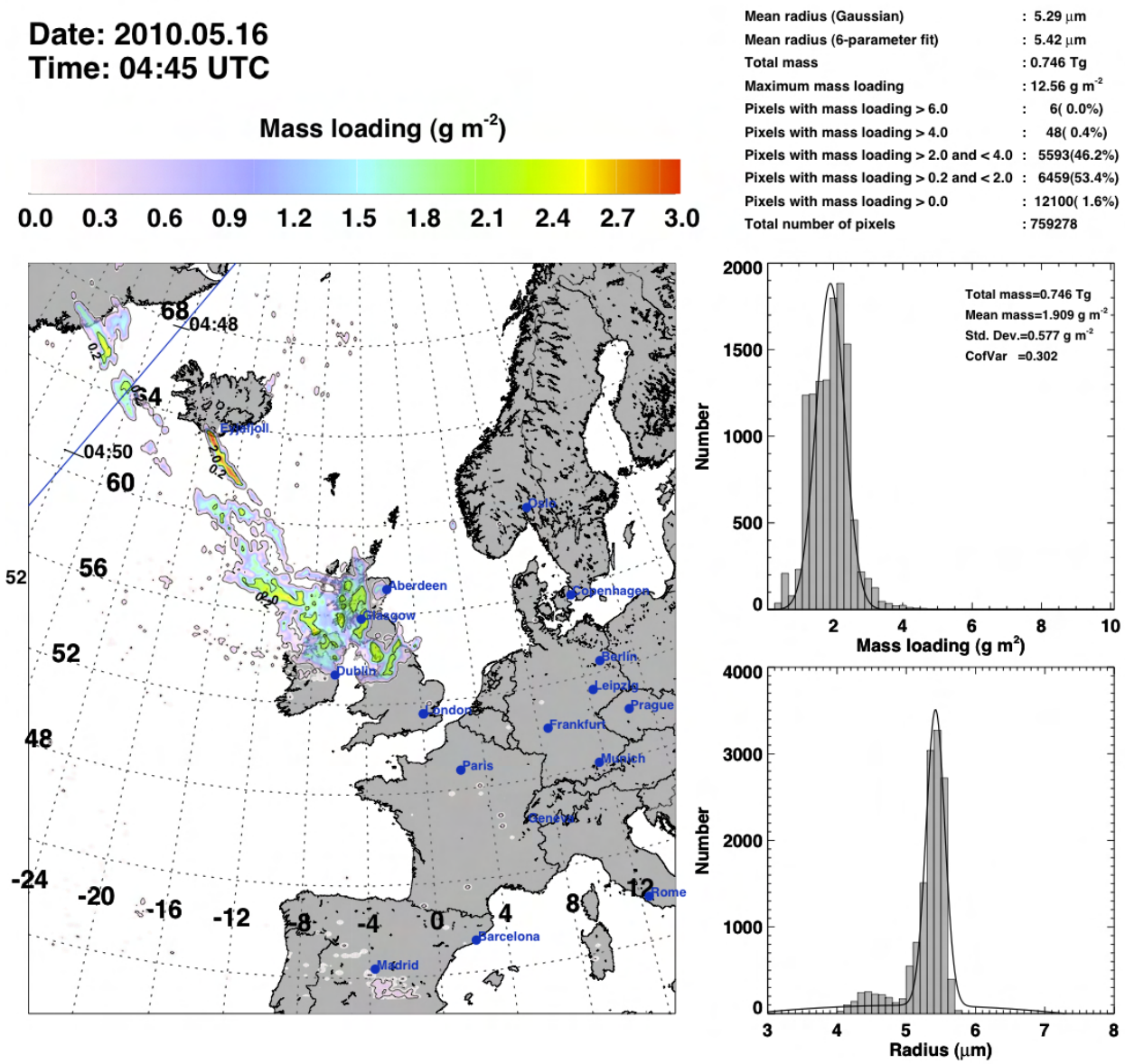

Figure 6.31: Date: 16 May 2010, Time: 04:45 UT.

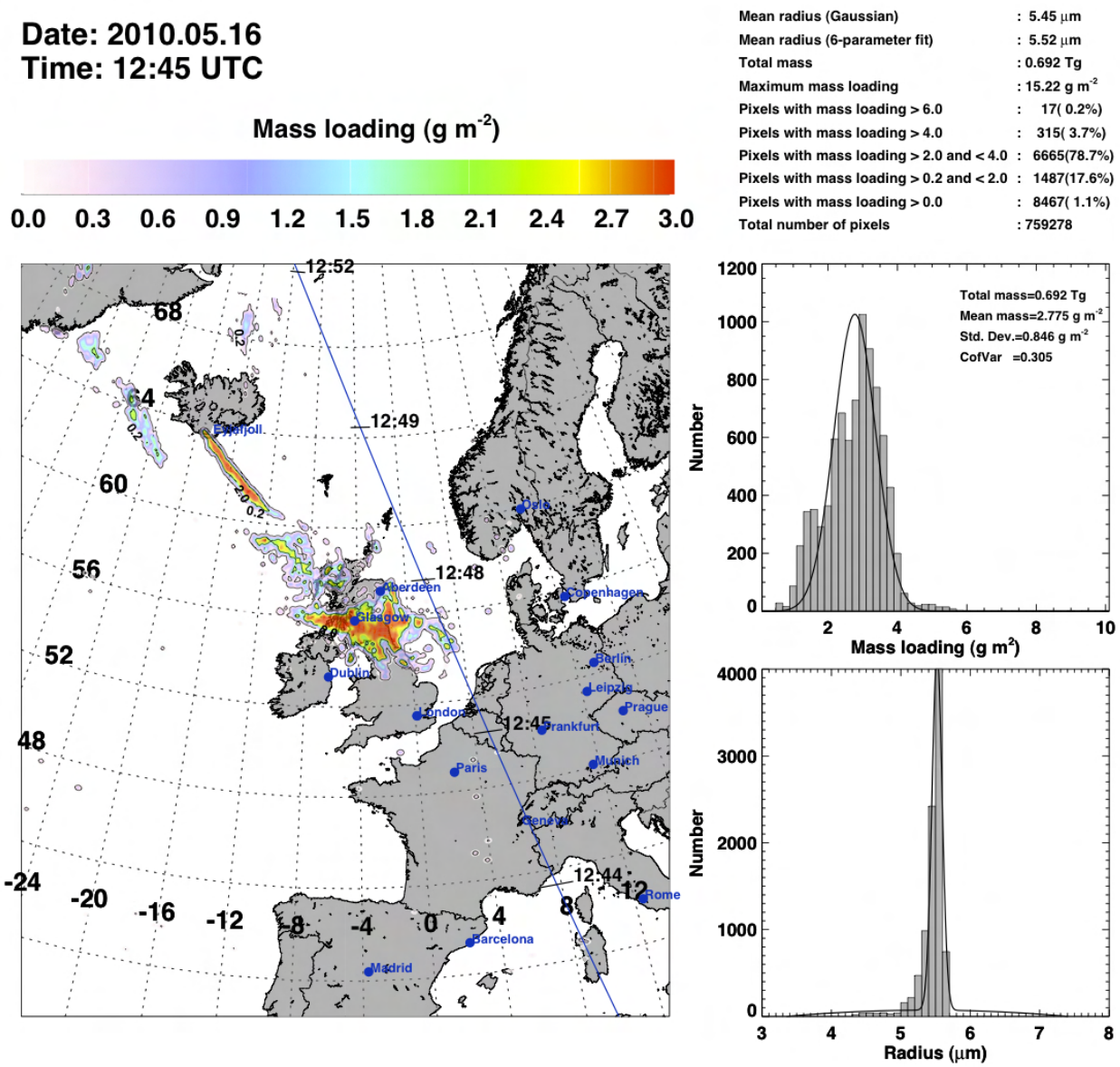

Figure 6.32: Date: 16 May 2010, Time: 12:45 UT.

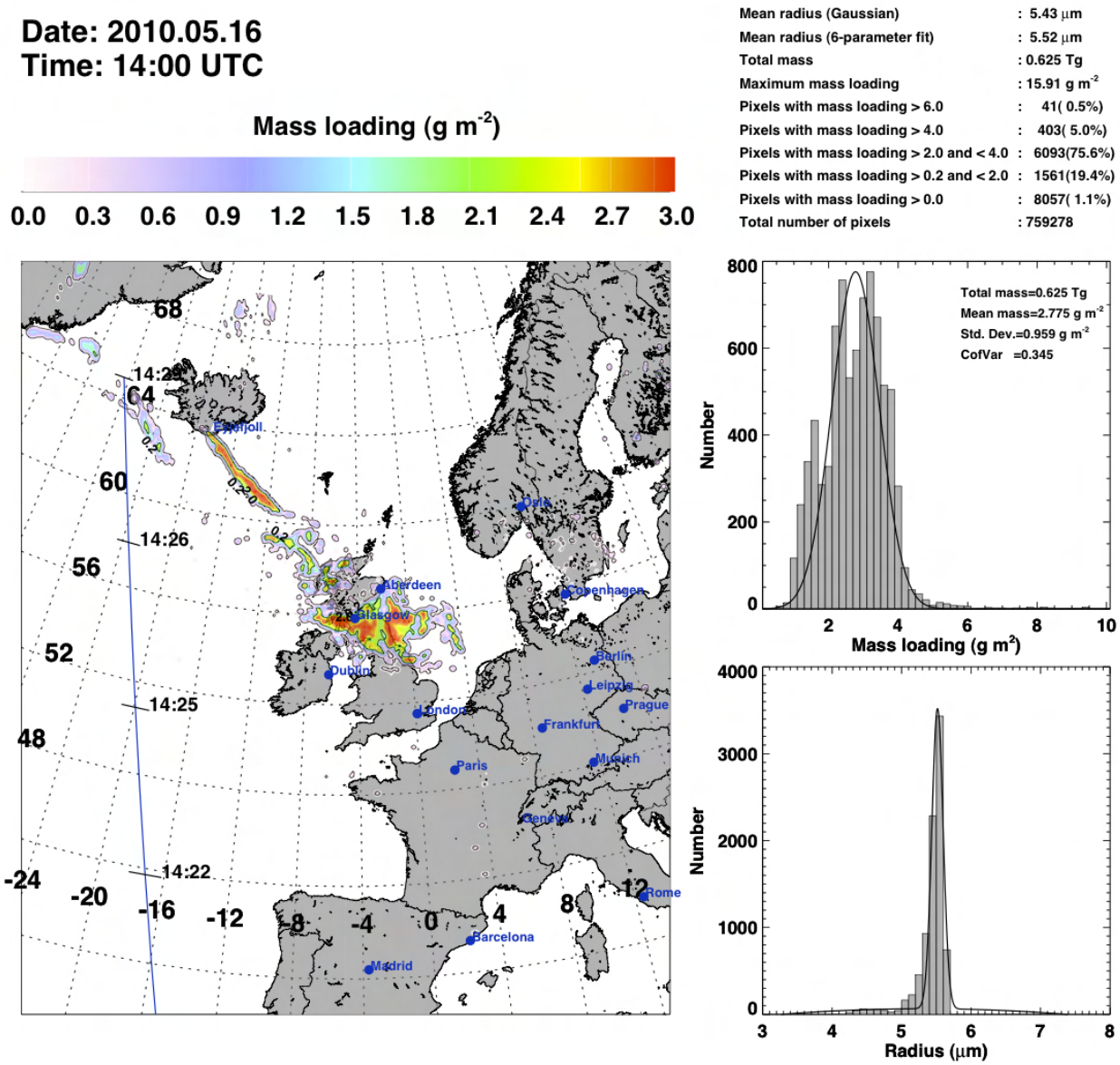

Figure 6.33: Date: 16 May 2010, Time: 14:00 UT.

6.2 CALIPSO

Calipso curtains and data were examined to estimate the ash height and thickness by correlating high backscatter with positions of SEVIRI ash. Table 6.1 lists the CALIPSO overpass coincidences with times when SEVIRI ash retrievals were possible. Mass concentration profiles from CALIPSO are being determined separately (Dave Winkler, private communication) which will allow a comprehensive validation to

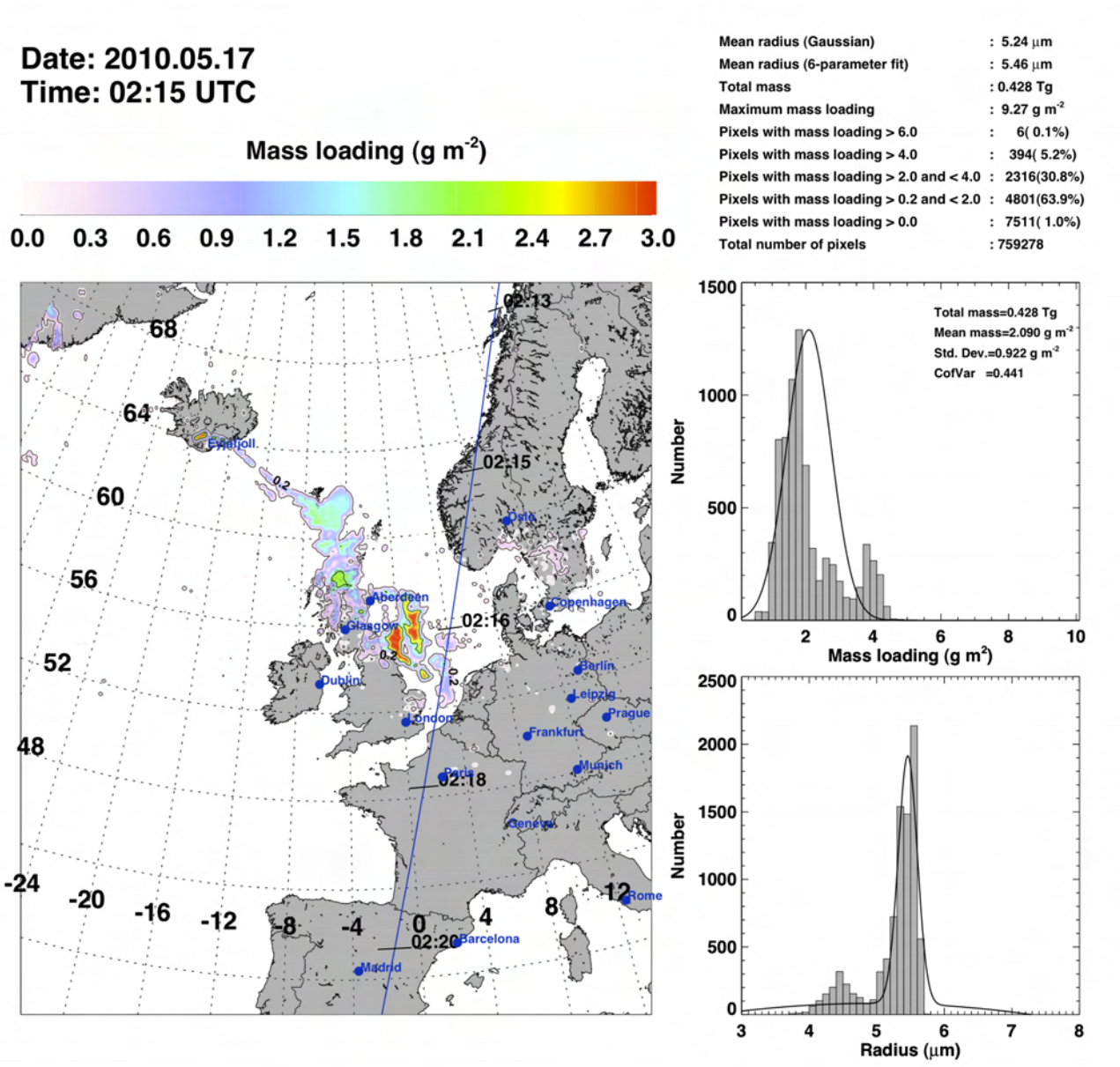

Figure 6.34: Date: 17 May 2010, Time: 02:15 UT.

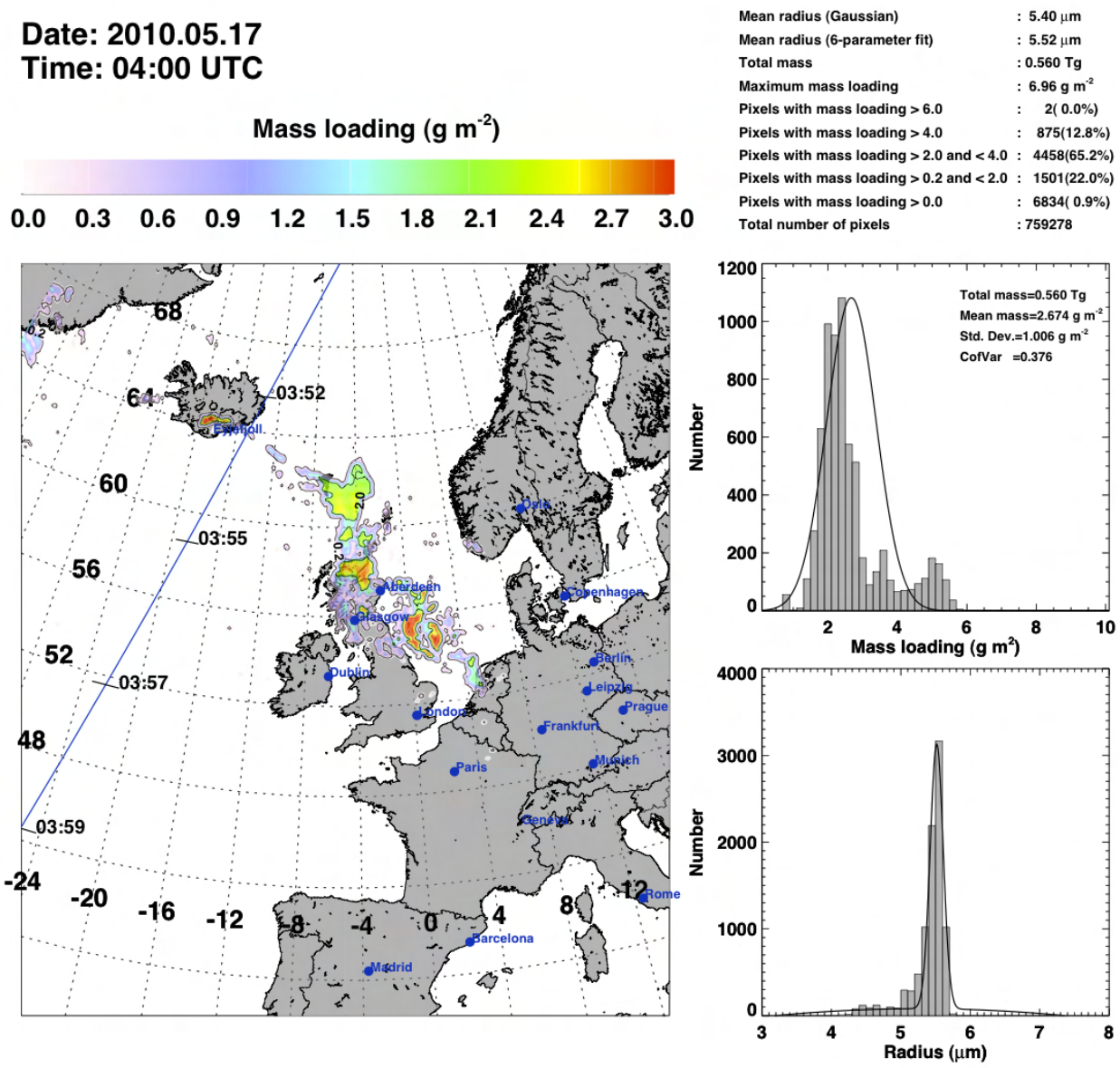

Figure 6.35: Date: 17 May 2010, Time: 04:00 UT.

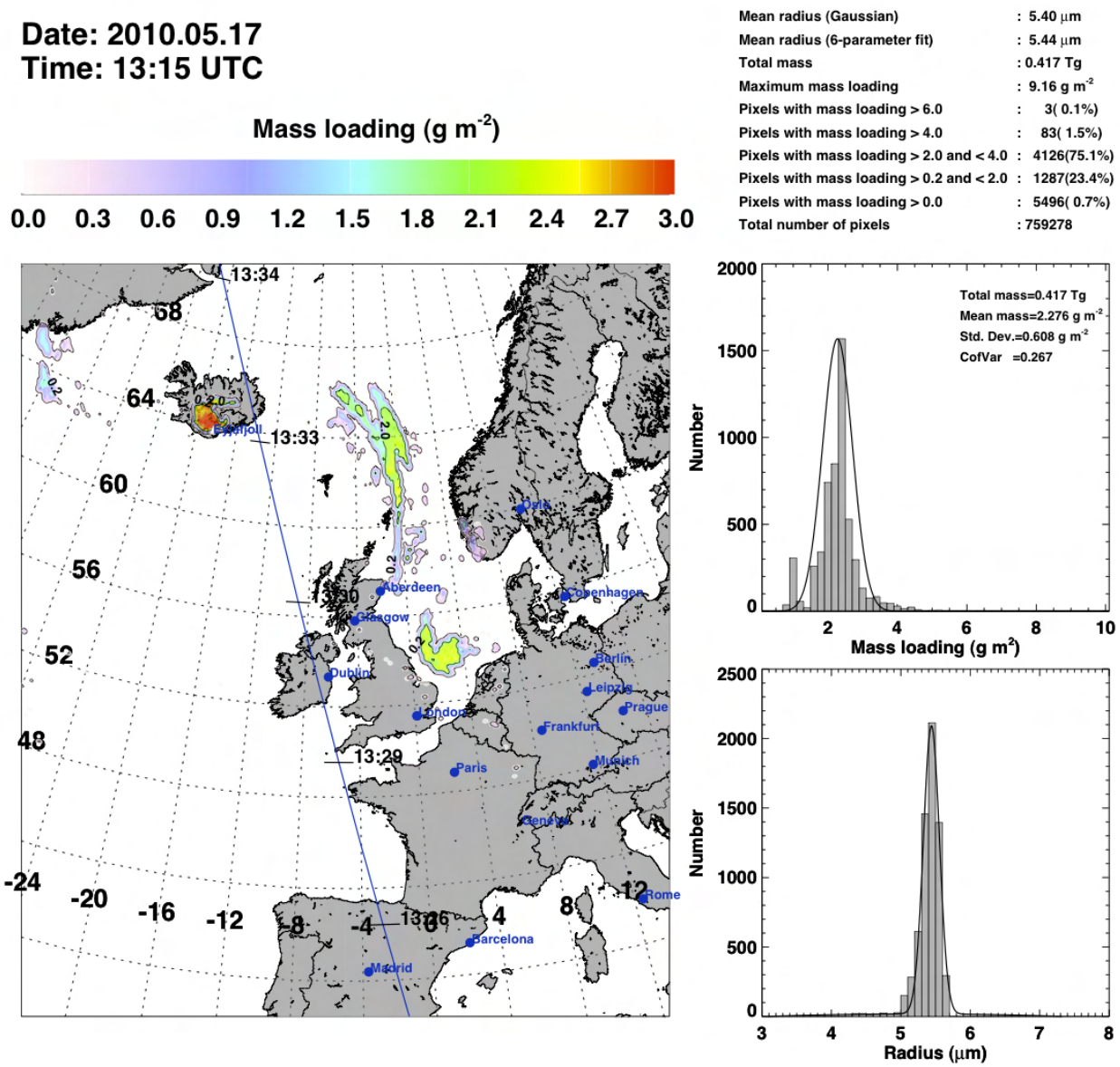

Figure 6.36: Date: 17 May 2010, Time: 13:15 UT.

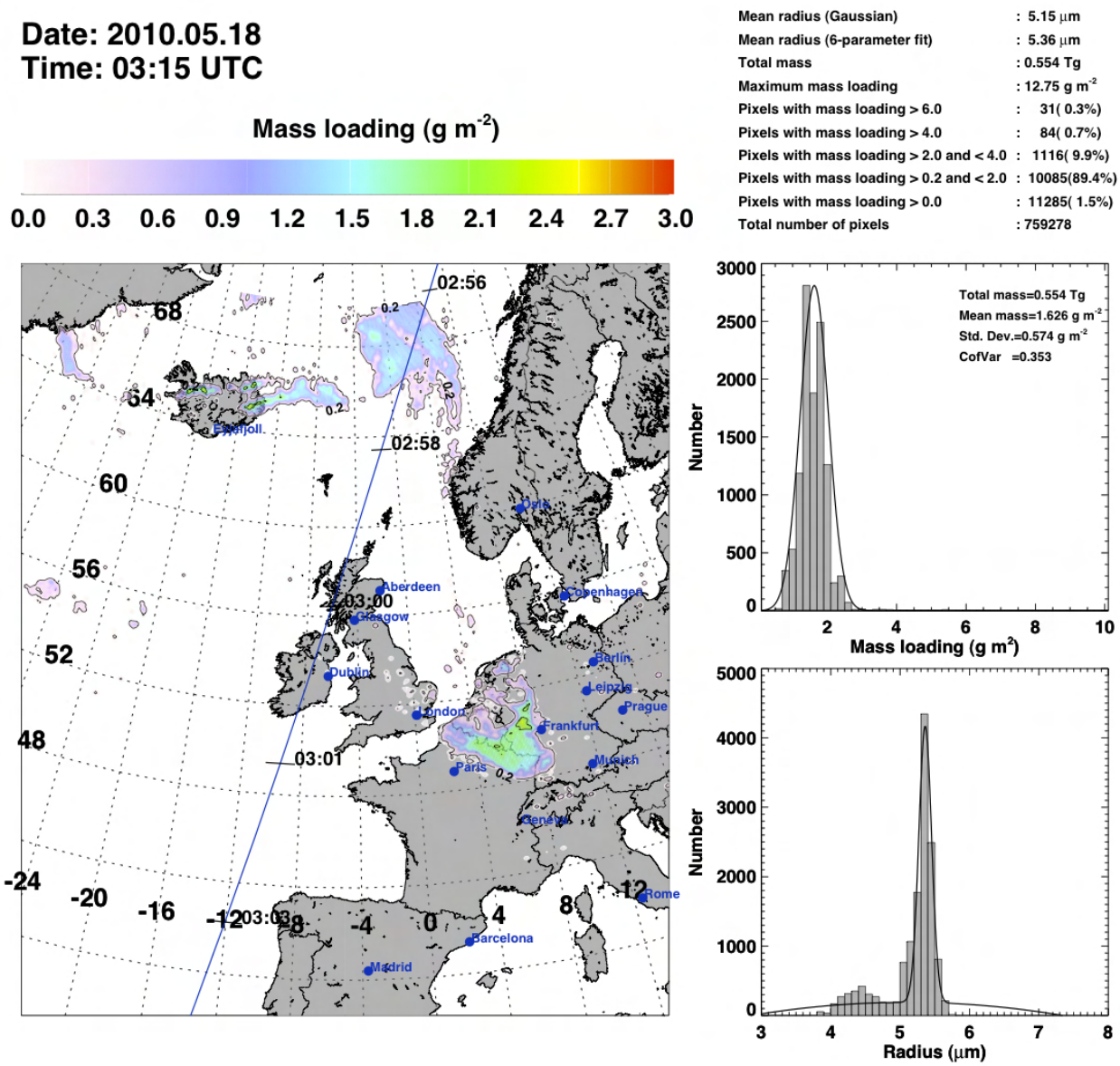

Figure 6.37: Date: 18 May 2010, Time: 03:15 UT.

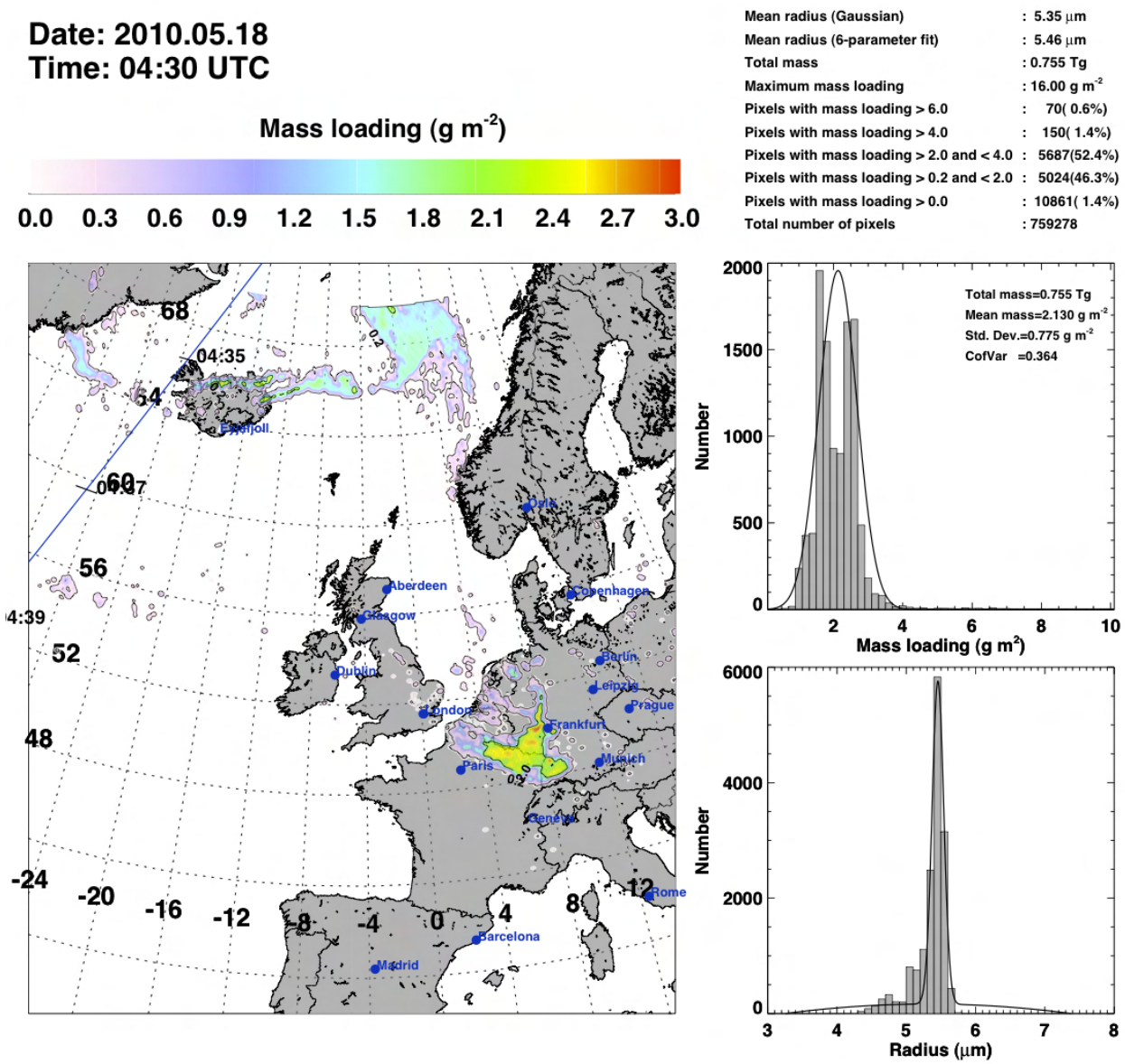

Figure 6.38: Date: 17 May 2010, Time: 04:30 UT.

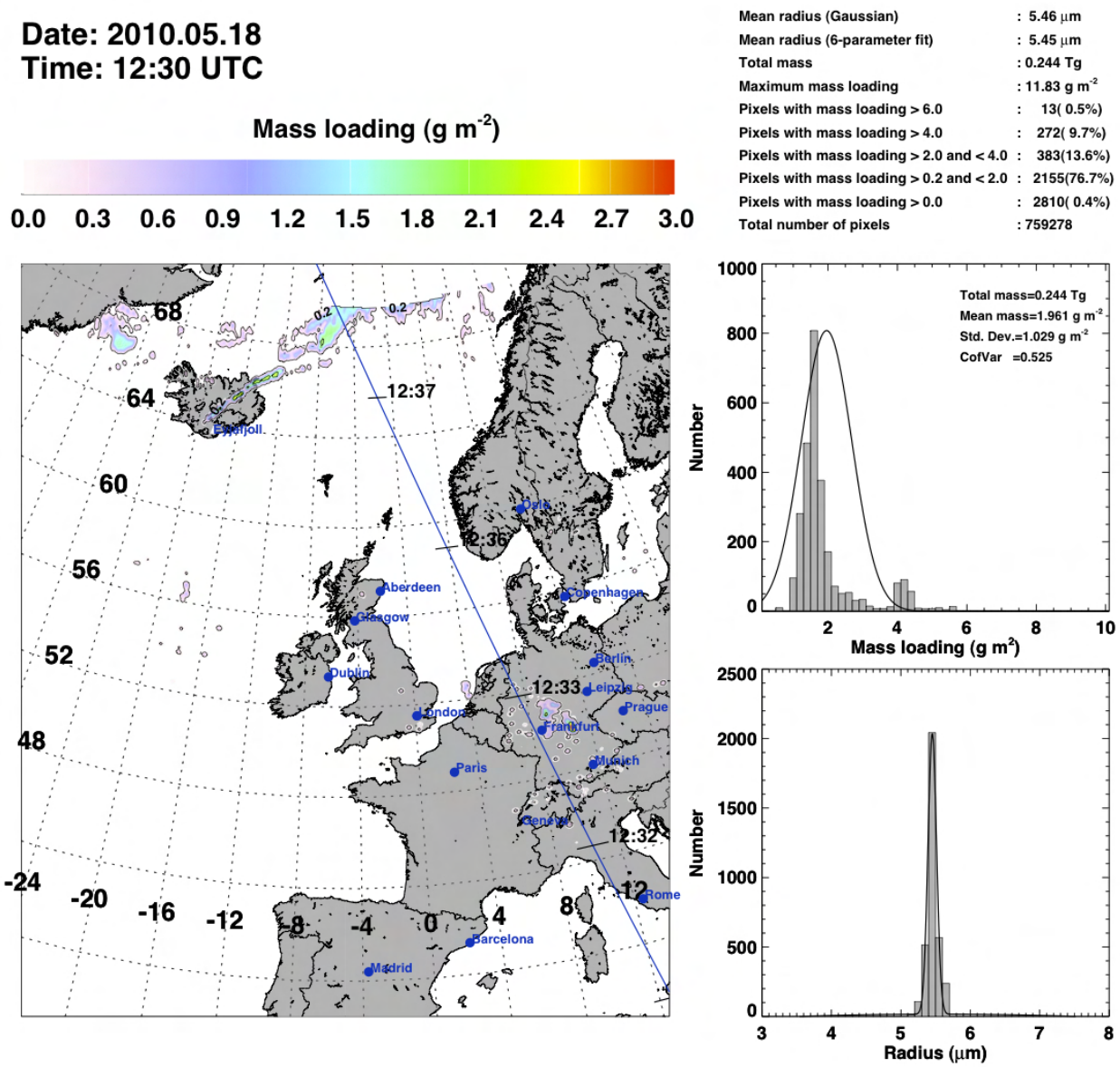

Figure 6.39: Date: 18 May 2010, Time: 12:30 UT.

Filename	Date	SEVIRI Time (UT)	CALIPSO Time (UT)
CAL LID L1-ValStage1-V3-01.2010-04-15T03-52-34ZN.hdf	15.04.2010	04:00	04:01
CAL LID L1-ValStage1-V3-01.2010-04-15T12-53-26ZD.hdf	15.04.2010	13:30	13:11
CAL LID L1-ValStage1-V3-01.2010-04-16T01-18-07ZN.hdf	16.04.2010	01:15	01:21
CAL LID L1-ValStage1-V3-01.2010-04-16T10-19-03ZD.hdf	16.04.2010	10:45	10:48
CAL LID L1-ValStage1-V3-01.2010-04-16T11-57-54ZD.hdf	16.04.2010	12:30	12:37
CAL LID L1-ValStage1-V3-01.2010-04-17T02-47-56ZD.hdf	17.04.2010	02:15	02:13
CAL LID L1-ValStage1-V3-01.2010-04-17T03-40-21ZN.hdf	17.04.2010	03:45	03:50
CAL LID L1-ValStage1-V3-01.2010-04-17T11-02-22ZD.hdf	17.04.2010	13:00	13:03
CAL LID L1-ValStage1-V3-01.2010-04-20T04-11-30ZN.hdf	20.04.2010	04:15	04:16
CAL LID L1-ValStage1-V3-01.2010-04-20T13-12-27ZD.hdf	20.04.2010	13:45	13:42
CAL LID L1-ValStage1-V3-01.2010-04-24T03-47-03ZN.hdf	24.04.2010	04:00	03:56
CAL LID L1-ValStage1-V3-01.2010-05-06T13-13-42ZD.hdf	06.05.2010	13:45	13:42
CAL LID L1-ValStage1-V3-01.2010-05-07T03-17-14ZN.hdf	07.05.2010	03:15	03:18
CAL LID L1-ValStage1-V3-01.2010-05-07T13-57-06ZD.hdf	07.05.2010	14:15	14:11
CAL LID L1-ValStage1-V3-01.2010-05-08T04-00-33ZN.hdf	08.05.2010	04:00	04:05
CAL LID L1-ValStage1-V3-01.2010-05-08T14-40-24ZD.hdf	08.05.2010	15:00	14:56
CAL LID L1-ValStage1-V3-01.2010-05-09T04-43-56ZN.hdf	09.05.2010	04:45	04:43
CAL LID L1-ValStage1-V3-01.2010-05-09T13-44-52ZD.hdf	09.05.2010	14:00	14:03
CAL LID L1-ValStage1-V3-01.2010-05-10T03-48-24ZN.hdf	10.05.2010	04:00	03:56
CAL LID L1-ValStage1-V3-01.2010-05-10T12-49-19ZD.hdf	10.05.2010	14:45	14:48
CAL LID L1-ValStage1-V3-01.2010-05-11T13-32-37ZD.hdf	11.05.2010	13:45	13:52
CAL LID L1-ValStage1-V3-01.2010-05-12T03-36-09ZN.hdf	12.05.2010	03:45	03:47
CAL LID L1-ValStage1-V3-01.2010-05-13T13-20-24ZD.hdf	13.05.2010	13:45	13:45
CAL LID L1-ValStage1-V3-01.2010-05-14T02-31-31ZD.hdf	14.05.2010	03:15	03:22
CAL LID L1-ValStage1-V3-01.2010-05-14T12-24-52ZD.hdf	14.05.2010	12:45	12:48
CAL LID L1-ValStage1-V3-01.2010-05-14T14-03-47ZD.hdf	14.05.2010	14:30	14:37
CAL LID L1-ValStage1-V3-01.2010-05-15T02-28-24ZN.hdf	15.05.2010	02:45	02:47
CAL LID L1-ValStage1-V3-01.2010-05-15T04-07-14ZN.hdf	15.05.2010	04:15	04:11
CAL LID L1-ValStage1-V3-01.2010-05-15T13-08-10ZD.hdf	15.05.2010	13:45	13:40
CAL LID L1-ValStage1-V3-01.2010-05-16T03-11-42ZN.hdf	16.05.2010	03:15	03:15
CAL LID L1-ValStage1-V3-01.2010-05-16T03-58-12ZD.hdf	16.05.2010	04:45	04:48
CAL LID L1-ValStage1-V3-01.2010-05-16T12-12-38ZD.hdf	16.05.2010	12:45	12:42
CAL LID L1-ValStage1-V3-01.2010-05-16T13-51-28ZD.hdf	16.05.2010	14:00	14:07
CAL LID L1-ValStage1-V3-01.2010-05-17T02-16-05ZN.hdf	17.05.2010	02:15	02:18
CAL LID L1-ValStage1-V3-01.2010-05-17T03-55-00ZN.hdf	17.05.2010	04:00	04:01
CAL LID L1-ValStage1-V3-01.2010-05-17T12-55-56ZD.hdf	17.05.2010	13:15	13:10
CAL LID L1-ValStage1-V3-01.2010-05-18T02-59-28ZN.hdf	18.05.2010	03:15	03:10
CAL LID L1-ValStage1-V3-01.2010-05-18T04-38-19ZN.hdf	18.05.2010	04:30	04:37
CAL LID L1-ValStage1-V3-01.2010-05-18T12-00-25ZD.hdf	18.05.2010	12:35	12:37

Table 6.1: CALIPSO-SEVIRI coincidences during April/May 2010.

be performed. In this study only a few cases have been examined.

6.3 Special Cases

6.3.1 Caliop

Two cases were selected for study with the Caliop lidar. The v2.0 Caliop products provide some information for identifying the scatterers responsible for the backscattered signal at 532 nm and 1064 nm. Figure 6.40 shows an example of a Caliop curtain with the circled area of high backscatter identified as possibly being due to ash. The corresponding SEVIRI image is shown in Figure 6.41. The CALIPSO orbit dissects the SE-

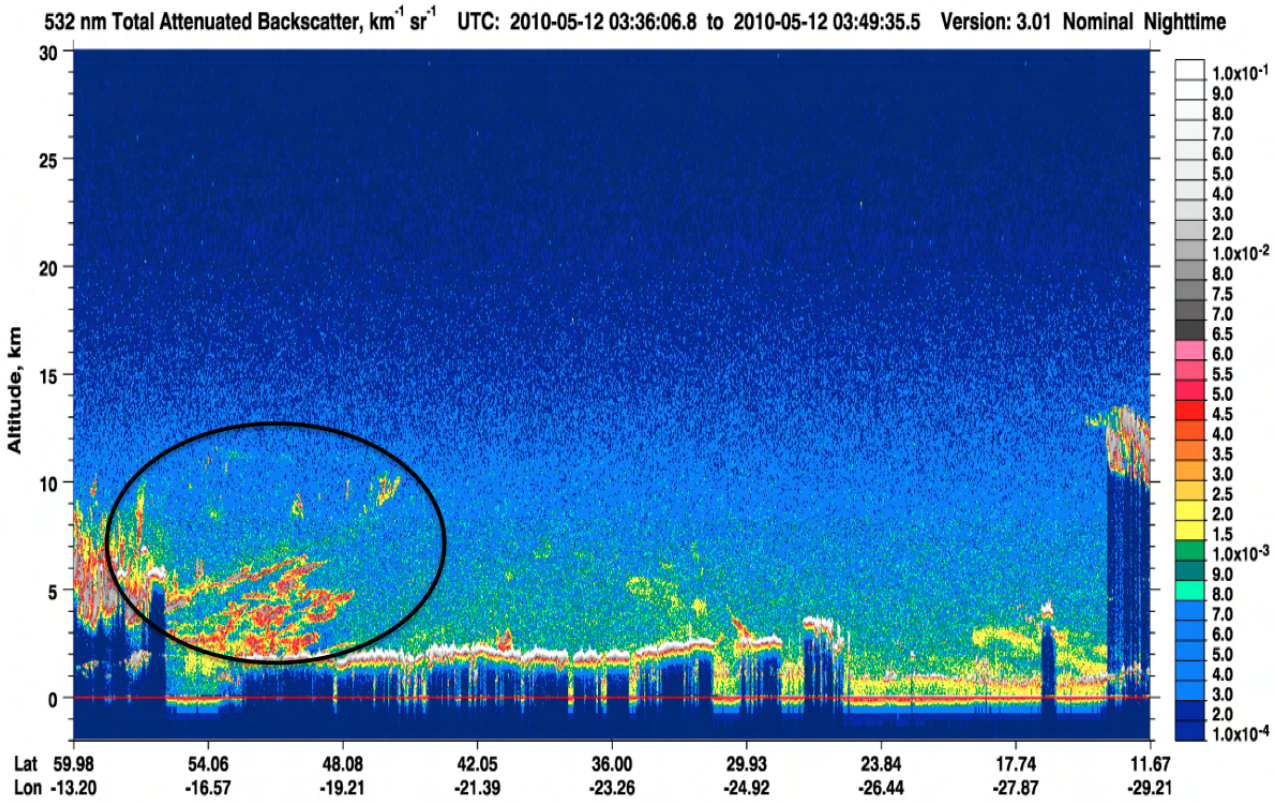

Figure 6.40: Caliop backscatter at 532 nm on 12 May 2010 at 03:30UT. The circled region is potentially backscatter due to volcanic aerosol.

VIRI ash mass loadings from approximately 48 °N to 56 °N between 20 °W and 16 °W, and it is concluded that the backscatter seen in the Caliop curtain in this region is most likely due to volcanic aerosol.

It is possible, under some assumptions, to infer the mass concentration. We use the following argument for this. The mass loading observed by SEVIRI may be written:

$$m_l = \int_{z_1}^{z_2} \rho(z) dz, \tag{6.2}$$

where, m_l is the mass loading, z_1 and z_2 are the heights of the lower and upper levels of the ash layer, respectively, and ρ is the mass concentration. Simplifying further by assuming that ρ is constant in the layer

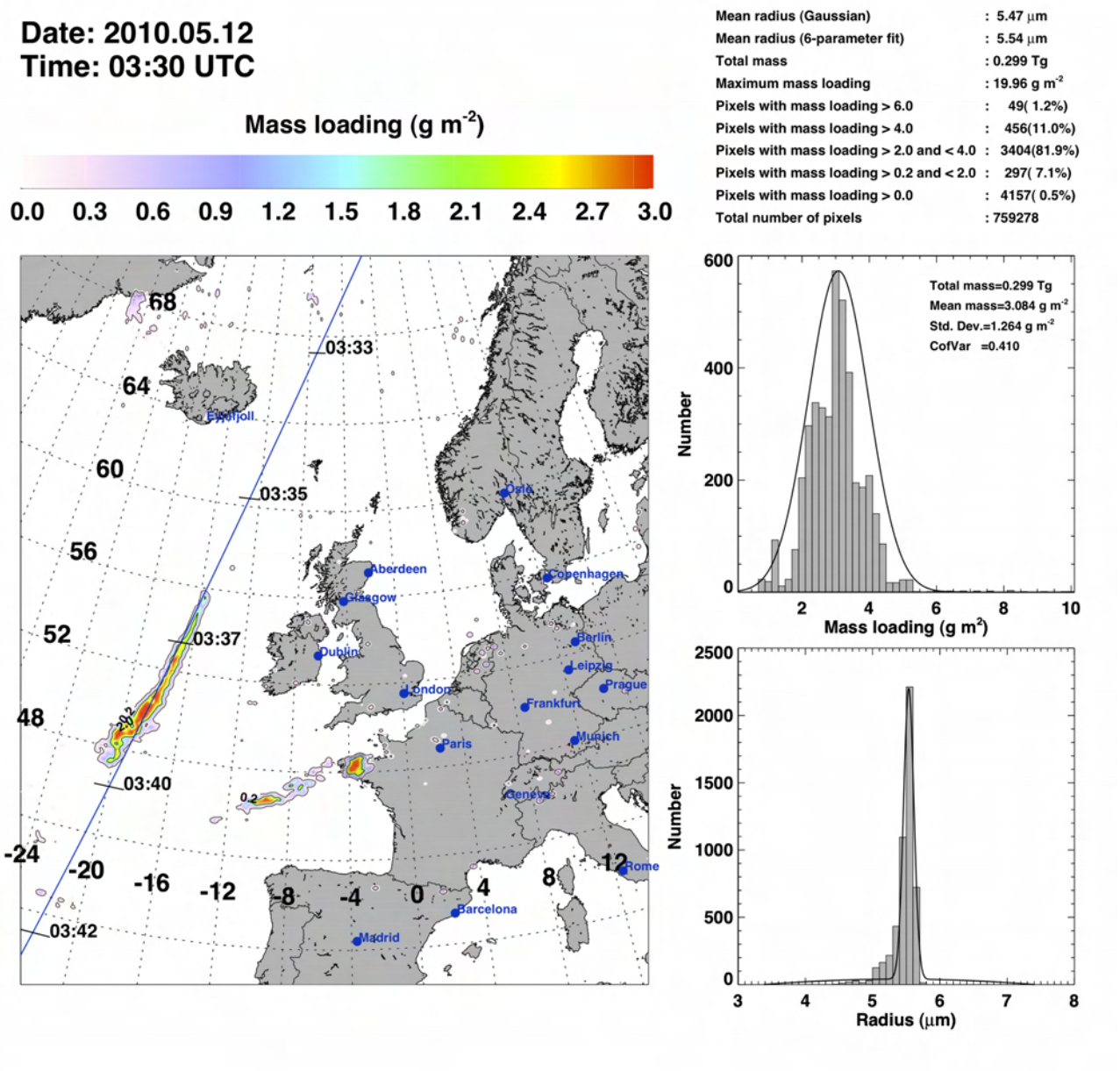

Figure 6.41: Date: 12 May 2010, Time: 03:30 UT.

and we can represent the aerosol as a single layer, we may write,

$$\rho = \frac{m_l}{\Delta z}, \tag{6.3}$$

where Δz=z_2-z_1. Thus, an estimate of the aerosol thickness is sufficient to provide an estimate of the mass concentration. In this case, $\Delta z \approx 3$ km, and $\rho \approx 1$ mg m^{-3}. In this case it is clear that the aerosol layer is not a single layer and it is also likely that the concentration is not constant within the layer (the variation of the backscatter in the Caliop curtain also suggests that the profile is not constant).

A second example is shown in Figure 6.42. Here the Caliop curtain has been overlaid onto the SEVIRI ash mass loading map and also the layer more closely approximates the assumptions employed. The layer thickness, $\Delta z \approx$ 1km, and the ash loading, $m_l \approx 3$ gm^{-2}, giving $\rho \approx 3$ mgm^{-3}.

6.3.2 Ground-based lidar

Several ground-based lidars of varying complexity and quality were able to capture data as the Eyjfjallajökull ash cloud passed over. Some of these lidars are able to distinguish meteorological scatterers from that due to ash cloud and with the addition of information about the aerosol it is possible to retrieve mass concentrations. Data from he lidars at Leipzig and Munich have recently been published by Ansmann *et al.* (2010). Figures 6.43 and 6.44 show lidar mass concentration profiles from Ansmann *et al.* (2010) overlaid onto the corresponding (coincident in time) SEVIRI ash mass loading maps. In these cases we can perform the integration of the profile and estimate m_l.

For Leipzig the integrated profile gives, m_l= 0.41 gm^{-2}, while for Munich m_l=0.23 gm^{-2}. These are in very good agreement with the SEVIRI estimates. It is also noticeable that there are much higher SEVIRI mass loadings observed over the region and assuming that the concentrations profiles are similar to those at Leipzig and Munich, the maximum mass concentrations must have exceeded the new thresholds quite easily in many places.

6.3.3 Photometers

Sun photometers measure the distribution and attenuation of solar radiation in several wavebands. They are therefore capable of detecting the presence of aerosols in the atmosphere above the instrument. A sun photometer at Barcelona was operating when a filament of the ash cloud from Eyjafjallajökull passed over. Figure 6.45 shows the optical depth (corrected for the background optical depth) as a function of time, with the SEVIRI mass concentration overlaid assuming three different cloud thicknesses. The plot shows excellent coincidence between the SEVIRI detection and the sun photometer measurements and suggest that these ground-based instruments may be useful for future ash aerosol validation.

6.3.4 FLEXPART

A new volcanic ash source term inversion scheme has recently been described by Stohl *et al.* (2011). This scheme uses the atmospheric Lagrangian dispersion model FLEXPART (Stohl *et al.*, 2005) to compare forecast movement of volcanic ash with satellite estimates. Since the SEVIRI data was used as part of the inversion process it would be improper to use these results as validation. Nevertheless, it is instructive to compare the SEVIRI mass loadings with the *a priori* and *a posteriori* results as this demonstrates some of

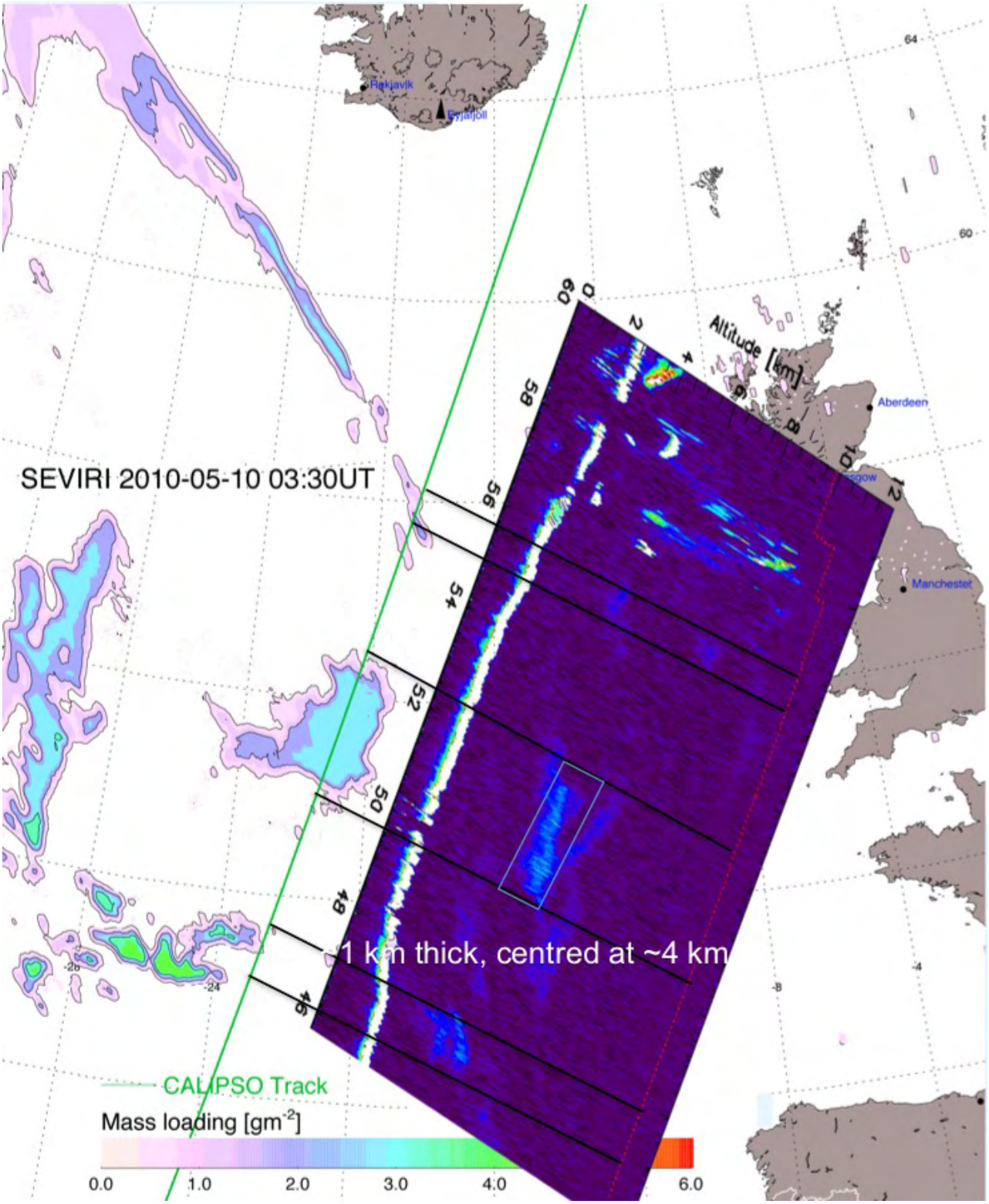

Figure 6.42: A segment of the Caliop backscatter curtain at 532 nm overlayed onto the SEVIRI ash mass loading map for 10 May, 2010 at 03:30 UT.

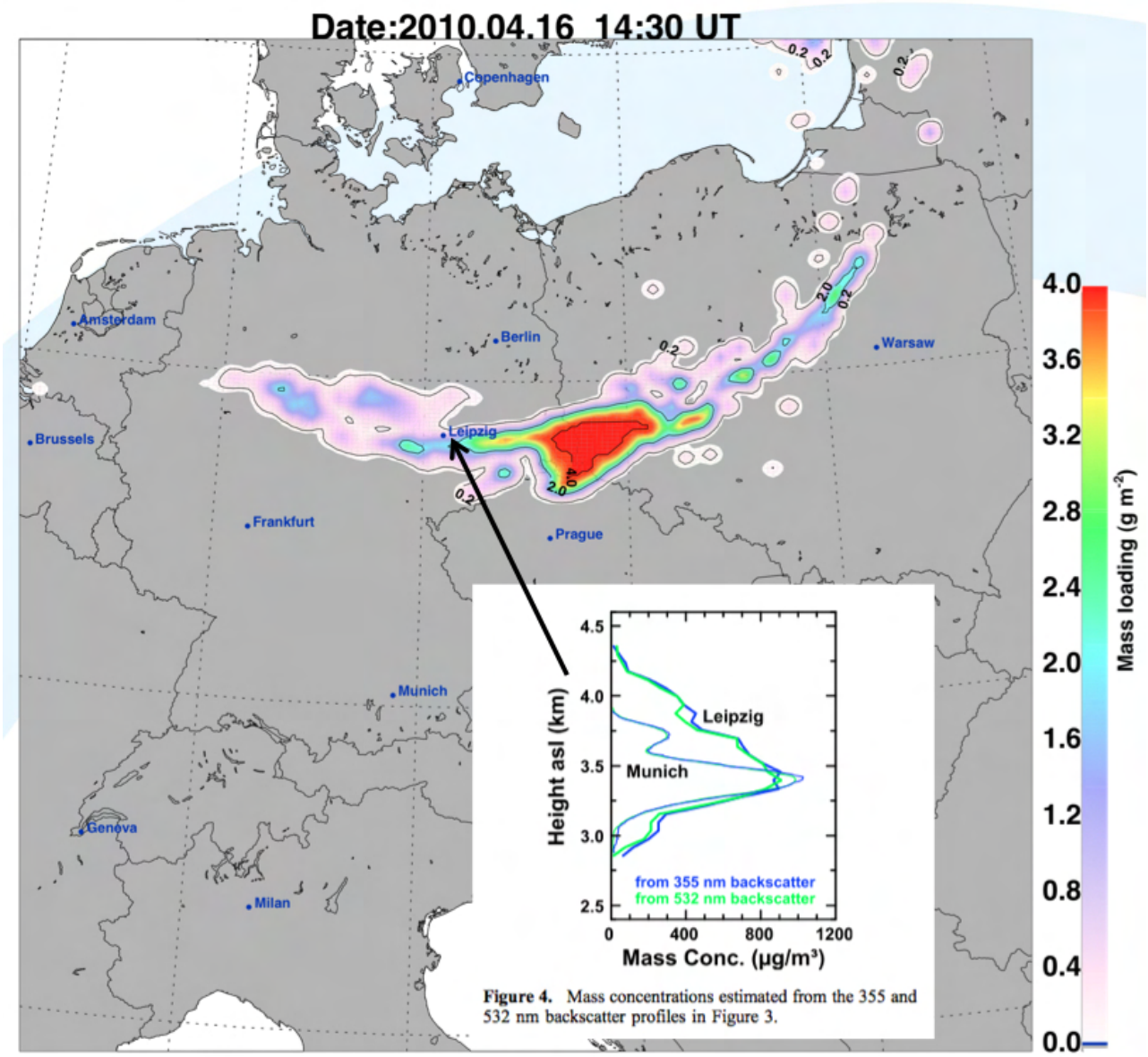

Figure 4. Mass concentrations estimated from the 355 and 532 nm backscatter profiles in Figure 3.

Figure 6.43: Ground-based lidar concentration profiles at Leipzig (after Ansmann *et al.* (2010)) and location in relation to SEVIRI ash detection at the same time.

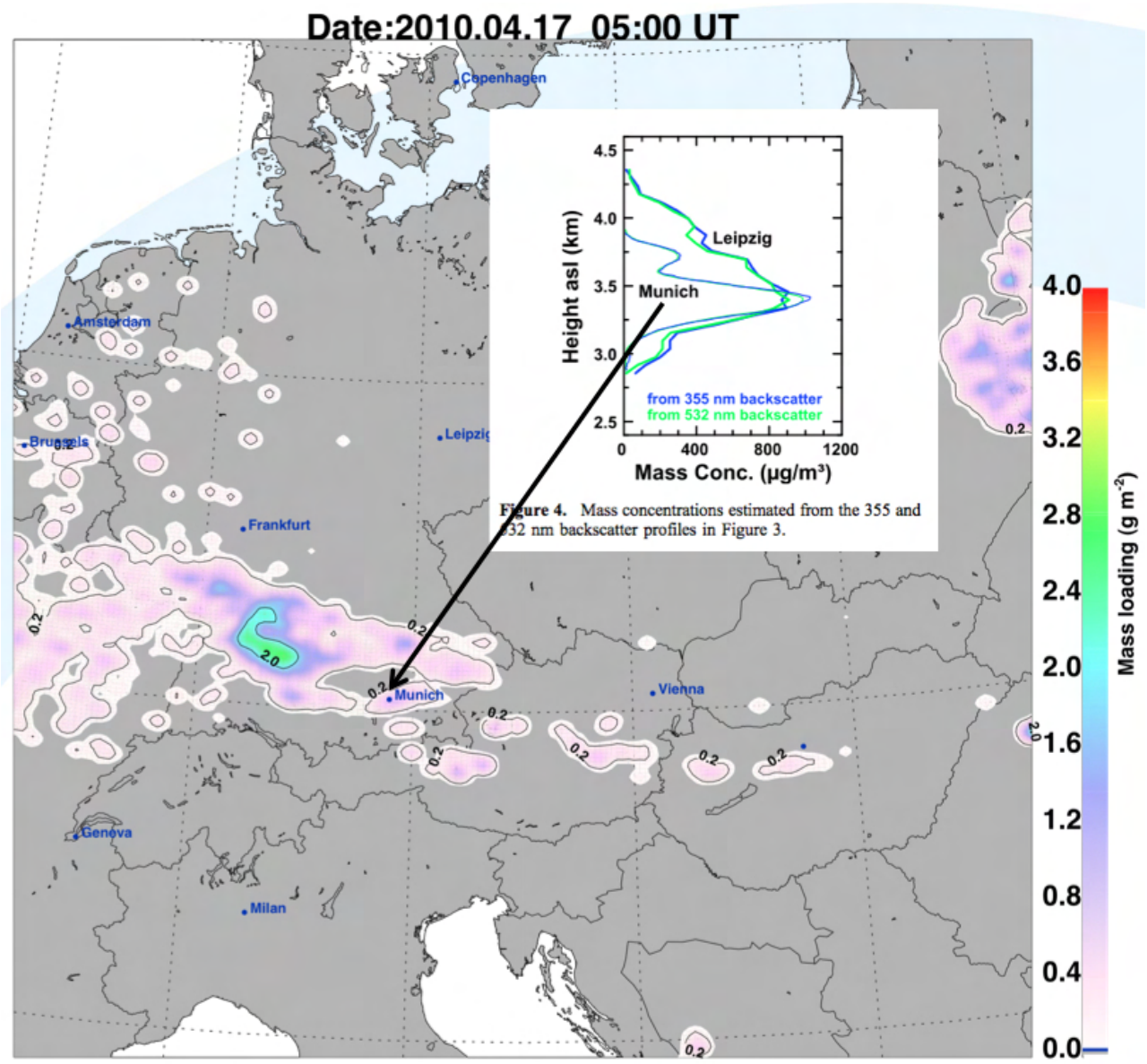

Figure 6.44: Ground-based lidar concentration profiles at Munich (after Ansmann *et al.* (2010)) and location in relation to SEVIRI ash detection at the same time. It can be seen that the the mass loading at Leipzig (the vertical integral of the concentration profile) would be larger than at Munich, in broad agreement with the SEVIRI retrievals.

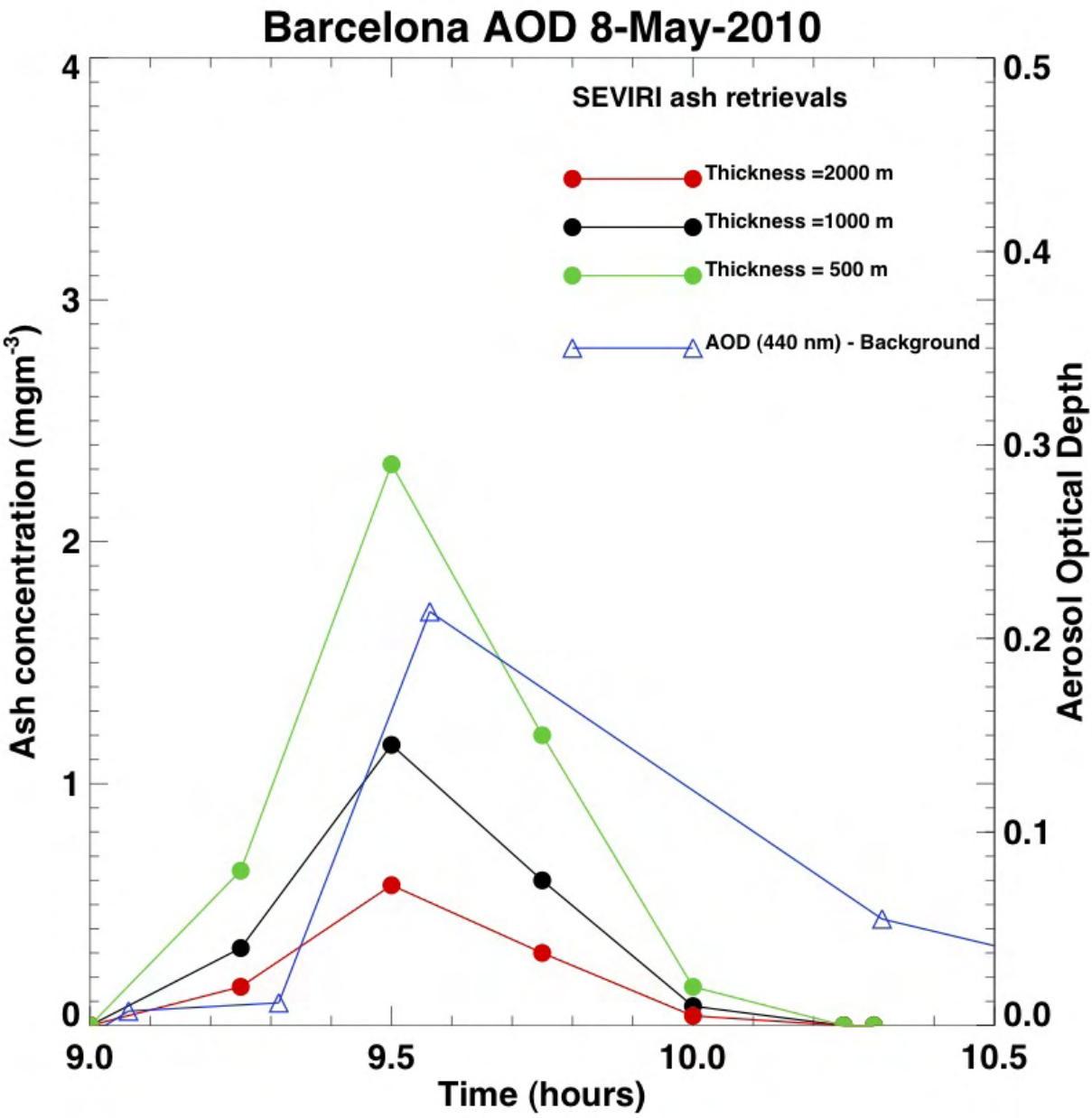

Figure 6.45: Sun photometer aerosol optical depth (AOD) and SEVIRI mass concentrations, assuming three different cloud thicknesses for a filament of the Eyjafjallajökull ash cloud on 8 May, 2010.

the deficiencies and attributes of the satellite retrievals. A GIF animation file (SEVIRIFLEXPART.gif) is included with this report showing SEVIRI mass loadings (left-panel), *a posteriori* loadings (middle-panel), and *a priori* (right-panel) from 9 May to 18 May, 2010 in 2 hourly intervals. Figure 6.46 shows one such panel taken from the GIF file.

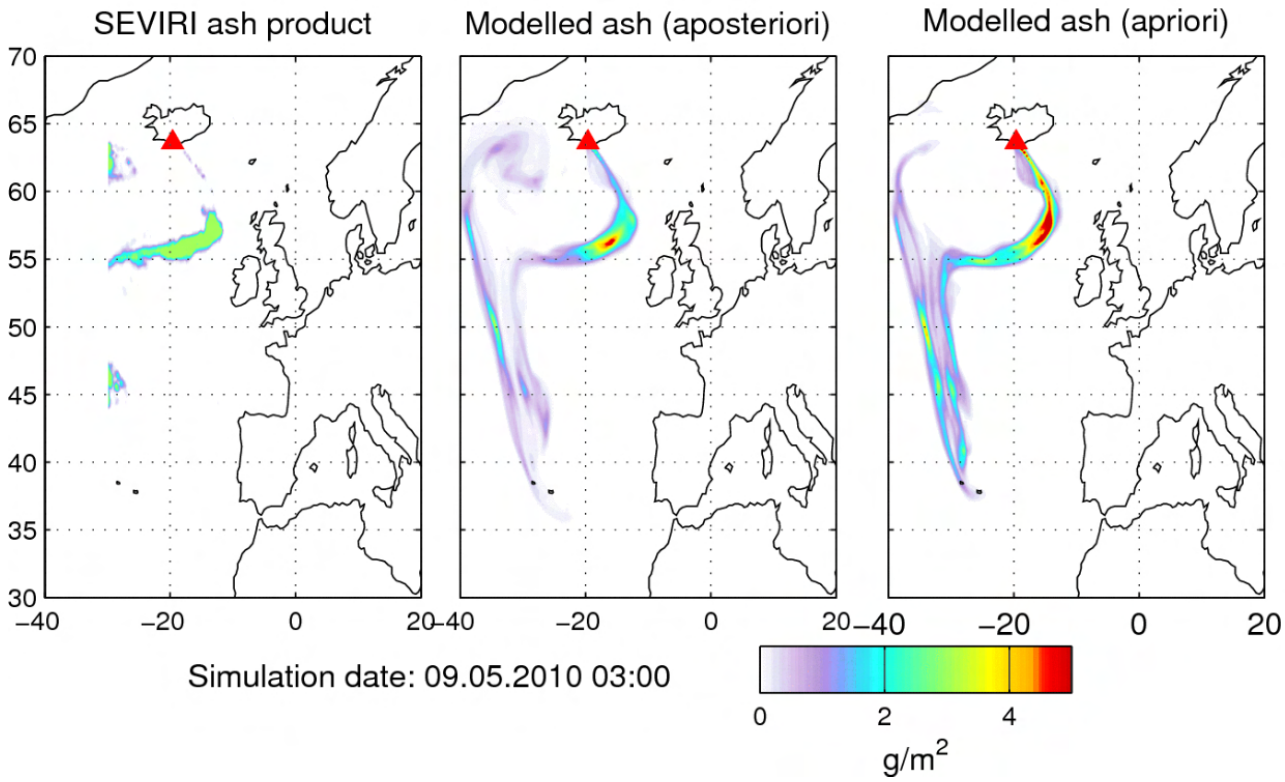

Figure 6.46: SEVIRI mass loading (left-panel), FLEXPART *a posteriori* (middle-panel), and FLEXPART *a priori* (right-panel) for 9 May 2010 at 03:00 UT. Units: gm^{-2}. A full GIF animation is available in the associated file: *SEVIRIFLEXPART.gif*

Chapter 7

Results–SO_2

7.1 Partial Column Abundances

Retrieval plots from four different satellite sensors (2 UV and 2 IR) are shown in the following subsections. GOME-2 and OMI are sensitive to SO_2 that is close to the surface; neither AIRS nor IASI sensors can detect SO_2 below 3 km or so, thus it is difficult to make detailed intercomparisons between the retrievals. In general all four sensors detected SO_2 on many occasions, especially in May over the north Atlantic.

7.1.1 GOME-2

Table 7.1 lists the GOME-2 data analysed in this study plots of all GOME-2 overpasses during the period of the study are shown in the following figures.

Filename	Date	Time (UT)	Filename	Date	Time (UT)
gome2 20100428 110821.dat	2010.04.28	11:08	gome2 20100428 124721.dat	2010.04.28	12:47
gome2 20100429 104715.dat	2010.04.29	10:47	gome2 20100429 122621.dat	2010.04.29	12:26
gome2 20100430 102356.dat	2010.04.30	10:24	gome2 20100430 120732.dat	2010.04.30	12:07
gome2 20100501 100256.dat	2010.05.01	10:03	gome2 20100501 114626.dat	2010.05.01	11:46
gome2 20100502 094156.dat	2010.05.02	09:42	gome2 20100502 112520.dat	2010.05.02	11:25
gome2 20100502 130426.dat	2010.05.02	13:04	gome2 20100503 110419.dat	2010.05.03	11:04
gome2 20100503 124325.dat	2010.05.03	12:43	gome2 20100504 104313.dat	2010.05.04	10:43
gome2 20100505 101955.dat	2010.05.05	10:20	gome2 20100505 120331.dat	2010.05.05	12:03
gome2 20100506 095848.dat	2010.05.06	09:59	gome2 20100506 114224.dat	2010.05.06	11:42
gome2 20100507 093748.dat	2010.05.07	09:37	gome2 20100507 112124.dat	2010.05.07	11:21
gome2 20100507 130030.dat	2010.05.07	13:00	gome2 20100508 110018.dat	2010.05.08	11:00
gome2 20100508 123924.dat	2010.05.08	12:39	gome2 20100509 103911.dat	2010.05.09	10:39
gome2 20100509 121817.dat	2010.05.09	12:18	gome2 20100510 101553.dat	2010.05.10	10:16
gome2 20100510 115929.dat	2010.05.10	11:59	gome2 20100511 095453.dat	2010.05.11	09:55
gome2 20100511 113829.dat	2010.05.11	11:38	gome2 20100512 093346.dat	2010.05.12	09:34
gome2 20100512 111722.dat	2010.05.12	11:17	gome2 20100512 125628.dat	2010.05.12	12:56
gome2 20100513 091246.dat	2010.05.13	09:13	gome2 20100513 105622.dat	2010.05.13	10:56
gome2 20100513 123528.dat	2010.05.13	12:35	gome2 20100514 103516.dat	2010.05.14	10:35
gome2 20100514 121422.dat	2010.05.14	12:14	gome2 20100514 135546.dat	2010.05.14	13:56
gome2 20100515 101157.dat	2010.05.14	10:12	gome2 20100515 115533.dat	2010.05.15	11:55
gome2 20100515 133439.dat	2010.05.15	13:34	gome2 20100516 095057.dat	2010.05.16	09:51
gome2 20100516 113433.dat	2010.05.16	11:34	gome2 20100516 131339.dat	2010.05.16	13:13
gome2 20100517 092957.dat	2010.05.17	09:30	gome2 20100517 111327.dat	2010.05.17	11:13
gome2 20100517 125233.dat	2010.05.17	12:52	gome2 20100518 090857.dat	2010.05.18	09:08
gome2 20100518 105227.dat	2010.05.18	10:52	gome2 20100518 123132.dat	2010.05.18	12:31
gome2 20100519 103120.dat	2010.05.19	10:31	gome2 20100519 121032.dat	2010.05.19	12:10
gome2 20100520 100808.dat	2010.05.20	10:08	gome2 20100520 115138.dat	2010.05.20	11:51
gome2 20100521 094702.dat	2010.05.21	09:47	gome2 20100521 113038.dat	2010.05.21	11:30
gome2 20100521 130944.dat	2010.05.21	13:09	gome2 20100522 110937.dat	2010.05.22	11:09
gome2 20100522 124843.dat	2010.05.22	12:48	gome2 20100523 104831.dat	2010.05.23	10:48
gome2 20100523 122737.dat	2010.05.23	12:27	gome2 20100524 102519.dat	2010.05.24	10:29

Table 7.1: GOME-2 data files.

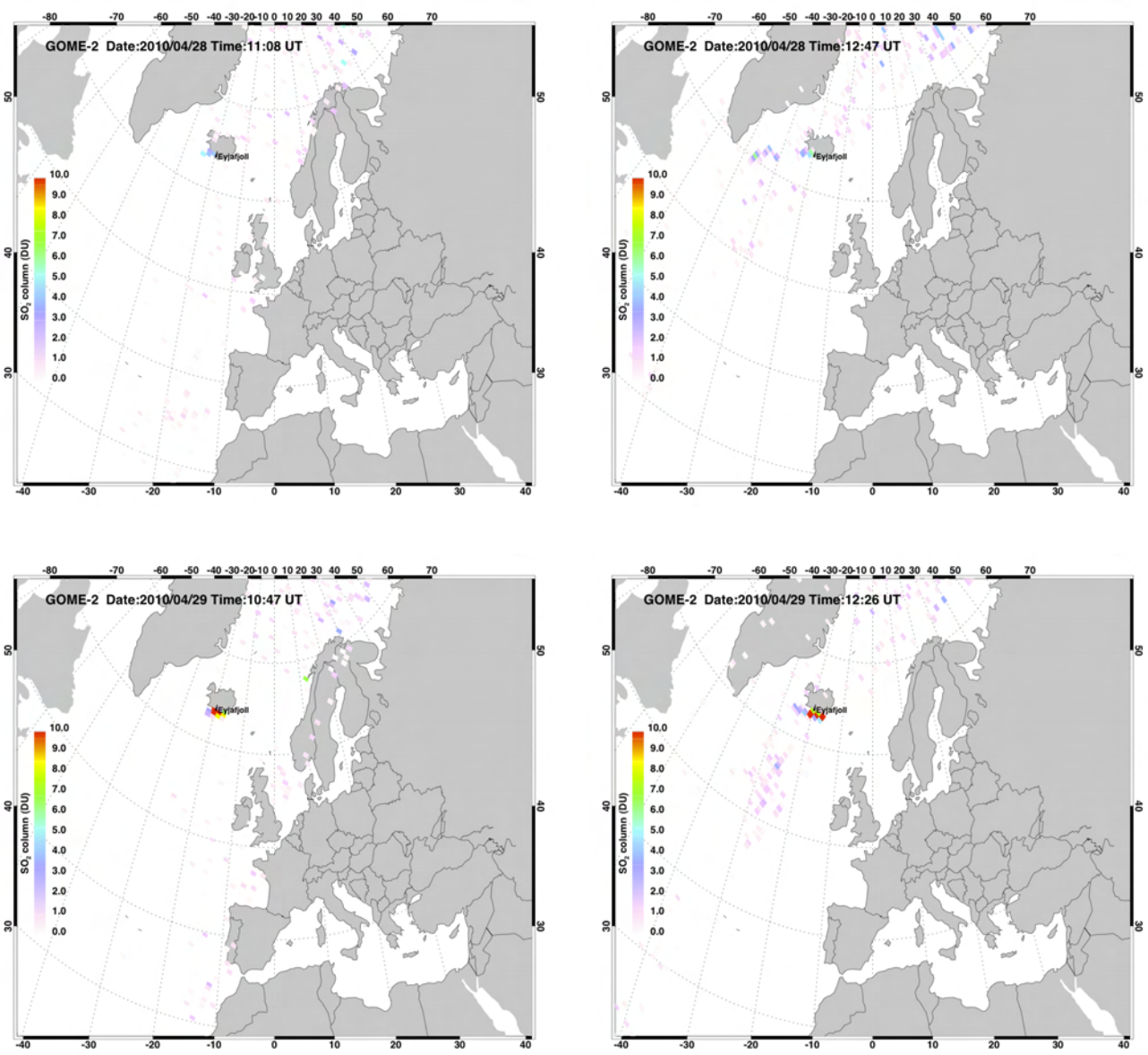

Figure 7.1: GOME-2 SO_2 partial column abundance in DU. Date and time of the orbit are shown at the top of each plot.

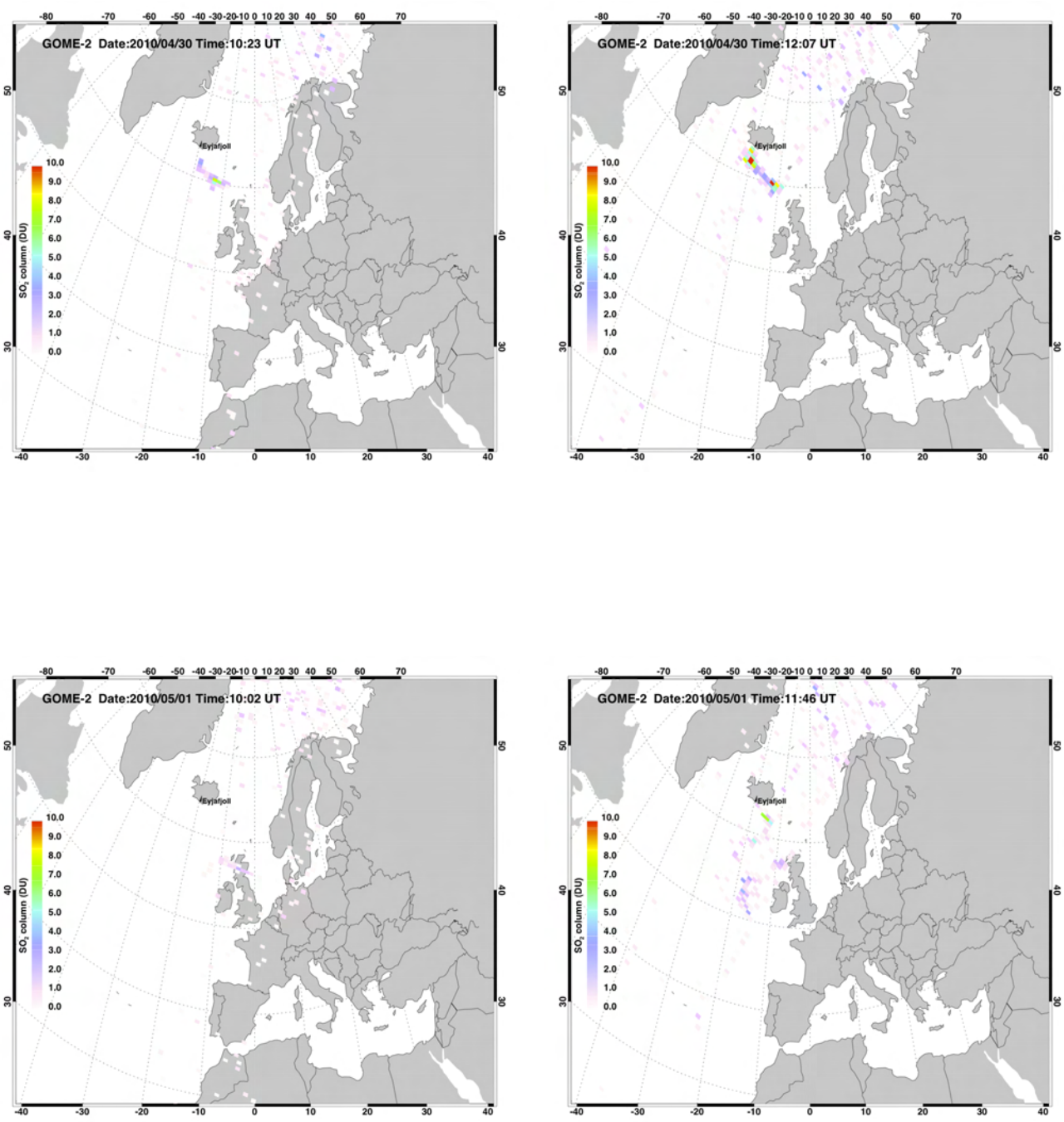

Figure 7.2: GOME-2 SO_2 partial column abundance in DU. Date and time of the orbit are shown at the top of each plot.

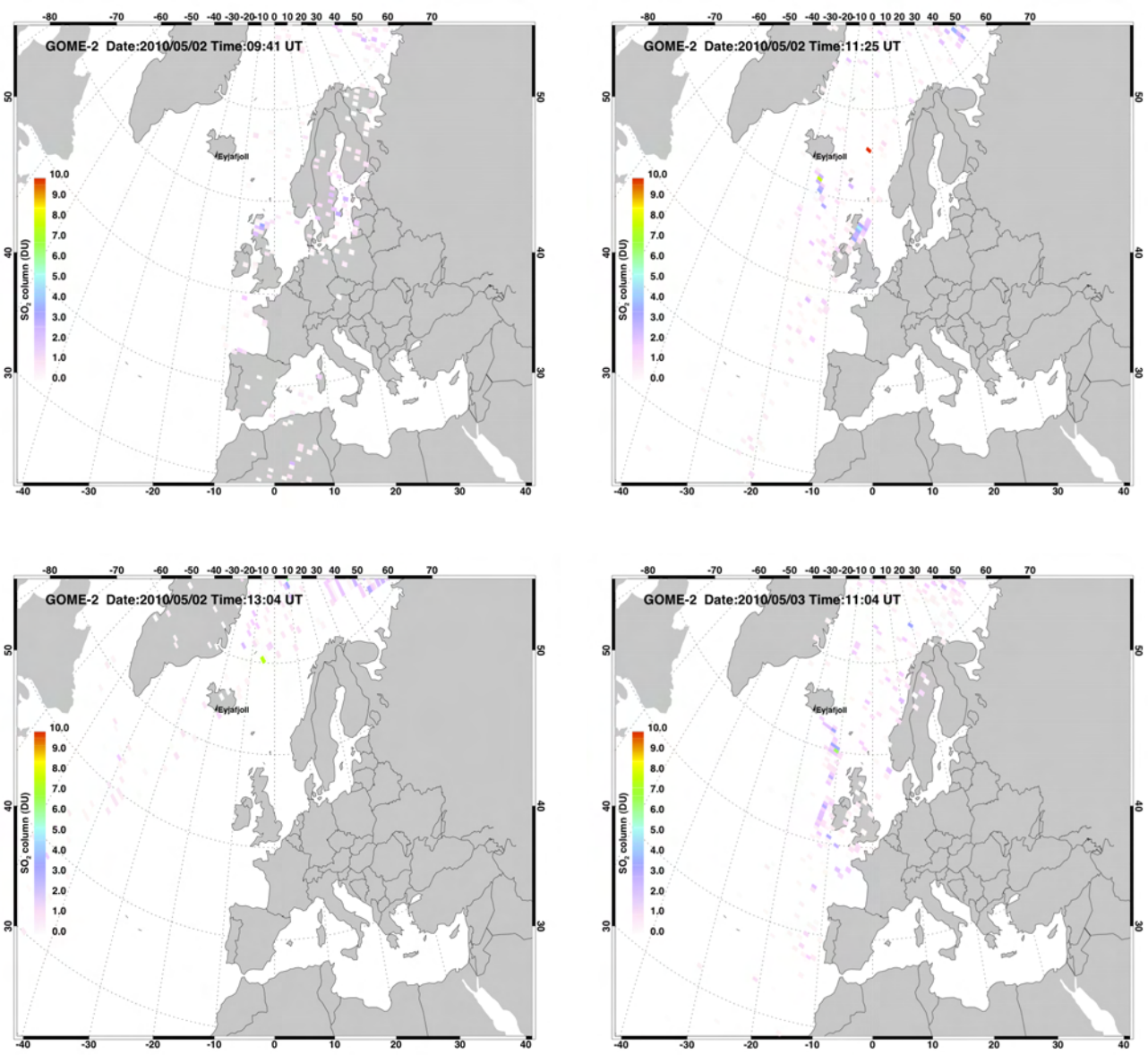

Figure 7.3: GOME-2 SO_2 partial column abundance in DU. Date and time of the orbit are shown at the top of each plot.

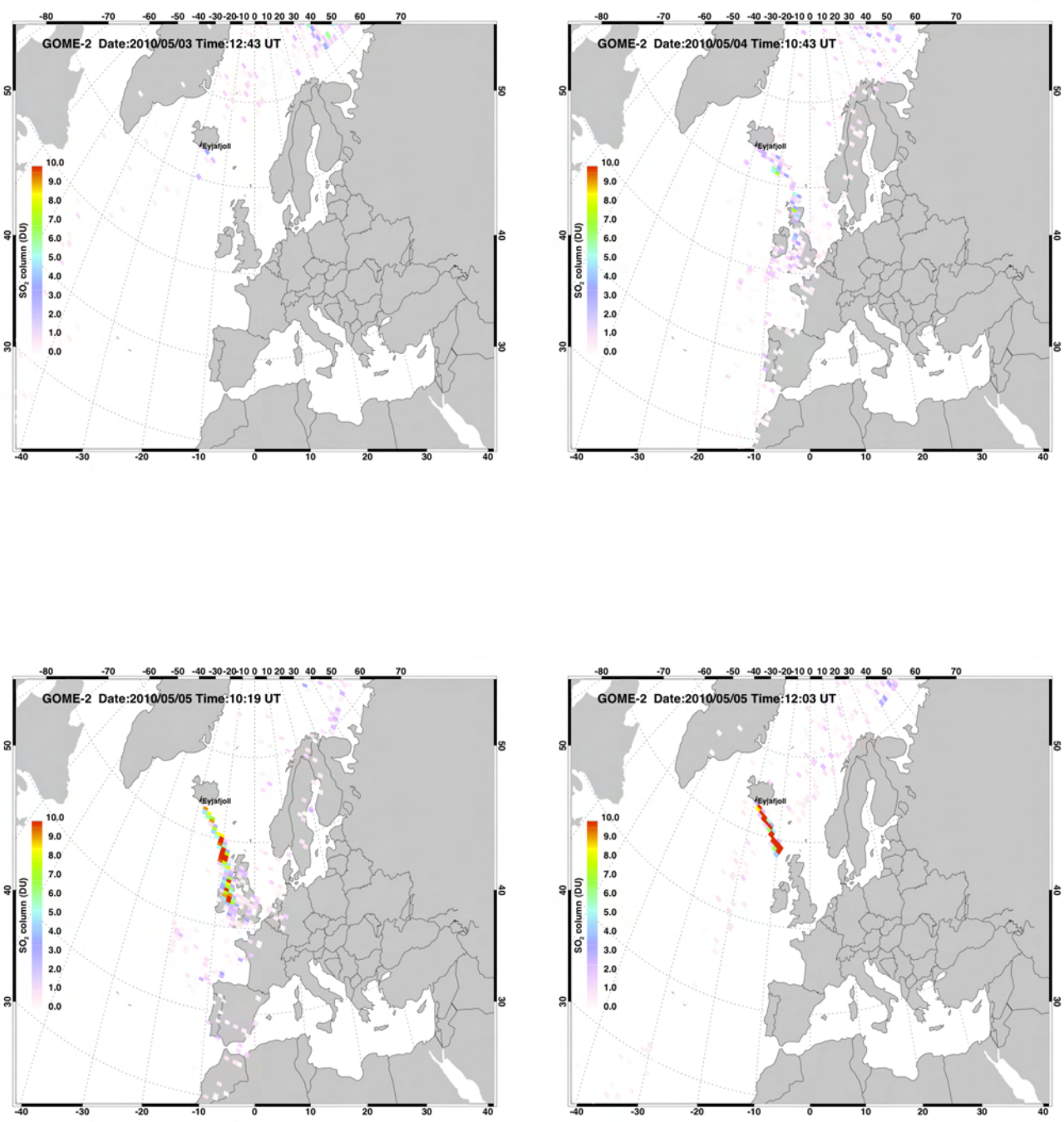

Figure 7.4: GOME-2 SO_2 partial column abundance in DU. Date and time of the orbit are shown at the top of each plot.

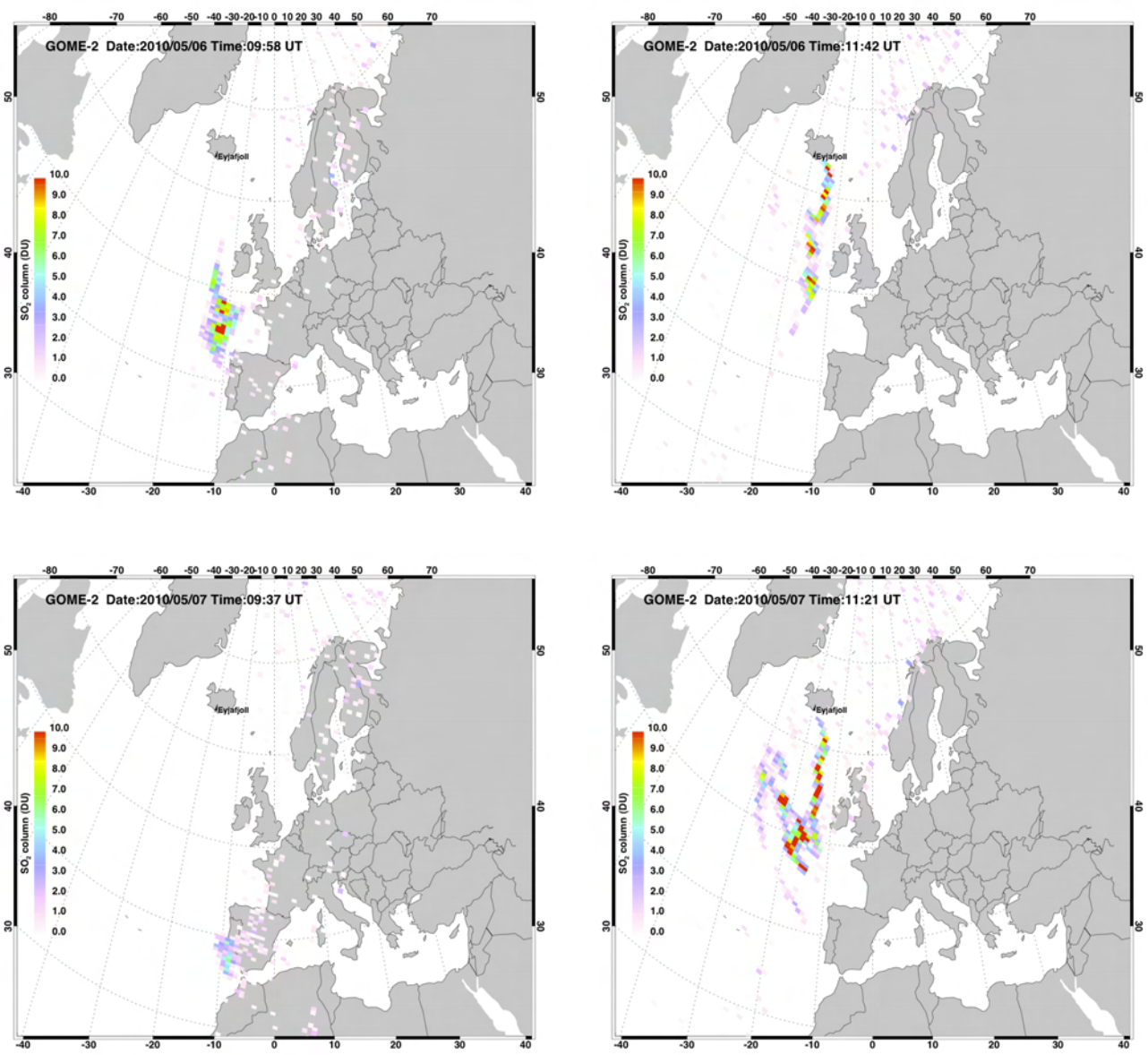

Figure 7.5: GOME-2 SO_2 partial column abundance in DU. Date and time of the orbit are shown at the top of each plot.

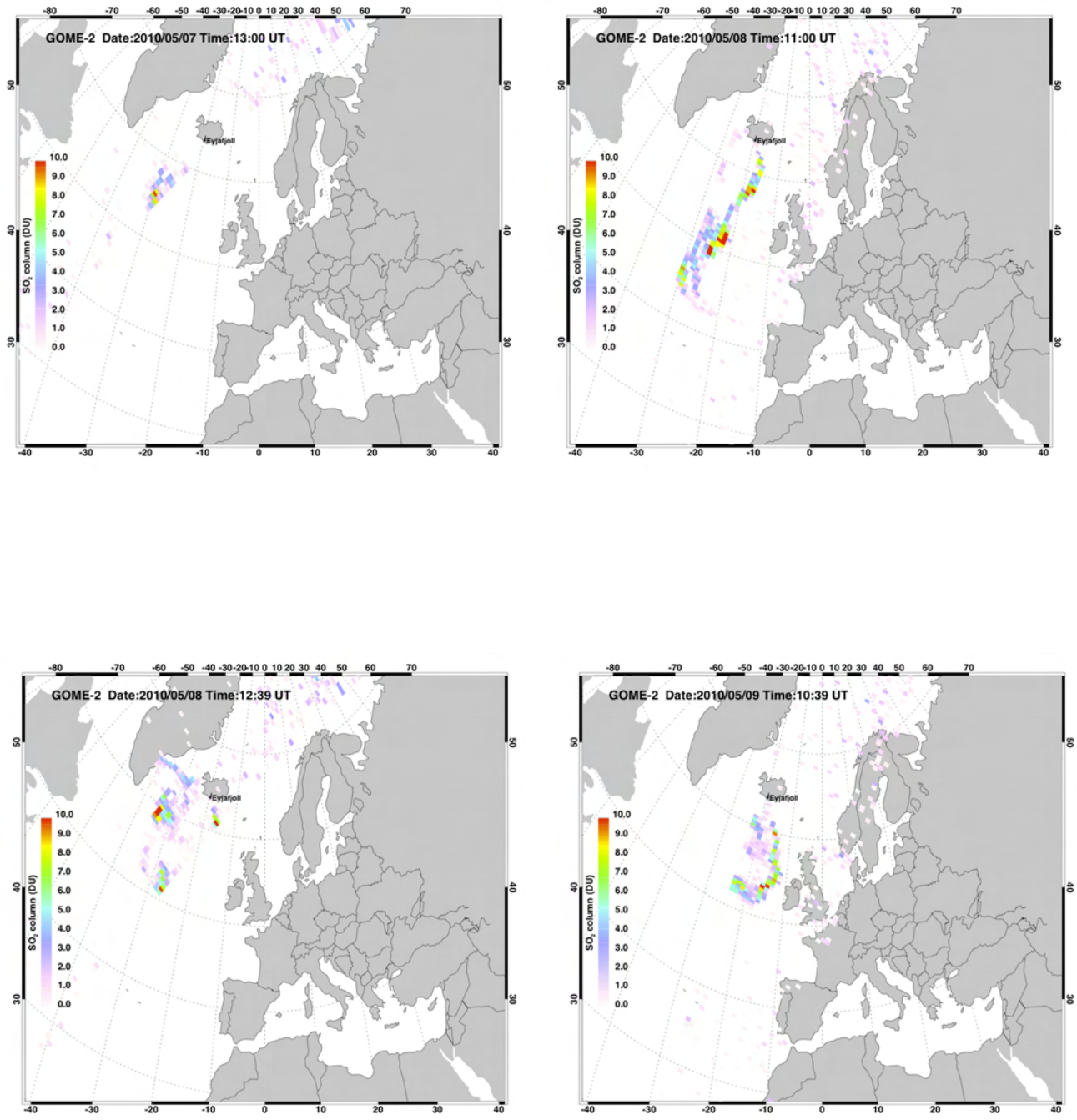

Figure 7.6: GOME-2 SO_2 partial column abundance in DU. Date and time of the orbit are shown at the top of each plot.

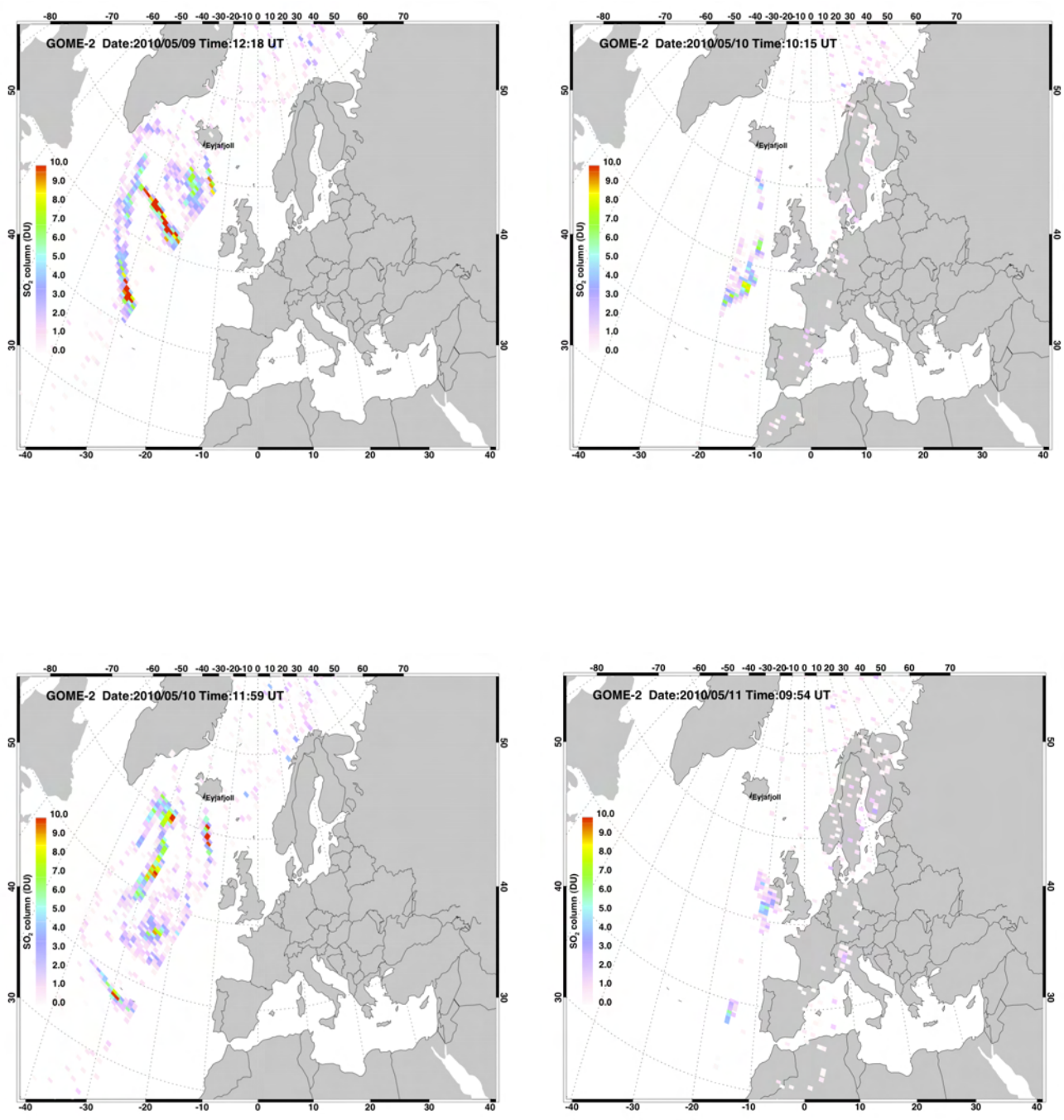

Figure 7.7: GOME-2 SO_2 partial column abundance in DU. Date and time of the orbit are shown at the top of each plot.

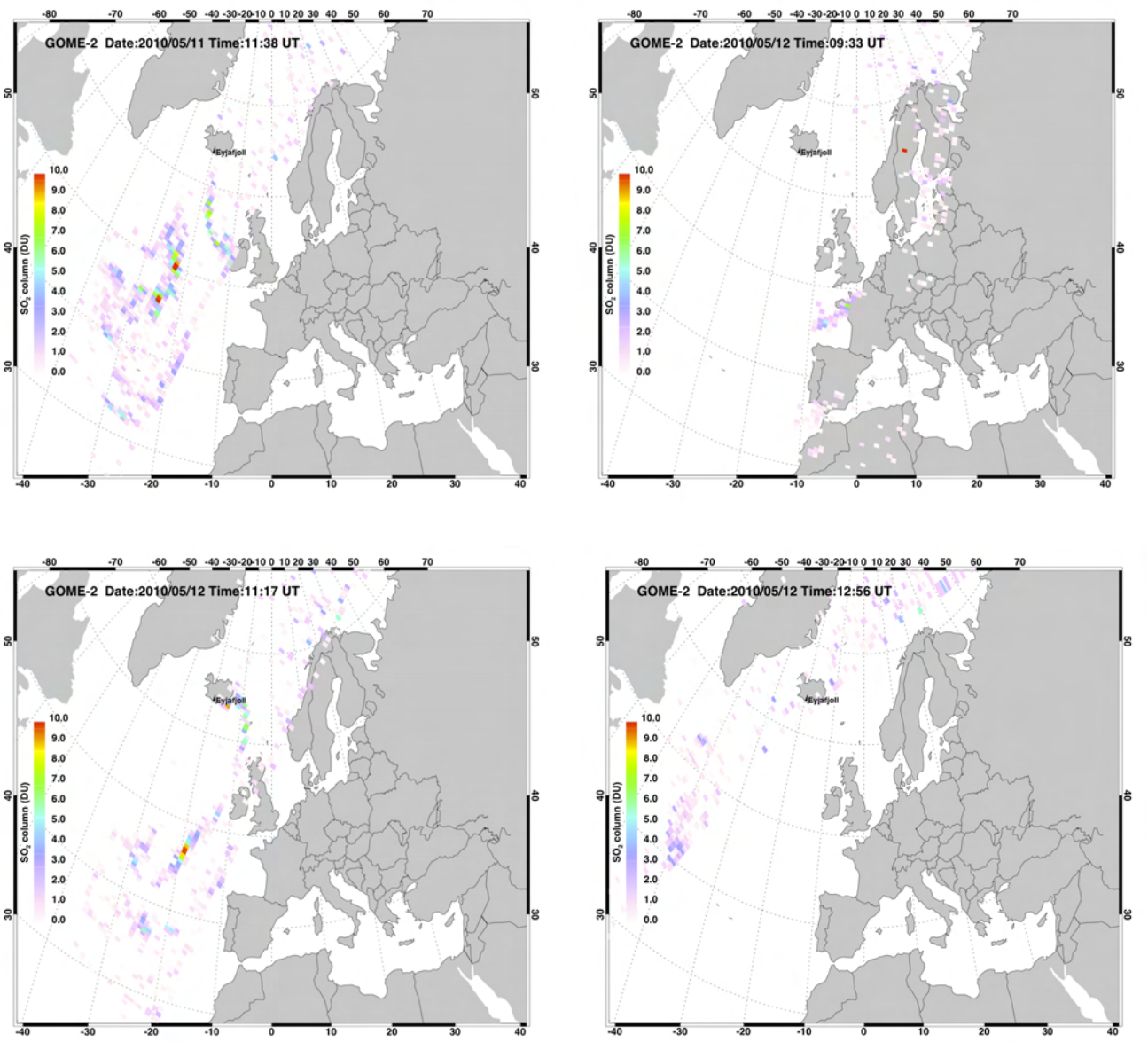

Figure 7.8: GOME-2 SO_2 partial column abundance in DU. Date and time of the orbit are shown at the top of each plot.

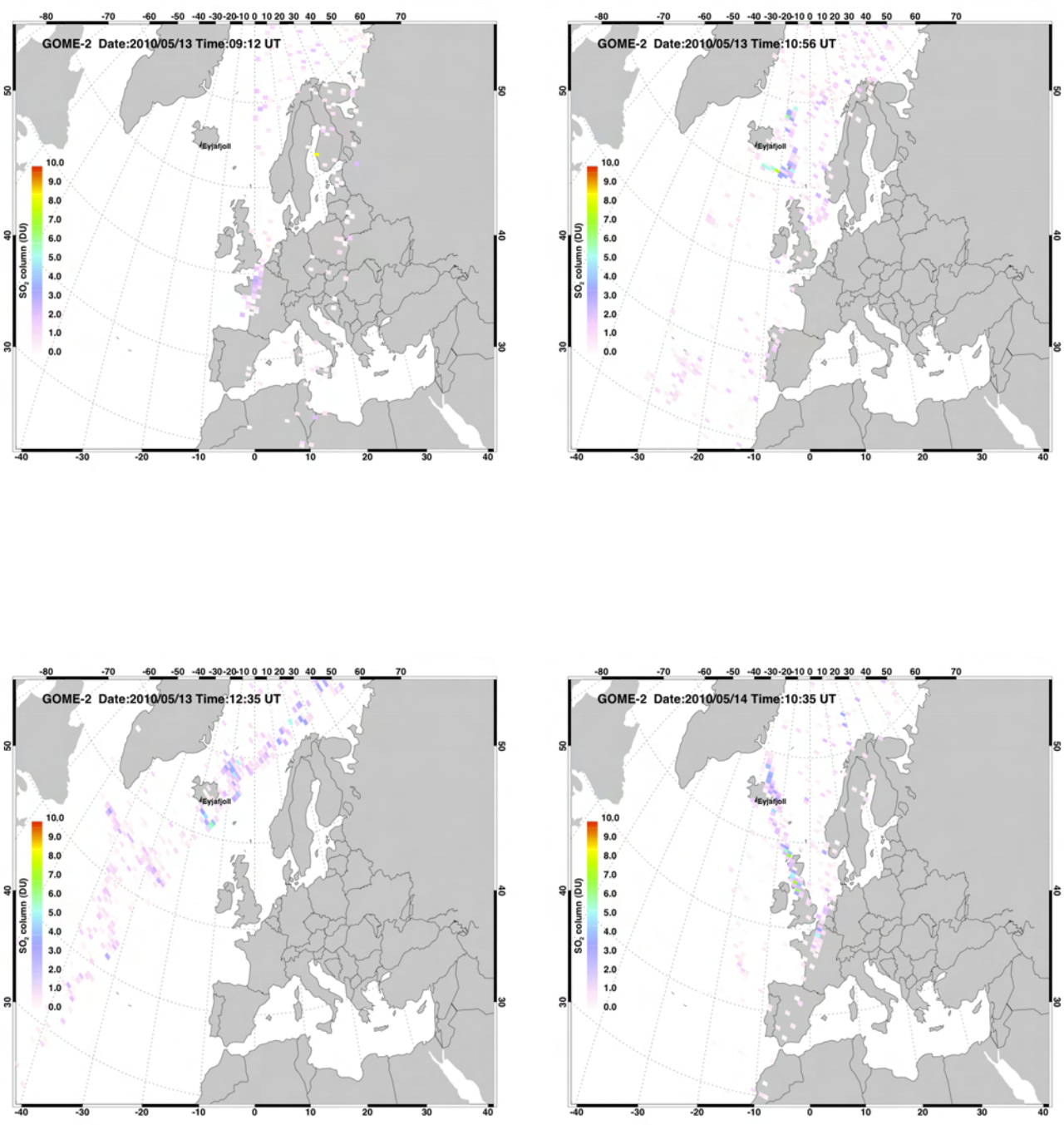

Figure 7.9: GOME-2 SO_2 partial column abundance in DU. Date and time of the orbit are shown at the top of each plot.

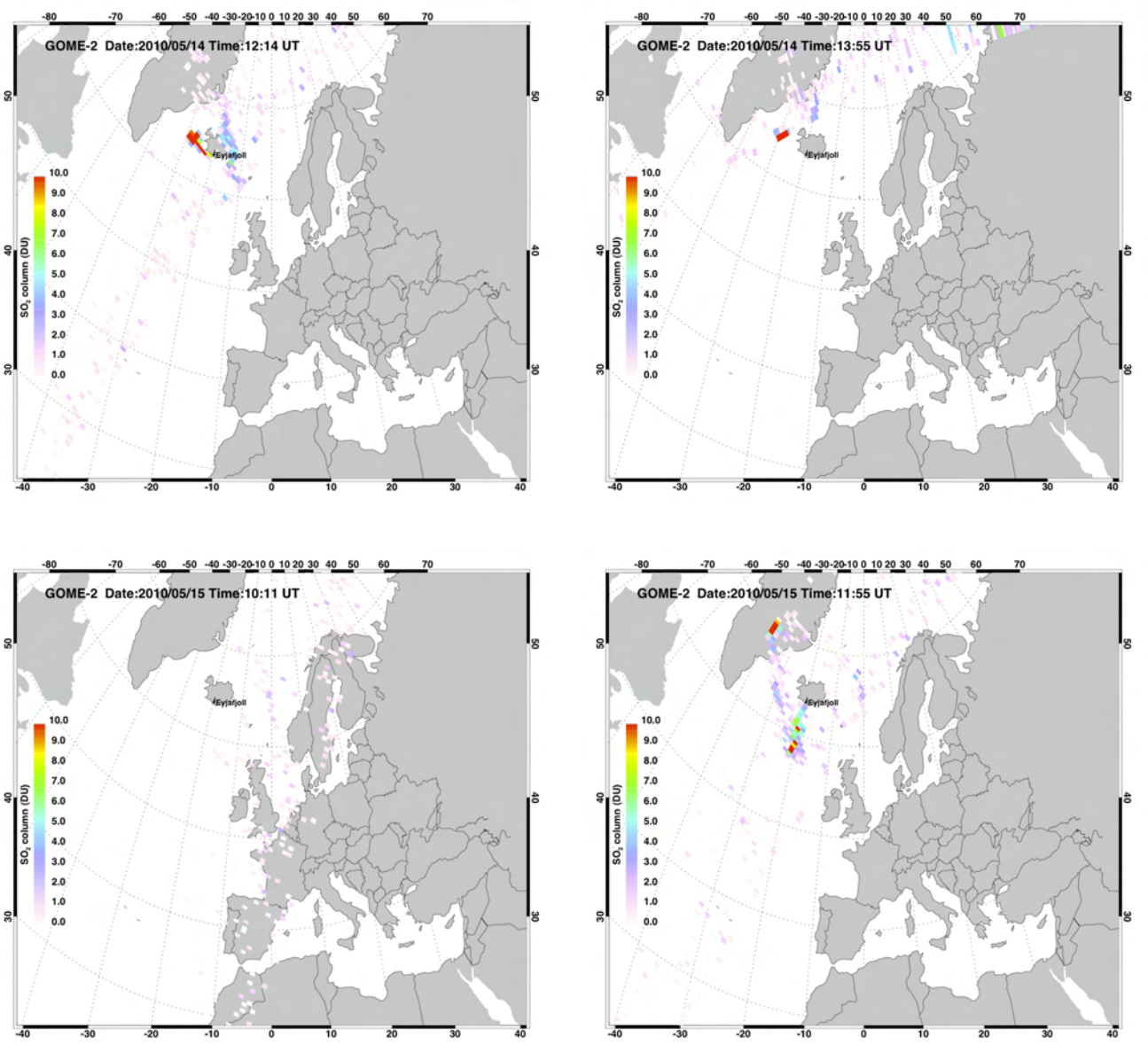

Figure 7.10: GOME-2 SO_2 partial column abundance in DU. Date and time of the orbit are shown at the top of each plot.

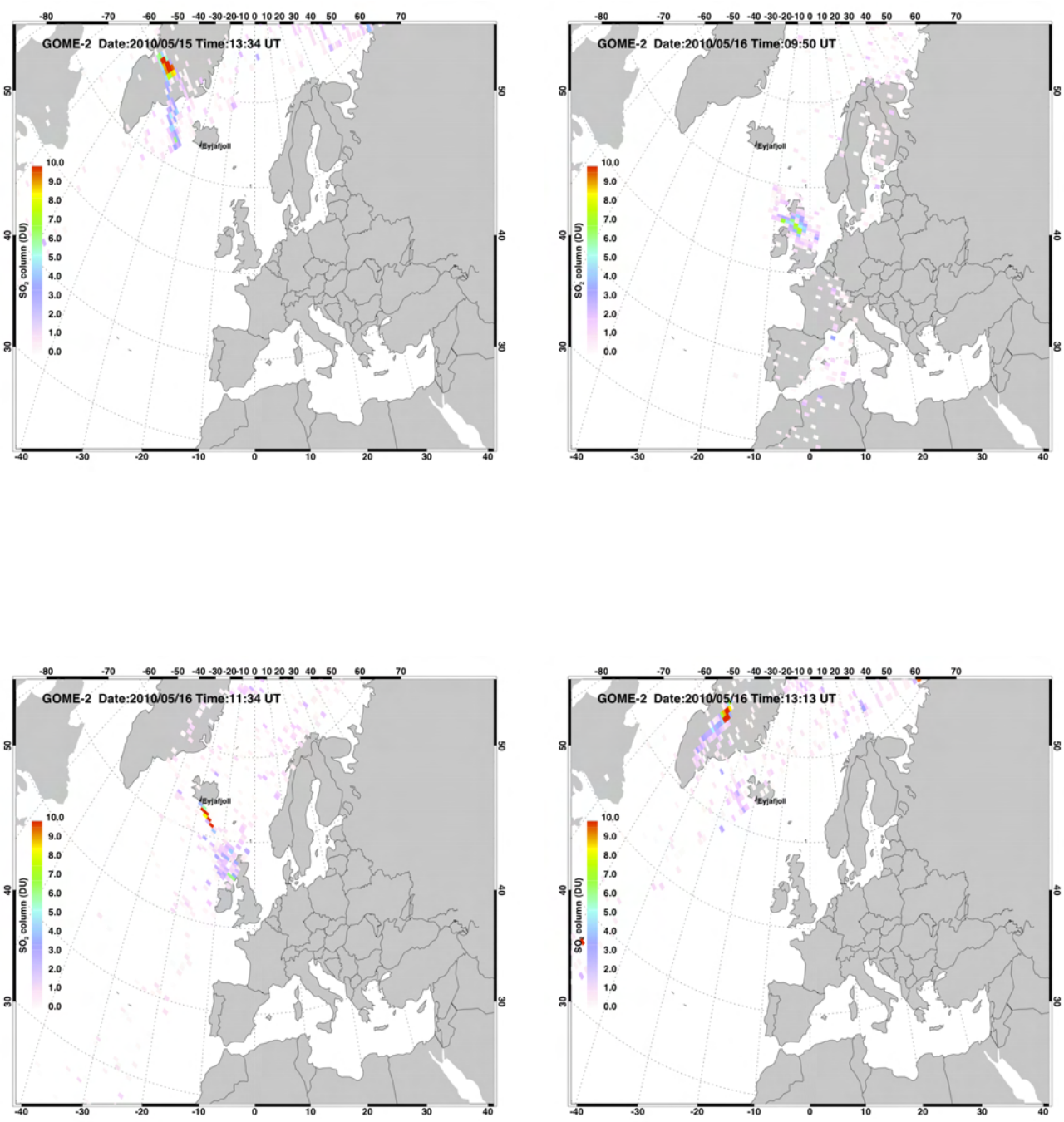

Figure 7.11: GOME-2 SO_2 partial column abundance in DU. Date and time of the orbit are shown at the top of each plot.

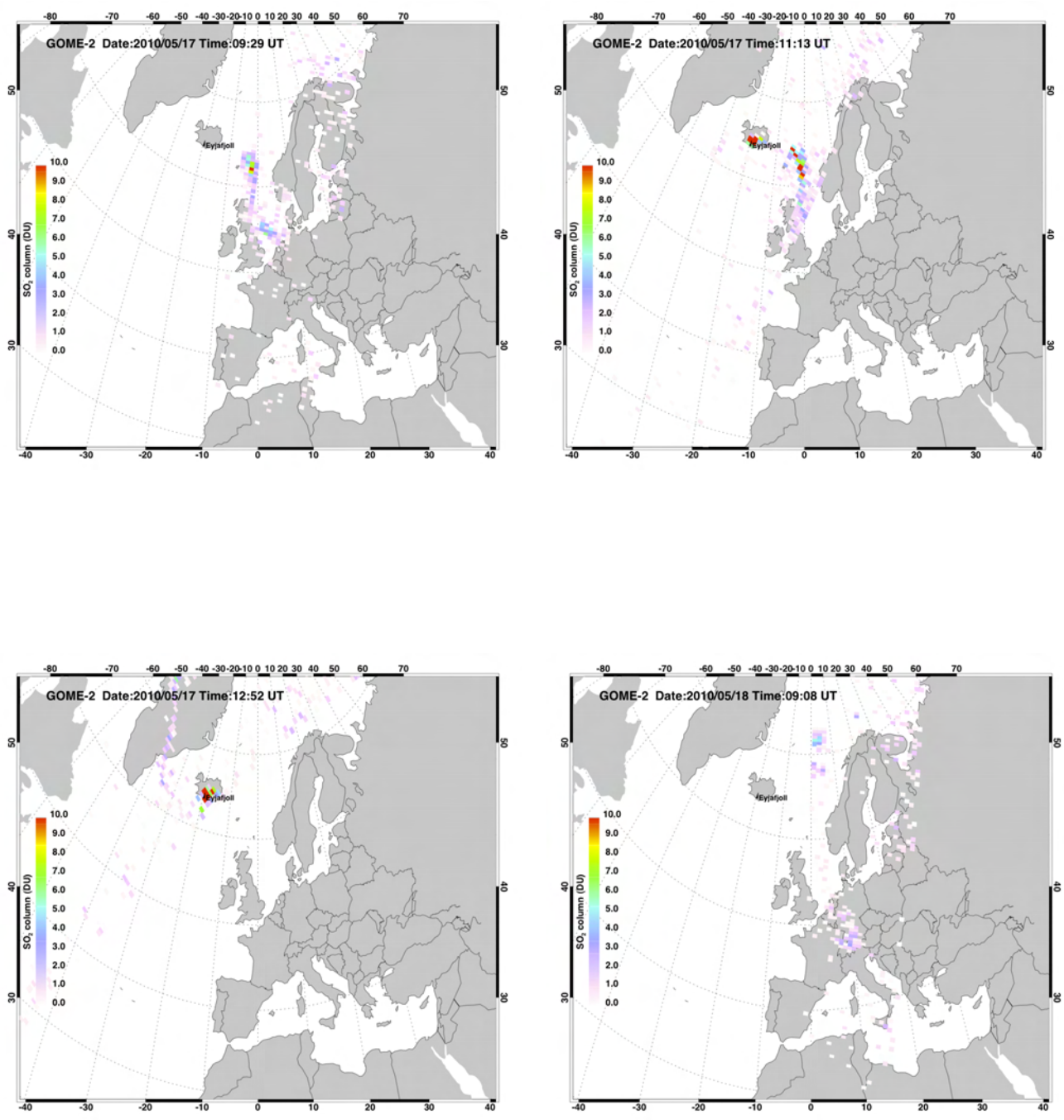

Figure 7.12: GOME-2 SO_2 partial column abundance in DU. Date and time of the orbit are shown at the top of each plot.

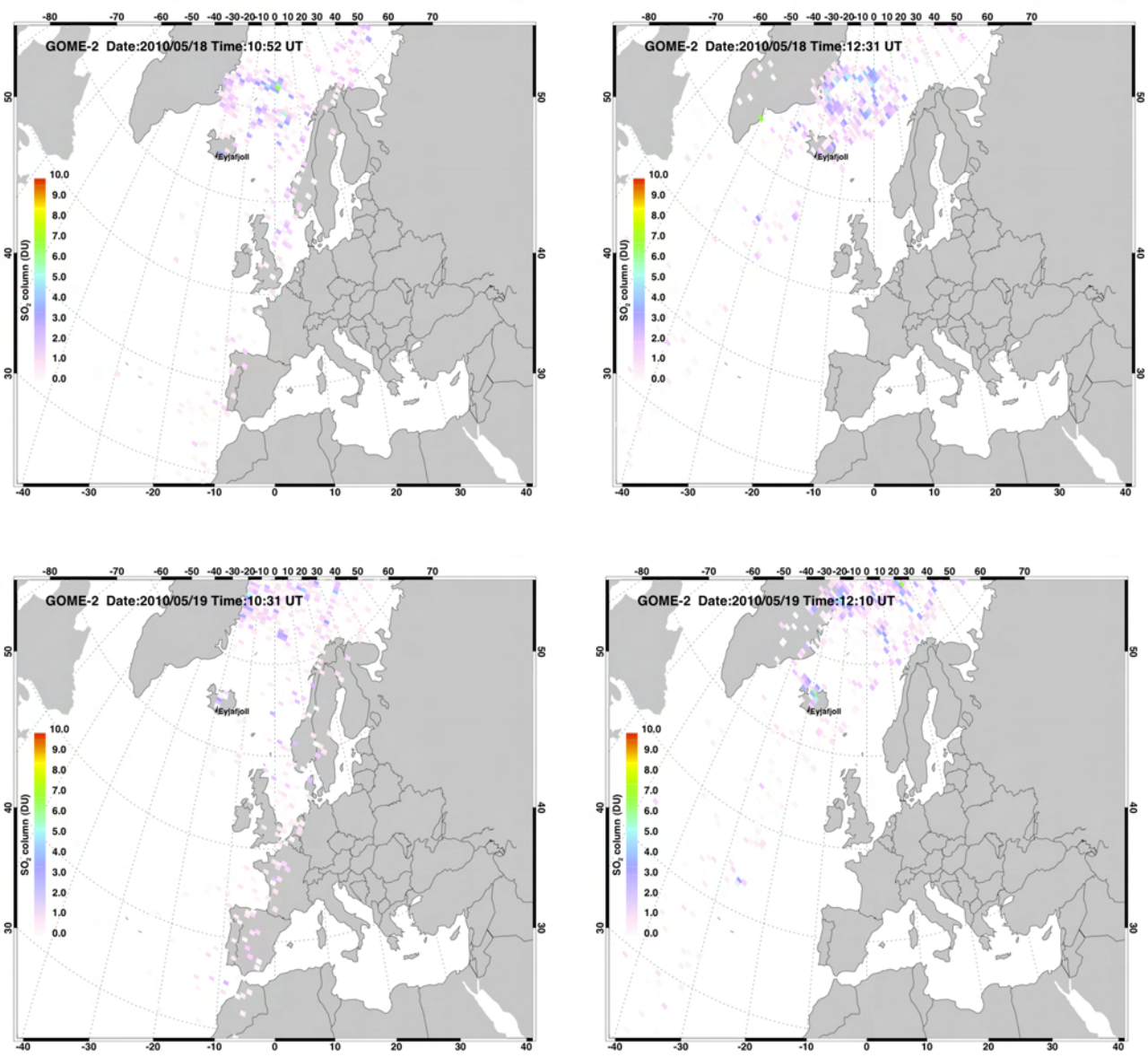

Figure 7.13: GOME-2 SO_2 partial column abundance in DU. Date and time of the orbit are shown at the top of each plot.

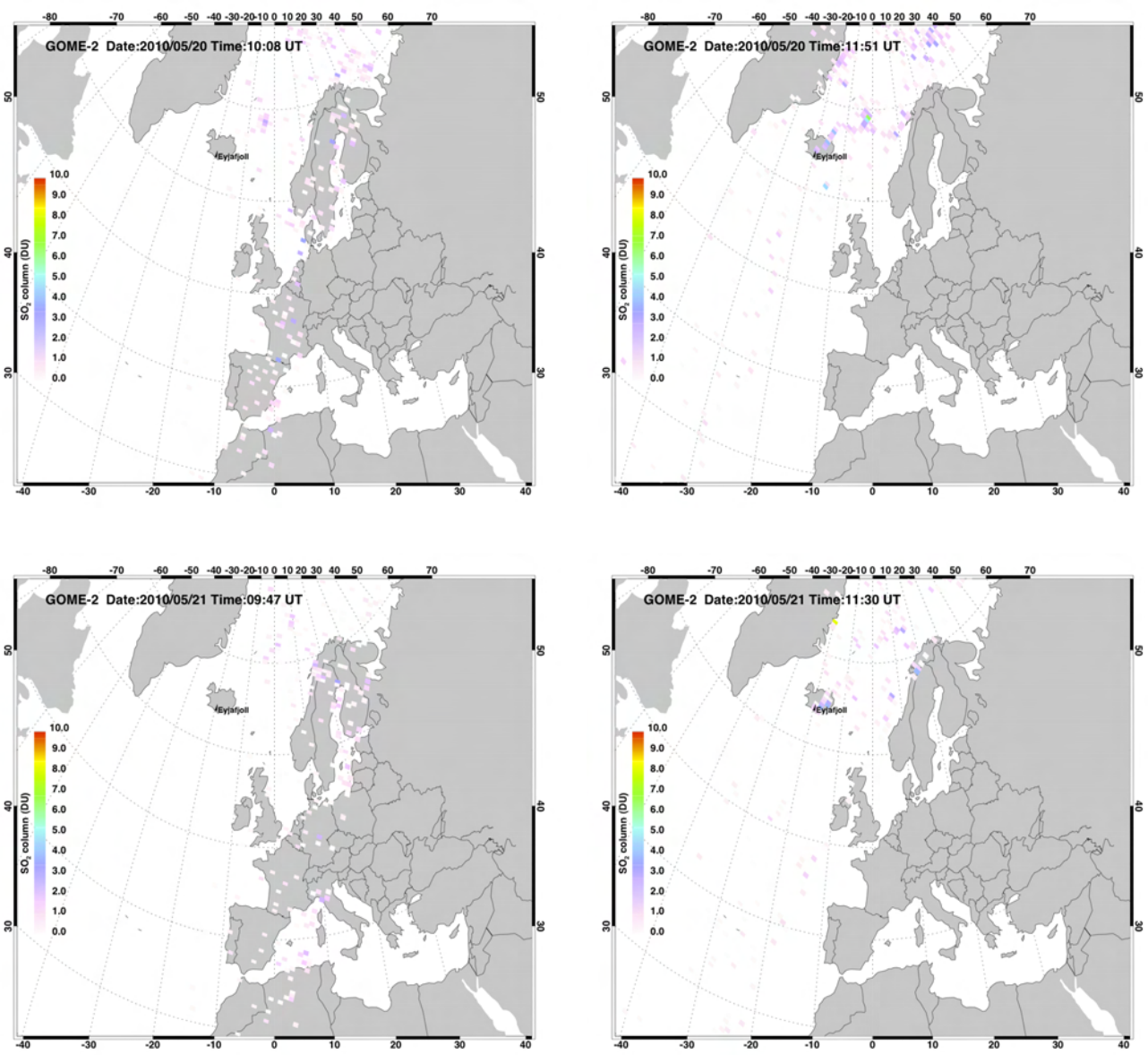

Figure 7.14: GOME-2 SO_2 partial column abundance in DU. Date and time of the orbit are shown at the top of each plot.

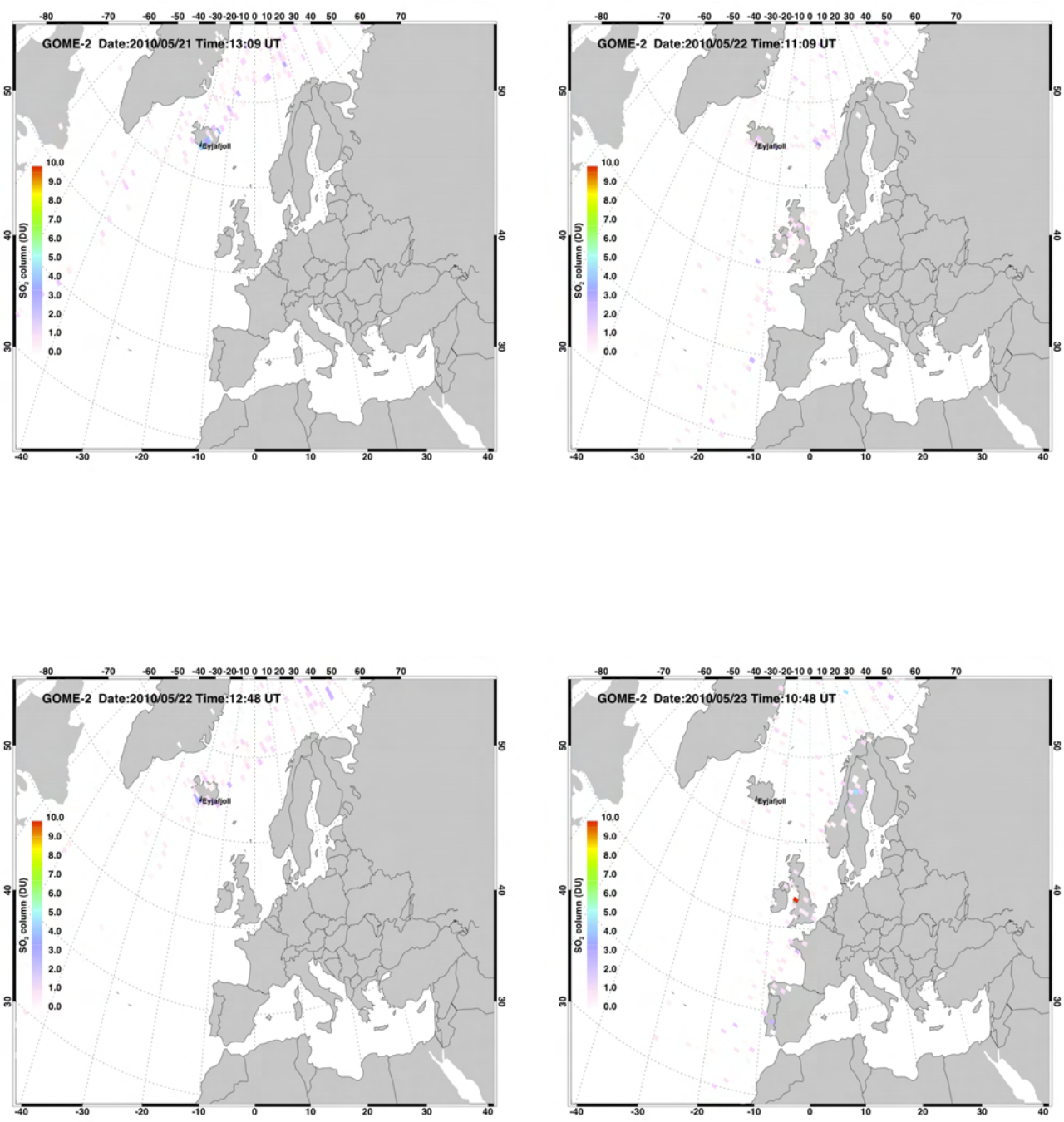

Figure 7.15: GOME-2 SO_2 partial column abundance in DU. Date and time of the orbit are shown at the top of each plot.

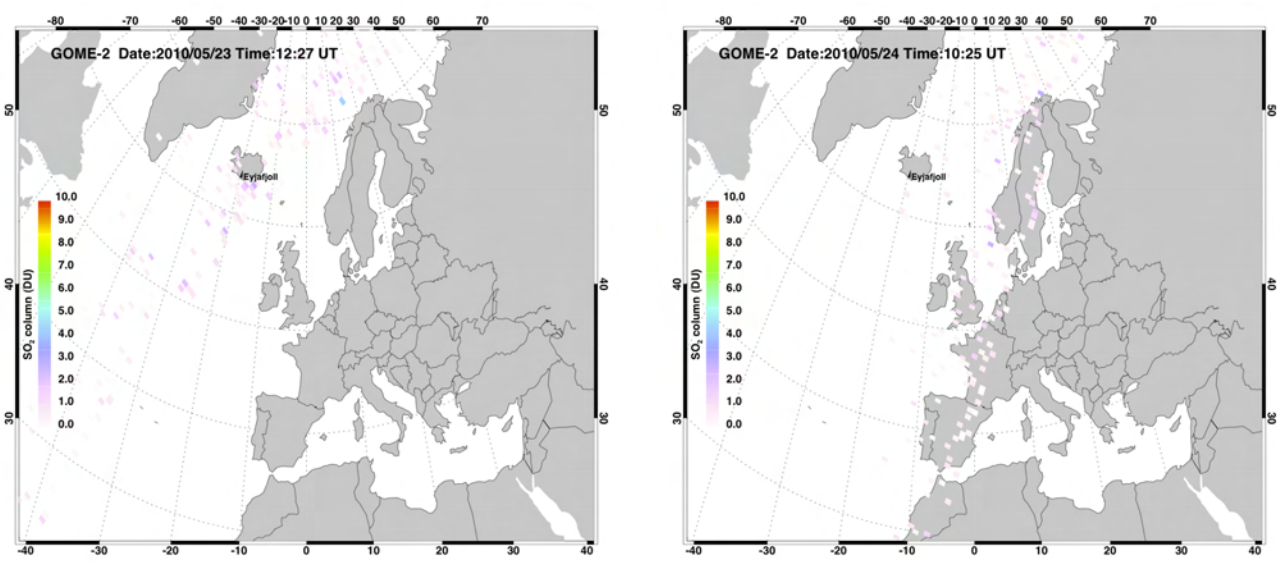

Figure 7.16: GOME-2 SO_2 partial column abundance in DU. Date and time of the orbit are shown at the top of each plot.

7.1.2 OMI

Table 7.2 lists the OMI data analysed in this study.

Filename
OMI-Aura L2-OMSO2 2010m0501t0920-o30816 v003-2010m0504t135059.he5
OMI-Aura L2-OMSO2 2010m0501t1059-o30817 v003-2010m0504t135103.he5
OMI-Aura L2-OMSO2 2010m0501t1238-o30818 v003-2010m0504t135100.he5
OMI-Aura L2-OMSO2 2010m0501t1417-o30819 v003-2010m0504t135259.he5
OMI-Aura L2-OMSO2 2010m0501t1555-o30820 v003-2010m0504t135345.he5
OMI-Aura L2-OMSO2 2010m0502t1003-o30831 v003-2010m0504t181448.he5
OMI-Aura L2-OMSO2 2010m0502t1142-o30832 v003-2010m0504t181446.he5
OMI-Aura L2-OMSO2 2010m0502t1321-o30833 v003-2010m0504t181442.he5
OMI-Aura L2-OMSO2 2010m0502t1500-o30834 v003-2010m0504t181447.he5
OMI-Aura L2-OMSO2 2010m0503t1047-o30846 v003-2010m0504t201613.he5
OMI-Aura L2-OMSO2 2010m0503t1225-o30847 v003-2010m0504t205250.he5
OMI-Aura L2-OMSO2 2010m0503t1404-o30848 v003-2010m0504t201731.he5
OMI-Aura L2-OMSO2 2010m0503t1543-o30849 v003-2010m0504t210207.he5
OMI-Aura L2-OMSO2 2010m0504t0951-o30860 v003-2010m0504t231549.he5
OMI-Aura L2-OMSO2 2010m0504t1130-o30861 v003-2010m0505t000840.he5
OMI-Aura L2-OMSO2 2010m0504t1309-o30862 v003-2010m0504t231502.he5
OMI-Aura L2-OMSO2 2010m0504t1448-o30863 v003-2010m0504t231549.he5
OMI-Aura L2-OMSO2 2010m0505t1034-o30875 v003-2010m0505t192627.he5
OMI-Aura L2-OMSO2 2010m0505t1352-o30877 v003-2010m0505t200817.he5
OMI-Aura L2-OMSO2 2010m0505t1531-o30878 v003-2010m0505t213310.he5
OMI-Aura L2-OMSO2 2010m0506t0939-o30889 v003-2010m0506t160113.he5
OMI-Aura L2-OMSO2 2010m0506t1118-o30890 v003-2010m0506t174313.he5
OMI-Aura L2-OMSO2 2010m0506t1257-o30891 v003-2010m0506t213709.he5
OMI-Aura L2-OMSO2 2010m0506t1436-o30892 v003-2010m0506t221913.he5
OMI-Aura L2-OMSO2 2010m0506t1614-o30893 v003-2010m0506t221911.he5
OMI-Aura L2-OMSO2 2010m0507t1022-o30904 v003-2010m0507t181343.he5
OMI-Aura L2-OMSO2 2010m0507t1201-o30905 v003-2010m0507t193455.he5
OMI-Aura L2-OMSO2 2010m0507t1340-o30906 v003-2010m0507t200059.he5
OMI-Aura L2-OMSO2 2010m0507t1519-o30907 v003-2010m0507t234723.he5
OMI-Aura L2-OMSO2 2010m0508t1106-o30919 v003-2010m0508t190954.he5
OMI-Aura L2-OMSO2 2010m0508t1244-o30920 v003-2010m0508t214137.he5
OMI-Aura L2-OMSO2 2010m0508t1423-o30921 v003-2010m0508t225319.he5
OMI-Aura L2-OMSO2 2010m0508t1602-o30922 v003-2010m0508t215241.he5
OMI-Aura L2-OMSO2 2010m0509t1010-o30933 v003-2010m0509t161933.he5
OMI-Aura L2-OMSO2 2010m0509t1149-o30934 v003-2010m0509t180328.he5
OMI-Aura L2-OMSO2 2010m0509t1328-o30935 v003-2010m0509t195457.he5
OMI-Aura L2-OMSO2 2010m0509t1507-o30936 v003-2010m0509t224725.he5
OMI-Aura L2-OMSO2 2010m0510t1053-o30948 v003-2010m0510t194512.he5
OMI-Aura L2-OMSO2 2010m0510t1232-o30949 v003-2010m0510t202543.he5
OMI-Aura L2-OMSO2 2010m0510t1411-o30950 v003-2010m0510t214726.he5

Table 7.2: OMI data files. The date field is ”2010m0521”=21 May 2010; the time field is ”t1532”=15:32 UT.

Filename
OMI-Aura L2-OMSO2 2010m0510t1550-o30951 v003-2010m0510t215648.he5
OMI-Aura L2-OMSO2 2010m0511t0958-o30962 v003-2010m0512t023851.he5
OMI-Aura L2-OMSO2 2010m0511t1137-o30963 v003-2010m0512t023851.he5
OMI-Aura L2-OMSO2 2010m0511t1316-o30964 v003-2010m0512t023939.he5
OMI-Aura L2-OMSO2 2010m0511t1454-o30965 v003-2010m0512t034743.he5
OMI-Aura L2-OMSO2 2010m0512t1041-o30977 v003-2010m0512t182951.he5
OMI-Aura L2-OMSO2 2010m0512t1220-o30978 v003-2010m0512t182904.he5
OMI-Aura L2-OMSO2 2010m0512t1359-o30979 v003-2010m0512t205240.he5
OMI-Aura L2-OMSO2 2010m0512t1538-o30980 v003-2010m0512t215408.he5
OMI-Aura L2-OMSO2 2010m0513t1124-o30992 v003-2010m0513t182046.he5
OMI-Aura L2-OMSO2 2010m0513t1303-o30993 v003-2010m0513t215400.he5
OMI-Aura L2-OMSO2 2010m0513t1442-o30994 v003-2010m0513t232729.he5
OMI-Aura L2-OMSO2 2010m0513t1621-o30995 v003-2010m0514t010932.he5
OMI-Aura L2-OMSO2 2010m0514t1029-o31006 v003-2010m0514t190324.he5
OMI-Aura L2-OMSO2 2010m0514t1208-o31007 v003-2010m0514t190326.he5
OMI-Aura L2-OMSO2 2010m0514t1347-o31008 v003-2010m0514t200325.he5
OMI-Aura L2-OMSO2 2010m0514t1525-o31009 v003-2010m0514t215730.he5
OMI-Aura L2-OMSO2 2010m0515t1112-o31021 v003-2010m0515t173415.he5
OMI-Aura L2-OMSO2 2010m0515t1251-o31022 v003-2010m0515t214255.he5
OMI-Aura L2-OMSO2 2010m0515t1430-o31023 v003-2010m0515t222354.he5
OMI-Aura L2-OMSO2 2010m0515t1609-o31024 v003-2010m0515t222440.he5
OMI-Aura L2-OMSO2 2010m0516t1017-o31035 v003-2010m0516t173147.he5
OMI-Aura L2-OMSO2 2010m0516t1155-o31036 v003-2010m0516t183248.he5
OMI-Aura L2-OMSO2 2010m0516t1334-o31037 v003-2010m0516t204405.he5
OMI-Aura L2-OMSO2 2010m0516t1513-o31038 v003-2010m0516t235640.he5
OMI-Aura L2-OMSO2 2010m0517t1100-o31050 v003-2010m0517t204601.he5
OMI-Aura L2-OMSO2 2010m0517t1239-o31051 v003-2010m0517t233225.he5
OMI-Aura L2-OMSO2 2010m0517t1418-o31052 v003-2010m0517t233324.he5
OMI-Aura L2-OMSO2 2010m0517t1557-o31053 v003-2010m0517t224426.he5
OMI-Aura L2-OMSO2 2010m0518t1004-o31064 v003-2010m0519t021747.he5
OMI-Aura L2-OMSO2 2010m0518t1143-o31065 v003-2010m0519t031707.he5
OMI-Aura L2-OMSO2 2010m0518t1322-o31066 v003-2010m0519t012219.he5
OMI-Aura L2-OMSO2 2010m0518t1501-o31067 v003-2010m0519t031728.he5
OMI-Aura L2-OMSO2 2010m0519t1048-o31079 v003-2010m0519t193716.he5
OMI-Aura L2-OMSO2 2010m0519t1227-o31080 v003-2010m0519t204222.he5
OMI-Aura L2-OMSO2 2010m0519t1405-o31081 v003-2010m0519t214409.he5
OMI-Aura L2-OMSO2 2010m0519t1544-o31082 v003-2010m0520t011119.he5
OMI-Aura L2-OMSO2 2010m0520t0952-o31093 v003-2010m0520t164104.he5
OMI-Aura L2-OMSO2 2010m0520t1131-o31094 v003-2010m0520t182414.he5
OMI-Aura L2-OMSO2 2010m0520t1310-o31095 v003-2010m0520t223210.he5
OMI-Aura L2-OMSO2 2010m0520t1449-o31096 v003-2010m0520t232234.he5
OMI-Aura L2-OMSO2 2010m0521t1035-o31108 v003-2010m0521t200814.he5
OMI-Aura L2-OMSO2 2010m0521t1214-o31109 v003-2010m0521t194218.he5
OMI-Aura L2-OMSO2 2010m0521t1353-o31110 v003-2010m0521t220452.he5
OMI-Aura L2-OMSO2 2010m0521t1532-o31111 v003-2010m0521t220403.he5

Table 7.2 continued.

7.1.3 AIRS

AIRS granules are listed in Table 7.3. The AIRS retrieval code is available at `http://web.me.com/fredprata/FredPrata/AIRS_SO2.html`.

Date	2010.04.14	Date	2010.04.15
Start time	03:05	Start time	13:29
End time	03:11	End time	13:35
AIRS Granule	031	AIRS Granule	135
Max SO_2 (DU)	8.21	Max SO_2 (DU)	11.76
Mass (Tg)	0.002	Mass (Tg)	0.005
Area (km^2)	29406	Area (km^2)	49129
Number of retrievals:	140	Number of retrievals:	222
Date	2010.04.16	Date	2010.04.16
Start time	01:17	Start time	02:53
End time	01:23	End time	02:59
AIRS Granule	013	AIRS Granule	029
Max SO_2 (DU)	12.02	Max SO_2 (DU)	11.05
Mass (Tg)	0.004	Mass (Tg)	0.004
Area (km^2)	38227	Area (km^2)	44719
Number of retrievals:	164	Number of retrievals:	209
Date	2010.04.17	Date	2010.04.24
Start time	13:17	Start time	03:41
End time	13:23	End time	03:47
AIRS Granule	133	AIRS Granule	037
Max SO_2 (DU)	9.95	Max SO_2 (DU)	20.20
Mass (Tg)	0.004	Mass (Tg)	0.004
Area (km^2)	51898	Area (km^2)	39884
Number of retrievals:	250	Number of retrievals:	186
Date	2010.04.24	Date	2010.05.04
Start time	13:23	Start time	02:41
End time	13:29	End time	02:47
AIRS Granule	134	AIRS Granule	027
Max SO_2 (DU)	12.78	Max SO_2 (DU)	10.64
Mass (Tg)	0.005	Mass (Tg)	0.000
Area (km^2)	51886	Area (km^2)	24533
Number of retrievals:	235	Number of retrievals:	111

Table 7.3: AIRS granule statistics for the 7.3 μm SO_2 retrievals.

Date	2010.05.05	Date	2010.05.06
Start time	13:05	Start time	02:29
End time	13:11	End time	02:35
AIRS Granule	131	AIRS Granule	025
Max SO_2 (DU)	16.63	Max SO_2 (DU)	16.54
Mass (Tg)	0.005	Mass (Tg)	0.001
Area (km^2)	49083	Area (km^2)	5290
Number of retrievals:	214	Number of retrievals:	9
Date	2010.05.06	Date	2010.05.06
Start time	02:35	Start time	04:05
End time	02:41	End time	04:11
AIRS Granule	026	AIRS Granule	041
Max SO_2 (DU)	18.76	Max SO_2 (DU)	25.45
Mass (Tg)	0.001	Mass (Tg)	0.004
Area (km^2)	4476	Area (km^2)	35769
Number of retrievals:	27	Number of retrievals:	177
Date	2010.05.06	Date	2010.05.06
Start time	04:11	Start time	12:11
End time	04:17	End time	12:17
AIRS Granule	042	AIRS Granule	122
Max SO_2 (DU)	17.80	Max SO_2 (DU)	28.58
Mass (Tg)	0.006	Mass (Tg)	0.005
Area (km^2)	52404	Area (km^2)	15256
Number of retrievals:	201	Number of retrievals:	23
Date	2010.05.06	Date	2010.05.06
Start time	13:41	Start time	13:47
End time	13:47	End time	13:53
AIRS Granule	137	AIRS Granule	138
Max SO_2 (DU)	25.04	Max SO_2 (DU)	62.58
Mass (Tg)	0.010	Mass (Tg)	0.021
Area (km^2)	79476	Area (km^2)	114409
Number of retrievals:	398	Number of retrievals:	577
Date	2010.05.07	Date	2010.05.07
Start time	03:11	Start time	03:17
End time	03:17	End time	03:23
AIRS Granule	032	AIRS Granule	033
Max SO_2 (DU)	21.30	Max SO_2 (DU)	26.61
Mass (Tg)	0.003	Mass (Tg)	0.018
Area (km^2)	30974	Area (km^2)	138919
Number of retrievals:	147	Number of retrievals:	748

AIRS granule statistics for the 7.3 μm SO_2 retrievals, continued.

Date	2010.05.07	Date	2010.05.07
Start time	04:53	Start time	12:53
End time	04:59	End time	12:59
AIRS Granule	049	AIRS Granule	129
Max SO_2 (DU)	7.99	Max SO_2 (DU)	10.06
Mass (Tg)	0.000	Mass (Tg)	0.000
Area (km^2)	2811	Area (km^2)	1540
Number of retrievals:	5	Number of retrievals:	5
Date	2010.05.07	Date	2010.05.07
Start time	14:23	Start time	14:29
End time	14:29	End time	14:35
AIRS Granule	144	AIRS Granule	145
Max SO_2 (DU)	18.58	Max SO_2 (DU)	29.77
Mass (Tg)	0.004	Mass (Tg)	0.020
Area (km^2)	22172	Area (km^2)	136031
Number of retrievals:	117	Number of retrievals:	733
Date	2010.05.08	Date	2010.05.08
Start time	03:59	Start time	13:29
End time	04:05	End time	13:35
AIRS Granule	040	AIRS Granule	135
Max SO_2 (DU)	31.43	Max SO_2 (DU)	23.42
Mass (Tg)	0.024	Mass (Tg)	0.012
Area (km^2)	176620	Area (km^2)	99869
Number of retrievals:	893	Number of retrievals:	444
Date	2010.05.08	Date	2010.05.09
Start time	13:35	Start time	02:59
End time	13:41	End time	03:05
AIRS Granule	136	AIRS Granule	030
Max SO_2 (DU)	50.29	Max SO_2 (DU)	11.87
Mass (Tg)	0.015	Mass (Tg)	0.005
Area (km^2)	101232	Area (km^2)	49173
Number of retrievals:	423	Number of retrievals:	256
Date	2010.05.09	Date	2010.05.10
Start time	03:05	Start time	03:41
End time	03:11	End time	03:47
AIRS Granule	031	AIRS Granule	037
Max SO_2 (DU)	24.90	Max SO_2 (DU)	16.12
Mass (Tg)	0.010	Mass (Tg)	0.003
Area (km^2)	65990	Area (km^2)	31046
Number of retrievals:	284	Number of retrievals:	139

AIRS granule statistics for the 7.3 μm SO_2 retrievals, continued.

Date	2010.05.10	Date	2010.05.10
Start time	03:47	Start time	13:23
End time	03:53	End time	13:29
AIRS Granule	038	AIRS Granule	134
Max SO_2 (DU)	13.26	Max SO_2 (DU)	15.16
Mass (Tg)	0.011	Mass (Tg)	0.004
Area (km^2)	120890	Area (km^2)	32834
Number of retrievals:	582	Number of retrievals:	147
Date	2010.05.11	Date	2010.05.11
Start time	02:47	Start time	04:29
End time	02:53	End time	04:35
AIRS Granule	028	AIRS Granule	045
Max SO_2 (DU)	23.21	Max SO_2 (DU)	13.10
Mass (Tg)	0.004	Mass (Tg)	0.004
Area (km^2)	43897	Area (km^2)	55834
Number of retrievals:	205	Number of retrievals:	258
Date	2010.05.11	Date	2010.05.13
Start time	14:05	Start time	04:11
End time	14:11	End time	04:17
AIRS Granule	141	AIRS Granule	042
Max SO_2 (DU)	17.17	Max SO_2 (DU)	26.70
Mass (Tg)	0.005	Mass (Tg)	0.008
Area (km^2)	47948	Area (km^2)	64433
Number of retrievals:	222	Number of retrievals:	197
Date	2010.05.13	Date	2010.05.16
Start time	13:53	Start time	04:47
End time	13:59	End time	04:53
AIRS Granule	139	AIRS Granule	048
Max SO_2 (DU)	26.93	Max SO_2 (DU)	19.59
Mass (Tg)	0.008	Mass (Tg)	0.012
Area (km^2)	72248	Area (km^2)	110749
Number of retrievals:	275	Number of retrievals:	416
Date	2010.05.16	Date	2010.05.17
Start time	14:23	Start time	02:11
End time	14:29	End time	02:17
AIRS Granule	144	AIRS Granule	022
Max SO_2 (DU)	29.15	Max SO_2 (DU)	19.39
Mass (Tg)	0.010	Mass (Tg)	0.017
Area (km^2)	75274	Area (km^2)	123209
Number of retrievals:	303	Number of retrievals:	528
Date	2010.05.17		
Start time	03:47		
End time	03:53		
AIRS Granule	038		
Max SO_2 (DU)	24.03		
Mass (Tg)	0.014		
Area (km^2)	104732		
Number of retrievals:	397		

AIRS granule statistics for the 7.3 μm SO_2 retrievals, continued.

Because the AIRS orbit data often do not cover the whole geographic region, it is preferable to plot the data at daily intervals. This has been done for all AIRS orbits from 4–19 May, 2010, when upper-troposphere SO_2 was observed to be greatest.

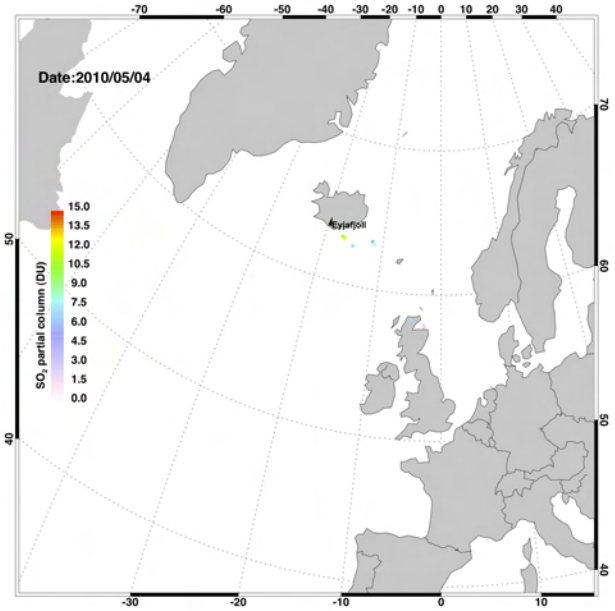

Figure 7.17: AIRS SO_2 partial column abundance in DU. Date is shown at the top of each plot.

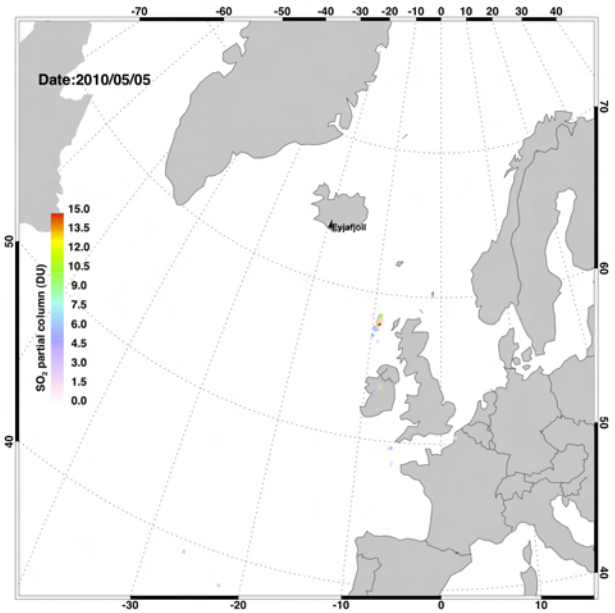

Figure 7.18: AIRS SO_2 partial column abundance in DU. Date is shown at the top of each plot.

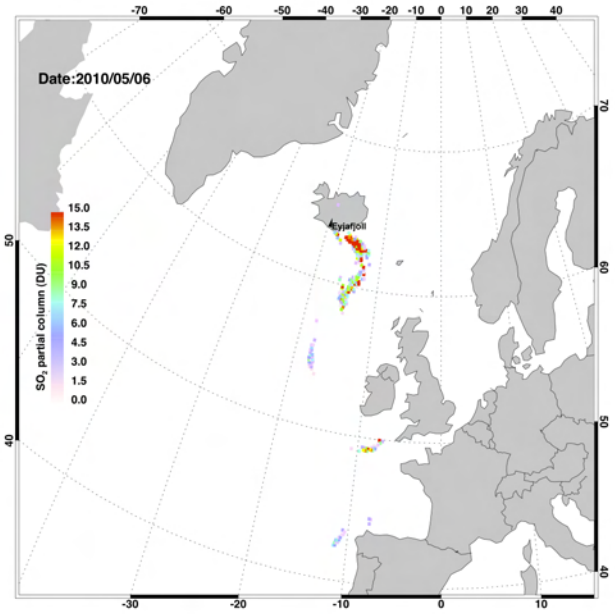

Figure 7.19: AIRS SO_2 partial column abundance in DU. Date is shown at the top of each plot.

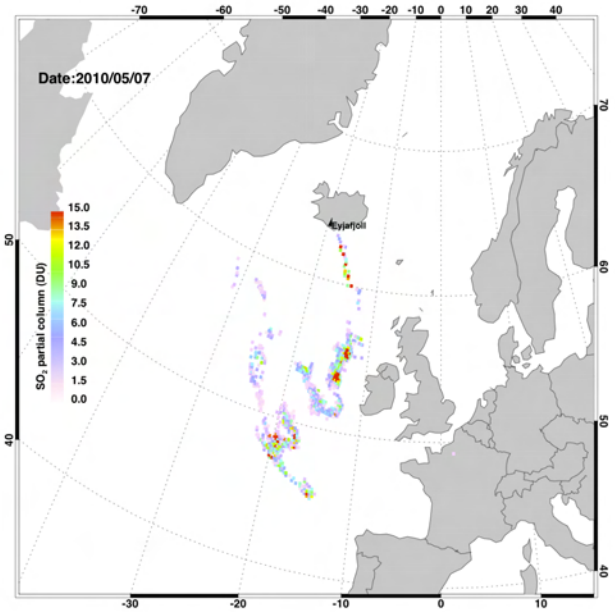

Figure 7.20: AIRS SO_2 partial column abundance in DU. Date is shown at the top of each plot.

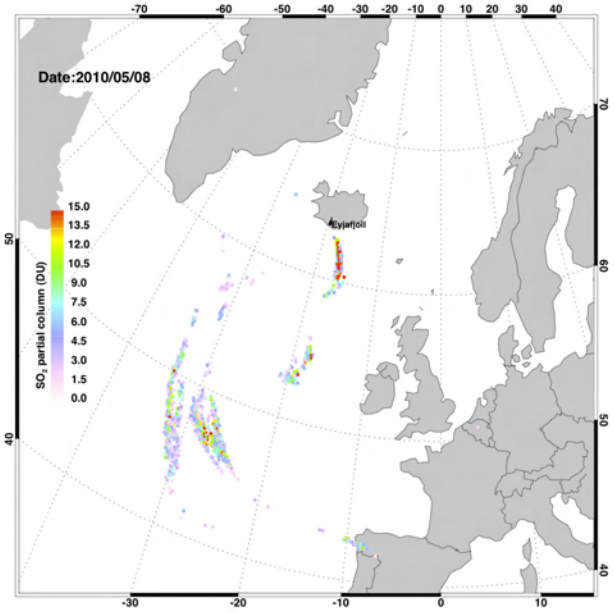

Figure 7.21: AIRS SO_2 partial column abundance in DU. Date is shown at the top of each plot.

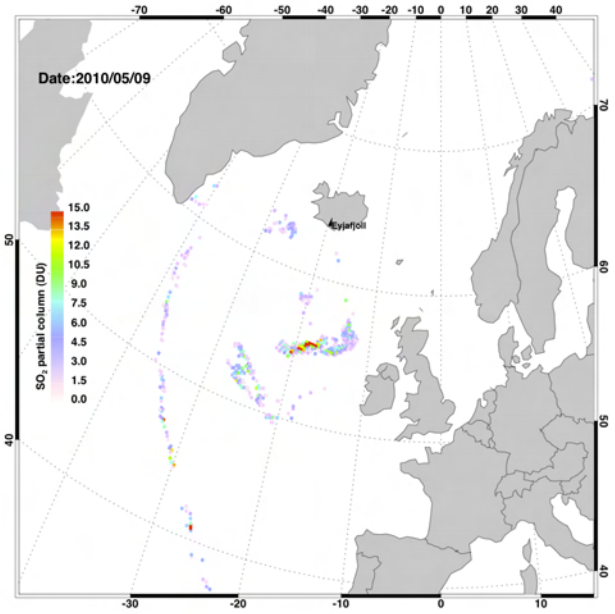

Figure 7.22: AIRS SO_2 partial column abundance in DU. Date is shown at the top of each plot.

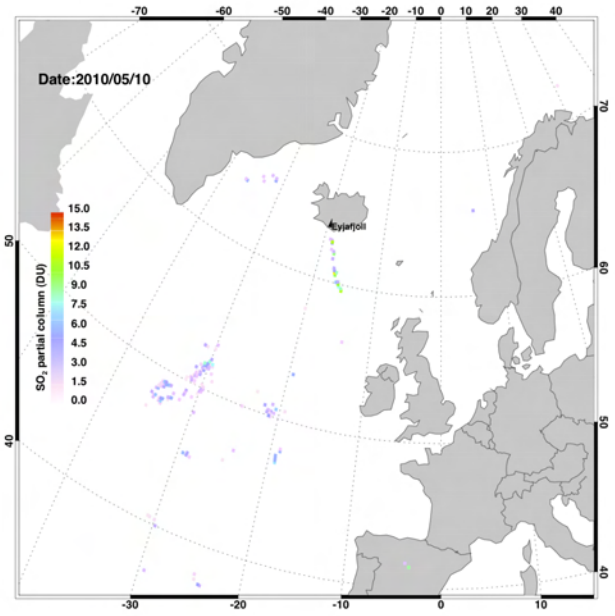

Figure 7.23: AIRS SO_2 partial column abundance in DU. Date is shown at the top of each plot.

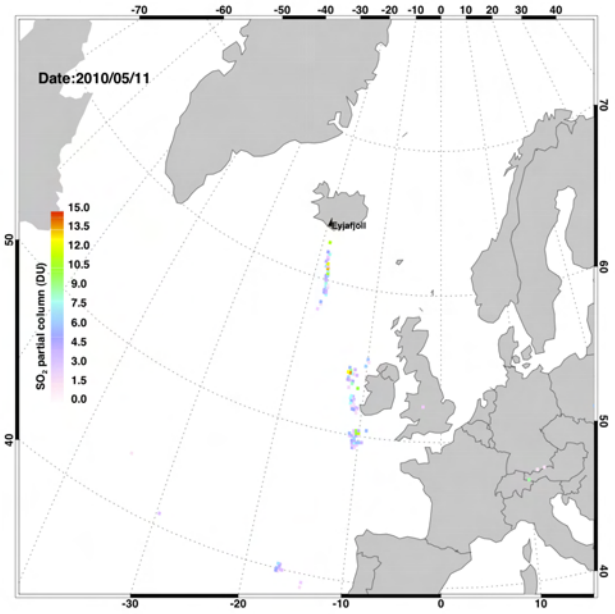

Figure 7.24: AIRS SO_2 partial column abundance in DU. Date is shown at the top of each plot.

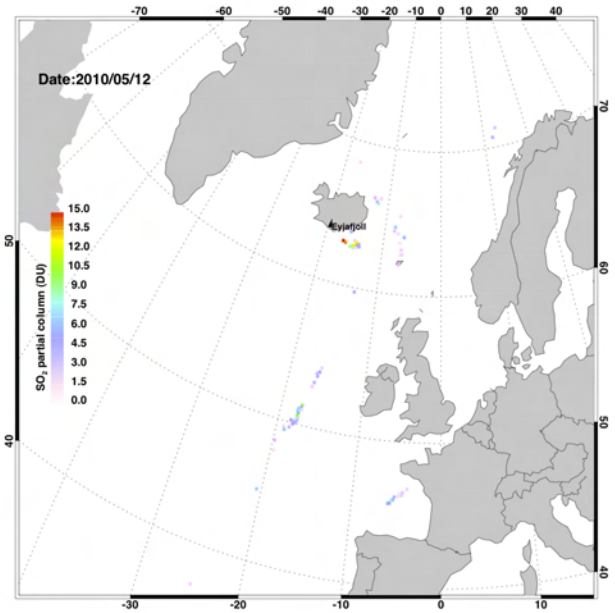

Figure 7.25: AIRS SO_2 partial column abundance in DU. Date is shown at the top of each plot.

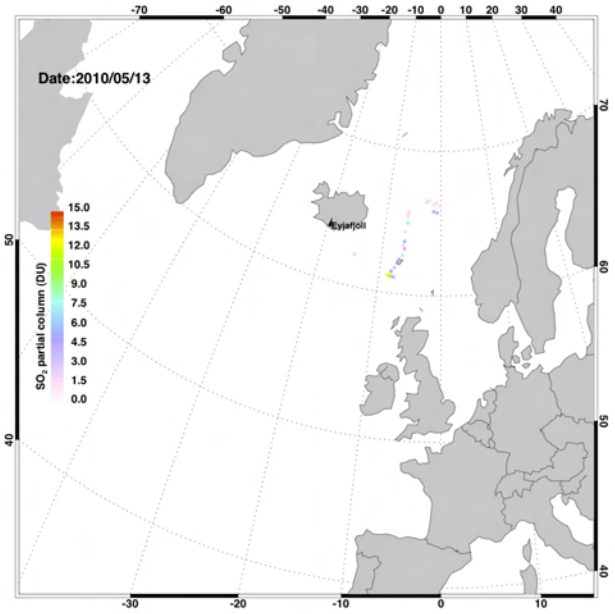

Figure 7.26: AIRS SO_2 partial column abundance in DU. Date is shown at the top of each plot.

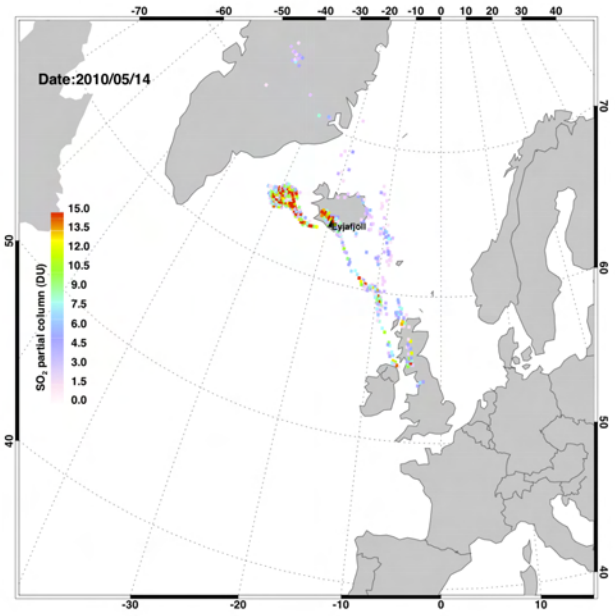

Figure 7.27: AIRS SO_2 partial column abundance in DU. Date is shown at the top of each plot.

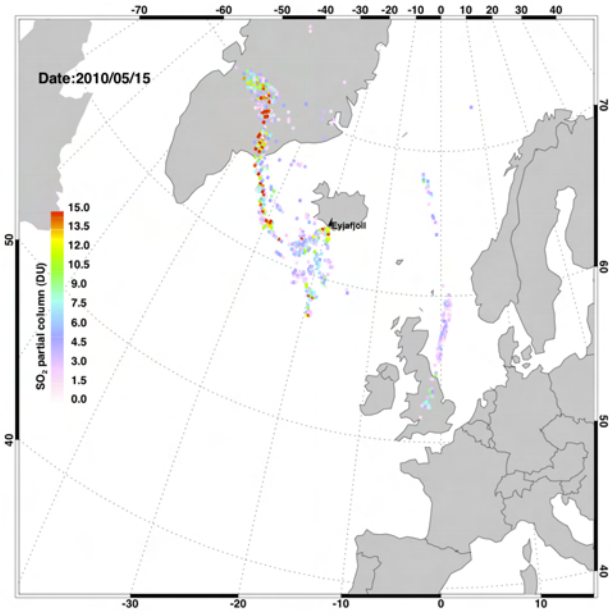

Figure 7.28: AIRS SO_2 partial column abundance in DU. Date is shown at the top of each plot.

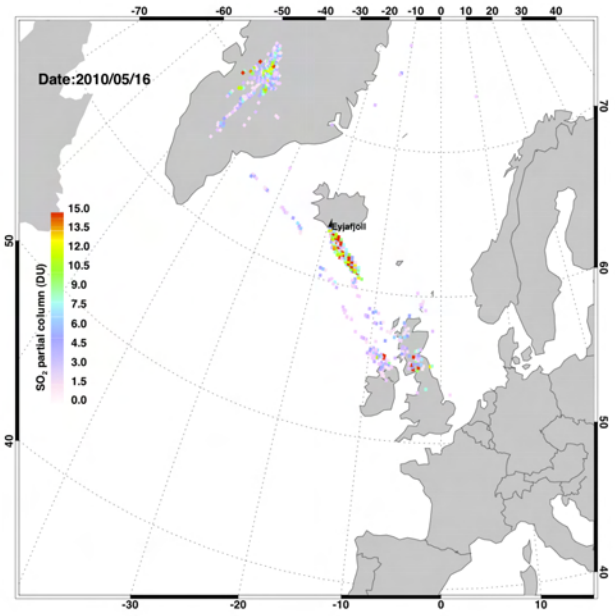

Figure 7.29: AIRS SO_2 partial column abundance in DU. Date is shown at the top of each plot.

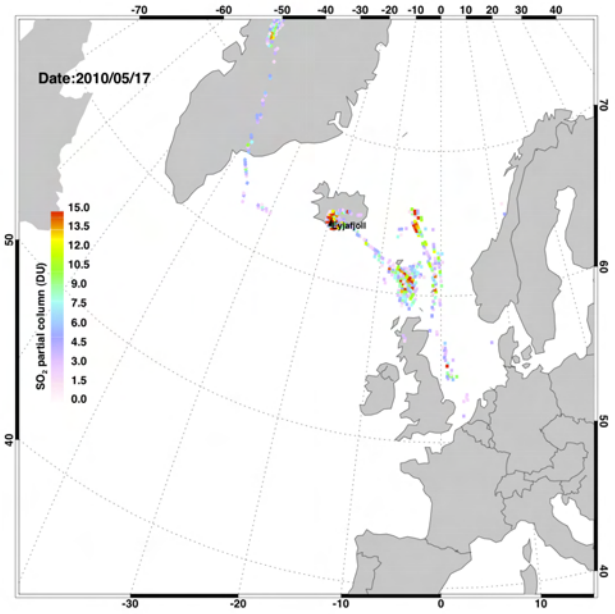

Figure 7.30: AIRS SO_2 partial column abundance in DU. Date is shown at the top of each plot.

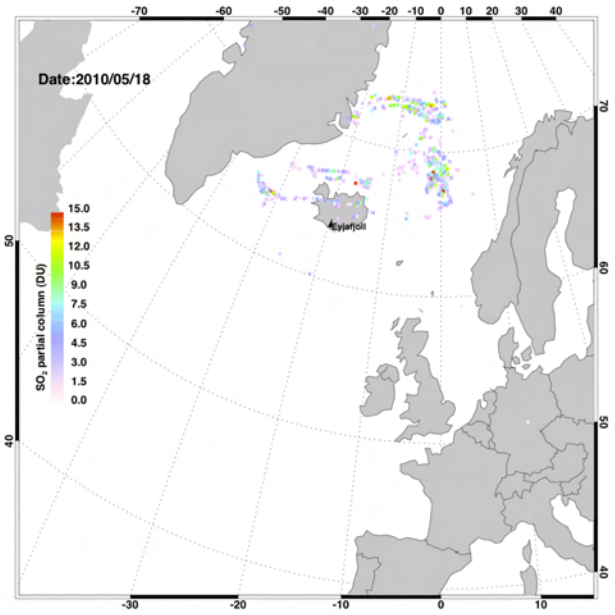

Figure 7.31: AIRS SO_2 partial column abundance in DU. Date is shown at the top of each plot.

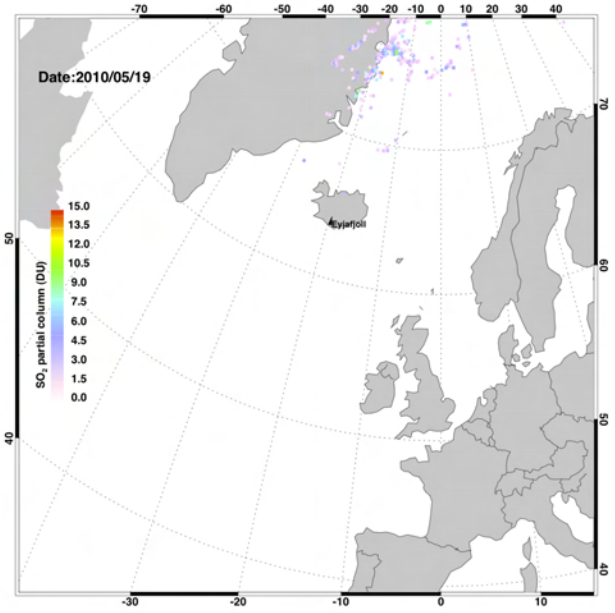

Figure 7.32: AIRS SO_2 partial column abundance in DU. Date is shown at the top of each plot.

7.1.4 IASI

IASI SO_2 and ash detections were supplied by L. Clarisse (Universite Libre de Bruxelles). These retrievals are preliminary and made using a fast calculation and are not expected to be very accurate. IASI provides

two overpasses per day at approximately 09:30UT and 21:30UT. An example of the IASI retrievals is shown in Figure 8.1.

7.2 Special cases

During April 2010, the SO_2 emissions from Eyjafjallajökull were low. After 2 May SO_2 emissions increased and there were many occasions where SO_2 and ash emissions were collocated, as well as times when they separated. We choose four occasions when AIRS, OMI and GOME-2 detected SO_2, while SEVIRI detected ash. Since AIRS detected SO_2, it suggests the SO_2 column abundance was large and in the upper troposphere. Thus we utilise the 7.3 μm scheme with SEVIRI channels 6.2, 7.3 and 12 μm channels. PLots for the fours cases are shown below; the IASI SO_2 and ash for the AM and PM overpasses are show in Figures 7.1–7.4.

In all cases it is possible to retrieve SO_2 from SEVIRI using the 7.3 μm scheme (see Chapter 5, Section 5.4), but a quantitative comparison shows poor quality. It is believed this is partly due opacity effects: for thick SO_2 clouds emission dominates over absorption and the assumptions used in the 7.3 μm scheme are violated, whereas for thin SO_2 clouds the inherent noise and loss in thermal contrast results in poor signal-to-noise. Nevertheless, it seems possible that SEVIRI data can be used to *fill-in* times when OMI/GOME-2/AIRS/IASI are not available. A method that links in an objective chemical forecasting and analysis scheme with these satellite retrievals is worthwhile pursuing.

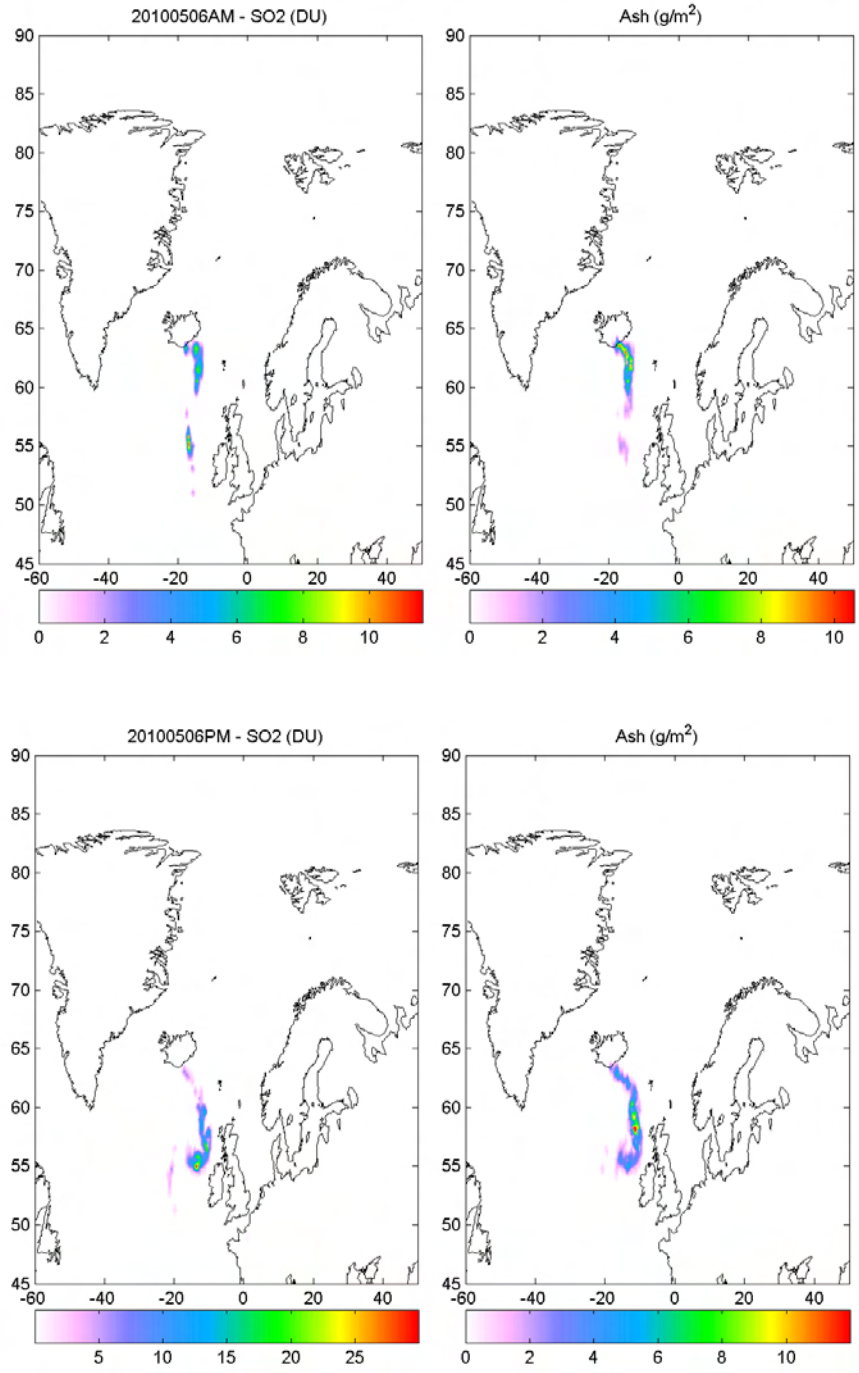

Figure 7.33: IASI SO_2 (left) and ash (right) retrievals for the morning overpass (top) and afternoon pass (bottom) on 6 May, 2010. Units are DU and gm^{-2}, respectively.

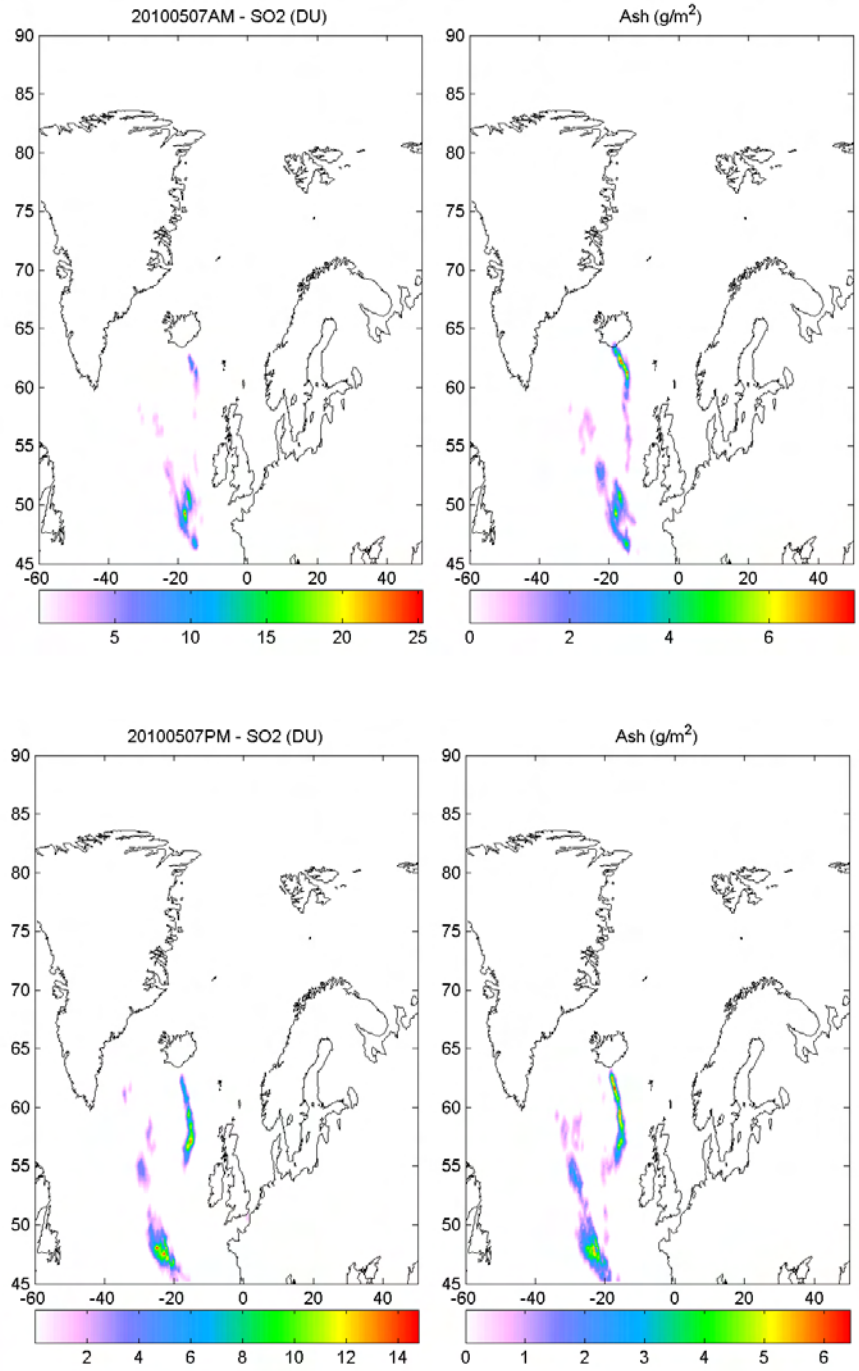

Figure 7.34: IASI SO_2 (left) and ash (right) retrievals for the morning overpass (top) and afternoon pass (bottom) on 7 May, 2010. Units are DU and gm^{-2}, respectively.

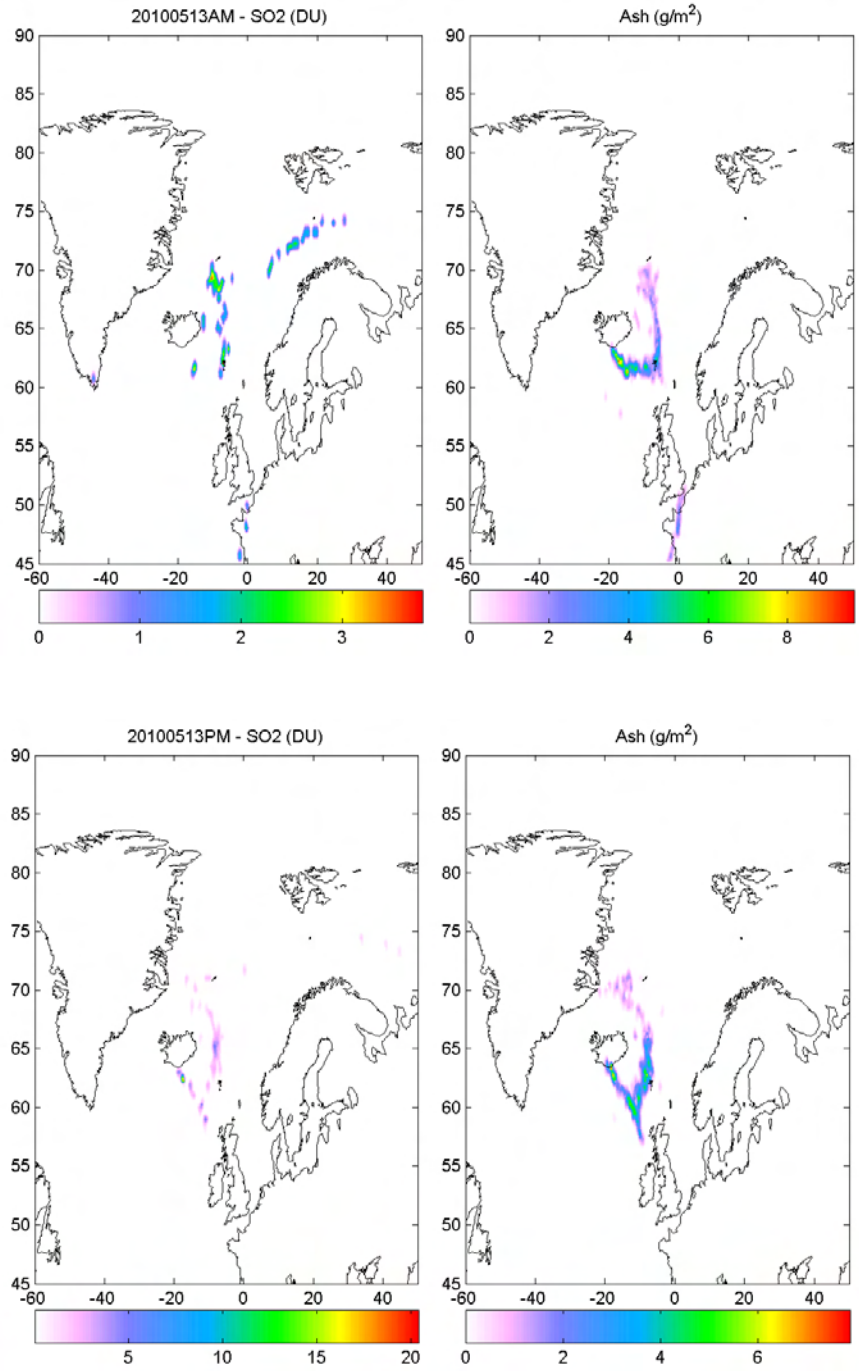

Figure 7.35: IASI SO_2 (left) and ash (right) retrievals for the morning overpass (top) and afternoon pass (bottom) on 13 May, 2010. Units are DU and gm^{-2}, respectively.

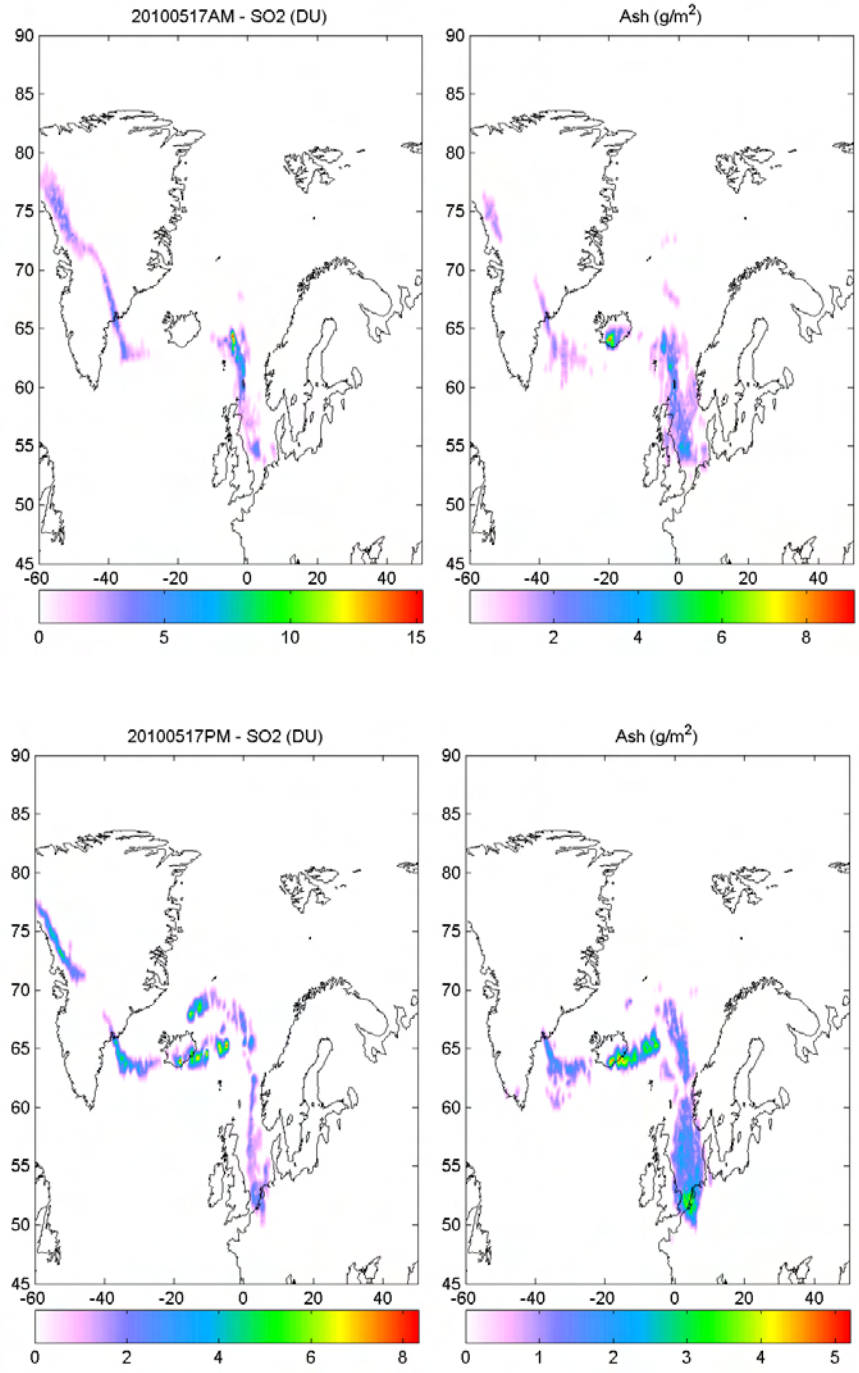

Figure 7.36: IASI SO_2 (left) and ash (right) retrievals for the morning overpass (top) and afternoon pass (bottom) on 17 May, 2010. Units are DU and gm^{-2}, respectively.

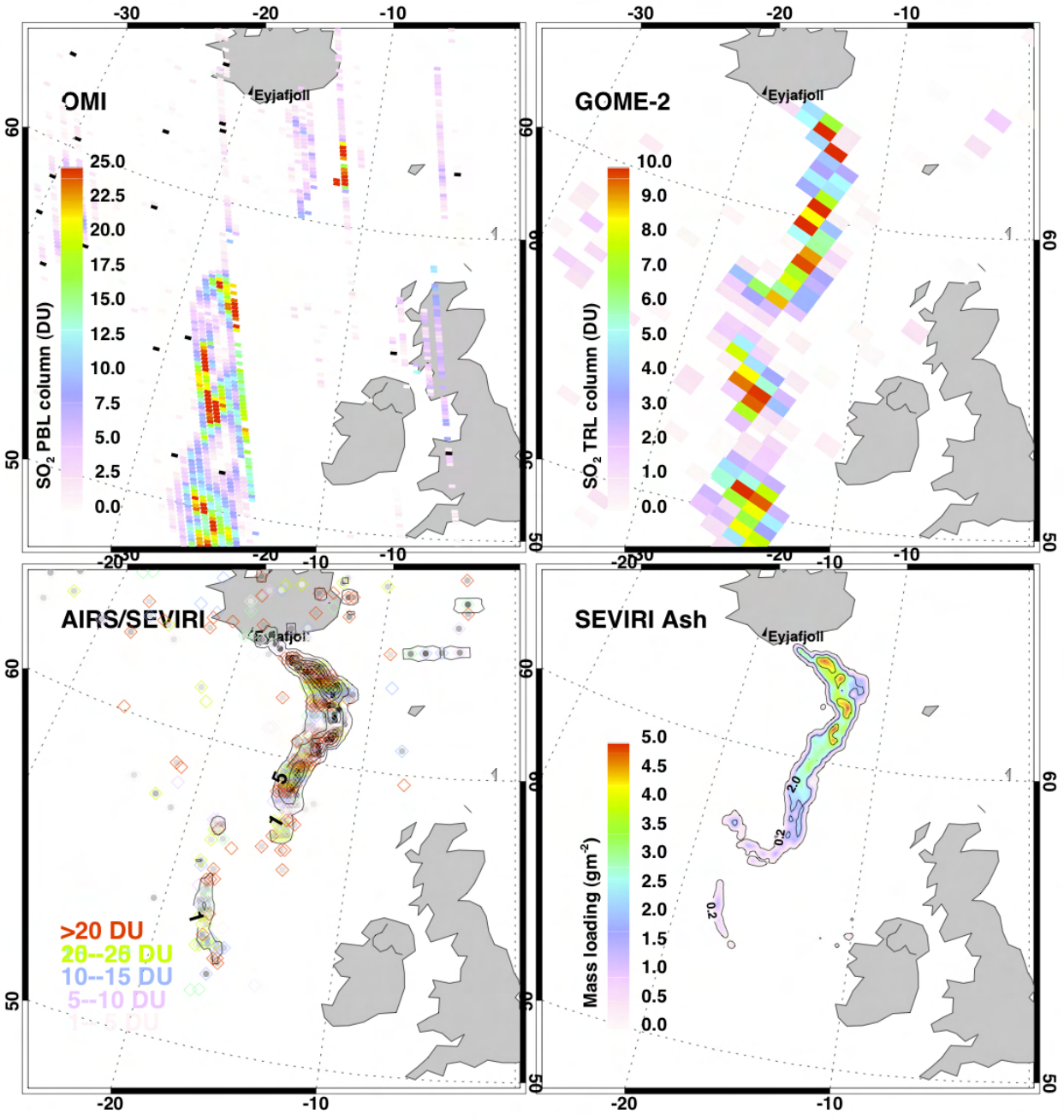

Figure 7.37: SO_2 and ash retrievals for 6 May, 2010. *Top-left panel* shows OMI planetary boundary layer (PBL) SO)2 retrievals; *top-right panel* shows GOME-2 retrievals, *bottom-left panel* shows AIRS retrievals (contours) with SEVIRI 7.3 μm retrievals indicated by the diamonds. *Bottom-right panel*: SEVIRI ash mass loading retrievals.

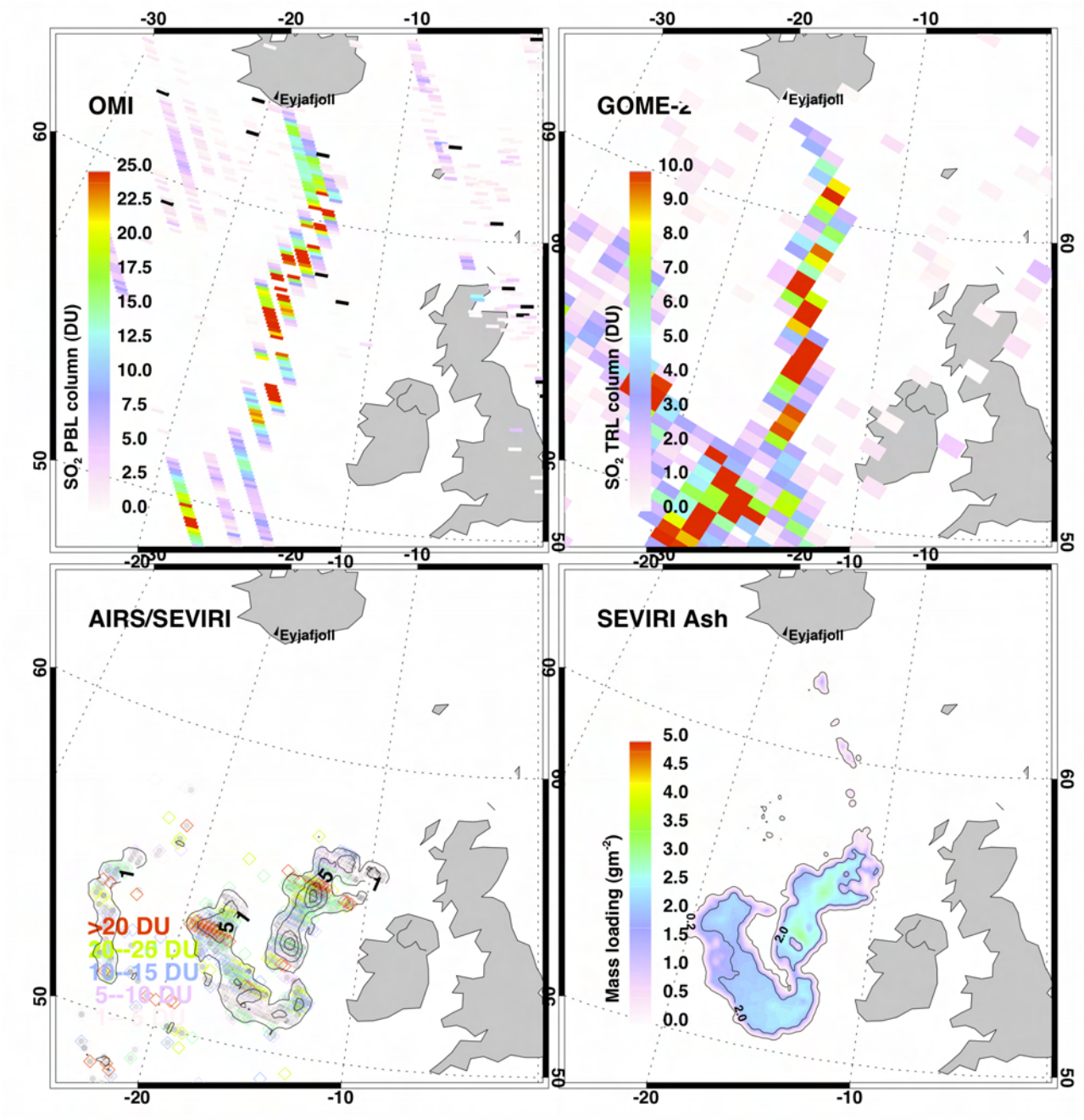

Figure 7.38: SO_2 and ash retrievals for 7 May, 2010. *Top-left panel* shows OMI planetary boundary layer (PBL) SO)2 retrievals; *top-right panel* shows GOME-2 retrievals, *bottom-left panel* shows AIRS retrievals (contours) with SEVIRI 7.3 μm retrievals indicated by the diamonds. *Bottom-right panel*: SEVIRI ash mass loading retrievals.

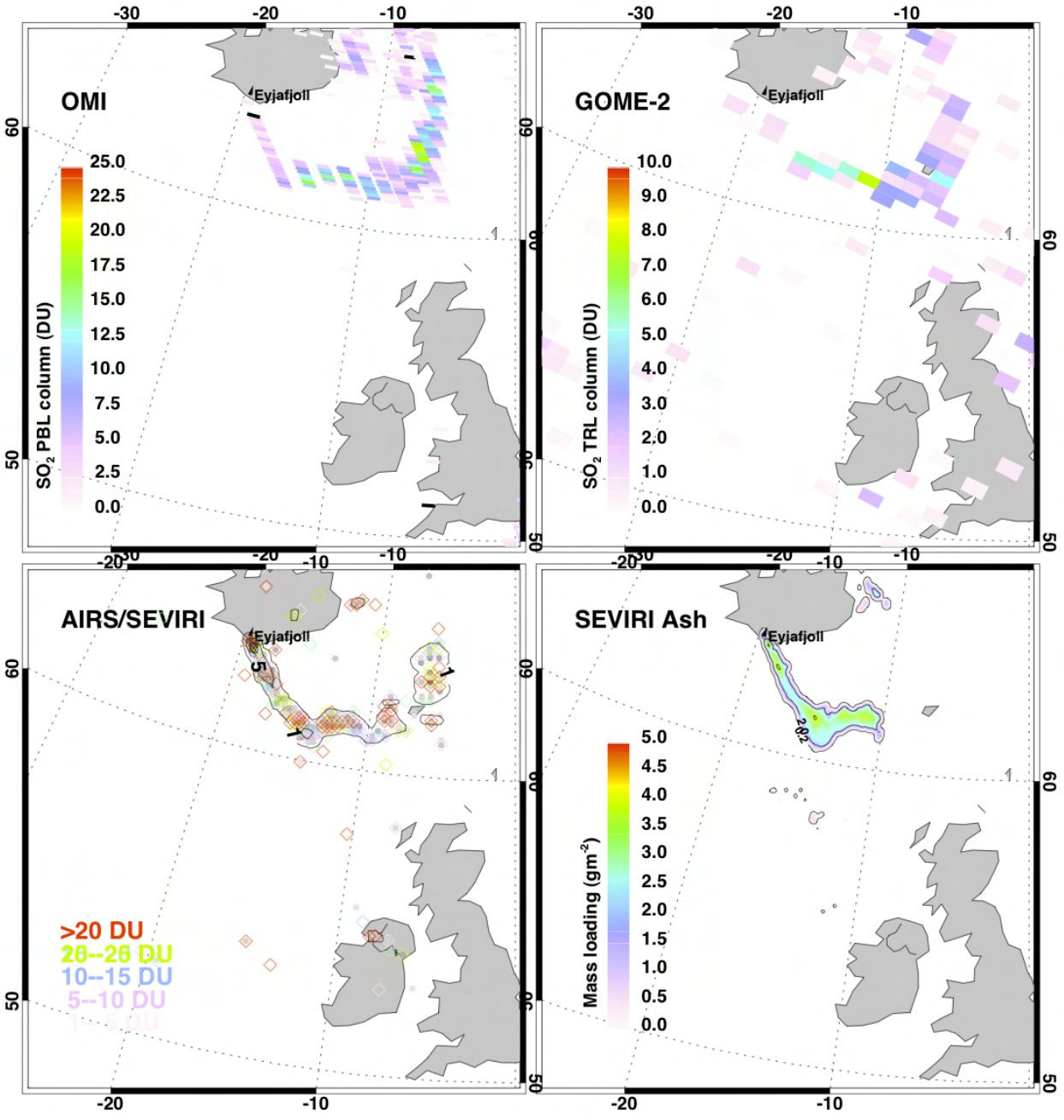

Figure 7.39: SO_2 and ash retrievals for 13 May, 2010. *Top-left panel* shows OMI planetary boundary layer (PBL) SO)2 retrievals; *top-right panel* shows GOME-2 retrievals, *bottom-left panel* shows AIRS retrievals (contours) with SEVIRI 7.3 μm retrievals indicated by the diamonds. *Bottom-right panel*: SEVIRI ash mass loading retrievals.

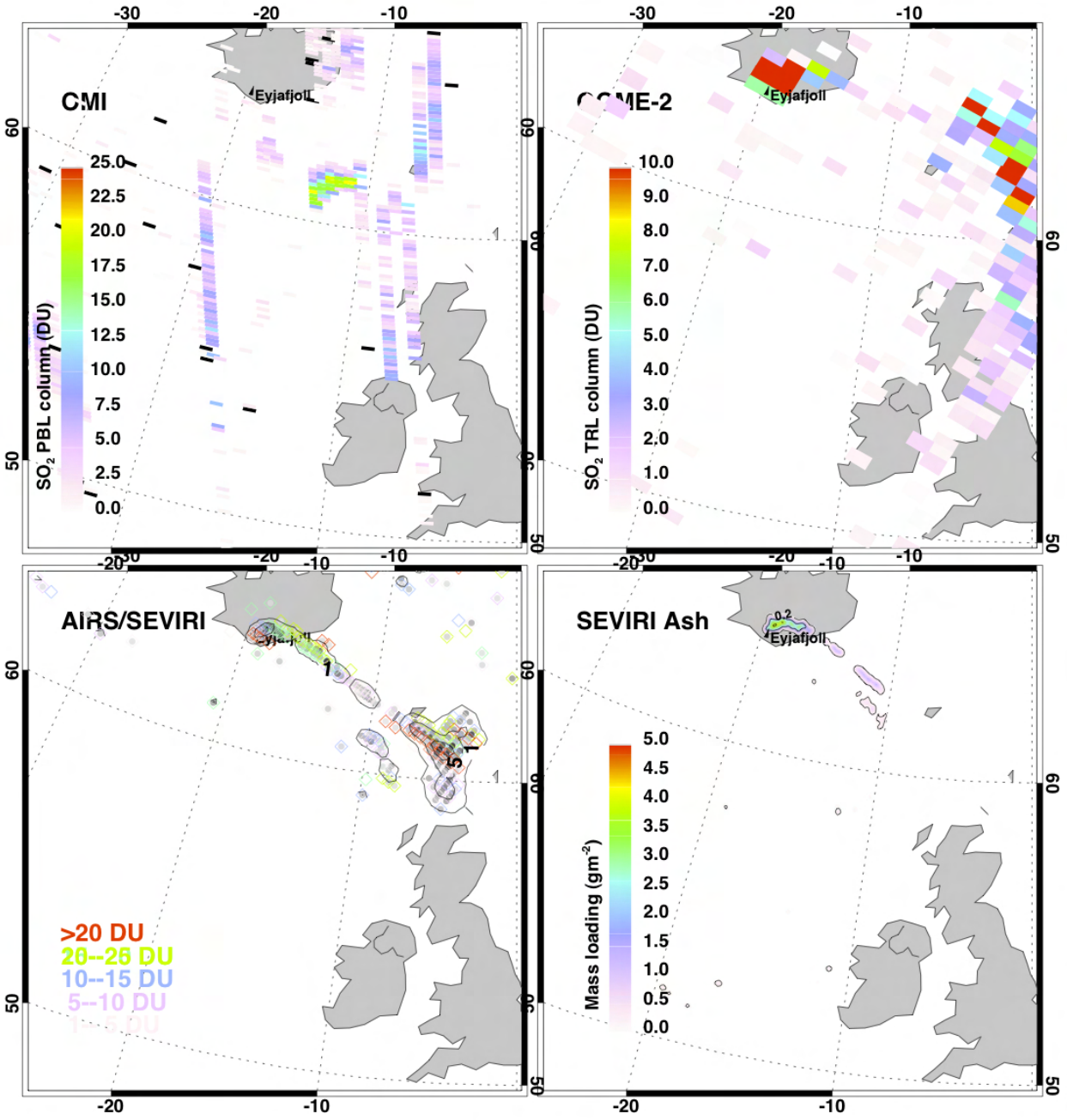

Figure 7.40: SO_2 and ash retrievals for 17 May, 2010. *Top-left panel* shows OMI planetary boundary layer (PBL) SO)2 retrievals; *top-right panel* shows GOME-2 retrievals, *bottom-left panel* shows AIRS retrievals (contours) with SEVIRI 7.3 μm retrievals indicated by the diamonds. *Bottom-right panel*: SEVIRI ash mass loading retrievals.

Chapter 8

Conclusions and Further Work

8.1 Ash retrievals

The retrieval algorithm proposed for determining ash mass loadings from SEVIRI infrared data has been implemented using IDL code and tested on several thousand (>3000) SEVIRI granules, each granule consisting of 759278 pixels. This large number of retrievals necessitates the use of a fast algorithm. The use of pre-computed look-up tables (LUTs) helps to speed up the processing. The algorithm appears to perform quite well based on a small number of validations and through informal comparisons with other retrieval schemes. Some issues that require further investigation include:

A1 **Improved pixel identification.** The algorithm operates only on those pixels deemed to contain ash. This first step is one of *discrimination* and improvements can be made by using more sophisticated cloud detection and perhaps utilising more SEVIRI channels. Daytime detection can be greatly improved by using the SEVIRI visible channels and it would be sensible to implement a daytime ash retrieval scheme and a nighttime scheme, separately. Unfortunately, it is the nighttime retrievals that are more difficult and need more research. Detection of thin ash layers over clear land surfaces (e.g. over Europe on the mornings of 16–19 April, 2010) are particularly difficult. It is recommended that better algorithms for detecting ash over clear land be investigated. Use of ancillary data, from a forecast surface temperature field may be of value in this regard. Some problems of ash identification were also noticed over the ocean with opaque low cloud (ocean stratiform clouds). In these cases the detection algorithm often confused meteorological cloud with ash cloud. Use of the 3.7 μm data during the night might alleviate this problem and also assist in identifying ash clouds over clear land surfaces.

A2 **Improved water vapour correction.** Although this is not a serious problem, improvements can be made by utilising independent estimates of water vapour and applying a correction to the affected SEVIRI IR channels. The strategy adopted here has been to apply a ”scene based” water vapour correction–this is fast and easy to implement, but is also less accurate. An alternate strategy is to utilise LUTs based on simulated radiances (and hence temperatures) determined using an RT model and analysis or forecast atmospheric temperature and humidity profiles. A third approach is to utilise a method based on characteristic (climatological) temperature differences, which can be used to infer

anomalous pixels (e.g. the RAT algorithm, see Table 4.4 and Pergola *et al.*, 2004). This approach implicitly includes water vapour effects.

A3 **Better refractive index data.** This and all other microphysical retrieval algorithms require accurate wavelength dependent refractive index data. Currently, very little is known about the variability of the refractive index of ash in the infrared region between 8–13 μm. A sensitive study would assist in assessing the impact of errors in the refractive index on ash mass loading retrieval. Likewise, better knowledge of the density of ash is needed.

A4 **Validation.** As far as we know there are no independent measurements of ash mass loading that can be directly compared with the SEVIRI (or any other satellite instrument) retrievals. *In situ* and remote estimates (e.g. lidar) of ash concentrations are sometimes made, but cloud geometry is required in order to convert SEVIRI mass loadings to mass concentrations. Intercomparisons with retrievals from others sensors (e.g. MODIS, IASI, AIRS, ASTER, AVHRR and AATSR) are all possible but since the models used are similar this is not a true independent validation. Use of the GOME-2 or OMI aerosol absorbing index (AAI) may be viable but so far there is little theoretical understanding of the AAI. The Caliop lidar on CALIPSO will provide an excellent tool for determining concentrations and it is strongly recommended that further work be done on this; specifically utilising the 40 or so coincidences identified in this study between SEVIRI and Caliop and correlating these with Caliop vertical mass concentrations.

A5 **Better radiative transfer.** The discrete ordinates model and plane parallel cloud model adopted here can be improved. There exist tools to model 3D clouds and include non-spherical particle shapes and polarisation effects. Although it is believed these are mostly second order corrections, it would be sensible to explore better RT models to gauge the size of the modelling errors.

A6 **SEVIRI ash product.** This study suggests that a SEVIRI ash mass loading product can be generated in near real-time and can be improved by the use of ancillary data, such as ECMWF forecast/analysis fields.

8.2 SO_2 retrievals

The SO_2 retrieval schemes based on GOME-2, OMI, AIRS and IASI are relatively mature and significant effort has been expended on developing SO_2 products and characterising errors. OMI and GOME-2 are more sensitive to small amounts of SO_2 and are able to detect SO_2 close to the surface and in the boundary layer. AIRS and IASI detect mid- to upper-troposphere SO_2 well and have the advantage of measuring SO_2 in low light and nighttime conditions. The current OMI row anomaly is of concern and it is recommended that a combination of IR and UV SO_2 products be examined to increase the spatial and temporal coverage of SO_2 detections from space. Work was done to investigate the correspondence between SO_2 and ash using data from GOOME-2, IASI, AIRS and SEVIRI (Thomas and Prata, 2011).

It was found that SEVIRI channels at 7.3 and 8.6 μm are sensitive to SO_2, but correlations with coincident OMI, GOME-2, AIRS and IASI retrievals were not very promising. This may be due different spatial (horizontal and vertical) resolutions of the sensors or an inability to correct the SEVIRI radiances for the compounding effects of clouds and water vapour. Thermal contrast and opacity effects (emission versus absorption) may also be reducing the correlation. Further work is needed on this problem, including:

S1 **Improved pixel identification.** In the same way as for ash identification, better methods for identifying pixels affected by SO_2 are needed. This is complex because one of the SEVIRI channels sensitive to SO_2 is also affected by ash absorption (IR86–SEVIRI channel).

S2 **Low-level and high-level SO_2.** More study is required (using radiative transfer models) to determine the sensitivity of the SEVIRI 7.3 μm and 8.6 μm channels to SO_2 in the lower and upper troposphere. This should be combined with water vapour sensitivity studies.

S3 **Regression schemes.** Although the regression analysis reported here was not very successful it is worth conducting a more detailed study that carefully uses well-chosen coincidences to establish regression coefficients for converting SEVIRI radiances to partial column SO_2. The benefit of this approach is that SEVIRI could be used to fill-in time periods when other sensors are not able to provide SO_2 estimates (e.g. polar orbiters).

S4 **Single-product SO_2.** Currently there are four satellite sensors capable of determining lower to upper troposphere SO_2 partial columns. These are: OMI, GOME-2, AIRS and IASI. MODIS and ASTER are also able to determine SO_2 under certain circumstances. It is recommended that a study combining these retrievals to provide a single, synergistic SO_2 product be undertaken. This product could then be used to investigate improved SEVIRI SO_2 retrievals.

S5 **SEVIRI SO_2 product.** Currently it is not recommended that a SEVIRI SO_2 product be generated as the circumstances under which SO_2 can be retrieved and the accuracies have not been established. For significant ($>$10 DU) upper-tropospheric SO_2 loadings the SEVIRI 7.3 μm retrieval scheme could be used provided a good pixel identification scheme is in place.

Acknowledgement. Lieven Clarisse and Helen Thomas are thanked for providing the IASI and GOME-2 data-sets, respectively.

Chapter 9

Bibliography

Bibliography

Ansmann, A. Tesche, M., Groß, S., Freudenthaler, V., Seifert, P., Hiebsch, A., Schmidt, J., Wandinger, U., Mattis, I., Müller, D., and Wiegner, M., 2010, The 16 April 2010 major volcanic ash plume over central Europe: EARLINET lidar and AERONET photometer observations at Leipzig and Munich, Germany, *Geophys. Res. Lett.*, **37**, L13810, doi:10.1029/2010GL043809.

Bailey, J.E., Dean, K., Dehn, J., and Webley, P. 2009, Integrated Satellite Observations of the 2006 Eruption of Augustine Volcano: U.S. Geological Survey Professional Paper XXXXX, 2009 (in press)

Barton, I.J., Prata, A.J., Watterson, I.G. and Young, S.A., 1992, Identification of the Mount Hudson volcanic cloud over SE Australia, *Geophys. Res. Lett.*, **19**, 1211–1214.

Battan, L.J., 1994, Fundmentals of Meteorology Englewood Cliffs, New Jersey, Prentice-Hall, 29-35 pp.

Berk, A., Bernstein, L. S., and Robertson, D. C., 1989, MODTRAN: A moderate resolution model for LOWTRAN 7, U. S., Air Force Phillips Laboratory, Nascom Air Force Base, MA, U. S. A., **AFGL-TR-89-0122.**.

Bingemer, H., H. Klein, M. Ebert, W. Haunold, U. Bundke, T. Herrmann, K. Kandler, D. Mller-Ebert, S. Weinbruch, A. Judt, K. Ardon-Dryer, Z. Levin, and J. Curtius, 2011, Atmospheric ice nuclei in the Eyjafjallajökull volcanic ash plume, *Atmos. Chem. Phys. Discuss.*, **11**, 2733–2748.

Briggs, G. A., 1975, Plume rise predictions. In *Lectures on Air Pollution and Environmental Impact Analyses*, pp. 59–111., American Meteorological Society, Boston.

Carn, S. A., Pallister, J. S., Lara, L., Ewert, J. W., Watt, S., Prata, A. J., Thomas, R. J., and Villarosa, G., 2009, The unexpected awakening of Chaitèn Volcano, Chile, EOS Trans., **90**(24), 205–206.

Casadevall, T. J., 1994, The 1989/1990 eruption of Redoubt Volcano Alaska: impacts on aircraft operations, J. Volcanol. Geotherm. Res, 62(30), 301–316.

Casadevall, T. J., Delos Reyes, P. J., and Schneider, D. J.: The 1991 Pinatubo Eruptions and Their Effects on Aircraft Operations. In C.G. Newhall, and R. S. Punongbayan (Eds.), 1996., Fire and Mud: eruptions and lahars of Mount Pinatubo, Philippines, 625–636, Quezon City: Philippines Institute of Volcanology and Seismology, Seattle: University of Washington Press.

Constantine, E. K., Bluth, G. J. S., and Rose, W. I., 2000, TOMS and AVHRR sensors applied to drifting volcanic clouds from the August 1991 eruptions of Cerro Hudson, AGU Monograph 116– Remote Sensing of Active Volcanism, Ed. by P. Mouginis-Mark, J. Crisp and J. Fink, pp. 45–64.

Clarisse, L., Hurtmans, D., Prata, A. J., Karagulian, F., Clerbaux, C., De Mazire,M., and P.-F. Coheur, 2010, Retrieving radius, concentration, optical depth, and mass of different types of aerosols from high-resolution infrared nadir spectra, *Appl. Opt.*, **49**(19), 3713–3722.

Clarisse, L., Prata, A. J., Lacour, J.-L., Hurtmans, D., Clerbaux, C., and P.-F. Coheur, 2010, A correlation method for volcanic ash detection using hyperspectral infrared measurements, *Geophys. Res. Lett.*, **37**, L19806, doi:10.1029/2010GL044828.

Clerbaux, C., Turquety, S., Hadji-Lazaro, J., George, M., Boynard, A, Pommier, M, Coheur, P.-F., Hurtmans, D., Wespes, C., Razavi, A., and Herbin, H., 2007, Monitoring of volcanic SO_2 using thermal infrared IASI/METOP sounders (TES, IASI), paper presented at the Support to Aviation Control Service meeting, Toulouse, 26-27 November, 2007.

Dean, K.G., Dehn, J., Papp, K.R., Smith, S., Izbekov, P., Peterson, R., Kearney, C., and Steffke, A., 2004, Integrated satellite observations of the 2001 eruption of Mt. Cleveland, Alaska *J. Volcanol. Geothermal Res.*,**135**, 51–73.

Dean, K., J. Dehn, K. Engle, P. Izbekov, K. Papp, and M. Patrick, 2002, Operational satellite monitoring of volcanoes at the Alaska Volcano Observatory. Adv. Environ. Monit. Model., 1, 3–35.

Dean, K., Bowling, S.A., Shaw, G., and, and Tanaka, H., 1994, Satellite Analyses Of Movement And Characteristics Of The Redoubt Volcano Plume, January 8, 1990 *J. Volcanol. Geothermal Res.*, **62**, p. 339–352.

Draxler, R. R., and Rolph, G. D., 2003, HYSPLIT (Hybrid Single-Particle Lagrangian Integrated Trajectory) model, Access via NOAA ARL READY Website: `http://www.arl.noaa.gov/ready/hysplit4.html`, NOAA Air Resources Laboratory, Silver Spring, MD, USA.

Ellrod, G. P., Connell, B. H., and Hillger, D. W., 2003, Improved detection of airborne volcanic ash using multispectral infrared satellite data, *J. Geophys. Res.*, **108**(D12), 4356, doi:10.1029/2002JD002802.

Emeis, S., W. Junkermann, K. Schäfer, R. Forkel, P. Suppan, H. Flentje, S. Gilge, W. Fricke, M. Wiegner, V. Freudenthaler, S. Groß, L. Ries, F. Meinhardt, C. Münkel, and F. Obleitner, 2010, Spatial structure and dispersion of the 16/17 April 2010 volcanic ash cloud over Germany, *Atmos. Chem. Phys. Discuss.*, **10**, 26117–26155.

Evans, B. T. N., 1988, An interactive program for estimating extinction and scattering properties of most particulate clouds, *Department of Defence Report* **MRL-R-1123**, Defence Science and Technology Organisation, Materials Research Laboratory, P.O. Box 50, Ascot Vale, Victoria 3032, Australia.

Fierstein, J., 2007, Explosive eruptive record in the Katmai region, Alaska Peninsula: an overview, *Bull. Volcanol.*, **69**, 469–509.

Flentje, H., Claude, H., Elste, T., Gilge, S., Köhler, U., C. Plass-Dülmer, C., Steinbrecht, W., Thomas, W., Werner, A., and W. Fricke, 2010, The Eyjafjallajökull eruption in April 2010 detection of volcanic plume using in-situ measurements, ozone sondes and a new generation ceilometer network, *Atmos. Chem. Phys. Discuss.*, **10**, 14947–14968.

Gangale, G., Prata, A. J., and L. Clarisse, 2009 The infrared spectral signature of volcanic ash determined from high-spectral resolution satellite measurements 'em Rem. Sens. Environ., **114**, 414–425.

Gasteiger, J., S. Groß, V. Freudenthaler, and M. Wiegner, 2010, Volcanic ash from Iceland over Munich: mass concentration retrieved from ground-based remote sensing measurements, *Atmos. Chem. Phys. Discuss.*, **10**, 26705–26750.

Goody, R. M., 1964, Atmospheric Radiation. I. Theoretical basis, *Oxford University Press*, Oxford, England, 436pp.

Griffith, D.W.T., 1996, Synthetic Calibration and Quantitative Analysis of Gas-Phase FT-IR Spectra, *Applied Spectroscopy*, **50**(1), 59–69.

Gu,Y., Rose, W. I., Schneider, D. J., Bluth, G. J. S., and I. M. Watson, 2005, Advantageous GOES IR results for ash mapping at high latitudes: Cleveland eruptions 2001, *Geophys. Res. Lett.*, **32**, L02305, doi:10.1029/2004GL021651.

Guffanti, M., Casadevall, T. J., and K. Budding, Encounters of Aircraft with Volcanic Ash Clouds: A Compilation of Known Incidents, 19532009, U.S. Geological Survey Data Series 545, ver. 1.0, 12 p., plus 4 appendixes including the compilation database [`http://pubs.usgs.gov/ds/545/`].

Hanstrum, B.N., and Watson, A.S., 1983, A case study of two eruptions of Mount Galunggung and an investigation of volcanic eruption cloud characteristics using remote sensing techniques, *Aust. Met. Mag.*,**31**, 131–177.

Harris, D.M., and Rose, W., 1983, Estimating Particle Sizes, Concentration, and Total Masss of in Volcanic Ash Clouds using Weather Radar *J. Geophys. Res.*, **88**, 10,969–10,983.

Harris, D.M., Rose, W., Roe, R., and Thompson, 1981, Radar Observations of Ash Eruptions, in Lipman, P.W., and Mullineaux, D.R., eds., The 1980 Eruptions of Mount St. Helens, Washington U.S. Geol. Survery Circular 1250, 323–333.

Heue, K.-P. , C. A. M. Brenninkmeijer, A. K. Baker, A. Rauthe-Schöch, D. Walter, T. Wagner, C. Hörmann, H. Sihler, B. Dix, U. Frieß, U. Platt, B. G. Martinsson, P. F. J. van Velthoven, M. Hermann, A. Zahn, and R. Ebinghaus, 2010, SO_2 and BrO observation in the plume of the Eyjafjallajökull volcano 2010: CARIBIC and GOME-2 retrievals *Atmos. Chem. Phys. Discuss.*, **10**, 29631–29682.

Hillger, D. W. and Clark, J. D., 2002a, Principal component image analysis of MODIS for volcanic ash. Part I: Most important bands and implications for future GOES imagers, *J. Appl. Meteorol.*, **41**, 985–1001.

Hillger, D. W. and Clark, J. D., 2002b, Principal component image analysis of MODIS for volcanic ash. Part II: Simulation of current GOES and GOES-M imagers, *J. Appl. Meteorol.*,**41**, 1003–1010.

Hofmann, D. J., and Rosen, J. M., 1984, Balloonborne particle counter observations of the El Chichón aerosol layers in the 0.01–1.8 μm radius range, *Geofisica International*, **23**, 155–185.

Holasek, R. E., and W. I. Rose, 1991, Anatomy of 1986 Augustine Volcano eruptions as recorded by multispectral images processing of digital AVHRR weather satellite data, *Bull. Volcanol.*, **53**, 42–435.

Holasek, R. E., Woods, A. W. and Self, S., 1996, Experiments on gas-ash separation processes in volcanic umbrella clouds, *J. Volcanol. Geotherm. Res.*,**70**, 169–181.

Holasek, R., and Self, S., 1995, GOES weather satellite observations and measurements of the May 18, 1980, Mt.St.Helens eruption *J. Geophys. Res.*, **100**, 8469–8487.

Holton, J., 2004, An introduction to dynamic meteorology San Diego, California, *Academnic Press*, 116–117 pp.

Ivlev, L. S., and Popova, S. I., 1973, The complex refractive indices of substances in the atmospheric-aerosol dispersed phase, *Atmospheric Oceanic Physics*, **9**(10), 587–591.

King, M. D., Harshvardhan, and Arking, A., 1984, A model of the radiative properties of the El Chichón stratospheric layer, *J. Climate Appl. Meteorol.*, **23**, 1121–1137.

Lacasse, C., Karlsdottir, S., Larsen, G., Soosalu, H., Rose, W.I., and Ernst, G.G.J., 2004, Weather radar observations of the Hekla 2000 eruption cloud, Iceland. *Bull. Volcanol.*, **66**, 457–473.

Lutgens, F.K., and Tarbuck, E.J., 1986, The Atmosphere: An Introduction to Meteorology Englewood Cliffs, New Jersey, Prentice-Hall, 154–160 pp.

Lutgens, F.K., and Tarbuck, E.J., 1995, The Atmosphere: Englewood Cliffs, New Jersey, Prentice-Hall, 462 pp.

Lynch, J.S., and Stephens, G., 1996, Mount Pinatubo: A satellite perspective of the June 1991 eruptions In Newhall, C., and Punongbayan, R.S., eds., Fire and Mud: Seattle, University of Washington Press, p. 637–646.

Malingreau, J. -P. and Kaswanda, 1986, Monitoring volcanic eruptions in Indonesia using weather satellite data: The Colo eruption of July 28, 1983, *J. Volcanol. Geothermal Res.*,**27**(1–2), 179–194.

Manins, P. C., 1985, Cloud heights and stratospheric injections resulting from a thermonuclear war, *Atmos. Environ.*, **19**(8), 1245–1255.

Marzano, F.S., Vulpiani, G., and Rose, W.I., 2006, Microphysical characterization of microwave radar reflectivity due to volcanic ash clouds *IEEE Trans. Geosci. Remote Sens.*, **44**, 313–327.

Masuda, K., and Takashima, T., 1990, Deriving cirrus information using the visible and near-ir channels of the future NOAA-AVHRR radiometer, *Remote Sens. Environ.*, **31**, 65—81.

Matson, M., 1984, The 1982 El Chichón volcano eruptions–a satellite perspective, *J. Volcanol. Geotherm. Res.*, **23**, 1–10.

Miller, T. P., and Casadevall, T. J., 1999, Volcanic ash hazards to aviation, Encyclopedia of Volcanoes, edited by H. Sigurdsson, B. Houghton, S. R. McNutt, H. Ryman, and J. Stix, Academic Press, San Diego, pp. 915–930.

Miller, T. P., and Chouet, B. A. (eds.), 1994, The 1989-1990 eruptions of Redoubt volcano, Alaska, *J. Volcanol. Geothermal Res.*, **62**(1): 530.

Mosher, F. R., 2000, Four channel volcanic ash detection algorithm, Preprint Volume, 10th Conf. Satellite Meteorol. and Oceanography, 9–14 January, 2000, Long Beach, California, 457–460.

Newell, R. E., and Deepak, A. (*Eds.*), 1982, Mount St. Helens eruptions of 1980: Atmospheric effects and potential climate impact, *NASA Workshop Report*, **NASA SP-458**, Scientific and Technical Information Branch, NASA, Washington, D. C., 119 pp.

Oswalt, J.S., Nichols, W., and O'Hara, J.F., 1996, Metereological Observations of the 1991 Mount Pinatubo Eruption In Newhall, C., and Punongbayan, R.S., eds., Fire and Mud, Eruption and Lahars of Mount Pinatubo Philippines, University of Washington Press, 625–636.

Pavalonis, M. J. Advances in Extracting Cloud Composition Information from Spaceborne Infrared Radiances: A Robust Alternative to Brightness Temperatures Part I: Theory, Submitted to *J. Appl. Meteorol.*.

Pavolonis, M. J. Advances in extracting cloud composition information from spaceborne infrared radiances: A robust alternative to brightness temperatures. Part II: Proof of concept. To be submitted to *J. Applied Meteor. and Climatol.*.

Pavolonis, M. J., Feltz, W. F., Heidinger, A. K., and Gallina, G. M., 2006, A daytime complement to the reverse absorption technique for improved automated detection of volcanic ash, *J. Atmos. Oceanic Technol.*, **23**, 1422–1444.

Pergola, N., Tramutoli, V., Marchese, F., Scaffidi, I., and Lacav, T., 2004, Improving volcanic ash cloud detection by a robust satellite technique, *Rem. Sens. Environ.*,**90**, 1–22.

Pieri, D., Ma, C., Simpson, J. J., Hufford, G., Grindle, T., and Grove, C., 2002, Analyses of in-situ airborne ash from the February 2000 eruption of Hekla volcano, Iceland, *Geohpys. Res. Lett.*, **29**(16), 10.1029/2001GL013688.

Prata, A. J., 1989a, Observations of volcanic ash clouds using AVHRR-2 radiances. *Int. J. Remote Sensing*, **10**(4-5), 751–761.

Prata., A. J., 1989b, Radiative transfer calculations for volcanic ash clouds, *Geophys. Res. Lett.*,**16**(11), 1293–1296.

Prata, A. J. and Barton, I. J., 1994, Detection and discrimination of volcanic ash clouds by infrared radiometry – I: theory. In: Casadevall, T. J., editor. Volcanic Ash and aviation safety: proceedings of the first International Symposium on Volcanic Ash and Aviation Safety; Seattle, Wash. Washington, D.C.: U.S. G.P.O., *U.S. Geological Survey bulletin*, **2047**, 305–311.

Prata, A. J., Bluth, G. J. S., Rose, W. I., Schneider, D. J., and Tupper, A. C., 2001, Comments on Failures in detecting volcanic ash from a satellite-based technique *Rem. Sensing Environ.*, **78**, 341–346.

Prata, A. J. and Grant, I. F., 2001, Retrieval of microphysical and morphological properties of volcanic ash plumes from satellite data: Application to Mt. Ruapehu, New Zealand., *Quart. J. Roy. Meteorol. Soc.*, **127**(576B), 2153–2179.

Prata, A. J., Rose, W. I., Self, S. and O'Brien, D. M., 2003, Global, long-term sulphur dioxide measurements from TOVS data: A new tool for studying explosive volcanism and climate, *Volcanism and the Earth's Atmosphere*, **Geophys. Monograph 139**, AGU, 75–92.

Prata, A. J., and Kerkmann, J., 2007, Simultaneous retrieval of volcanic ash and SO_2 using MSG-SEVIRI measurements, *Geophys. Res. Lett.*,**34**, L05813, doi:10.1029/2006GL028691.

Press, W. H., Flannery, B. P., Teukolsky, S. A., and Vetterling, W. T., 1986, Numerical Recipes, *Cambridge University Press*, 818 pp.

Przedpelski, Z. J., and Casadevall, T. J., 1994, Impact of volcanic ash from 15 December 1989 Redoubt volcano eruption on GE CF6-80C2 turbofan engines, *In Volcanic ash and aviation safety: Proc. of the First International Symposium on Volcanic Ash and Aviation Safety*, US. Geological Survey Bulletin **2047**, 129–135, Seattle, Washington, July, 1991.

Randel, D. L., Vonder Harr, T. H., Ringerud, M. A., Stephens, G. L., Greenwald, T. J., and C. L. Combs, 1996, A new global water vapor dataset, *Bull. Amer. Meterol. Soc.*, **77**(6), 1233–1246.

Rodgers, C. D., 2000, Inverse Methods for Atmospheric Sounding: Theory and Practice, *World Scientific Publishing Co., Pte.,Ltd.*, PO Box 128, Farrer Rd., Singapore, 238pp.

Rothman, L. S., A. Barbe, D.C. Benner, L.R. Brown, C. Camy-Peyret, M.R. Carleer, K. Chance, C. Clerbaux, V. Dana, V.M. Devi, A. Fayt, J.-M. Flaud, R.R. Gamache, A.Goldman, D. Jacquemart, K.W. Jucks, W.J. Lafferty, J.-Y. Mandin, S.T. Massie, V. Nemtchinov, D.A. Newnham, A. Perrin, C.P. Rinsland, J. Schroeder, K.M. Smith,M.A.H. Smith, K. Tang, R.A. Toth, J. Vander Auwera, P. Varanasi, and K. Yoshino, 2003, The HITRAN Molecular Spectroscopic Database: Edition of 2000 Including Updates of 2001, *J. Quant. Spec. Rad. Trans.*, **82**, (1-4).

Rose, W.I., Kostinski, A.B., and Kelly, L., 1995, Real-Time C-Band Radar Observations of 1992 Eruption Clouds from Crater Peak, Mount Spurr Volcano, Alaska US Geologic Survey Bull. 2139, 19–26.

Rose, W. I., Delene, D. J., Schneider, D. J., Bluth, G. J. S., Kruger, A. J., Sprod, I., McKee, C., Davies, H. L., and Ernst, G. J.: Ice in the 1994 Rabaul eruption: Implications for volcanic hazard and atmospheric effects, *Nature*, **375**, 477–479, 1995.

Rose, W. I., G. J. S. Bluth, *et al.*, 2000, Integrating retrievals of volcanic cloud characteristics from satellite remote sensors: a summary, *Phil. Trans. Roy. Soc. Lond.*, **Series A**–*Mathematical Physical And Engineering Sciences*, **358**(1770): 1585–1606.

Rose, W. I., Bluth, G. J. S. and I. M Watson, 2004, Ice in Volcanic Clouds: When and Where? Proceedings of the 2nd International Conference on Volcanic Ash and Aviation Safety, OFCM Washington D. C., Session 3, 61.

Sawada, Y., 1987, Study on analysis of volcanic eruptions based on eruption cloud image data obtained by the Geostationary Meteorological Satellite (GMS), Technical Reports of the Meteorological Research Institue, 22, 335 pp.

Sawada, Y., 1996, Detection of explosive eruptions and regional tracking of volcanic ash clouds with geostationary meteorological satellites (GMS), Monitoring and Mitigation of Volcano Hazards, Scarpa, R. and Tilling, RI. (eds.), Springer-Verlag Berlin Heidelberg, pp. 299–314.

Schmetz, J., Pili, P., Tjemkes, S., Just, Dieter, Kerkmann, J., Rota, S., and A. Ratier, 2002, An introduction to Meteosat Second Generation (MSG) Bull. Amer. Meteorol. Soc., DOI: 10.1175/ BAMS-83-7-Schmetz-1; DOI: 10.1175/BAMS-83-7-Schmetz-2, 977–989.

Schneider, D. J., Rose, W. I., and Kelley, L., 1995, Tracking of 1992 eruption clouds from Crater Peak of Mount Spurr volcano, Alaska, using AVHRR, U. S. Geol. Survey Bull., 2139, 27–36.

Schneider, D. J., Rose, W. I., Coke, L. R., and Bluth, G. J. S., 1999, Early evolution of a stratospheric volcanic eruption cloud as observed with TOMS and AVHRR, *J. Geophys. Res.*, **104**(D4), 4037–4050.

Searcy, C., Dean, K., and Stringer, W., 1998, PUFF: A high-resolution volcanic ash tracking model *J.Volcanol. Geothermal Res.*, **80**, 1–16.

Schumann, U., B. Weinzierl, O. Reitebuch, H. Schlager, A. Minikin, C. Forster, R. Baumann, T. Sailer, K. Graf, H. Mannstein, C. Voigt, S. Rahm, R. Simmet, M. Scheibe, M. Lichtenstern, P. Stock, H. Rba, D. SchŁuble, A. Tafferner, M. Rautenhaus, T. Gerz, H. Ziereis, M. Krautstrunk, C. Mallaun, J.-F. Gayet, K. Lieke, K. Kandler, M. Ebert, S. Weinbruch, A. Stohl, J. Gasteiger, H. Olafsson, and K. Sturm, 2010, Airborne observations of the Eyjafjalla volcano ash cloud over Europe during air space closure in April and May 2010, *Atmos. Chem. Phys. Discuss.*, **10**, 22131–22218.

Sparks, R.S.J., Bursik, M.I., Carey, S.N., Gilbert, R.S., Glaze, L.S., Sigurdsson, H., and Woods, A.W.: Volcanic Plumes New York, John Wiley and Sons, 574 pp., 1997.

Simpson, J. J., Hufford, G., Pieri, D., and Berg, J.: Failures in detecting volcanic ash from a satellite-based technique, *Remote Sens. Environ.*, **72**, 191–217, 2000.

Simpson, J. J., Hufford, G., Pieri, D., Servranckx, R. and Berg, J., 2002, The February 2001 Eruption of Mount Cleveland, Alaska: Case Study of an Aviation Hazard, *Weather and Forecasting*, **17**, 691–704.

Sokolik, I. N., and Toon, O. B., 1999, Incorporation of mineralogical composition into models of the radiative properties of mineral aerosol from UV to IR wavelengths, *J. Geophys. Res.*, **104** (D8), 9423–9444.

Stamnes, K. and Swanson, R. A., 1981, A new look at the discrete ordinates method for radiative transfer calculations in anisotropically scattering atmospheres, *J. Atmos. Sci.*, **38**, 387–399.

Stohl, A., A. J. Prata, S. Eckhardt, L. Clarisse, A. Durant, S. Henne, N. I. Kristiansen, A. Minikin, U. Schumann, P. Seibert, K. Stebel, H. E. Thomas, T. Thorsteinsson, K. Trseth, and B. Weinzierl, 2011, Determination of time- and height-resolved volcanic ash emissions for quantitative ash dispersion modeling: The 2010 Eyjafjallajökull eruption, *Atmos. Phys. Chem. Discuss.*, *Accepted.*

Stohl, A., Forster, C., Frank, A., Seibert, P., and Wotawa, G., 2005 Technical note: The Lagrangian particle dispersion model FLEXPART version 6.2. *Atmos. Chem. Phys.*, **5**, 2461–2474.

Thomas, H. E. and Prata, A. J., 2011, Sulphur dioxide as a volcanic ash proxy during the AprilMay 2010 eruption of EyjafjallajökullVolcano,Iceland, *Atmos. Chem Phys. Discuss.*, **11**, 7757–7780.

Tupper, A., Carn, S. A., Davey, J., Kamada, Y., Potts, R. J., Prata, A. J., and Tokuno, M., 2004, An evaluation of volcanic cloud detection techniques during recent significant eruptions in the western Ring of Fire, *Remote Sens. Environ.*, **91**, 27–46.

Tupper A, Itikarai I, Richards, M. S., *et al.*, 2007, Facing the challenges of the International AirwaysVolcano Watch: the 2004/05 eruptions of Manam, Papua New Guinea. *Weather and Forecasting*,**22**(1):175–191.

Turco, R.P., Toon, O.B., Whitten, R.C., Hamill, P., and Keesee, R.G., 1983, The 1980 eruptions of Mt. St. Helens: Physical and chemical processes in the stratospheric clouds *J. Geophys. Res.*, **88**, 5299–5319.

Volz, F. E., 1973, Infrared optical constants of ammonium sulfate, Sahara dust, volcanic pumice, and flyash, *Appl. Opt.*, **12**(3), 564–568.

Watkin, S.C., 2003, The application of AVHRR data for the detection of volcanic ash in a Volcanic Ash Advisory Centre, *Meteorol. Appl.*, **10**, 301–311.

Watson, I. M., Realmuto, V. J., Rose, W. I., Prata, A. J., Bluth, G. J. S., Gu, Y., Bader, C. E., and T. Yu, 2004, Thermal infrared remote sensing of volcanic emissions using the moderate resolution imaging spectroradiometer, *J. Volcanol. Geotherm. Res.*, **135**, 75–89.

Webley, P. W., Atkinson, D., Collins, R. L., Dean, K., Fochesatto, J., Sassen, K., Cahill, C. F., Prata, A. J., Flynn, C. J. and K. Mizutani, 2008, Predicting and validating the tracking of a volcanic ash cloud during the 2006 eruption of Mt. Augustine volcano, *Bull. Amer. Meteorol. Soc.*, DOI:10.1175/2008BAMS2579.1, 1647–1657.

Wen, S., and Rose, W. I., 1994, Retrieval of sizes and total masses of particles in volcanic clouds using AVHRR bands 4 and 5, *J. Geophys. Res.*, **99**(D3), 5421–5431.

Winker D. M., Hunt, W. H., and McGill, M. J, 2007, Initial performance assessment of CALIOP, *Geophys. Res. Lett.*,**34**, L19803, doi:10.1029/2007GL030135.

Wood, J., Scott, C., and Schneider, D., 2007, WSR-88D radar Observations of Volcanic Ash, Fourth International Workshop on Volcanic Ash World Meterological Organization (WMO) in close collaboration with the International Civil Aviation Organziation (ICAO) and the Civil Aviation Authority of New Zealand: Rotorua, New Zealand.

Woods, A.W., and Self, S., 1992, Thermal disequilibrium at the top of volcanic clouds and its effect on estimates of the column height *Nature*, **355**, 628–630.

Yu, T., Rose, W. I. and Prata, A. J., 2002, Atmospheric correction for satellite-based volcanic ash mapping and retrievals using split window IR data from GOES and AVHRR, *J. Geophys. Res.*, **107**(D16), 4311, 10.1029/2001JD000706.

Zehner, C. (Editor), 2010, Monitoring volcanic Ash from Space ESA-Eumetsat workshop on the 14 April to 23 May 2010 eruption at the Eyjafjll volcano, South iceland, STM-280, ESA/Esrin, 58pp, July, 2010.

Chapter 10

Appendix I: List of Acronyms

ASTER	Advanced Spaceborne Thermal Emission and Reflection Radiometer
AIRS	Atmospheric InfraRed Spectrometer
ATSR	Along-Track Scanning Radiometer
AVHRR	Advanced Very High Resolution Radiometer
CALIPSO	Cloud-Aerosol Lidar and Infrared Pathfinder Satellite Observations
DOAS	Differential Optical Absorption Spectroscopy
GOES	Geosynchronous Orbiting Environmental Satellite
GOME	Global Ozone Monitoring Experiment
HIRS	High resolution InfraRed Sounder
HYSPLIT	HYbrid Single-Particle Lagrangian Integrated Trajectory
IASI	Infrared Atmospheric Sounding Interferometer
IR	InfraRed
MetOP	Operational meteorological satellite
MLS	Microwave Limb Sounder
MODIS	Moderate Resolution Imaging Spectroradiometer
MSG	Meteosat Second Generation
MUT	Mid and Upper- Troposphere
NOAA	National Oceanographic and Atmospheric Administration
OMI	Ozone Monitoring Instrument
PUFF	Volcanic Ash Tracking Model
SCIAMACHY	SCanning Imaging Absorption SpectroMeter for Atmospheric ChartographY
SEVIRI	Spinning Enhanced Visible and InfraRed Imager
TIROS	Television and Infrared Orbiting Satellite
TOMS	Total Ozone Mapping Spectrometer
UTLS	Upper Troposphere Lower Stratosphere
UV	Ultra-Violet
VISSR	Visible and Infrared Spin Stabilised Radiometer

Chapter 11

Appendix II: The data-set

Data

The input SEVIRI data set used in this consists of a subset of the full-disk data. Each subset is designated as a granule and consists of:

1 1537 pixels by 494 lines of calibrated, geolocated brightness temperatures.

2 Five SEVIRI infrared channels: 6.3, 7.3, 8.6, 11.0 and 12.0 μm.

3 A time slot at each 15 minute interval starting on 14.04.2010 00:00 UT and ending on 22.05.2010 23:45 UT.

Ancillary data

Ancillary data used:

1 **SEV1_GEOLOC.hdf**. A file containing longitudes and latitudes for the full-disk. An IDL routine is used to read this file and provide a subset for the 1537x494 granule.

2 **volcano_catalog**. Data-base of holocene volcano locations and activity parameters.

3 **c07042010.txt, c05052010.txt**. CALIPSO ground track data for April and May 2010.

IDL routines

The following IDL routines (listings provided in Appendix III) were used in this study.

Routine	Purpose
bright.pro	Inverse Planck function
get_sublonlat.pro	Returns longitudes and latitudes
parallax.pro	Implement parallax correction
read_SEVIRI.pro	Reads SEVIRI subset brightness temperatures
read_SEVI_geo.pro	Loads the gelocation file
SPT_TL_VIEW_ANGLES.pro	Calculates SEVIRI geometrical parameters
wv_correction.pro	Water vapour correction
get_mass.pro	Calculates pixel ash mass loading
read_volcano_catalog.pro	Iterrogates the volcano catalog and returns location of named volcano
read_calipso_orbit	Reads the CALIPSO ground-track data
RTGRetrieval.pro	Radius, optical depth, general retrieval

Look-up tables

The following look-up tables were generated by the RT model. The file naming convention is:

domTsSSSTcCCC.txt

where,
SSS=Surface temperature (K)
CCC=Cloud-top temperature (K)

T_s	T_c	Filename
225	200	domTs225Tc200.txt
...	200	...
305	200	domTs305Tc200.txt
230	205	domTs230Tc200.txt
...	205	...
305	205	domTs305Tc205.txt
...	...	...
305	300	domTs305Tc300.txt

Each file contains a header, similar to:

```
90.00000       89.69636       88.41199       86.14771       82.97526
78.98523       74.27671       68.94904       63.09620       56.80390
50.14837       43.19667       36.00768       28.63359       21.12194
13.52020
WAVENUMBER                = 836.36
EXTINCTION EFFICIENCY     = 0.179
PARTICLE SIZE             =   0.25 microns
SURFACE TEMPERATURE       =  305.0 K
```

```
CLOUD TEMPERATURE        =  230.0 K
SINGLE SCATTERING ALBEDO= 0.24420E+00
ASYMMETRY PARAMETER      = 0.63855E-01
```

The first set of 16 numbers are the Guassian quadrature angles (in degrees), followed by:
the central wavenumber of the SEVIRI channel,
extinction efficiency,
particle size (radius),
surface temperature,
cloud (top) temperature,
single scattering ablbedo,
asymmetry parameter.

After this there are 400 x 16 temperatures (K) corresponding to optical optical depths from 0.02 to 7.98 in steps of 0.02, defined in column 1. This is then repeated for the second SEVIRI channel and then repeated again for each radius step, starting at 0.25 μm and ending at 32 μm.